Stochastic Performance Analysis and Staged Control System Designs for Space Based Interferometers

by

Kuo-Chia Liu

B.S., University of Maryland at College Park (1996)
M.S., University of Maryland at College Park (1998)

Submitted to the Department of Aeronautics and Astronautics
in partial fulfillment of the requirements for the degree of

Doctor of Philosophy

at the

MASSACHUSETTS INSTITUTE OF TECHNOLOGY

June 2003

Author ....
Department of Aeronautics and Astronautics
May 16, 2003

Certified by ....
David W. Miller
Associate Professor of Aeronautics and Astronautics
Thesis Committee Chairman

Certified by ....
Jonathan P. How
Associate Professor of Aeronautics and Astronautics

Certified by ....
Carl A. Blaurock
Senior Engineer, Mide Technology Corporation

Accepted by ....
Edward M. Greitzer
H.N. Slater Professor of Aeronautics and Astronautics
Chair, Committee on Graduate Students

Stochastic Performance Analysis and Staged Control System Designs for Space Based Interferometers

by

Kuo-Chia Liu

Submitted to the Department of Aeronautics and Astronautics
on May 16, 2003, in partial fulfillment of the
requirements for the degree of
Doctor of Philosophy

Abstract

Space based interferometry missions have the potential to revolutionize astrometry, providing observations of unprecedented accuracy. Realizing the full potential of these interferometers poses several significant technological challenges. One of the most significant challenges is regulating the light pathlength, from the collecting telescopes to the combining instrument, with nanometer accuracy, despite the presence of vibration induced by internal and external disturbance sources.

Due to the wide range of disturbances that act on the optical instruments, a single actuator with simultaneously large control authority and high bandwidth would be necessary to meet the stabilization requirements. Unfortunately no single actuator can meet these requirements. Therefore, a suite of actuators with overlapping strokes and bandwidths is employed; such a construction is termed a "staged actuation system." The objective in the thesis is to develop "staging control" strategies that specify how to utilize the individual actuators in a staged system to satisfy the stabilization requirements.

The first task in the staging control design process is to evaluate how actuator capabilities and constraints affect the system performance. Two analytical techniques, based on stochastic Lyapunov and stochastic linearization methods, are utilized to predict the steady-state, closed-loop performance in the presence of actuator nonlinearities such as saturation and quantization. These nonlinearities can severely restrict the achievable performance, and careful consideration of their effects is vitally important for staged controller designs. Using this performance prediction methodology, a control synthesis framework is developed which extends $\mathcal{H}_2$-optimization techniques by incorporating the effects of actuator nonlinearities.

The newly developed framework is then proposed as a formal synthesis tool for staging controller designs. The proposed technique estimates and can directly shape the probability of saturation of each actuator, and determines optimal "hand-offs" of control authority between the actuators. Due to the $\mathcal{H}_2$ setting, the controller designs arise directly as solutions of the corresponding necessary conditions, allowing system design studies to be performed easily and quickly. The proposed staged controllers have been demonstrated to achieve the nanometer level stabilization requirements under the expected disturbance environments for space interferometers. The new synthesis technique is also used to analytically quantify the achievable performance and the sensitivity of a particular staging configuration to the individual actuator parameters (size and bandwidths).

Thesis committee chairman: David W. Miller
Title: Associate Professor of Aeronautics and Astronautics

Acknowledgments

The journey of obtaining a Ph.D. has been absolutely incredible and could not have been completed without the help of so many people. I would like to first thank my family for their constant love and support. They have always believed that I would one day get this degree, even though I have doubted myself at times.

I would also like to thank my committee members for helping me through this difficult process. Dave, my thesis advisor, has provided me with the opportunity to work on many exciting projects in the Space Systems Lab (SSL) and given me sage advice that will continue to benefit me in the years to come. I have been very lucky to have such an understanding and knowledgeable advisor. I would like to thank Jon for all his deep questions. The thesis has become much stronger after addressing his challenges and concerns. Carl, thank you so much for all the discussions on optical delay line and actuator modelling. I have learned a lot from you and hope to continue to work with you in the future.

The staff at the SSL has also given me all the help that I could ever ask for. Paul and Ray, thank you so much for your technical support on thruster and hardware issues, respectively. Sharon, thank you for your administrative support on my fellowship and for going out of your ways to do nice things for me. Marilyn, I don't think I can ever thank you enough for all your help. I really appreciate the extra work that you had to do to assist me finishing a thesis away from MIT.

I would like to acknowledge Oliver Lay at JPL for answering all my optics and interferometry related questions. Thank you also for reading my optics chapter and giving me very useful feedback. I also want to thank Professor Wesley Traub at Harvard and Mr. David Dunmeyer at MIT for enhancing my understanding of optics.

There is a saying that being in graduate school is similar to be on an emotional roller coaster ride. I have had many great friends who have shared laughs with me at good times and comforted me at not so pleasant times. I would like to thank Arthur, Becky, Laila, and Mark for reading chapters of my thesis and giving me invaluable writing suggestions. I especially want to thank Arthur and Becky for helping me with last minute thesis formatting problems as I frantically tried to print out the final copy. Since I spent the past 8 months away from MIT, I needed a lot of help to get everything done. Jorge and John, thank you so much for printing out drafts of my thesis and delivering them to the desired locations.

In addition to thesis help, Brett, Greg, and Mitch have been older brothers to me and have given me guidance on how to survive my graduate years at MIT. Karen has been a dear friend who has always checked on my well being, especially after I isolated myself in the thesis production vault. Alvar, thank you for always being so sweet and fixing all my computer problems. Becky has been both my roommate and officemate for the last two years. I am grateful to have such a great friend who makes me laugh and listens to my complaints.

Finally I would like to dedicate this thesis to the greatest man in my life, my husband Rob. Thank you so much for your patience and love while I tried to finish my thesis. You have taken care of everything in my life so I could concentrate on thesis writing. I owe you many months of house chores, cooking, and laundry. I am so grateful to have you by my side as I cross the Ph.D. finish line. I look forward to making the rest of your life as happy as you have made mine.

Contents

List of Figures

List of Tables

Chapter 1

Introduction

1.1 Motivation

The existence of Earth-like planets outside of our solar system, and the possibility of extraterrestrial life residing on them, have intrigued people for many years. Indeed, the search for extra-solar, life-harboring planets has become a primary focus of NASA space research [56]. In an attempt to detect candidate planetary systems, new technologies have been developed to enhance the accuracy of astronomical observations [1, 5]. One promising technology proposed by NASA's Origins Program is optical interferometry, whereby small telescopes separated by large distances can act as a much larger telescope. Such an interferometric system can obtain a level of resolution similar to that provided by an equivalent single, large telescope, without the extreme mass and concurrent expense of a large space structure.

Ground-based interferometer facilities have been constructed and have demonstrated the effectiveness of the proposed technology. However, the science capabilities of these interferometers are limited by two factors: achievable baseline and atmospheric distortions. For example, the separation distance required for imaging Earth-like planets may be on the order of hundreds of meters [2]. In order to implement such a baseline on the ground, a large piece of land, ideally flat, is needed to house the collecting apertures, beam transport pipes, and other infrastructure [76]. Such space may not be readily or inexpensively available. Even if the physical land is available, atmospheric conditions at the desired location must also be favorable. Atmospheric turbulence can severely degrade the accuracy of interferometric measurements [8].

The limitations mentioned above can be avoided by sending interferometers into space, where the observations made by the system would not be corrupted by atmospheric distortions and large baselines can be achieved. The interferometric combination of two or more small Hubble-type telescopes could provide observations superior to those possible with any existing astronomical apparatus. Two such missions are currently planned by the NASA Jet Propulsion Laboratory (JPL). The Space Interferometry Mission (SIM), scheduled for launch in 2009, has a 10 m baseline with two 0.3 m diameter apertures located on a common truss platform. The most recent architectural design of SIM is illustrated in Figure 1-1(a). The mission aims to measure the position and distance of stars throughout the galaxy several hundred times more accurately than any existing system [83]. However, the SIM mission does not have sufficient baseline to detect and image Earth-like extra-solar planets, and building a larger truss to hold two or more apertures at longer baselines may be prohibitively complex and expensive.

A second NASA mission, the Terrestrial Planet Finder (TPF), plans to study planetary systems outside of our solar system using either a large-baseline nulling interferometer or a coronagraph. Under the nulling interferometer proposal, one architecture suggests placing the apertures on individual spacecraft and flying the spacecraft in formation to provide baselines from 75 m up to 1 km. The specific architecture configuration of the TPF mission is not yet determined. A representative configuration consisting of a fleet of several free-flying apertures together with a combiner spacecraft is illustrated in Figure 1-1(b).

Although space interferometers are not affected by atmospheric turbulence and baseline constraints, there are many other technical challenges that need to be overcome before their full potential can be realized. The light rays collected from each telescope in a multi-aperture array must be relayed to the combiner instrument, where they interfere, creating fringe patterns. However, the desired interference pattern is obtained only if the differential light pathlength from the different telescopes is regulated to the nanometer level, despite the presence of structural vibration and perturbations caused by other internal and external disturbances. Meeting such stringent performance requirements poses tremendous technological challenges that stretch the current state-of-the-art.

In order to achieve the stabilization requirements posed by space interferometer missions, an active control system is required to continuously adjust the optical geometry so as to maintain the required pathlength. The design of such a control system would be

(a)

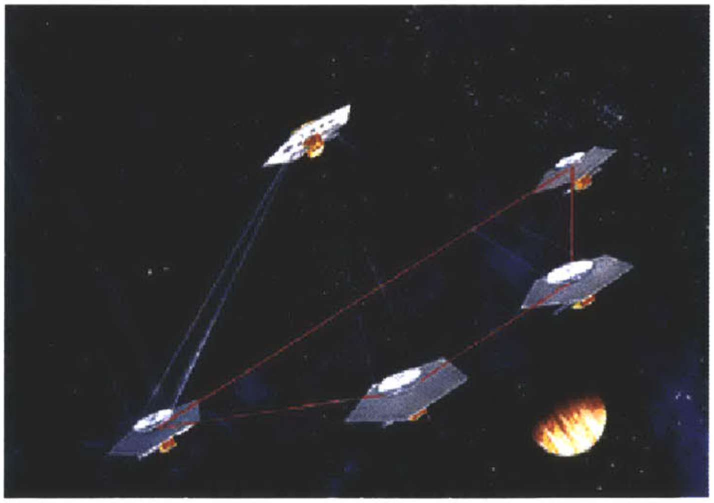

(b)

Figure 1-1: (a) Current Space Interferometry Mission architecture concept (http://planetquest.jpl.nasa.gov/SIM/sim_index.html) (b) Terrestrial Planet Finder free flyer design concept (http://ast.star.rl.ac.uk/darwin/talk) straightforward if a single actuator were available which simultaneously provided the authority, bandwidth, and accuracy needed to suppress the complete range of disturbances acting on the combining optics. Unfortunately such an actuator does not exist, and instead a suite of actuators with overlapping strokes and bandwidths is used to approximate the functionality of this ideal single actuator. For example, relatively large force, low bandwidth actuators can slowly move the spacecraft, while smaller high bandwidth actuators can rapidly adjust the position of optical mirrors in the interferometer.

If all the actuators can be made to collaborate appropriately, the complete feedback control system will be capable of meeting the interferometer stabilization requirements. However, coordinating such a suite of actuators to achieve the desired performance can be a significant challenge. This thesis aims to address this challenge in order to realize the full potential of space interferometer systems.

1.2 Research Objectives and Approach

The approach taken in this research is to first identify the range of perturbations to the optical geometry that can be tolerated while still achieving the detection threshold for extra-solar planet detection. Since these perturbations are unlikely to be deterministic, they are modelled as Gaussian random variables. The allowable tolerance is expressed as the maximum root-mean-square (RMS) perturbation to the optical pathlength which still allows the detection criterion to be satisfied.

These geometric perturbations will have a physical manifestation as the relative motion of the optical components on the interferometer, and hence the second task is to develop a model of these motions and the effect of control inputs on each degree of freedom. Random pathlength variations in the interferometer are then modelled as arising from stochastic disturbance inputs into this physical model. Examples of such disturbances are solar pressure acting on the spacecraft, thermal effects flexing the mirrors, and vibration transmitted through the structure to the optical equipment from other spacecraft systems (such as a spinning reaction wheel). The actuator constraints are modelled as a combination of linear and nonlinear elements. Bandwidth constraints are modelled with linear filters, while saturation (maximum output), resolution (minimum output), and quantization effects are modelled as algebraic input nonlinearities.

The complete system model is thus represented by a set of nonlinear stochastic differential equations. Determining if the output of this system (pathlength variations) satisfies a specified RMS constraint is a nontrivial problem, requiring the solution of the Fokker-Planck equation to determine the steady-state probability density function of the closed-loop state vector. Exact solutions of this equation are not possible in general, but approximate solutions can be determined for the class of nonlinearities considered, under the assumption that the closed-loop density can be well approximated as Gaussian. Two different approaches are investigated to develop this approximation: one based on stochastic linearization, and the other based on stochastic versions of the classical Lyapunov theorems. Each approach generates a collection of coupled nonlinear algebraic equations that must be solved simultaneously to predict the output variance. It is shown that these equations are formally dual to each other, and both sets produce the same predictions.

The predictions made by these techniques are typically within 10% of the values computed by exact solution of the Fokker-Planck equation (where possible) or determined by numerical simulation of the nonlinear differential equations. This approximation is in contrast to predictions of the output variance made by assuming the actuators are linear. The error in linear predictions can become extremely large, and can even predict essentially no pathlength variations, when in fact the variations are substantial. Indeed, the nonlinear analysis shows that the disturbance suppression capabilities of the system are fundamentally limited by the bandwidth and nonlinear characteristics of each actuator. These limits must be taken into account in the design of a control law for each actuator.

The task of the controller for a space interferometer is thus to keep the RMS pathlength variations below a specified level, taking into account the individual constraints on each actuator. Additionally, the controller should attempt to minimize the mechanical wear, or electrical power consumption, of each actuator, as quantified by the RMS magnitude of the corresponding control input. Using the variance prediction techniques described above, a modified $\mathcal{H}_2$ control design strategy is utilized to accomplish this tradeoff. Finally, the new methodology is applied to the problem of controlling optical pathlength in a space interferometer. Basing the controller design on a modified modern control framework allows rapid and automatic computation of new controller designs as a function of the system or actuator parameters. Such a control algorithm permits a family of trade studies to be conducted in a timely fashion. Several such trade studies are presented to demonstrate the utility of the proposed approach.

Goals of the research

The main objectives of this thesis are summarized as follows:

- Develop a methodology that quantifies the effect of random perturbations to the interferometer optics, and determine the maximum RMS level of perturbations that the interferometer can tolerate while still satisfying extra-solar planet detection criteria.

- Characterize the linear and nonlinear actuator constraints in an interferometer pathlength control system, given that each actuator has drastically different authority and frequency bandwidth. The nonlinear constraints considered are saturation, resolution, and quantization effects.

- Develop an analytical approximation tool to predict the expected RMS output from a dynamic system subjected to random disturbance inputs and actuator nonlinearities.

- Incorporate the actuator constraints, disturbance models, and optical geometry dynamics into the controller design and develop a systematic method for determining a feedback control algorithm that optimally utilizes a given suite of actuators to achieve the specified level of closed-loop RMS performance.

- Explore the design implications of the resulting control strategies in terms of the specific physical properties of each actuator.
  - Quantify the admissible disturbance levels as a function of actuator size and bandwidth.
  - Quantify the utilization of each actuator, in particular the amount of time it spends in saturation, as a function of disturbance level, actuator size and bandwidth.

- Analyze the optimal "hand-off" of control authority between actuators which is determined by the proposed control algorithm as a function of actuator bandwidth and nonlinearities.

1.3 Summary of Previous Work

A review of previous work is presented in this section.

1.3.1 Optical requirements for nulling interferometers

The TPF mission uses nulling interferometry to eliminate the bright light coming from the star and allow the dimmer, reflected light from the extra-solar planet to be observed. The idea of using a nulling interferometer to search for extra-solar planets was first proposed by Bracewell and McPhie [5]. They suggested the detection of such planets by destructively interfering light from two telescopes to effectively null out the starlight emission. However, a two-aperture configuration is only sufficient for detecting Jupiter-size planets, and thus, Angel and Wolf later suggested a four-aperture array capable of detecting Earth-like planets [1]. Recently many multi-aperture arrays have been proposed to provide deeper starlight nulling and improve the resolving power of the interferometric system [40, 51, 88].

Most of the work to date on the TPF mission has focused on the static, architectural concepts or mirror designs. Four industry teams including Ball Aerospace, Boeing, Lockheed Martin, and Northrop Grumman have conducted extensive reviews of various TPF architectural designs, on topics ranging from array configurations and combiner instrumentation to preliminary spacecraft model, launch, and deployment logistics. The reports that summarize their reviews are available at the official JPL website [79]. This thesis also studies a linear-array interferometer configuration by looking at variations in the number of apertures, the baseline, and aperture diameters. A similar, but more comprehensive, configuration analysis of a nulling interferometer is presented in [48].

These architectural reviews assume that the interferometer configuration can be maintained perfectly. However, this idealized assumption will likely be violated when apertures are placed on multiple spacecraft or a long truss structure that is perturbed by external and onboard disturbances. Even at this initial design phase, it is necessary to estimate how much the actual interferometer configuration may deviate from the ideal one, while still ensuring good interferometric measurements. Such estimates can provide an initial measure on how well a dynamic stabilization system must perform. A general statistical analysis that models the dynamic deviations as random variables provides a RMS bound on the acceptable deviation levels. This type of analysis has been performed for ground-based interferometers to determine RMS wavefront errors as a function of telescope alignment and atmospheric distortion [64]. More recently, Mennesson et al. [52] conducted a similar analysis for a two-aperture nulling space interferometer; however, the extension from their existing work to a multi-aperture system is not obvious. Since Earth-like planet detection will require more than two apertures, this thesis develops a method that estimates the allowable RMS deviations for a general two-dimensional interferometer array based on an optical metric that measures the depth and width of the null created by the interferometer [72].

1.3.2 Nonlinear performance prediction

As discussed above, the system model considered in the thesis is a set of nonlinear stochastic differential equations (SDEs) which can be expressed as

$$\begin{aligned} dx &= Axdt + B_1dw + B_2\phi(u)dt \\ y &= C_1x \end{aligned}$$

where $\phi(u)$ describes actuator nonlinearities, the additive disturbance w is a zero-mean, Gaussian stochastic process, and y denotes the performance output. The formal definition and general properties of SDEs are discussed extensively in [11, 58]. Explicit solutions to the above equations usually do not exist. Numerical simulations can be used to approximate the steady-state RMS performance $\hat{\sigma}_y$ for a given control u, but such a technique can be inaccurate and very time consuming [7].

A Lyapunov criterion can be used to establish the existence of a stationary probability distribution of the system states described above [89]. This criterion is based on results first obtained by Has'minskǐ [25] with additional results provided by Wonham [87] and Mao [49]. In addition, Zakai [89] shows that the stationary statistics of the closed-loop system can be estimated based on the Lyapunov analysis. Thygesen [77] extends Zakai's discussion in a survey paper, and summarizes various Lyapunov methods addressing different properties of solutions to stochastic differential equations.

Lyapunov methods that incorporate stochastic analysis techniques will be referred to as *stochastic* Lyapunov theory in this thesis to differentiate it from the common deterministic Lyapunov theory [34]. Although the stochastic Lyapunov theory can provide estimates on the stationary properties of the closed-loop system, it is still non-trivial to apply such methods to predict the RMS output performance, $\hat{\sigma}_y$ for a given system. This thesis utilizes results obtained from stochastic Lyapunov theory [77, 89] to extend Zakai's results to develop an analytical prediction tool that estimates $\hat{\sigma}_y$.

Another approach of approximating the steady-state output performance is to linearize the nonlinear function $\phi(u)$. If such an approximation can be accomplished, the RMS $\hat{\sigma}_y$ of the resulting "linearized" system can be easily computed from linear system and stochastic process theory [32, 60]. One common method of linearizing a nonlinear function $\phi(u)$ is to assume that u operates near a nominal point u_o and approximate the nonlinear function as $\phi(u) = Nu$, where $N = d\phi/du$ evaluated at u_o [34]. However, if the actual signal u deviates greatly from the nominal value u_o, this approximation is no longer accurate, and a better approximation can be obtained by changing the linear gain N as a function of the input u. This gain variation depending on the input is the basic idea behind quasi-linearization, which is used extensively in the describing function work discussed in [20].

The resulting quasi-linearized system can be expressed as

$$dx = Ax\,dt + B_1 dw + B_2 N(u) u\,dt.$$

In the case where the system is subjected to random inputs, the term N is also called the stochastic or statistical linearization gain [19, 20, 21, 69]. It is important to notice that the system is not truly linear, since $N(u)$ depends on the input u. If a feedback design is used, i.e. $u = Kx$, then there exists a circulatory problem - the input u depends on the solution x to the above stochastic different equation, which depends on N, which is a function of u. As a result, a set of consistency constraints must be satisfied, leading to a set of coupled equations that must be solved simultaneously.

This thesis aims at developing an analytical tool to estimate $\hat{\sigma}_y$ from both stochastic Lyapunov and stochastic linearization theories. Furthermore, it will show that the two methods are dual and provide the same analytical prediction.

1.3.3 Control with saturating actuators

Saturation is one of the most commonly observed nonlinearities in actuators. In addition to limitations on physical movements, the electrical input - voltage or current - that drives the actuators is also limited. Since saturation is present for all control applications, it has been an active controls research topic. For work on saturating actuators prior to 1995, Bernstein and Michel provide an extensive list of literature in this field indicating more than 150 references [3].

More recently there has been a renewed interest in the study of linear systems subjected to input saturations. The recent work can be divided into two categories - (1) deterministic stabilization and (2) stochastic stabilization - where the system is perturbed by deterministic and stochastic disturbances, respectively. Under the first category, the work can be further divided into saturation avoidance and saturation allowance. It has been demonstrated that an $\mathcal{H}_\infty$-framework can be used for saturation avoidance problems [66, 67]. However, this type of strategy is generally considered too conservative and limits the achievable performance of the system [3]. Hence saturation allowance techniques are usually preferred and have been developed more extensively.

The work related to deterministic stabilization with saturation allowance mainly focuses on the closed-loop stability issues of the system. Sussmann et al., Teel, and Tyan and Bernstein have separately demonstrated techniques for achieving *global* stabilization for classes of linear systems with saturating actuators [73, 74, 82]. In particular, Sussmann's work requires that the linear part of the system has no eigenvalues with positive real part, and that the pair (A, B) is stabilizable. Teel and Tyan have focused on global stabilization of systems with multiple integrators.

Paré et al. have obtained semi-global stability results for linear systems that can be open-loop unstable [61, 62]. Their control design framework is based on LMI/BMI optimization techniques, and the resulting output feedback controller can either maximize the region of attraction, maximize (deterministic) disturbance rejection, or optimize the $\mathcal{L}_2$-gain performance. The semi-global stability results can also be derived from nonlinear control techniques such as those presented in [29, 44, 70, 75]. Other related work on saturating actuators, including anti-windup control designs, is discussed in [36, 55, 63].

For the class of problems considered in this thesis, the perturbations are stochastic disturbances, so the above control techniques cannot be applied directly since they do not account for the random aspect of the problem. Furthermore, deterministic stability analysis typically requires an upper bound on the magnitude of the input disturbance. However, such a bound may not exist for stochastic perturbations, especially for those with the Gaussian density functions assumed in this thesis. As a result, the stochastic stabilization framework is more appropriate for solving the problems at hand.

Florchinger [15] has started a new wave of research interest in stochastic stabilization problems for nonlinear systems. Pan and Başar have demonstrated global asymptotic stability in probability [59] for the class of strict-feedback systems. Deng and Krstić [12] solved the stochastic disturbance attenuation problems, even for nonlinear systems with parametric uncertainty. Unfortunately, these recent results all assume multiplicative disturbance models, in which the entering stochastic disturbances are multiplied by functions of the system state that approach zero as the state does. Such a model allows for powerful asymptotic stability results to be obtained, but it does not apply to the additive noise models considered in this thesis. For these cases the best that can be done is to bound the variance of the closed-loop state (and output) deviations from the origin.

As discussed above, estimating the performance output variance would require solving the Fokker-Plank equation for the probability density function, but the explicit solution to this equation generally does not exist. Liberzon and Brockett presented a framework based on stochastic Lyapunov theory to obtain the exact closed-loop probability density function for a linear system with saturating and quantized inputs [42]. Although they have shown that the resulting density function is piecewise Gaussian, Liberzon does not suggest a control synthesis technique in [42].

A different approach for stabilizing a single saturating actuator with stochastic disturbances is presented by Gökçek et al. [21]. Their framework combines LQR/LQG optimal control design and stochastic linearization to approximate the saturation effects. This work also provides an estimate of the closed-loop, steady-state RMS output from the resulting "linearized" system. However, Gökçek et al. have only formally examined single-input systems with saturation. The extension to multi-input systems, and to other types of input nonlinearity, is not straightforward. Moreover, the stability analysis presented in their work relies on deterministic Lyapunov techniques, and hence does not accurately account for the impact of the stochastic disturbances.

In this thesis, the exact density function computed in [42] is approximated by a single, continuous Gaussian function, and stochastic Lyapunov and stochastic linearization theory are used to develop a performance prediction tool for a large class of linear systems with actuator nonlinearities. This tool is then used in a control synthesis framework, where $\mathcal{H}_2$ optimization is used to achieve the desired performance while minimizing mechanical/electrical power usage. The control synthesis proposed here is a multi-input extension of the single saturating actuator work presented in [21].

1.3.4 Other actuator nonlinearities

Other common nonlinear actuator effects include resolution/deadzone and quantization of input commands. The resolution/deadzone nonlinearity may arise from the minimum movement of a mechanical drive, and quantization is a result of the digital to analog conversion. Control designs and stability analysis of resolution/deadzone and quantization effects are described in [10, 16] and [45, 39, 6, 41, 68], respectively. This work is mostly based on deterministic systems with a focus on stability analysis.

As discussed in the previous section, Liberzon and Brockett [42] have characterized the quantization plus saturation effects on the closed-loop density function. It is also important to point out that quantization effects have often been modelled as added white noise with uniform distribution [17]. The assumptions behind such a model will be reviewed in this thesis, and the additive noise model can be used to characterize quantization effects when appropriate.

Since most of the work that considers actuator nonlinearities does not take into account stochastic perturbations, the performance prediction analysis and control synthesis framework described at the end Section 1.3.3 will be generalized to incorporate resolution/deadzone and quantization effects.

1.3.5 Interferometer Pathlength Control

Current pathlength control algorithms for testbed versions of space interferometers are based on classical, single loop-shaping designs [23, 27, 46, 57]. These designs have been tested on a staged optical delay line system that consists of a voice coil as the coarse stage and a PZT actuator as the fine stage. The closed-loop performance obtained in the laboratory environment is in the range of 3-30 nm. Additionally, a dynamic nonlinear compensator has also been suggested in [27, 46], which is claimed to globally stabilize the system, albeit without a formal proof. In this design, the voice coil loop is actually designed to be unstable in isolation, requiring the action of the PZT to ensure closed-loop stability. This feature is felt to be necessary to improve the low frequency rejection properties of the system.

There are several disadvantages associated with such designs. First, the loop shaping processes can be difficult and time consuming, requiring substantial manual “tweaking” of the controller parameters to obtain the desired loop shapes while still ensuring nominal stability. Additionally, the nonlinear design with the unstable voice coil loop may not be sufficiently robust; in the event that the PZT fails, or its performance is degraded, the entire system may be destabilized. Finally, in both techniques, it is difficult to predict the performance of the closed-loop system in the event that the PZT or voice coil saturates. Indeed estimates of the expected saturation states of the actuators is one of the key metrics that JPL has identified as a desired design parameter [31].

The objective of the control design developed in this thesis is to formalize the construction of a control system for these devices within the modern control framework. Such a technique would allow quick generation of control designs automatically, without the need to manually tune the control parameters. It will be demonstrated that the control design proposed here can achieve comparable performance to those cited above, within this systematic framework. This design also properly accounts for the saturation effects of the actuators and directly provides accurate estimates of the amount of time each actuator spends in saturation.

1.4 Thesis Outline

The thesis begins by providing a brief introduction to optical imaging and interferometry in Chapter 2. Following the background material on optical systems, analyses of TPF array configurations as a function of the number of apertures, baseline, and aperture diameters are presented. Next, a statistical methodology for estimating the largest RMS configuration perturbations that are tolerable for planet detection is developed and applied to a linear-array TPF configuration.

The overall dynamic model of the interferometer system is then presented in Chapter 3. This model includes the plant dynamics, disturbance models, and actuator constraints. Four types of actuator constraints, including saturation, resolution, quantization, and bandwidth, and their effects on the system performance are studied in this chapter. A brief review of the actuators used in the interferometer pathlength control system is also included to demonstrate that these actuators have drastically different properties, such as stroke range and bandwidth. Such a suite of actuators is defined as a "staged actuation system", and the strategy to control these actuators in order to achieve the desired performance is defined as a "staging control" methodology.

In Chapter 4, a set of nonlinear stochastic differential equations (SDEs) are used to characterize the overall system model presented in Chapter 3. Some properties of SDEs and possible solutions for this set of equations are discussed in the chapter. Since the exact solution for these equations is rarely available, two approximate methods are presented to estimate the output variance of the system. These methods are based on stochastic Lyapunov and stochastic linearization theories, and several examples are included to demonstrate the utility of these analytical approximation tools.

With the tools from Chapter 4 to determine accurate estimates of the RMS output performance, the attention turns to the design of controllers that can meet the RMS stabilization requirements. A control synthesis framework is formally presented in Chapter 5; the controller is designed to minimize an $\mathcal{H}_2$ cost function that penalizes output variance and control variance simultaneously. The full-state feedback problem is first solved and applied to both a single-actuator and two-actuator example problems. The control design technique is then extended to incorporate probability of saturation penalties. This extension allows the tuning of the actuator saturation state directly. The output feedback extension of the full-state feedback design is discussed at the end of Chapter 5.

The analysis and design framework developed in this thesis is applied to the interferometer pathlength control problems in Chapter 6. Numerous examples and trade studies including the effects of disturbance spectra, frequency "hand-off", and minimization of electrical power are illustrated here to demonstrate the capabilities of the tools developed in this thesis. Finally, Chapter 7 provides a summary of the important findings in each chapter, lists the major contributions of the thesis, and recommends future work directions for staged control system designs of space interferometers.

Chapter 2

Aperture Physics and Optical Stability Requirements

An important task in the initial design phase of space interferometry systems is to convert observational requirements into dynamical stability requirements on the optical components. "Dynamic stability", as discussed in this chapter, refers to the magnitude of the deviations of the optical states of the system from their reference positions, typically quantified by root-mean-square (RMS) deviations. Essentially, the analysis below seeks to quantify the magnitude of the RMS "jitter" the optics can tolerate, while still providing acceptable observations. "Stability" in this chapter is thus distinct from control-theoretic notions of stability, such as non-divergence in the sense of Lyapunov [34]. This equally important sense of stability will be examined in Chapter 4.

To develop the necessary analytical machinery, Sections 2.1 and 2.2 below review the process by which an optical system transforms light into images. The duality between Fraunhofer diffraction and Fourier analysis is exploited to develop a concise formalism for describing the relationship between properties of the optics and corresponding properties of the resulting image. Section 2.3 describes the application of this analysis method to the technique of nulling interferometry, and describes the relationship between typical observational requirements and the corresponding optical performance requirements that must be satisfied to meet the viewing objectives.

The idealized optical systems described in the first three sections can never be obtained in practice; the individual components of the system are inevitably subjected to small distortions and disturbances. For terrestrial applications of interferometry, the dominant distortion is due to the atmosphere. For a space interferometry mission, there will be perturbations due to onboard vibrations, thermal expansion and contraction, etc. Since the forms of these disturbances are not known precisely, they are assumed to be random in nature and will hence provoke a corresponding random behavior in the optical metrics. Section 2.4 quantifies the effects of these random perturbations on the optical performance metrics and determines the bounds on the magnitude of the perturbations which will still allow the viewing objectives to be met.

2.1 Single-Aperture Physics

The objective of this section is to review the relationship between the properties of the aperture of an optical system and the corresponding image created as light passes through this aperture. The discussion below is based on a synthesis of the material in [4, 22, 26, 86]. By describing the physics of interferometric phenomena in a more familiar mathematical framework, this discussion may be particularly helpful for engineers without specific optics backgrounds, but with the typical exposure to linear systems theory and Fourier/Laplace analysis.

2.1.1 One-dimensional apertures

Light waves propagated from a distant point source can be considered to be planar when they reach the collecting instrument. For simplicity these waves are treated as monochromatic with a single wavelength, λ, and an angular spatial frequency $k = 2\pi/\lambda$. Incident planar waves parallel to a one-dimensional (1D) aperture are illustrated in Figure 2-1. The first objective is to model flux density distribution (wave amplitude per area) of the image of this light source at point P located at (X, Z) from the center of the aperture. Analysis of this idealized example will provide the building blocks for determining the image created by more complex light distributions in the sky.

According to the Huygens-Fresnel Principle, each differential length of the aperture dS can be considered filled with secondary point sources, with emergent wave amplitude $\epsilon\, dS$, where ϵ is the source strength per unit length, assumed to be constant over the entire aperture [26]. The plane wave is thus essentially broken into infinitesimal "wavelets" across

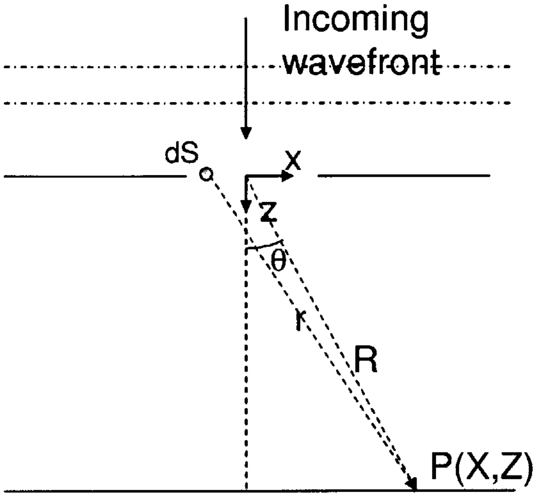

Figure 2-1: Geometric definitions for wave propagating through an one-dimensional single slit aperture

the aperture, each of which is propagated forward to the point P. The wave amplitude contribution from each wavelet at P is given by

$$dU(P) = \frac{\epsilon}{r} e^{i(\omega t - kr)} dS, \tag{2.1}$$

where r is the distance from the differential element dS to P, ω is the angular temporal frequency, and t is time.

The location of the elementary wavelet dS is denoted by x in the aperture plane, and let r and R be the distances to P from the element dS and the origin of the aperture coordinates, respectively, as shown in Figure 2-1. The distances r and R can then be expressed as a function of the geometric coordinates of $P(X, Z)$,

$$\begin{aligned} r &= ((X-x)^2 + Z^2)^{1/2} \\ R &= (X^2 + Z^2)^{1/2}. \end{aligned}$$

Expressing r in terms of R and eliminating Z,

$$\begin{aligned} r &= (X^2 + Z^2 - 2xX + x^2)^{1/2} \\ &= R(1 + \frac{x^2}{R^2} - \frac{2xX}{R^2})^{1/2}. \end{aligned}$$

Using the Fraunhofer approximation, $R \gg x$, the second term x^2/R^2 is approximately 0 so that,

$$r \approx R(1 - \frac{2xX}{R^2})^{1/2}.$$

The binomial expansion $(1-\delta)^{1/2} \approx 1-\delta/2$ further simplifies this term as,

$$r \approx R(1-\frac{xX}{R^2}). \tag{2.2}$$

The differential wave amplitude in a plane where R is approximately constant can be then written as

$$dU(X) = \frac{\epsilon}{R} e^{i(\omega t - kR)} e^{ikXx/R} dS. \tag{2.3}$$

Note that after this simplification dU no longer depends on Z, since the image plane is assumed to be approximately a constant distance R away from the aperture plane. The total light amplitude in the image plane is simply the sum of all the wavelet contributions across the aperture -

$$U(X) = \int_{\text{ap}} dU = \frac{1}{R} e^{i(\omega t - kR)} \int_{\text{ap}} \epsilon e^{ikXx/R} dx. \tag{2.4}$$

The phase term $e^{i(\omega t - kR)}$ is approximately uniform across the observation plane. Since the interest is in the relative amplitude distribution, this term as well as $1/R$ can be grouped into the constant ϵ without loss of generality [26].

The above analysis assumes that all parts of the aperture pass the incident light wave without distortion. More generally, the wave amplitude and phase may be changed by different amounts at different points in the aperture. To model this situation, the uniform amplitude flux of each wavelet ϵ is replaced by the *aperture function* $A(x)$, and the resulting complex amplitude at $P(X)$ is given by

$$U(X) = \int_{\text{ap}} A(x) e^{ikXx/R} dx, \tag{2.5}$$

which agrees with the above when $A(x) = \epsilon$ for all $x \in \text{ap}$.

If the amplitude is expressed in terms of angle of diffraction, θ, measured relative to the z axis as shown in Figure 2-1, then

$$X/R = \sin\theta \approx \theta.$$

Equation 2.5 becomes

$$U(\theta) = \int_{\text{ap}} A(x) e^{ik\theta x} dx. \tag{2.6}$$

so that the amplitude U is seen to be the Fourier transform of the aperture function $A(x)$.

The wave amplitude $U(\theta)$ is in general a complex number which cannot be measured directly by a physical light detector. Instead such a detector measures the *irradiance* or *intensity* I, defined as the squared magnitude of the amplitude U, with units of [Watts/m]:

$$I(\theta) = |U(\theta)|^2.$$

As an example, the aperture in Figure 2-1 is a single slit with width a. The aperture function is defined by

$$A(x) = \begin{cases} 1 & |x| \leq a \\ 0 & \text{otherwise} \end{cases}$$

and the corresponding amplitude computed from Equation 2.6 is,

$$\begin{aligned} U(\theta) &= \int_{-a/2}^{+a/2} e^{ik\theta x} dx \\ &= \frac{1}{ik\theta}\left[e^{ik\theta a/2} - e^{-ik\theta a/2}\right] = \frac{\sin(k\theta a/2)}{k\theta a/2} a \\ &= \frac{\sin(a\pi\theta/\lambda)}{a\pi\theta/\lambda} a = a \operatorname{sinc}(a\pi\theta/\lambda), \end{aligned}$$

where the definition of angular spatial frequency $k = 2\pi/\lambda$ has been used. The measured intensity is then

$$I(\theta) = |U(\theta)|^2 = \operatorname{sinc}^2(a\pi\theta/\lambda)a^2,$$

which is the familiar diffraction equation associated with the single-slit experiment,

Figure 2-2(a) shows the aperture function $A(x)$ for this 1D slit shape. The Fourier transform of this "box-like" function is the sinc function as shown in Figure 2-2(b), which is also the wave amplitude in the image plane. Figure 2-2(c) shows the normalized intensity $I(\theta)/I_{max}$ as a function of $\theta/(\lambda/a)$. The zeros of intensity occur when

$$\begin{aligned} &a\theta\pi/\lambda = n\pi, \quad n = [1, 2, \ldots] \\ &n\lambda = a\theta \end{aligned}$$

describing the locations of the minima of the diffraction pattern. Finally, the *angular resolution*, or *minimum resolving power*, for the aperture is defined by the first minimum of the intensity function, $\Delta\theta = \lambda/a$.

2.1.2 Two-dimensional apertures

The above discussion can easily be generalized to a two-dimensional (2D) aperture. The (x, y, z) coordinates originate at the center of the aperture, with z pointing in the direction

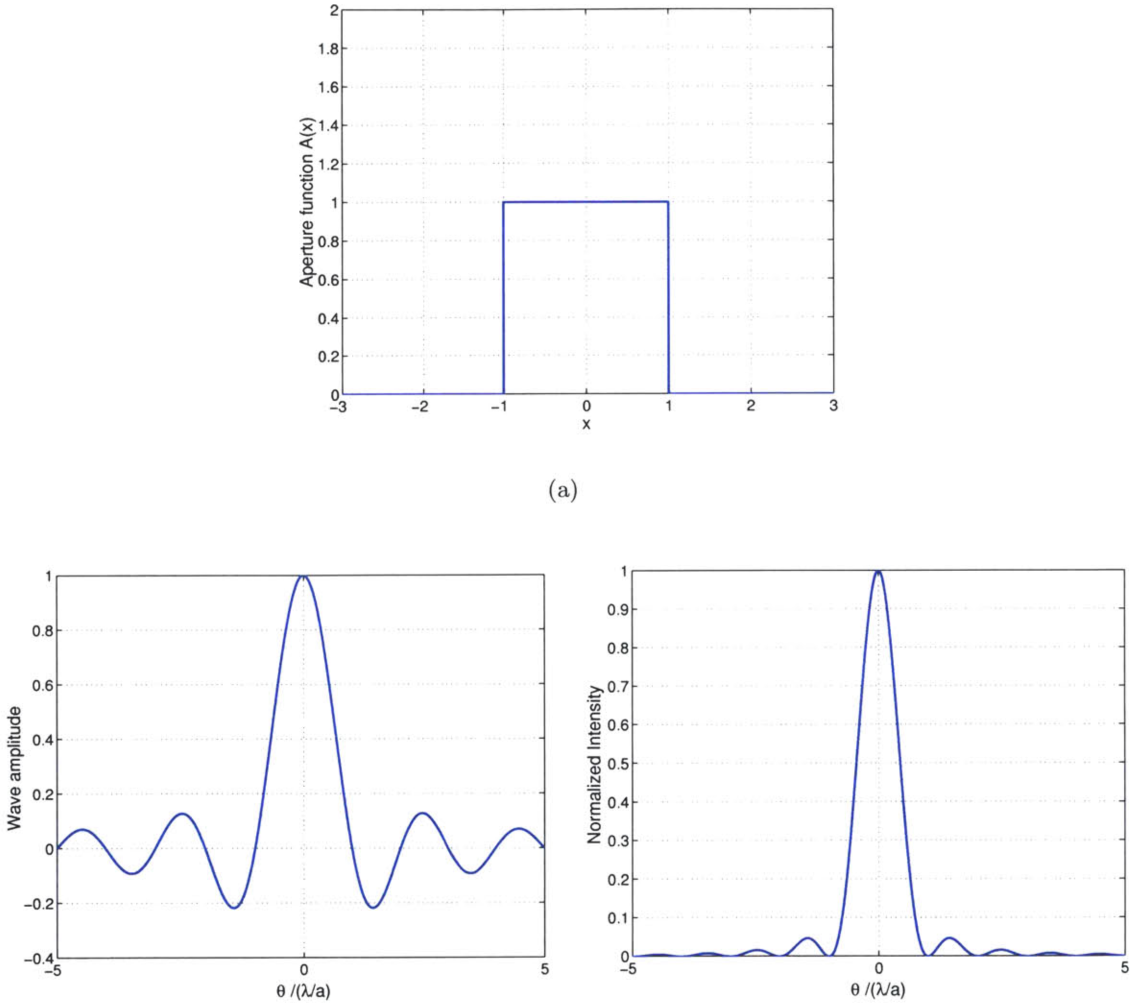

(a)

(b)

(c)

Figure 2-2: One-dimensional single slit aperture: (a) Single-slit aperture function (b) Wave amplitude function (c) Irradiance pattern of wave propagation as shown in Figure 2-3. Assuming far-field observation, or Fraunhofer diffraction, where $R^2 \gg x^2 + y^2$, the complex wave amplitude at an arbitrary point $P(X, Y)$ is the 2D version of Equation 2.5,

$$U(X,Y) = \int\int_{\text{ap}} A(x,y)e^{ik(Xx+Yy)/R}dxdy. \tag{2.7}$$

where dS changes from length dx in the 1D case to the differential area $dx\,dy$ in the 2D case. The wave amplitude is again the Fourier transform of the aperture function. The image plane is thus equivalent to the Fourier plane where Fraunhofer diffraction approximation is valid.

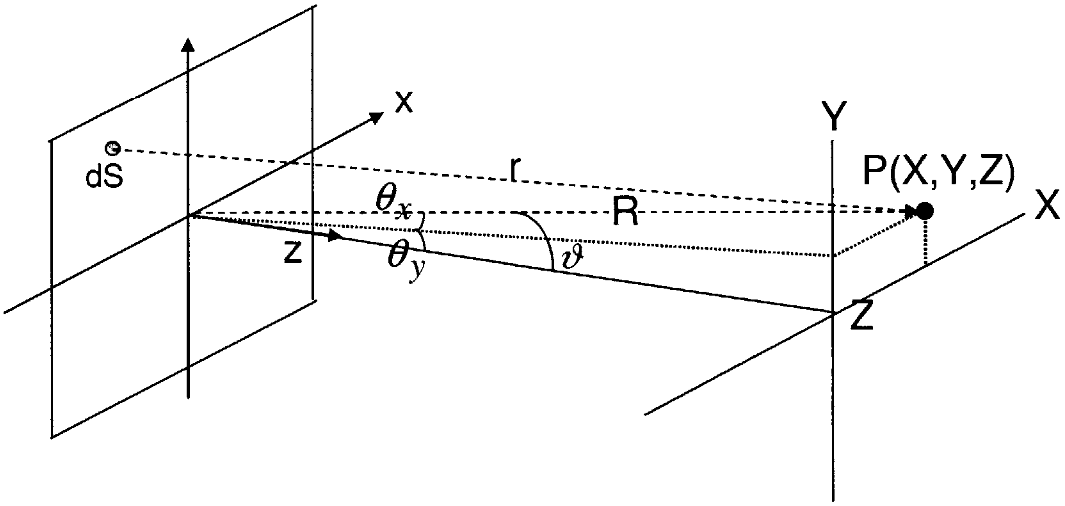

Figure 2-3: Geometry of the two-dimensional aperture and the observational plane

Now consider two popular 2D aperture shapes - rectangular and circular. The aperture function of a rectangular aperture with length a and width b can be defined as,

$$A(x,y) = \begin{cases} 1 & \text{if } |x| \le a \text{ and } |y| \le b \\ 0 & \text{otherwise} \end{cases}$$

or equivalently $A(x,y) = A(x)A(y)$, where

$$A(x) = \begin{cases} 1 & \text{if } |x| \le a \\ 0 & \text{otherwise} \end{cases} \qquad A(y) = \begin{cases} 1 & \text{if } |y| \le b \\ 0 & \text{otherwise} \end{cases}$$

The wave amplitude is computed as

$$U(X,Y) \;=\; \left[\int_{-a/2}^{a/2} A(x)e^{ikXx/R}dx\right]\left[\int_{-b2}^{b/2} A(y)e^{ikYy/R}dy\right]$$

$$= \left[\frac{\sin(akX/2R)}{akX/2R}\right]\left[\frac{\sin(bkY/2R)}{bkY/2R}\right]ab$$

$$= ab\,\mathrm{sinc}\left(\frac{akX}{2R}\right)\,\mathrm{sinc}\left(\frac{bkY}{2R}\right). \tag{2.8}$$

$$\tag{2.9}$$

The detected intensity $I = |U|^2$ is then

$$I(X,Y) = a^2b^2\,\mathrm{sinc}^2\left(\frac{akX}{2R}\right)\,\mathrm{sinc}^2\left(\frac{bkY}{2R}\right) \tag{2.10}$$

To illustrate these ideas, Figure 2-4(a) shows a rectangular aperture function, and Figure 2-5(a) shows the corresponding intensity in the image plane. This intensity is also commonly called the *point spread function* (PSF), because it describes how a point source gets spread in the image plane into an intensity pattern similar to Figure 2-5.

For a circular aperture of diameter D, whose aperture function is shown in Figure 2-4(b), the coordinate transformation,

$$x = \alpha\cos\beta \qquad y = \alpha\sin\beta$$
$$X = p\cos(q) \quad Y = p\sin(q)$$

allows the complex amplitude to be expressed as

$$U(p,q) = \int_{\alpha=0}^{D/2}\int_{\beta=0}^{2\pi} e^{(ikp\alpha/R)\cos(\beta-q)}\alpha d\alpha d\beta, \tag{2.11}$$

After performing the integration, the amplitude function is given by

$$U(p) = \frac{\pi D^2}{2R^2}\frac{J_1(kDp/2R)}{kDp/2R},$$

where J_1 is the Bessel function of order 1. Due to the assumed aperture symmetry, the amplitude depends only on the radial coordinate $p^2 = X^2 + Y^2$. Since $p/R = \sin\vartheta \approx \vartheta$ as shown in Figure 2-3, the amplitude can also be expressed as

$$U(\vartheta) = \frac{\pi D^2}{4R^2}\frac{2J_1(kD\vartheta/2)}{kD\vartheta/2}, \tag{2.12}$$

with corresponding intensity

$$I(\vartheta) = I(0)\left[\frac{2J_1(kD\vartheta/2)}{kD\vartheta/2}\right]^2, \tag{2.13}$$

where $I(0) = (\pi D^2/(4R^2))^2$.

Figure 2-5(b) illustrates the intensity pattern of the Fraunhofer diffraction for this circular aperture. The intensity has "ripples" uniformly extending from the central peak in all directions, a shape known as the Airy pattern. By contrast, there are only two sets of "ripples" in the rectangular case, one along each coordinate axis, corresponding to a single dimension of the Fourier transform of the box (rectangle) function.

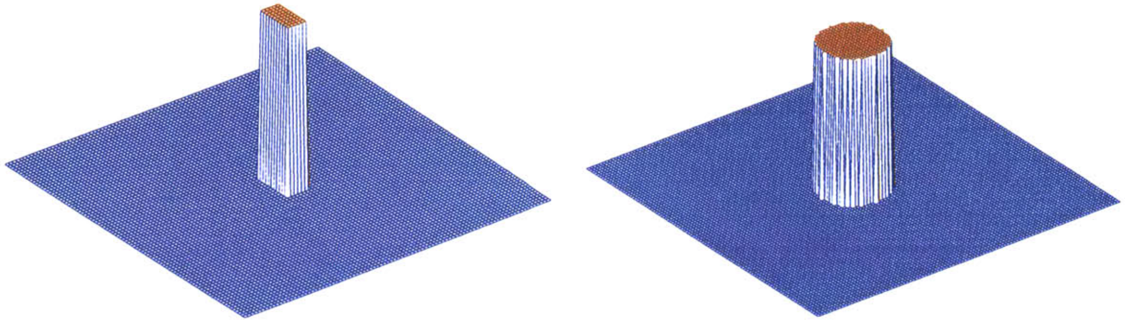
(a) (b)

Figure 2-4: Two-dimensional aperture function: (a) Rectangular aperture (b) Circular aperture

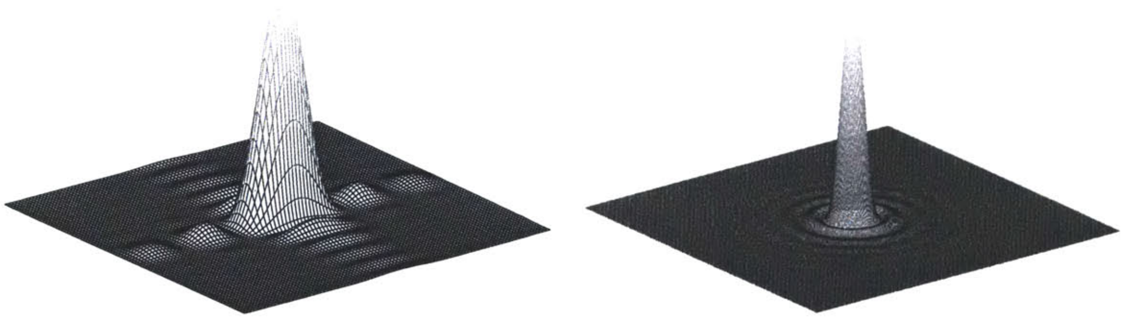
(a) (b)

Figure 2-5: Detected intensity I: (a) Rectangular aperture (b) Circular aperture

In general, the far-field assumptions of Fraunhofer diffraction would require the detecting instrument to be kilometers away from the aperture. If the observation plane is too close to the aperture, phase contaminations will distort the Fourier transform of the aperture function $A(x, y)$. Fortunately a lens can be placed after the diffracting aperture to focus the incoming waves to an image plane (or focal plane) located at the focal distance F from the aperture. As a result, the Fraunhofer diffraction can be observed on the focal plane of the lens rather than at a large distance R away. Assuming that phase distortion and curvature of the lens are small (so that $A(x, y)$ is still close to constant across the aperture), all the equations presented above hold when a lens is used to produce the Fraunhofer diffraction pattern. It is only necessary is to replace the distance R with the lens focal length F in Equation 2.7, i.e.

$$U(X,Y) = \int\int_{\text{ap}} A(x,y)e^{ik(Xx+Yy)/F}dxdy. \tag{2.14}$$

With this formulation, it is clear that *a lens creates a Fourier transform of the source image in its own focal plane.*

Finally, consider the case where the source has nonzero dimensions, as opposed to the simple point source considered above. A distributed source can be modelled as a two-dimensional shape filled with single point sources, and the intensity observed in the image plane is then the integration of the individual point source contributions over the entire distribution:

$$I_i(X,Y) = \int \text{PSF}(X - x_s, Y - y_s)I_s(x_s, y_s)dx_s\,dy_s, \tag{2.15}$$

where I_s is the intensity distribution of the source, and (x_s, y_s) are the Cartesian coordinates of the source as shown in Figure 2-6. This equation assumes that the point spread function is shift-invariant, so that shifting the point source location in the object plane only causes a corresponding shift of the intensity in the focal plane. While this shift invariance is not strictly true when factors such as lens imperfections and coherence are taken into account, the approximation is good enough for the discussion considered here.

2.1.3 Optics and linear system theory

As seen in Equation 2.15, the process of computing the image plane intensities for an arbitrary source distribution is equivalent to computing the response of a linear time-invariant dynamical system. The input to the optical system is a 2D source (intensity distribution) and the output is a 2D image. The point spread function is analogous to the impulse response of a linear system, and the output image is the convolution of the point spread function with the source input.

Linear systems theory extensively uses the concept of the transfer function, which is the Laplace (or Fourier) transform of the impulse response. Convolution with the impulse

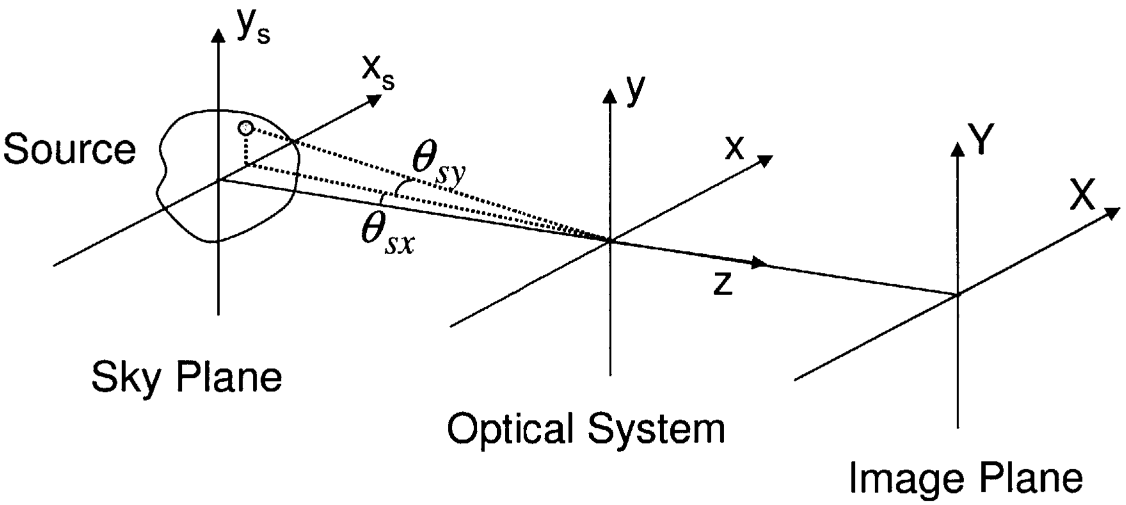

Figure 2-6: Simple geometry of a two-dimensional optical imaging system

response is equivalent to multiplication by the transfer function in the Fourier domain. Analogously, the *optical transfer function* (OTF) is the Fourier transform of the point spread function, and multiplying the OTF by the Fourier transform of the source intensity distribution I_o yields the Fourier transform of the image intensity I_i. Because of the way the PSF is computed from the amplitude U, the OTF can also be expressed as the convolution of the aperture function with its complex conjugate. Table 2.1 summarizes the Fourier relationships developed in this section.

Table 2.1: Summary of Fraunhofer diffraction using Fourier transform $\mathcal{F}$

$A(x,y)$ Aperture function	$*$ Convolution	$A^*(x,y)$ Complex conjugate aperture function	$=$	OTF(X,Y) Optical transfer function
$\mathcal{F}\downarrow\ \uparrow\mathcal{F}^{-1}$		$\mathcal{F}\downarrow\ \uparrow\mathcal{F}^{-1}$		$\mathcal{F}^{-1}\downarrow\ \uparrow\mathcal{F}$
$U(X,Y)$ Fraunhofer amplitude	$\times$ Multiplication	$U^*(X,Y)$ Complex conjugate amplitude	$=$	$I(X,Y) = \text{PSF}(X,Y)$ Point spread function

2.2 Multi-Aperture Physics

In the multi-aperture case, the shift and linearity properties of Fourier transform can be used to derive the intensity functions. The spatial shift property states that if the Fourier transform of $A(x, y)$ is $U(X, Y)$, and a and b are arbitrary constants, then the shift in position of the function $A(x \pm a, y \pm b)$ will result in the transform $e^{\pm ik(aX+bY)/R} \cdot U(X, Y)$, and hence a shift in spatial position is equivalent to a linear phase shift in frequency. For example, suppose a rectangular aperture with sides a and b is shifted along the x-axis by a distance s. The corresponding wave amplitude in the image plane is computed as

$$\begin{aligned} U(X,Y) &= \int_{-b/2}^{b/2} \int_{-a/2+s}^{a/2+s} e^{ik(Xx+Yy)/R} dx dy \\ &= \left[\int_{-b/2}^{b/2} e^{ikYy/R} dy \right] \left[\int_{-a/2+s}^{a/2+s} e^{ikXx/R} dx \right] \\ &= \left[b \frac{\sin(bkY/2R)}{bkY/2R} \right] \frac{e^{iksX/R}}{ikX/R} \left[e^{iakX/2R} - e^{-iakX/2R} \right] \\ &= ab\, e^{iksX/R} \operatorname{sinc}\left(\frac{akX}{2R} \right) \operatorname{sinc}\left(\frac{bkY}{2R} \right), \end{aligned} \tag{2.16}$$

Equation 2.16 is the shifted version of Equation 2.9.

The other important property of the Fourier transform is the linearity property, which states that the Fourier transform of a linear combination of functions is equal to the linear combination of Fourier transforms of each individual function. In particular, if functions $A(x, y)$ and $B(x, y)$ have Fourier transforms $U(X, Y)$ and $V(X, Y)$, respectively, and α and β are arbitrary constants, then

$$\mathcal{F}\{\alpha A(x, y) + \beta B(x, y)\} = \alpha U(X, Y) + \beta V(X, Y).$$

Consider two identical rectangular apertures with the side lengths a and b, where one aperture is shifted in the x direction by $+s$ and the other $-s$. From the shifting property, the respective image amplitudes for a point source are

$$\begin{aligned} U_+(X,Y) &= ab\, e^{iksX/R} \operatorname{sinc}\left(\frac{akX}{2R} \right) \operatorname{sinc}\left(\frac{bkY}{2R} \right) \\ U_-(X,Y) &= ab\, e^{-iksX/R} \operatorname{sinc}\left(\frac{akX}{2R} \right) \operatorname{sinc}\left(\frac{bkY}{2R} \right) \end{aligned}$$

Using the linearity property, the total amplitude is then

$$\begin{aligned} U(X,Y) &= U_+ + U_- \\ &= 2\,ab\, \cos(ksX/R) \operatorname{sinc}\left(\frac{akX}{2R} \right) \operatorname{sinc}\left(\frac{bkY}{2R} \right), \end{aligned} \tag{2.17}$$

and the detected intensity is given by

$$\begin{aligned} I(X,Y) &= U^2(X,Y) = 4a^2b^2\,[\mathrm{sinc}^2(akX/2R)\,\mathrm{sinc}^2(bkY/2R)]\,cos^2(ksX/R), \\ &= 2a^2b^2\,[\mathrm{sinc}^2(akX/2R)\mathrm{sinc}^2(bkY/2R)]\,[1+\cos(2ksX/R)], \end{aligned}$$

Using the diffraction angle substitutions, $\theta_x \approx \sin(\theta_x) = X/R$ and $\theta_y \approx \sin(\theta_y) = Y/R$ as shown in Figure 2-3, and normalizing the intensity by its maximum $4a^2b^2$

$$I_n(\theta_x,\theta_y) = 1/2\,[\mathrm{sinc}^2(ak\theta_x/2)\,\mathrm{sinc}^2(bk\theta_y/2)]\,[1+\cos(2ks\theta_x)] \tag{2.18}$$

The normalized intensity is thus a cosine term modulated by the Fraunhofer diffraction of a single aperture, as illustrated in Figure 2-7 for intensity variations in the θ_x direction. The single slit diffraction pattern (dashed line) acts as a modulation on the higher frequency oscillations arising from the new cosine term. The addition of a second aperture has created a family of *interference fringes* oscillating under the single slit diffraction envelope.

The first zero of the normalized intensity I_n function defines the angular resolution of the imaging system. In the single aperture case this zero occurs at λ/a. In the two aperture case, however the first zero is then located at $\lambda/2B$, where $B = 2s$ is the distance between the centers of the two apertures. Therefore, the interference created by a second aperture creates an optical system with significantly better angular resolution than a single aperture system, provided the aperture separation B is much greater than the aperture width a.

With the above theory in place, the general expression for the point spread function of an N_a-aperture optical system can be derived. Using linearity, the total amplitude at point $P(X,Y)$ is the sum of the amplitude contributions from each aperture,

$$U(X,Y) = \sum_{j=1}^{N_a} U_j(X,Y).$$

Using the shift rule defined by Equation 2.16, each of the amplitudes is

$$U_j(X,Y) = e^{ik(x_jX+y_jY)/R}\left(\int\int_{\mathrm{ap}} A_j(x,y)e^{ik(Xx+Yy)/R}dxdy\right),$$

where (x_j,y_j) and $A_j(x,y)$ are the j^{th} aperture center location and aperture shape function, respectively. Combining the above two equations,

$$\begin{aligned} U(X,Y) &= \sum_{j=1}^{N_a} e^{ik(x_jX+y_jY)/R}\left(\int\int_{\mathrm{ap}} A_j(x,y)e^{ik(Xx+Yy)/R}dxdy\right), && (2.19) \\ &= \sum_{j=1}^{N_a} G_j(X,Y)e^{ik(x_jX+y_jY)/R}, && (2.20) \end{aligned}$$

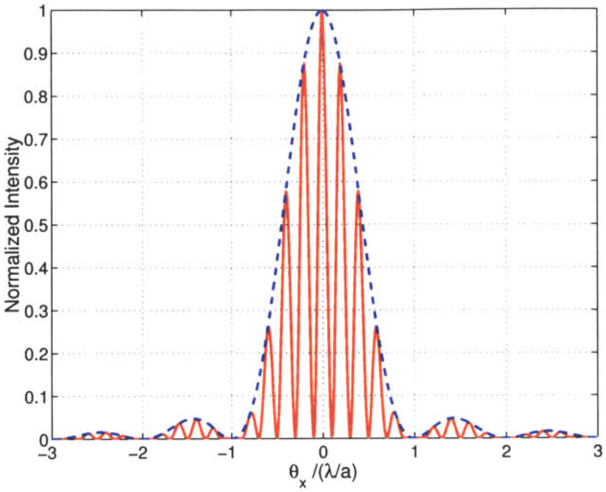

Figure 2-7: Normalized intensity along the θ_x direction of two rectangular apertures $(2s/a) = 5$

where G_j is the parenthesized term in Equation 2.19, and corresponds to the Fraunhofer diffraction amplitude of the j^{th} aperture (defined by Equation 2.7). The resulting intensity detected at point $P(X, Y)$ in the image plane is given by

$$\begin{aligned} I(X,Y) &= |U(X,Y)|^2 \\ &= \left| \sum_{j=1}^{N_a} G_j(X,Y) e^{ik(x_j X + y_j Y)/R} \right|^2 . \end{aligned} \tag{2.21}$$

Defining the diffraction angles $\theta_x = X/R$ and $\theta_y = Y/R$, the point spread function is equivalently

$$\text{PSF}(\theta_x, \theta_y) = I(\theta_x, \theta_y) = \left| \sum_{j=1}^{N_a} G_j(\theta_x, \theta_y) e^{ik(x_j \theta_x + y_j \theta_y)} \right|^2 . \tag{2.22}$$

and the image plane intensity is given by

$$I_i(\theta_x, \theta_y) = \int \text{PSF}(\theta_x - \theta_{sx}, \theta_y - \theta_{sy}) \;\; I_s(\theta_{sx}, \theta_{sy}) \;\; d\theta_{sx}\, d\theta_{sy}, \tag{2.23}$$

where $(\theta_{sx}, \theta_{sy})$ are angular coordinates of the source as shown in Figure 2-6, and I_s is the intensity distribution of the source.

2.3 Interferometry and Planet Finding

The multi-aperture physics described above provides the basic mathematics for the study of interferometry. The interference patterns created by the additional apertures can provide the optical system with increased resolving power, enabling more sensitive and accurate observations. Recently, a novel use of interferometry has been proposed, with direct application to the detection of extra-solar planets. This section describes this application, and performs a trade analysis for the aperture sizes and relative placement as a function of the planet finding objectives.

2.3.1 Beam combination

There are two general methods for combining light rays received from different collecting telescopes. The multi-aperture physics presented in Section 2.2 describes a simple beam combination technique, where a lens is placed after the apertures to focus the beams onto a detector. Since the focused images are superposed in the detector plane, fringes will form across the combined image and appear spatially on the detector. This technique is also known as *image plane* interferometry. In practice mirrors and lenses are often used to scale down the input beam size while preserving the relative wavefront geometry between different beams before focusing them onto a detector. From the above discussion, when light passing through different apertures combines onto a common image plane, the resulting pattern of interference fringes is described by Equations 2.22 and 2.23 above.

More commonly, however, mirrors and beam-splitters are used to first combine the light beams from different collector telescopes and then focus the superposed beams onto the detector [80]. Since the combined beams are completely overlapped, the spatially modulated fringes observed in the image plane interferometry no longer exist. Typically a spot detector is used to measure the combined beam intensity, or equivalently, measure light intensity at a single point in the image plane. This process, known as *pupil plane* interferometry, is slightly different from the focal plane imaging process discussed above. Focal plane imaging describes the intensity distribution across the entire focal plane by convolving the point spread function (PSF) with the sky intensity distribution. The pupil plane description, on the other hand, describes how a single point in the focal plane is coupled to the intensity distribution in the sky.

To develop the pupil plane idea mathematically, evaluate Equation 2.23 at a fixed point in the image plane, typically $(\theta_x, \theta_y) = (0,0)$ for convenience. The intensity measured by a detector at this location is then

$$I_{det} = I(0,0) = \int \mathrm{PSF}(-\theta_{sx}, -\theta_{sy})\ I_s(\theta_{sx}, \theta_{sy})\ d\theta_{sx}\, d\theta_{sy} \tag{2.24}$$

Assuming the aperture shapes are symmetric and the aperture centers are symmetrically placed, $\mathrm{PSF}(-\theta_{sx}, -\theta_{sy}) = \mathrm{PSF}(\theta_{sx}, \theta_{sy})$, so that

$$I_{det} = I(0,0) = \int IR(\theta_{sx}, \theta_{sy})\ I_s(\theta_{sx}, \theta_{sy})\ d\theta_{sx}\, d\theta_{sy} \tag{2.25}$$

where $IR(\theta_{sx}, \theta_{sy}) = PSF(\theta_{sx}, \theta_{sy})$ is called the *interferometer response function.* Note that the detected intensity for the pupil plane interferometer is only a function of the coordinates on the sky. Moreover, this intensity is the integral of the *product* of the interferometer response with the sky brightness distribution. The detected intensity for the pupil plane interferometer can thus be visualized by projecting the interferometer response function onto the sky. Light sources at sky coordinates where the response function is large will contribute strongly to the detected intensity; sources at coordinates where the response function is zero will not contribute at all to the detected intensity. For this reason the interferometer response function IR is often called the “transmission map on the sky” [52].

2.3.2 Nulling interferometry

The transmission map perspective suggests another use for an array of apertures: nulling interferometry. This technique uses the interference pattern from an array of apertures to null out the bright light of an on-axis source, allowing fainter, nearby light sources to be more strongly perceived [72]. To accomplish this, the apertures are configured so that the transmission map has a destructive interference fringe centered on the array axis $\theta_x = 0$, $\theta_y = 0$. This idea is illustrated in Figure 2-8. Note that the subscript s in $(\theta_{sx}, \theta_{sy})$ is eliminated from Equation 2.22 in this section for ease of notation.

To determine the necessary aperture configuration for implementing this idea, recall that the transmission map for a collection of N_a apertures is given by Equation 2.22:

$$IR(\theta_x, \theta_y) = \left| \sum_{j=1}^{N_a} G_j(\theta_x, \theta_y) e^{ik(\theta_x x_j + \theta_y y_j)} a_j e^{i\phi_j} \right|^2, \tag{2.26}$$

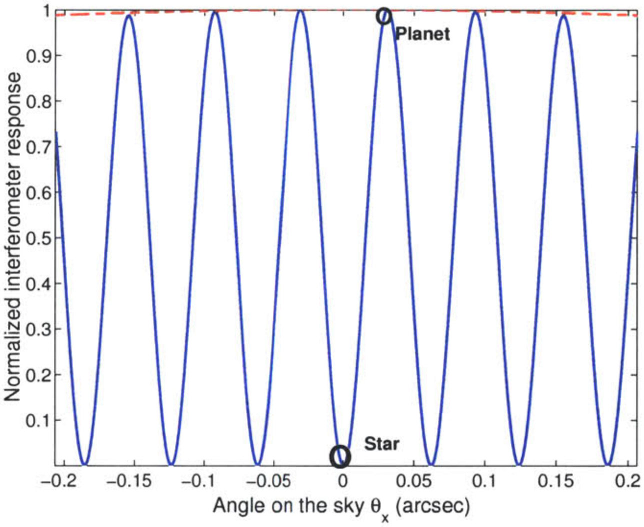

Figure 2-8: Normalized interferometer response function for a family of apertures

where x_j and y_j are the coordinates of the center of the jth aperture and G_j is given by

$$G_j(\theta_x, \theta_y) = \int\int_{\mathrm{ap}_j} A_j(x, y) e^{ik(\theta_x x + \theta_y y)} dx dy. \tag{2.27}$$

Equation 2.26 has introduced the flexibility to assign different transmission efficiencies to the different apertures, via the gains a_j and the phases ϕ_j. The phase, in particular is what allows the destructive interference bands to be moved to the desired location.

Consider for example an $N_a = 2$ aperture interferometer with identical circular apertures of diameter D. The transmission map is

$$IR(\theta_x, \theta_y) \propto \left[\frac{2J_1(kD\vartheta)}{kD\vartheta}\right]^2 (1 + \cos(k(\theta_x x_{12} + \theta_y y_{12}) + \phi_{12})). \tag{2.28}$$

where $\vartheta = \sqrt{\theta_x^2 + \theta_y^2}$, $x_{12} = x_1 - x_2$, $y_{12} = y_1 - y_2$, and $\phi_{12} = \phi_1 - \phi_2$ (the efficiencies $a_1 = a_2$ have been assumed here). If the relative phase ϕ_{12} between the two apertures is taken to be π, the normalized interferometer response in the θ_x direction is as shown in Figure 2-8, which demonstrates the desired central destructive interference. Note also in this figure that the modulating diffraction pattern, shown by the dashed line, is essentially constant over the first several interference fringes.

For an arbitrary number of apertures, the transmission map is

$$IR(\theta_x, \theta_y) \quad = \quad \sum_{j=1}^{N_a} G_j^2 + \sum_{i=1}^{N_a-1} \sum_{l=i+1}^{N_a} 2G_i G_l \cos\left(k\theta_x(x_i - x_l) + k\theta_y(y_i - y_l) + \phi_i - \phi_l\right)$$

$$= \sum_{j=1}^{N_a} G_j^2 + \sum_{i=1}^{N_a-1} \sum_{l=i+1}^{N_a} 2G_iG_l \cos\left(k(\theta_x x_{il} + \theta_y y_{il}) + \phi_{il}\right), \tag{2.29}$$

where $(\cdot)_{il}$ denotes the difference between the quantities $(\cdot)_i$ and $(\cdot)_l$. For a N_a-aperture system, there are $N_a - 1$ unique difference terms per variable. For example in a four-aperture system, the unique x difference terms are x_{12}, x_{13}, and x_{14}, whereas x_{23} may be written as $x_{13} - x_{12}$ and similar expressions can be obtained for x_{24} and x_{34}. Specific choices of the number of apertures N_a, the phase shifts ϕ_{il} and the relative aperture placements x_{il}, y_{il} will depend upon the nulling requirements of the particular application, such as the planet finding scenario discussed in the next section.

2.3.3 Extrasolar planet detection

Bracewell and McPhie [5] were the first to suggest that nulling interferometry could be used to search for extrasolar planets. Nulling the bright light of a distant star could allow the much fainter reflected light of its companion planets to be detected. Angel and Woolf [1] carefully analyzed the two-element interferometer suggested by Bracewell and determined that, while it might be sufficient to detect Jupiter-class planets, it might not provide sufficient sensitivity to detect planets as close to their parent star as the Earth is to the Sun. To achieve this level of sensitivity, three or more apertures in 1-dimensional or 2-dimensional array configurations have been proposed in [1, 40, 51, 88]. These apertures may either be placed on separated spacecraft or on a single structurally connected spacecraft. Figures 2-9(a) and 2-9(b) illustrate these two concepts for the TPF mission.

Since a star has finite dimension, the transmission map null has to be sufficiently wide to adequately suppress the star's brightness. A natural choice of performance metric for a proposed interferometer design is thus a measure of the combined depth and width of the response null. The *null depth* (*ND*) is defined as the ratio between the intensity evaluated at the extra-solar star limb (L) and at its first maximum or possible planet location (P) (see Figure 2-8).

$$ND = \frac{IR\Big|_{(\theta_x,\theta_y)=(\theta_{xL},\theta_{yL})}}{IR\Big|_{(\theta_x,\theta_y)=(\theta_{xP},\theta_{yP})}} = \frac{IR|_L}{IR|_P} \tag{2.30}$$

where $(\theta_{xP}, \theta_{yP})$ are the angular coordinates of the first interference maximum, and $(\theta_{xL}, \theta_{yL})$ are the coordinates of a point on the star limb.

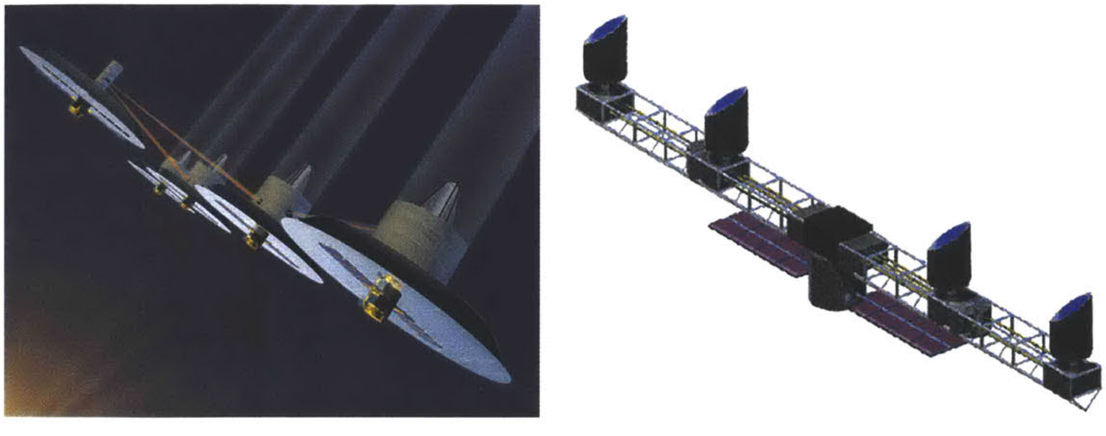

(a) (b)

Figure 2-9: Terrestrial Planet Finder nulling interferometer configurations: (a) Separated spacecraft (b) Structurally-connected spacecraft

To detect an Earth-class planet around a Solar-sized star at a distance of approximately 10 parsecs, which is the nominal TPF mission, the required null depth is at least 10^{-6} across a stellar disk which subtends a diameter of approximately 10^{-3} arcsecs [88]. This requirement is illustrated in Figure 2-10. The base of the rectangular box shown in the plot denotes the desired level of null depth 10^{-6}; it extends from the center of the star $\theta_x = 0$ until the vertical side of the rectangle which indicates the estimated angular radius of the star, which here is 5×10^{-4} arcsecs.

Equation 2.29 can be used to analyze the combinations of aperture numbers, sizes, and locations that are capable of meeting this requirement. Since from Equation 2.30, null depth uses the response function values only for a small range of angles on the sky, the diffraction envelopes G_j are nearly constant, and the interferometer response simplifies to

$$\begin{aligned} IR(\theta_x, \theta_y) &\propto \left| \sum_{j=1}^{N_a} D_j e^{ik(\theta_x x_j + \theta_y y_j)} e^{i\phi_j} \right|^2 && (2.31) \\ &\propto \sum_{k=1}^{N_a} D_k^2 + \sum_{i=1}^{N_a - 1} 2 D_i D_l \cos(k(\theta_x x_{il} + \theta_y y_{il}) + \phi_{il}), && (2.32) \end{aligned}$$

where circular apertures have been assumed, each of diameter D_j.

Woolf and Angel [88] have suggested the use of a linear nulling interferometer with the same separation distance between each adjacent aperture. With these assumptions, the

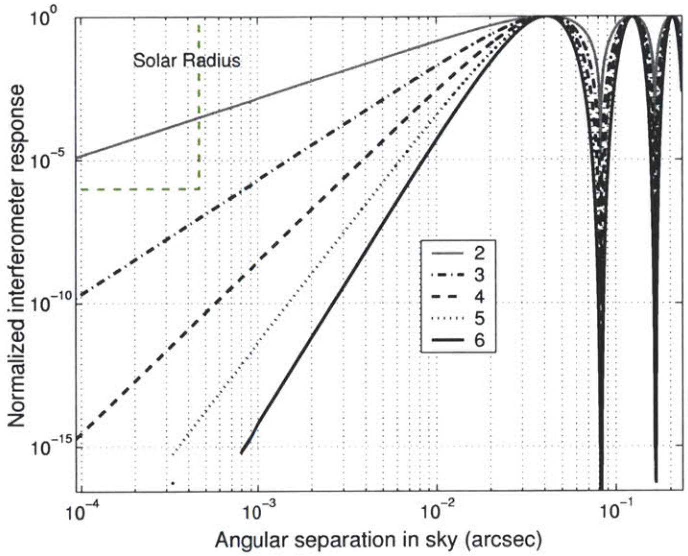

Figure 2-10: Normalized interferometer response function (null depth) for a family of apertures

aperture diameters needed to give the transmission map a central null can be determined from the coefficients of the polynomial $p(x) = (1 + x)^{N_a}$; the corresponding phase shifts follow a similar regular pattern. Table 2.2 gives the specific values for the first five values of N_a.

Table 2.2: Linear array nulling interferometer configuration

No. of Apertures N_a	$p(x) = (1+x)^{N_a - 1}$	Aperture Diameters	Phase shifts
2	$1 + x$	$D = [1\ 1]$	$\phi = [0\ \pi]$
3	$1 + 2x + x^2$	$D = [1\ 2\ 1]$	$\phi = [0\ \pi\ 0]$
4	$1 + 3x + 3x^2 + x^3$	$D = [1\ 3\ 3\ 1]$	$\phi = [0\ \pi\ 0\ \pi]$
5	$1 + 4x + 6x^2 + 4x^3 + x^4$	$D = [1\ 4\ 6\ 4\ 1]$	$\phi = [0\ \pi\ 0\ \pi\ 0]$

Figure 2-10 illustrates a family of interferometer response curves for various number of apertures, derived by using the values in Table 2.2 and Equation 2.31. The distance between adjacent apertures is set to 25 m for this example. Since the array is linear, y_j can be set to 0 without loss of generality.

In order to achieve the desired null depth (10^{-6}), the normalized interferometer response must be below the rectangular bounding box. As illustrated by the plot, at least three apertures are needed to satisfy this requirement. It should be emphasized that the null depths computed here are idealistic, since it does not take into account any optical imperfections or vibrational problems onboard the spacecraft. The effects of dynamic perturbations on the null depth is examined in the next section.

In addition to the number of apertures used in the interferometer configuration, there are other parameters that can alter the quality of the null. One such parameter is the total baseline, or length, of the interferometric array. Consider for example the above linear array with diameters ratios in the 1-3-3-1 configuration, and equally spaced apertures centered at $x_1 = -B/2$, $x_2 = -B/6$, $x_3 = B/6$, and $x_4 = B/2$, where B is the total baseline. Figure 2-11 shows the normalized IR as a function of angle θ_x on the sky for three different values of B. For this example, the first constructive peak occurs at $\theta_x = 3\lambda/(2B)$. Therefore, as the baseline length increases, the first peak appears closer to the line-of-sight ($\theta_x = 0$), and the null depth margin is decreased and may not be sufficient to suppress the starlight.

The minimum baseline can be determined by the apparent width of the star and the null depth requirement. If the baseline is variable, the interferometric system is then capable of observing different size stars. Long baseline can be used to observe smaller stars or stars that are further away, and short baseline can provide wider null in order to reduce the light from bigger or closer stars. Recall that the baseline also controls the angular resolution of the interferometric system; as the baseline length increases, the angular resolution improves. There is thus a tradeoff between getting sharper images (better resolution) and nulling the central star light.

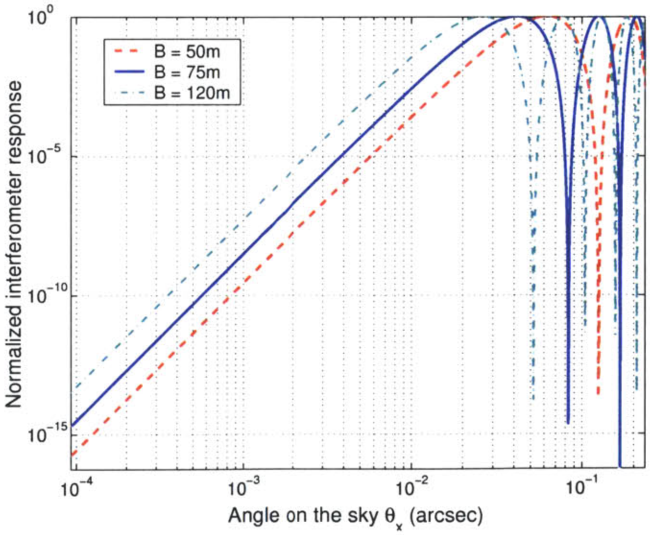

Figure 2-11: Normalized interferometer response of a 1-3-3-1 linear array with changing baseline

Wolf and Angel's formula for linear array designs is sufficient but not necessary. Mennesson et. al. [52] show that the general conditions required for a sufficiently wide and deep null for TPF detection criteria are:

$$\sum_{j=1}^{N_a} e^{i\phi_j} = 0, \qquad \sum_{j=1}^{N_a} p_j e^{i\phi_j} = 0, \qquad \sum_{j=1}^{N_a} p_j^2 e^{i\phi_j} = 0,$$

where $p_j = D_j x_j$. While few exact solutions for these equations are known, and none at all for $N_a \geq 5$, the assumption of symmetry can be very helpful in finding special case solutions. For a symmetric, four-aperture system, the above constraints simplify to

$$L_i D_i = L_o D_o, \tag{2.33}$$

where L_i is the inner aperture location, D_i is the inner aperture diameter, and the subscript o denotes the outer aperture properties. This simplification also assumes that 0 and π phase shifts ϕ_j are added alternately to the apertures in the array.

The above conditions can be met in any symmetric linear array with the diameter configuration

$$D = [D_o \; D_i \; D_i \; D_o] \tag{2.34}$$

and the center locations

$$\begin{aligned} L &= \left[-\frac{B}{2} \; - L_i \; L_i \; \frac{B}{2}\right], &(2.35)\\ L_i &= \frac{B}{2}\frac{D_o}{D_i} \\ & &(2.36) \end{aligned}$$

where B is the total length of the baseline. Thus, the outer and inner aperture diameters can be chosen independently, subject only to the constraint $D_i > D_o$, so long as the aperture spacing is adjusted by the diameter ratio.

Figure 2-12 shows the *IR* of a linear four-aperture system with two different inner diameters; the total baseline B of each array has been adjusted so that the configuration has the same null depth of Angel and Woolf's 1-4-4-1 configuration. The former has a baseline of 76 m, while the new 1-2-2-1 and 1-3-3-1 configurations have baselines of 71.2 m and 75 m respectively. The new nulling array proposed here may be advantageous if there are size or weight constraints on the optics carried by each spacecraft. A factor of 2 or larger reduction in required size and weight can translate to a tremendous cost savings for space missions.

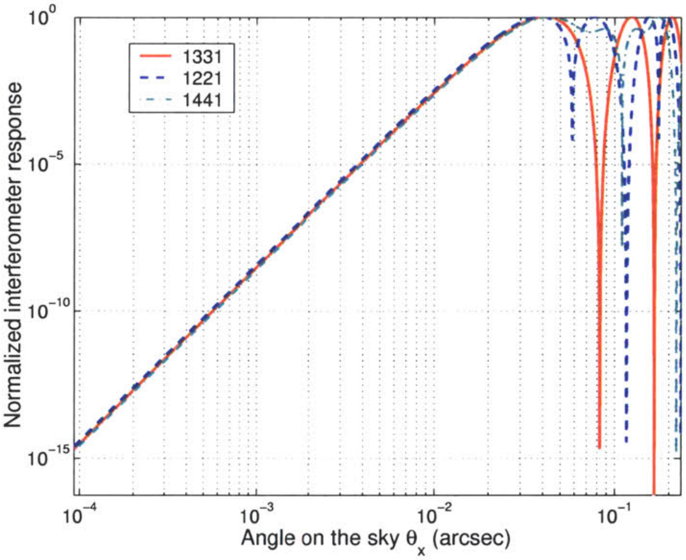

Figure 2-12: Normalized interferometer response of a four-aperture system with varying inner diameter

2.4 Derivation of Statistical Requirements for TPF

The discussion in the previous section has examined the tradeoffs between the design parameters of a nulling interferometry system in order to meet a particular planet finding objective. The resulting aperture geometries, if perfectly maintained, will provide the required depth and breadth of nulling to permit the sensing of Earth-class extrasolar planets. Unfortunately, it is unlikely that these geometric relationships can be perfectly maintained during observations. The optics are mounted on movable platforms (spacecraft) whose positions may be perturbed by environmental disturbances, such as gravity fields and solar pressure. Moreover, the optics themselves may be subject to mechanical vibration or thermal expansion and contraction. As a result, the geometric relationships among the optical components of the interferometer will tend to change slightly due to these unavoidable physical effects.

Since in general a deterministic model for these disturbances does not exist, this section models them as random, and attempts to characterize the variance in null depth as a function of the statistics of the random perturbations. The perturbations considered here are aperture shear motion $(\delta x_j, \delta y_j)$ and the optical path difference (OPD) jitter $2\pi/\lambda\, d_j = kd_j$. When the aperture shear is the only source of disturbances, the OPD is assumed to be controlled perfectly, i.e. OPD = 0. Similarly, OPD is the residual small jitter where any nominal large pathlength difference has been compensated by servo mechanisms in the optical mirrors. All perturbations are considered to be zero mean and mutually uncorrelated.

Recall that null depth is defined by Equation 2.30,

$$ND = \frac{IR_L}{IR_P} = \frac{IR(\theta_{xL}, \theta_{yL})}{IR(\theta_{xP}, \theta_{yP})} \tag{2.37}$$

where IR_L is the interferometer response evaluated at the star limb, IR_P is the response evaluated at the first maximum. When geometric perturbations are present, the response function can be written as

$$\begin{aligned} IR(\theta_x, \theta_y, \delta p) \propto \sum_{k=1}^{N_a} D_k^2 + 2 \sum_{i=1}^{N_a-1} \sum_{l=i+1}^{N_a} D_i D_l \times \\ \cos\left(k(x_{il} + \delta x_{il})\,\theta_x + k(y_{il} + \delta y_{il})\,\theta_y + \phi_{il} + k\delta d_{il}\right). \end{aligned} \tag{2.38}$$

where the vector of perturbations δp contains the $N_a - 1$ unique combinations of each of the terms δx_{il}, δy_{il}, and δd_{il}, and hence δp has length $3(N_a - 1)$.

The fact that the interferometer response changes as a function of the perturbations means that the null depth will also change. The objective is to quantify the expected value $E\{ND(\delta p)\}$ as a function of the statistics of δp. To this end, expand ND to the second order as a function of δp about the nominal condition $\delta p = 0$:

$$\begin{aligned} ND(\delta p) &= ND_o + \sum_{m=1}^{3(N_a-1)} \frac{\partial ND}{\partial \delta p_m}\delta p_m + \frac{1}{2}\sum_{m=1}^{3(N_a-1)}\sum_{n=1}^{3(N_a-1)} \frac{\partial^2 ND}{\partial \delta p_m \partial \delta p_n}\delta p_m\,\delta p_n \\ &= ND_o + J\delta p + \frac{1}{2}\delta p^T H \delta p, \end{aligned} \tag{2.39}$$

where ND_o is the nominal null depth. The vector J and matrix H are respectively the gradient and Hessian of ND with respect to δp, evaluated at $\delta_p = 0$. Note in particular that J and H are thus constants in the above second order expansion of ND.

Taking expected values of Equation 2.39, and recalling that δp is assumed to be zero-mean, a second-order estimate of the mean null depth is

$$\begin{aligned} E\{ND\} &\approx ND_o + \frac{1}{2}\sum_{m=1}^{3(N_a-1)}\sum_{n=1}^{3(N_a-1)} \frac{\partial^2 ND}{\partial \delta p_m \partial \delta p_n}\sigma^2_{p_m p_n} \\ &= ND_O + \frac{1}{2}E\{\delta p^T\, H\, \delta p\} \\ &= ND_O + \frac{1}{2}tr(H\Sigma_p). \end{aligned} \tag{2.40}$$

where $tr(\cdot)$ denotes the trace operator, and $\Sigma_{\delta p}$ is the $3(N_a - 1) \times 3(N_a - 1)$ covariance matrix of δp, $\Sigma_{\delta p} = E\{\delta p \delta p^T\}$. The term $\sigma^2_{p_m p_n}$ is the cross variance of the m^{th} and n^{th} perturbation variables in δ_p, and hence corresponds to the element in the mth row and nth column of $\Sigma_{\delta p}$.

Now the null depth Hessian H must be evaluated in terms of the perturbed interferometer response IR:

$$H = \frac{1}{IR_P}\left(\frac{\partial^2 IR_L}{\partial \delta p^2} - 2\frac{1}{IR_P}\frac{\partial IR_P}{\partial \delta p}\frac{\partial IR_L}{\partial \delta p} - ND_o\frac{\partial^2 IR_P}{\partial \delta p^2}\right). \tag{2.41}$$

The first order IR partial derivatives can be computed directly from Equation 2.38 as

$$\begin{aligned}
\frac{\partial IR}{\partial x_{il}} &= -2kD_iD_l\theta_x \sin(\beta_{il}) \\
\frac{\partial IR}{\partial y_{il}} &= -2kD_iD_l\theta_y \sin(\beta_{il}) \\
\frac{\partial IR}{\partial d_{il}} &= -2kD_iD_l \sin(\beta_{il}),
\end{aligned}$$

where $\beta_{il} = kx_{il}\theta_x + ky_{il}\theta_y + \phi_{il}$, and the second order partials are

$$\begin{array}{ll}
\frac{\partial^2 IR}{\partial x_{il}^2} = -2k^2D_iD_l\theta_x^2\cos(\beta_{il}) & \frac{\partial^2 IR}{\partial d_{il}^2} = -2k^2D_iD_l\cos(\beta_{il}) \\
\frac{\partial^2 IR}{\partial y_{il}^2} = -2k^2D_iD_l\theta_y^2\cos(\beta_{il}) & \frac{\partial^2 IR}{\partial d_{il}\partial x_{il}} = -2k^2D_iD_l\theta_x\cos(\beta_{il}) \\
\frac{\partial^2 IR}{\partial y_{il}\partial x_{il}} = -2k^2D_iD_l\theta_x\theta_y\cos(\beta_{il}) & \frac{\partial^2 IR}{\partial d_{il}\partial y_{il}} = -2k^2D_iD_l\theta_y\cos(\beta_{il})
\end{array}$$

To illustrate this methodology, a linear four-aperture, nulling interferometer array is used to estimate the mean ND distortion $E\{ND\} - ND_o$ as a function of the covariance of the perturbations δp. The configuration parameters used for this example are listed in Figure 2-13(a), and its geometry is illustrated in Figure 2-13(b) The interferometer has a total baseline of 75 m and the incident light wavelength is assumed to be 10 μm. Some simplifying assumptions are used for this set of analyses: (1) All perturbations are zero-mean and uncorrelated; the latter assumption implies that the covariance matrix is diagonal; (2) the aperture shear terms have the same variances ($\sigma^2_{\delta x_{il}} = \sigma^2_{\delta x}$), and OPD perturbations also have the same variances ($\sigma^2_{\delta d_{il}} = \sigma^2_{\delta d}$). Since a linear array is considered here, i.e. $y_j = 0$, the interferometer response depends on a single dimension ($I_r(\theta_x, \theta_y) = I_r(\theta_x)$), and the deviations of y_j do not affect the null depth in this formulation.

As discussed in the previous section, the $1-3-3-1$ configuration has a nominal null depth of about 3×10^{-11} as shown in Figure 2-10. The perturbed null depth as a function of standard deviation (RMS) of $\sigma_{\delta x}$ and $\sigma_{\delta d}$ are shown in Figures 2-14(a) and 2-14(b),

	1	2	3	4
x_i (m)	-37.5	-12.5	12.5	37.5
y_i (m)	0	0	0	0
D_i (m)	1	3	3	1
ϕ_i (rad)	0	π	0	π

(a)

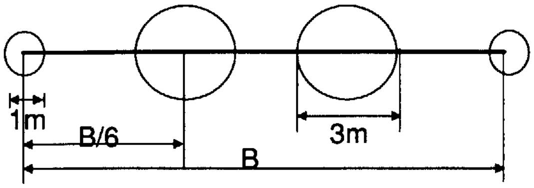

(b)

Figure 2-13: (a)Parameters for a 75 m, four-aperture linear nulling interferometer configuration (b)Geometric configuration for the four-aperture linear array

respectively. To maintain the desired 10^{-6} null depth, the aperture shear in the x axis must be kept below 1.3 m RMS, if there are no OPD perturbations. The null depth is much more sensitive to OPD variations; RMS OPD must be maintained below 3nm in order to satisfy the sensing requirement.

The above example assumes that the nominal wavelength is at 10 μm. The TPF mission is currently expecting the observation wavelength to be in a range of 7 and 20 μm. In order to understand the effects of wavelength on the dynamical requirements, four nominal wavelengths (λ = 7, 10, 15, 20 μm) are chosen to repeat the perturbation analysis above. Figure 2-15(a) and 2-15(b) show that as the wavelength decreases, the RMS requirements on aperture shear and OPD become tighter in order to achieve 10^{-6} null depth. RMS aperture shear motion must be held below 0.9 and 2.5 m depending on the wavelength, while the required RMS OPD is in the range of 2-5 nm.

The RMS requirements are expected to get more stringent if both perturbations are present simultaneously. Figure 2-16(a) shows the equal null depth contour as a function of both RMS requirements. Following the desired null depth (10^{-6}) contour line, as the RMS requirement on δx increases (loosens), the corresponding RMS requirements on OPD decreases (tightens). The contour plot illustrating the wavelength effect is shown in Figure 2-16(b). The subscript on λ in this plot indicates the wavelength in μm. As wavelength decreases, the RMS requirements also become more stringent.

These analyses assume that the perturbations are uncorrelated. If the apertures are located on different spacecraft, this assumption is fairly reasonable. If the apertures are part of a single large structure, the uncorrelated assumptions would not be as accurate. However,

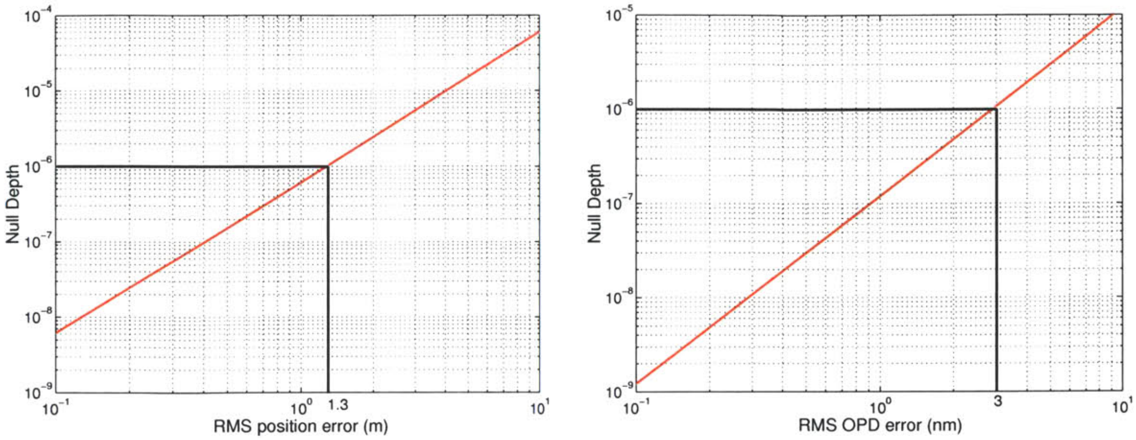

(a)

(b)

Figure 2-14: (a) Mean null depth as a function of RMS aperture shear δx disturbances (b) Mean null depth as a function of RMS OPD δd disturbances

this methodology can be used for both scenarios if the cross-correlation between different perturbation parameters can be estimated. If the covariance matrix $\Sigma_{\delta p}$ can be estimated from a dynamical analysis of the structure containing the apertures, the methodology above can be directly employed to estimate the mean null depth degradation.

OPD stability requirements in the 3nm range have been subsequently confirmed by [52] using a different analysis technique. The RMS requirement on aperture shear δx or baseline sensitivity is much looser; although, it assumes that OPD is controlled perfectly during baseline shifts, which may be unrealistic. As a result the nanometer level OPD requirement will likely drive the design of the system. Stabilizing the OPD on the nanometer level poses difficult technical challenges and pushes the limits of the sensor and actuator technologies. The following chapters discuss the development of a staging control strategy that can assure this level of stabilization with a typical suite of actuators on the spacecraft and optics.

2.5 Summary

The first part of this chapter introduces basic ideas of Fourier optics and interferometry. Special attention is given to nulling interferometry, since it has been identified as a key technology for extra-solar planet detection. Several configuration studies are performed on

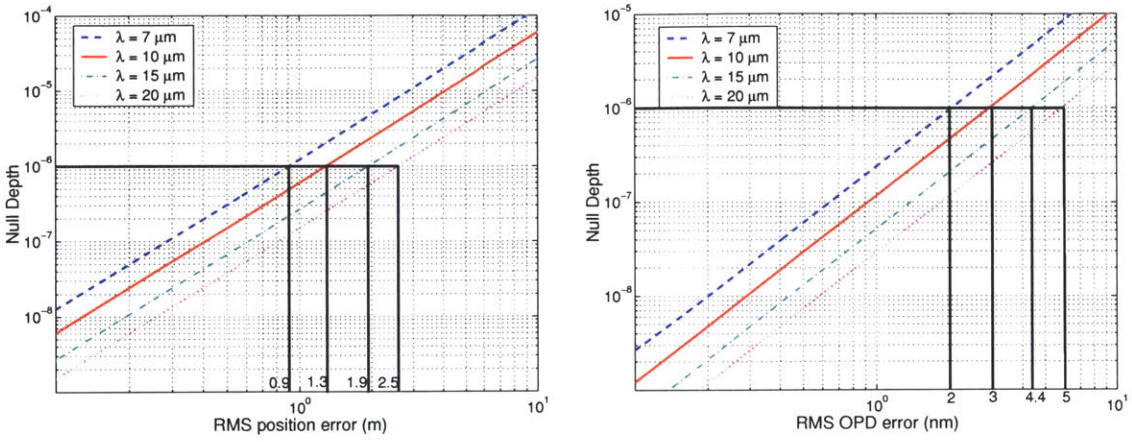

(a)

(b)

Figure 2-15: (a) Change of mean null depth as a function of RMS aperture shear for various wavelengths (b) Change of mean null depth as a function of RMS OPD for various wavelengths

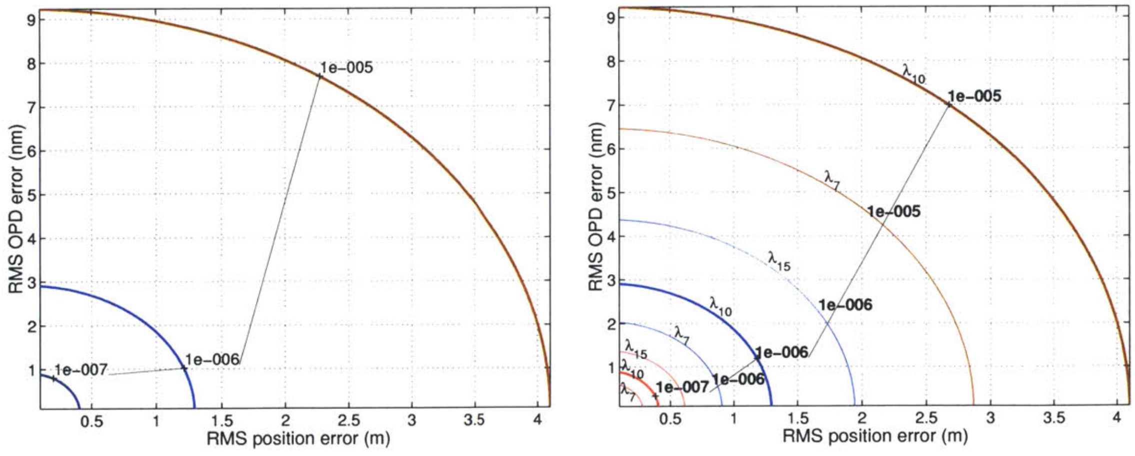

(a)

(b)

Figure 2-16: (a) Mean null depth contours as a function of RMS aperture shear and RMS OPD for a nominal wavelength of 10μm (b) Mean null depth contour for various level of wavelengths linear-array, nulling interferometers. These studies focus on how the interferometer response changes as a function of the number of apertures, the baseline, or the aperture diameter. A desirable interferometer response can be determined by choosing the appropriate aperture location, size, and phase.

The ideal response derived from configuration studies can only be achieved if the interferometer geometry is maintained perfectly. Unfortunately, the optical instruments will be perturbed by external and onboard disturbances during the mission, so it is important to estimate the amount of dynamic perturbations that the nulling interferometer can tolerate and still meet the planet detection criterion. A statistical analysis is developed to quantify the maximum random disturbances allowed in order to achieve a 10^{-6} null depth. This analysis is applied to a four-aperture linear interferometer array, and dynamic disturbances on aperture shear and OPD are considered. Other disturbance types may also be incorporated as long as the perturbed null depth can be approximated accurately using second order approximations.

In reality it is unlikely that the magnitude of the perturbations will be below the specified level identified in this chapter. Therefore, closed-loop control must be used to maintain the optical geometric perturbations within the specified tolerances. Before designing appropriate control algorithms to achieved the desired performance, the next chapter describes the overall system model and actuator nonlinearities that may affect the system performance.

Chapter 3

Dynamical Models and Actuator Constraints

When the idealized aperture and detector geometry described in the previous chapter are implemented on physical devices, the perturbations discussed above will arise from relative motion between these devices. In order to maintain the desired geometry for observational requirements, active control of each of the dynamic degrees of freedom is required. This chapter will examine the dynamical equations that relate the motions of the optical degrees of freedom to the physical disturbance sources and control inputs acting on the system. It will also discuss the characteristics of the actuators used to generate these control inputs for typical space interferometry systems.

To make the initial discussion more concrete, consider a separated space interferometer such as the JPL Starlight mission, utilizing two spacecraft. Both the collector (spacecraft #1) and the combiner (spacecraft #2) carry a light-collecting aperture as illustrated in Figure 3-1(a). Spacecraft #2 also carries a combining instrument, photo detector, and optical delay lines. The baseline displacement between the centers of the two spacecraft is x_{12}, and relative motion of the spacecraft will change this baseline. This baseline motion will alter the interferometer response in a manner described in the previous chapter. Chemical or electrical thrusters on each satellite are usually employed to maintain a desired baseline.

The optical path difference (OPD) of this configuration is a significant parameter in the interferometer response. In this configuration, the OPD is defined by the difference between the left light pathlength (from aperture 1 to combiner) and the right light pathlength (from aperture 2 to combiner). The left pathlength is approximately the baseline x_{12}, and the right pathlength is the distance travelled in a fixed delay line, d_f, plus the distance travelled in an active delay line, d_a, so the total OPD is $x_{12}+d_f+d_a$. The fixed delay line is designed to take out most of the pathlength difference caused by the nominal baseline length, $x_{12}+d_f \approx 0$, and the active delay line is then responsible for any small residual OPDs caused by baseline perturbations from the nominal, or internal distortions in the optical pathlength.

Figure 3-1(b) shows a more detailed model of a typical active optical delay line (ODL). The optical assembly is mounted on a movable cart, providing a dynamic degree of freedom x_{cart}. This degree of freedom can be controlled by an attached DC motor, which moves the cart assembly along a short track. The assembly itself has both a primary mirror and a secondary mirror which reflect the light that enters the delay line. Small changes of the pathlength can be made by changing the relative position of these mirrors, contributing two new degrees of freedom: x_p for the location of the primary mirror, and x_s for the location of the secondary mirror. Typically, control of the primary mirror location is accomplished by a linear voice coil actuator, while control of the secondary mirror is accomplished by a linear piezoelectric stack.

The total OPD is thus determined by the relative displacements of the spacecraft, cart, primary, and secondary mirrors, controlled respectively by thrusters, motor, voice coil and piezo actuators. Even for this relatively simple interferometer, there are a large number of degrees-of-freedom that can influence the desired optical geometry. Each degree of freedom may be affected by unwanted disturbances from either the environment, or from the actions of other electromechanical systems that interact with, or support, operation of the interferometer. For example, there may be solar pressure or gravity gradients acting on the spacecraft, and onboard mechanisms such as reaction wheels or cryogenic coolers may introduce unwanted vibrations to the apertures and mirrors. The role of the individual actuators is to suppress the effects of these disturbances to a specified level.

Section 3.1 begins by discussing the generalized plant and disturbance models which are used in the subsequent analyses in this thesis. The characteristics of the individual actuators defined above will be presented in Section 3.2, including a discussion of the linear and nonlinear constraints governing each actuator. Understanding the effects of these nonlinear constraints, and designing control strategies which accommodate them, will form the bulk of the analysis in later chapters of this thesis. Finally, Section 3.3 looks at the complete suite of typical actuators for an interferometry problem, and discusses the *staged* nature of this system, employing actuators with overlapping frequency responses and maximum output ranges. The challenges of designing an active control strategy for such a system using conventional design methods are identified.

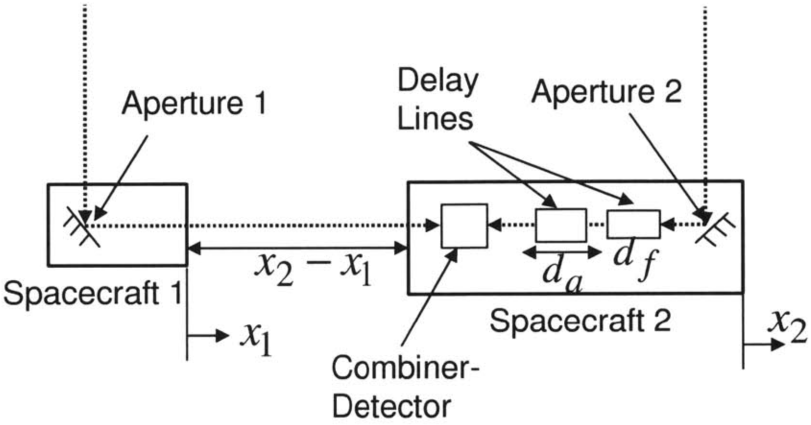

(a)

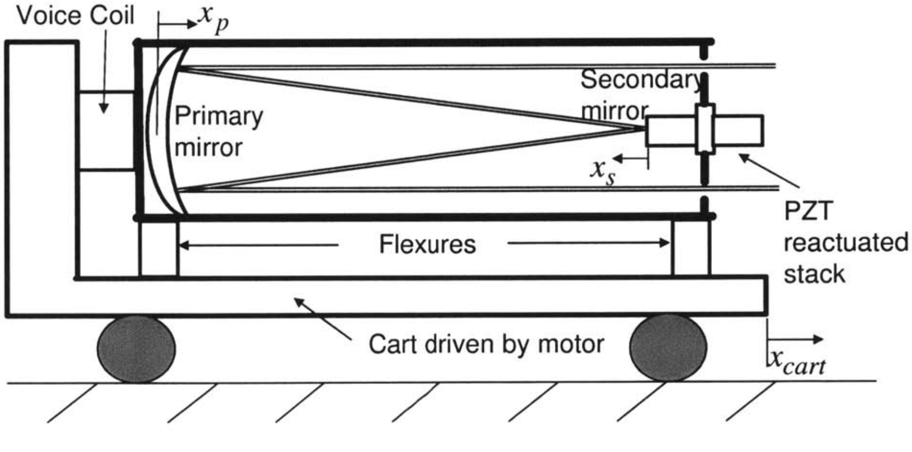

(b)

Figure 3-1: (a) Diagram of a two-aperture space interferometer setup (b) Typical optical delay line schematic

3.1 Plant and Disturbance Model

3.1.1 Nominal model

The situation under consideration may be represented by a schematic of the form

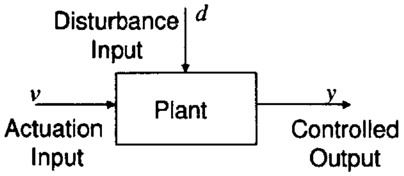

In this diagram, the "plant" corresponds to the dynamic behavior of the spacecraft and its attached optical components. For relatively small deviations from their nominal equilibria, linear models can be developed for the motions of each degree of freedom in the system, using Newton's laws, finite element methods, measurement models, or a combination of all of the above. The resulting dynamics can be written in the linear state-space form,

$$\dot{x} = Ax + B_1 d + B_2 v,$$

where the state vector x contains the physical variables describing the motion of the system, e.g. the position and velocity of each degree of freedom, and the matrices (A, B_1, B_2) are assumed to be constant. The vector d represents the physical disturbances that act to move each degree of freedom away from its nominal value, and the vector v represents the control inputs to the system that attempt to maintain each component at its desired position. The controlled output y measures how close the overall optical geometry coincides with the desired geometry. As shown above, this output can be expressed as a linear combination of the relative positions in the state vector x

$$y = C_1 x.$$

Based on the results of the previous chapter, the output of interest will nominally be OPD, and the goal will be to maintain this quantity as close to zero as possible. However, the discussions below are relevant for any optical metric which can be written in the form above.

The performance of the optical system thus depends on the natural dynamics of the system, the disturbance inputs, and the control inputs. Unfortunately, the natural dynamics of the plant are not likely to react to the disturbances in a manner that will allow the optical performance constraints identified above to be satisfied at all times. In order to meet the tight tolerances posed by interferometry missions, feedback control is often employed, specifying how the inputs v must be selected as a function of the dynamic perturbations in x.

Before designing such a control law, however, additional structure must be placed on the class of disturbances assumed to be acting on the optical system. Although disturbance modelling is not a focus of this thesis, a brief discussion on the development and incorporation of a disturbance model in the overall system is presented in the next section.

3.1.2 Stochastic disturbance model

In space, disturbances may come from atmospheric drag, solar radiation pressure, thermal flux, and magnetic field effects, among others. In addition, spacecraft mechanisms can also be sources of perturbations. For example, fans, pumps, cryogenic coolers, reaction wheels, and thrusters can induce significant vibrations onboard the spacecraft. References [14] and [24] provide a more comprehensive description of spacecraft disturbances - the general trend is that external/environmental disturbances typically act in the low frequency region, whereas many of the internal mechanisms may induce mid- to high frequency range disturbances. The low frequency, external disturbances tend to act on the spacecraft itself, pushing it away from its nominal position, while the high frequency disturbances excite vibrations in the spacecraft structure and optical instruments.

Disturbances may be modelled deterministically or stochastically. For example, deterministic models of solar pressure and magnetic field effects may be derived directly from physical principles [37] or from empirical data [81]. On the other hand, electrical noise generated by electromechanical systems is essentially random, and similarly an unbalanced reaction wheel may impart unpredictable forces to the spacecraft structure. Since deterministic models of disturbances are rarely available, a stochastic model may be the more realistic option at the design phase.

If a disturbance is random in nature, methods based on stochastic processes can be applied to characterize its behavior [60]. A wide-sense stationary (WSS) stochastic process $x(t)$ has constant mean,

$$E\{x(t)\} = \eta, \tag{3.1}$$

and an autocorrelation function depending only on the elapsed interval $\tau = t_1 - t_2$:

$$R_{xx}(\tau) = E\{x(t+\tau)x^*(\tau)\}. \tag{3.2}$$

The power spectral density (PSD) is defined as the Fourier transform of the autocorrelation function,

$$S_{xx}(\omega) = \int_{-\infty}^{+\infty} R_{xx}(\tau)e^{-j\omega\tau}d\tau, \tag{3.3}$$

and the covariance, or average-power of x can be computed by

$$E\{|x(t)|^2\} = R_{xx}(0) = \frac{1}{2\pi}\int_{-\infty}^{+\infty} S(\omega)d\omega,$$

which is proportional to the area under the PSD curve.

A special case of these stochastic processes is stationary white noise $w(t)$, where its autocorrelation and PSD are given by

$$\begin{aligned} R_{ww}(\tau) &= q\delta(\tau), \\ S_{ww}(\tau) &= q. \end{aligned}$$

The number q is called the "intensity" of the noise. The PSD for white noise is a constant over all frequencies and thus $w(t)$ has infinite average power. Clearly this signal is only a mathematical abstraction, since no physical signal can have infinite energy. However such a process has tremendous mathematical utility, and one example of its functionality is illustrated here.

Under appropriate assumptions [60], a WSS process $x(t)$ can be modelled as the response of a linear, minimum-phase system driven by a zero-mean, unit-intensity white noise, $w(t)$,

$$x(t) = \int_{-\infty}^{\infty} w(t-\alpha)g(\alpha)d\alpha,$$

where $g(t)$ is the impulse response of the minimum-phase system. If x can be modelled by such a system, the PSD of x can be computed by

$$S_{xx}(\omega) = G(\omega)G^*(\omega)S_{ww}(\omega),$$

where G is the Fourier transform of the impulse response $g(t)$. Since $w(t)$ is a unit-intensity white noise, its PSD, S_{ww}, is simply 1, and the above expression simplifies to

$$S_{xx}(\omega) = G(\omega)G^*(\omega). \tag{3.4}$$

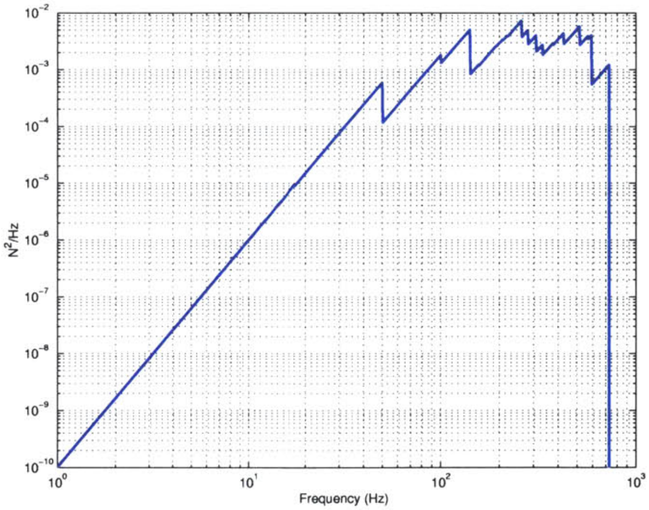

Figure 3-2: Power spectral density of a broad-band reaction wheel disturbance. [57](wheel speed range:$[0, 3000]$ rpm)

Thus, given a specific PSD of process $x(t)$, a minimum-phase filter G can be found that corresponds to the model of a system with transfer function G driven by white noise. This filter is also known as the innovations filter [60].

In practice, the PSD of the disturbance can either be obtained mathematically or estimated from experimental data. For example, a representative PSD plot of a broad-band reaction wheel disturbance model [57, 24] is shown in Figure 3-2. This figure shows that the reaction wheel generates mid- to high frequency range disturbances. Reaction wheel disturbances are anticipated to be the largest disturbance source onboard the spacecraft in interferometry missions [13, 24, 38, 50, 57], and the PSD shown in Figure 3-2 will often be used as a representative disturbance in the control designs of later chapters. Other representative disturbance PSDs for the spacecraft environment can be found in [24].

Given a PSD for the disturbance, the corresponding innovations filter can be found from Equation 3.4. This filter can then be absorbed into the overall dynamical model of the system using state augmentation as shown in Figure 3-3. Expressing the innovations filter in state-space form

$$\begin{aligned} \dot{x}_d &= A_d x_d + B_d w \\ d &= C_d x_d. \end{aligned}$$

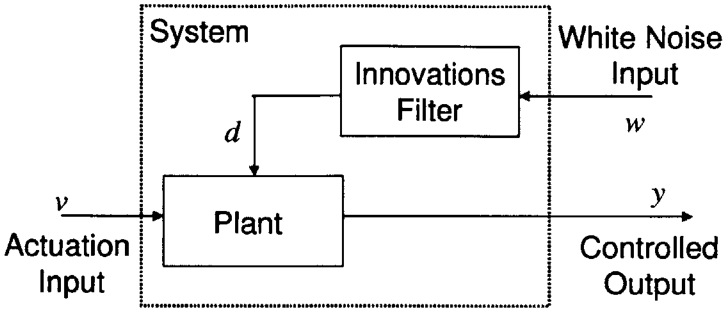

Figure 3-3: Integrate disturbance model into system model

and combining with the plant model

$$\begin{aligned}\dot{x}_p &= A_p x_p + B_w d + B_u u \\ y &= C_p x_p.\end{aligned}$$

the integrated model is given by

$$\begin{aligned}\begin{bmatrix}\dot{x}_p \\ \dot{x}_d\end{bmatrix} &= \begin{bmatrix}A_p & B_w C_d \\ 0 & A_d\end{bmatrix}\begin{bmatrix}x_p \\ x_d\end{bmatrix} + \begin{bmatrix}0 \\ B_d\end{bmatrix} w + \begin{bmatrix}B_u \\ 0\end{bmatrix} u \\ y &= \begin{bmatrix}C_p & 0\end{bmatrix}\begin{bmatrix}x_p \\ x_d\end{bmatrix}\end{aligned}$$

The above expression models the case that the disturbance acts as an input to the plant dynamics. Alternately, the disturbance can be modelled as acting directly on the output y, using

$$\begin{aligned}\dot{x}_p &= A_p x_p + B_u u \\ y &= C_p x_p + d,\end{aligned}$$

so that the corresponding integrated model becomes

$$\begin{aligned}\begin{bmatrix}\dot{x}_p \\ \dot{x}_d\end{bmatrix} &= \begin{bmatrix}A_p & 0 \\ 0 & A_d\end{bmatrix}\begin{bmatrix}x_p \\ x_d\end{bmatrix} + \begin{bmatrix}0 \\ B_d\end{bmatrix} w + \begin{bmatrix}B_u \\ 0\end{bmatrix} u \\ y &= \begin{bmatrix}C_p & C_d\end{bmatrix}\begin{bmatrix}x_p \\ x_d\end{bmatrix}\end{aligned}$$

Regardless of how the disturbance enters the plant, the integrated model has the general form

$$\dot{x} = Ax + B_1 w + B_2 u$$

$$y = C_1 x$$

Once the plant and disturbances have been integrated into a linear model of this form, the effects of the disturbances on the system performance can be formally analyzed.

3.1.3 Stochastic performance analysis

The dynamical model of the uncontrolled system is given by

$$\dot{x} = Ax + B_1 w,$$

where w is a stationary Gaussian process (or white noise), i.e. at each time t the probability density function of $w(t)$ is Gaussian. The mean of the process x can be computed from taking the expectation of the dynamical equation:

$$\dot{\bar{x}}(t) = A\bar{x}(t) + B_1\bar{w}(t). \tag{3.5}$$

The covariance matrix is defined by $\Sigma_{xx}(t) = E\{[x(t) - \bar{x}][x(t) - \bar{x}]^T\}$ with its dynamics described by [32],

$$\dot{\Sigma}_{xx} = A\Sigma_{xx} + \Sigma_{xx}A^T + B_1 B_1^T. \tag{3.6}$$

The initial conditions on (3.5) and (3.6) are $\bar{x}_o$ and Σ_{xx_o} respectively, and $\bar{x}_o$ is assumed to be uncorrelated from the random noise $w(t)$.

Since A and B_1 are constant, independent of time, it is possible that the time-varying statistical properties may asymptotically become constant. If A is Hurwitz (all eigenvalues in the open left half of the complex plane), the mean $\bar{x}$ converges to $\bar{x} = -A^{-1}B_1\bar{w}$, and the covariance converges to a constant matrix Σ_{xx} given by

$$A\Sigma_{xx} + \Sigma_{xx}A^T + B_1 B_1^T = 0. \tag{3.7}$$

Using computing software such as MATLAB, the solution Σ_{xx} of this equation can be obtained easily, and the covariance matrix of the system outputs can then be calculated as

$$\Sigma_{yy} = C_1 \Sigma_{xx} C_1^T. \tag{3.8}$$

and the mean value of the output is $\bar{y} = -C_1 A^{-1} B_1 \bar{w}$. Note in particular that if w is zero mean, the state and output will also be zero mean, and this assumption will be made throughout this thesis. The RMS deviation of each individual output from its mean value of zero is then simply the square root of the i^{th} diagonal element of Σ_{yy}. If there is only one controlled output, then its RMS deviation from zero is given by $\sigma_{yy} = \sqrt{C_1 \Sigma_{xx} C_1^T}$.

If the interferometric system were ideally linear over an arbitrarily large range of inputs and outputs, techniques such as those above would be sufficient to accurately predict the performance of the system for a specified feedback control law. However, in reality the actuators have constraints and limitations, such as maximum stroke or force output and minimum resolution. These are nonlinear characteristics, whose effects cannot be accurately modelled using the formulas above. While the usual practice is to simply ignore these effects and to design a control algorithm that tries to keep the actuators operating in their linear range, the extremely tight tolerances on a space interferometry system require that the effects of these nonlinearities be addressed directly.

If the nonlinear actuator characteristics are taken into account, an appropriate state-space model could be written as

$$\dot{x} = Ax + B_1 w + B_2 \phi(u) \tag{3.9}$$

$$y = C_1 x \tag{3.10}$$

with actuator constraints and nonlinearities described by the function $\phi(\cdot)$. However, accurately predicting the RMS performance of this system is nontrivial, not to mention the task of designing a control law capable of maintaining the required tolerances. New methods for analytically predicting the steady-state performance of the above model is the focus of Chapter 4, and controller design is examined in Chapter 5. Before exploring how to modify the above stochastic analysis for the nonlinear input problem, however, the remainder of the current chapter defines the specific class of actuator nonlinearities considered in this thesis.

3.2 Actuator Characteristics

For the actuators described above – thrusters, motors, voice coils, piezos – the input to the actuator is electrical (voltage or current) and the output is mechanical (displacement or force). The input to the mechanical degrees of freedom in the optical system is given by $v = \phi(u)$, where ϕ is a possibly nonlinear function describing how the mechanical inputs v depend on the actuating electrical signal u. The purpose of this section is to examine the common kinds of nonlinearities ϕ which are present in the above set of actuators.

3.2.1 Saturation

One of the most common actuator constraints is saturation, defined as the maximum possible output that can be obtained from the actuation system. For example, there is an upper limit to the amount of force that a given thruster or motor can apply, regardless of the magnitude of the actuating electrical signal. Saturation effects can be modelled as a limiter with input-output relationships shown in Figure 3-4(a). Of course, the driving electrical signal to the actuator is itself limited, and in practice it is common to match the electrical limits to the mechanical stroke constraints at DC. For example, the typical voltage input to a PZT actuator is limited to ±10 V, which in turn generates the maximum stroke (extension) of $\pm 10\mu$m at DC.

To illustrate the effects that saturation can have on performance, consider the following simple, first-order system

$$\begin{aligned} \dot{x} &= -x + \phi(u) + w \\ u &= kx \end{aligned} \tag{3.11}$$

where the function $\phi(\cdot)$ describes the saturation function, w is the unit-intensity white noise, and $k = -10$ for this example. Since it is nontrivial to analytically predict the steady-state performance of a nonlinear system, the performance is analyzed numerically.

With no feedback control ($k = 0$), the dynamics are linear and Equation 3.7 predicts the steady-state variance of $\sigma_x^2 = 0.5$. With the feedback control above, if the actuator were ideally linear, Equation 3.7 can again be used to compute that $\sigma_x^2 = 1/(2(1+k)) = 0.0455$, or an order of magnitude reduction from the open-loop variance. In the following discussion, the ideal linear output variance is denoted by σ_L^2.

In order to obtain the steady-state performance of the actual nonlinear system, the saturation function in Figure 3-4(a) is used and the dynamics are simulated with a fixed-step, fourth order Runge-Kutta algorithm with a time step of $\delta t = 10^{-4}$ s and a total simulation time of $T = 200$ s. To numerically compute the steady-state performance, the first 20 s of data are ignored, and the remaining data are used to provide the unbiased estimate of the variance,

$$\sigma_x^2 = \frac{1}{N-1}\sum_{i=1}^{N}(x_i - \bar{x})^2, \tag{3.12}$$

where $\bar{x} = 1/N(\sum_{i=1}^{N} x_i)$, and N is the number of time steps ($T/\delta t$).

Figure 3-4(b) shows the degradation of performance caused by actuator nonlinearities. On the vertical scale is the closed-loop performance normalized by the performance obtained using a linear actuator. This performance ratio is plotted against the saturation level of the actuator normalized by the standard deviation of the input u. For saturation levels greater than $3\sigma_u$, the performance is the same as in the linear control case, since the actuator is rarely saturating. The performance gets worse as the saturation level decreases relative to σ_u, which indicates that the actuator becomes less effective due to saturation limitations. As the maximum actuator output shrinks towards zero, the closed-loop variance approaches the open-loop variance $(10 \times \sigma_L^2)$, since little effective control is being applied to the system in this limit. This simple example demonstrates that the saturation level can greatly affect system performance, and the degree of its effects on the performance depends on the size of the control signal (σ_u).

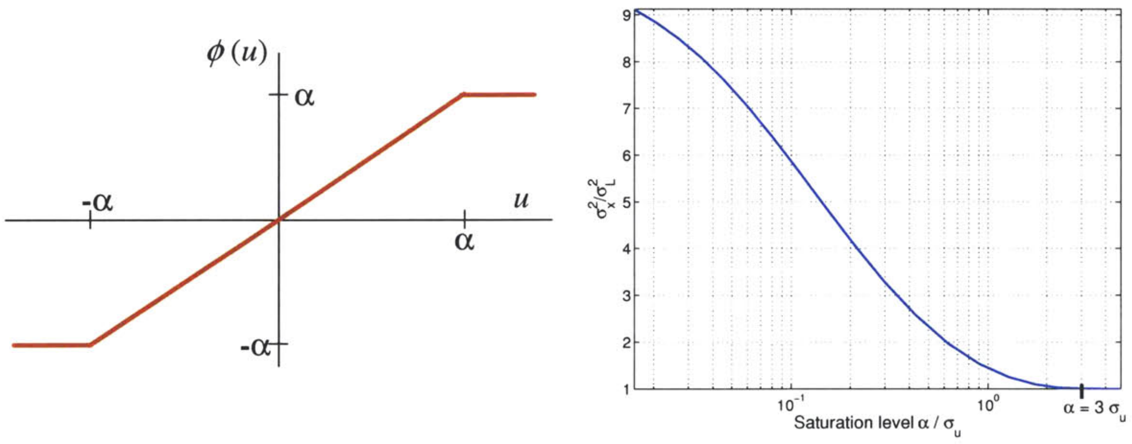

(a)

(b)

Figure 3-4: (a) Saturation model of actuator constraint (b)Ratio between nonlinear performance variance and linear performance variance as a function of normalized saturation level (α/σ_u)

3.2.2 Resolution

In addition to saturation effects, resolution is another common nonlinear constraint. Resolution is defined as the minimum physical output of the actuator, usually modelled as a small dead band around the zero input level, with a "jump" in the output to a nonzero level once the actuating signal exceeds the dead band. A model of resolution effects is shown in Figure 3-5(a). This kind of effect is typical in mechanical systems with friction, or electrical systems with thresholding. It can also be used to characterize the behavior of the minimum on-time of electrical or chemical thrusters. In electrical systems, a voltage or current threshold is usually present to eliminate electrical noise, so no electrical signal is generated if the voltage or current is below the noise threshold. Note that the size of the deadzone and the level of jump do not have to be the same in Figure 3-5(a); they are shown to be the same in the plot for simplicity.

In order to qualitatively understand the effects of resolution, the steady-state performance is computed for the same 1 DOF example above, where the nonlinear function ϕ is now a resolution function as shown in Figure 3-5(a). The same numerical algorithm is used for this analysis, and the result is illustrated in Figure 3-5(b). At "fine" levels of resolution ($r < 1.5\sigma_u$), the system performance is unaltered from the linear control case. As the resolution becomes "coarser", with the deadband size $2r$ increasing, a larger portion of the signal into the actuator becomes ineffective in producing an output from the actuator. When most of the control signal is within the deadzone or $2r > 3\sigma_u$, the system performance starts to deviate greatly from the linear performance and degrades monotonically as a function of the resolution level r.

The effect of resolution on system performance again depends on the size of the control signal σ_u relative to the resolution deadband. Realistic values of actuator resolution r for actuators used on space interferometer missions are discussed in Section 3.3.

3.2.3 Quantization

Quantization is a nonlinear actuator phenomenon that may cause effects similar to those of resolution. Quantization effects are roundoff errors introduced by digital to analog (D/A) conversion, and a sample input-output characterization of a quantizer is shown in Figure 3-6(a). These effects have been studied extensively in the digital control community, since most modern computer controlled systems are subject to these effects.

One common method of predicting the effects of quantization on system performance replaces the quantizer with an additive noise model as shown in Figure 3-6(b). In this model the input noise is a sequence of random variables u with a uniform probability density function ranges from $-q/2$ to $q/2$ and a variance of $q^2/12$, where q is the quantization level

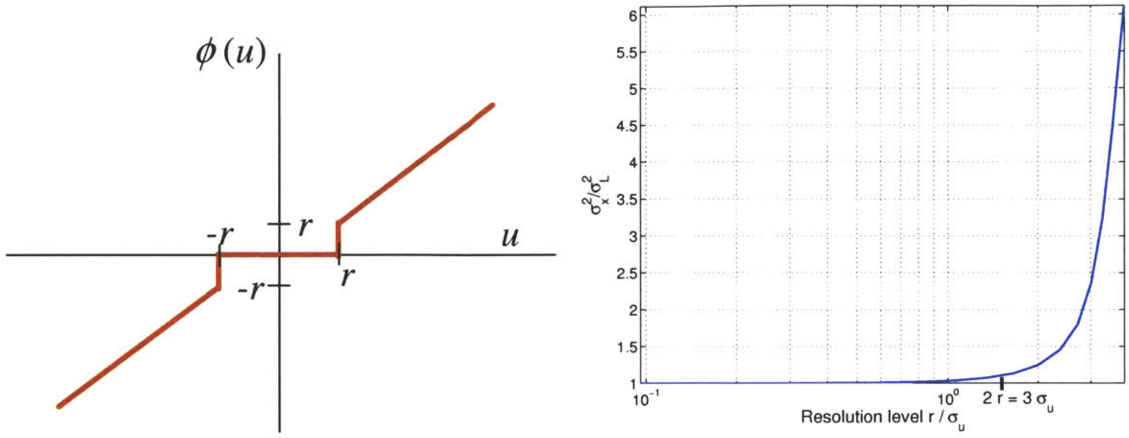

(a) (b)

Figure 3-5: (a) Resolution model of actuator constraint (b)Ratio between nonlinear performance variance and linear performance variance as a function of normalized resolution level (r/σ_u)

[17]. The validity of this equivalent additive noise model is examined here. Denote the output from the quantizer as v and let the output from the additive noise model be $\tilde{v}$. The characteristic function, $\Phi_u(x)$, of the input is defined as the Fourier transform of its probability density function, $p_u(u)$,

$$\Phi_u(x) = \int_{-\infty}^{\infty} p_u(u) e^{jxu} du = E\{e^{jux}\}. \tag{3.13}$$

If the characteristic function is bandlimited,

$$\Phi_u(x) = 0 \quad \text{for} \quad |u| > \tfrac{2\pi}{q} \ , \tag{3.14}$$

then the output of the quantizer v has the same probability moments $E\{v^n\}$ as the output from the additive noise model $E\{\tilde{v}^n\}$ [85], justifying use of the additive noise model in these circumstances.

However, physical signals are rarely ideally bandlimited. For example, the Gaussian density function is not perfectly bandlimited since its characteristic function approaches zero only asymptotically. Fortunately most signals are approximately bandlimited, and with sufficiently small quantization levels the stochastic assumptions for the additive noise model are satisfied closely enough that negligible error is introduced into the analysis. Indeed, if the input is Gaussian with variance σ_u^2, the additive noise model is a good approximation to the effects of resolution provided that $\sigma_u > q$ [85].

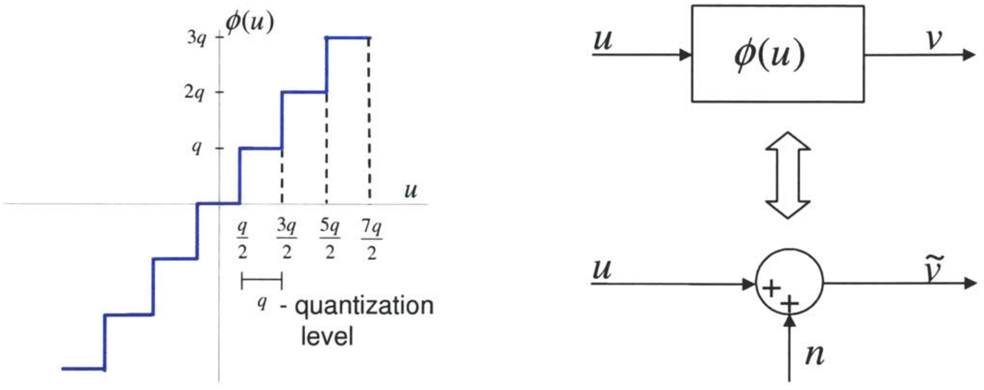

(a)

(b)

Figure 3-6: (a) Output of a quantizer as a function of the input signal (b) Stochastic model of quantization effects is an additive noise with uniform density function

The numerical simulation above is again used to examine the steady-state, closed-loop performance σ_x^2. For this example, there are no saturation or resolution effects; the nonlinear function ϕ only describes the quantizer. The solid line in Figure 3-7 shows the steady-state variance ratio (σ_x^2/σ_L^2) as a function of normalized quantization level (q/σ_u). Recall that σ_L^2 is the closed-loop performance obtained with an ideal linear actuator. At low quantization levels where $q < 3\sigma_u$, the nonlinear performance is similar to the linear control case. The performance degrades quickly as the quantization level increases above this threshold. It should be emphasized that both resolution and quantization have an effective deadband size of $2r$ and q, respectively. Therefore, the two effects are seen to have essentially identical behavior, causing the system performance to deviate from the linear performance when the induced deadzone size is greater than $3\sigma_u$. This result is expected since 99.7% of control signal becomes zero after passing the deadband and would be ineffective on the plant.

The solid line in the figure shows the performance when a quantizer is implemented, and the dashed line illustrates the performance when the equivalent additive noise model is used. Note that the two predictions deviate greatly when $q > \sigma_u$ or $q/\sigma_u > 1$. As discussed above, if σ_u is greater than the quantization level q, the additive noise model is expected to provide a good statistical description of the quantizer. However, when the assumption is no longer true, the performance of the additive model deviates from the quantizer as shown in Figure 3-7. It is also interesting to note that the additive noise model tends to over predict the output variance, and hence, this model is overly conservative for large quantization levels. The results shown in this section demonstrate that quantization may or may not significantly affect the steady-state variance of x, depending on the relative size of the quantization level and the control signal σ_u. Typical values of the quantization level are a function of the bit resolution used in the D/A converter.

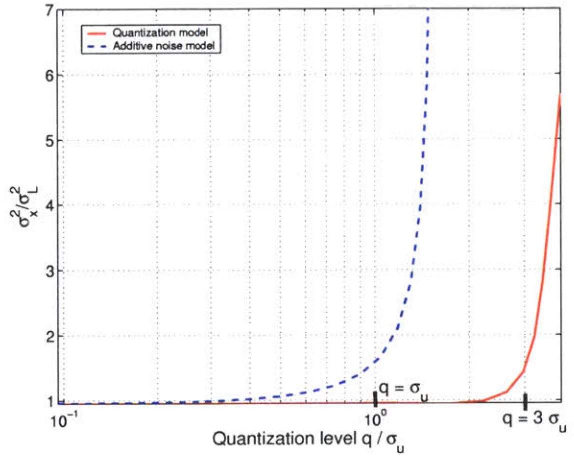

Figure 3-7: Steady-state performance variance as a function of quantization level: Solid line - actual quantizer. Dashed line - modelling quantizer as additive noise

3.2.4 Bandwidth

In addition to the nonlinear effects described above, most actuators also have bandwidth limitations. The bandwidth is defined as the frequency range where the actuator can follow the input without much error, or where the actuator output is essentially the same as its input (classically, within 3 dB). The actuator bandwidth can be limited by the rise time of the amplifier current or the stiffness of the mechanical system. For the electromechanical devices considered in this thesis, both the electrical and mechanical time constants may be useful for characterizing actuator bandwidth. The electrical time constants are usually at least an order of magnitude smaller than the mechanical time constants in typical applications. The bandwidth limitation of the actuator is modelled as a low pass filter, and a representative first order low pass filter with corner frequency at 1 Hz is shown in

Figure 3-8(a).

In order to study the effect of actuator bandwidth on the system performance, the scalar example above is used again, and the actuator is assumed to have no nonlinearities $\phi(u) = u$. The dynamics of the system are modified slightly to incorporate the bandwidth limitations on the actuator,

$$\begin{aligned} \dot{x} + x &= w + v \\ u &= kx. \end{aligned}$$

The following transfer function from commanded input u to actual input v is used to model actuator bandwidth:

$$V(s) = G_a(s)U(s), \tag{3.15}$$

where $G_a(s)$ is a first order, low pass filter with corner frequency or bandwidth ω_a. The steady-state performance σ_x^2 is plotted as a function of ω_a as illustrated in Figure 3-8(b). The controller gain k is again set at -10 for this example. Note that as the bandwidth decreases, the actuator is not as effective in rejecting the full spectrum of the disturbances, and the corresponding closed-loop performance deteriorates as the actuator bandwidth decreases.

It is worth noting that the above analysis is conducted at a fixed controller gain. For a linear system, the effective bandwidth of the actuation system can be increased by increasing the controller gain. However, if saturation is taken into account, the bandwidth will be ultimately limited since the controller gain cannot increase without bound due to saturation effects. This limitation will be analyzed in greater detail in Chapter 4.

3.2.5 Composite model

Pulling together the above observations, the principal parameters governing the operation of the actuators examined in this thesis are: saturation limits α, resolution level r, quantization level q, and bandwidth of operation ω_a. The first three of these characteristics are modelled as nonlinear, time-domain phenomena, whereas the bandwidth of the actuators may be modelled as a roll-off in the frequency response implemented by a linear transfer function. A plot of a typical function ϕ incorporating the nonlinear effects (saturation, resolution, and quantization) is shown in Figure 3-9.

These effects may be incorporated into the generalized system models from Section 3.1 in the following fashion. The integration of the bandwidth model into the system model

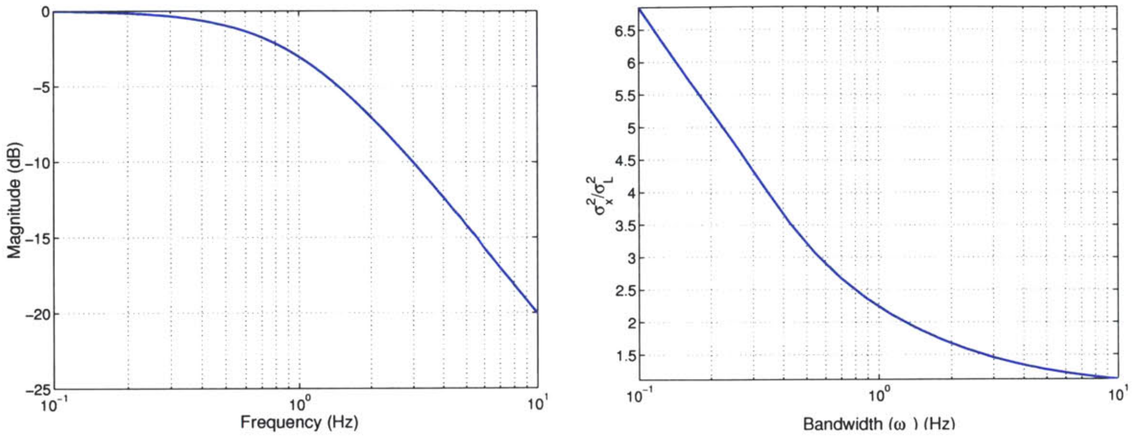

(a) (b)

Figure 3-8: (a) Representative frequency model for characterizing actuator bandwidth limitations (b) Steady-state performance variance as a function of the bandwidth (ω_a)

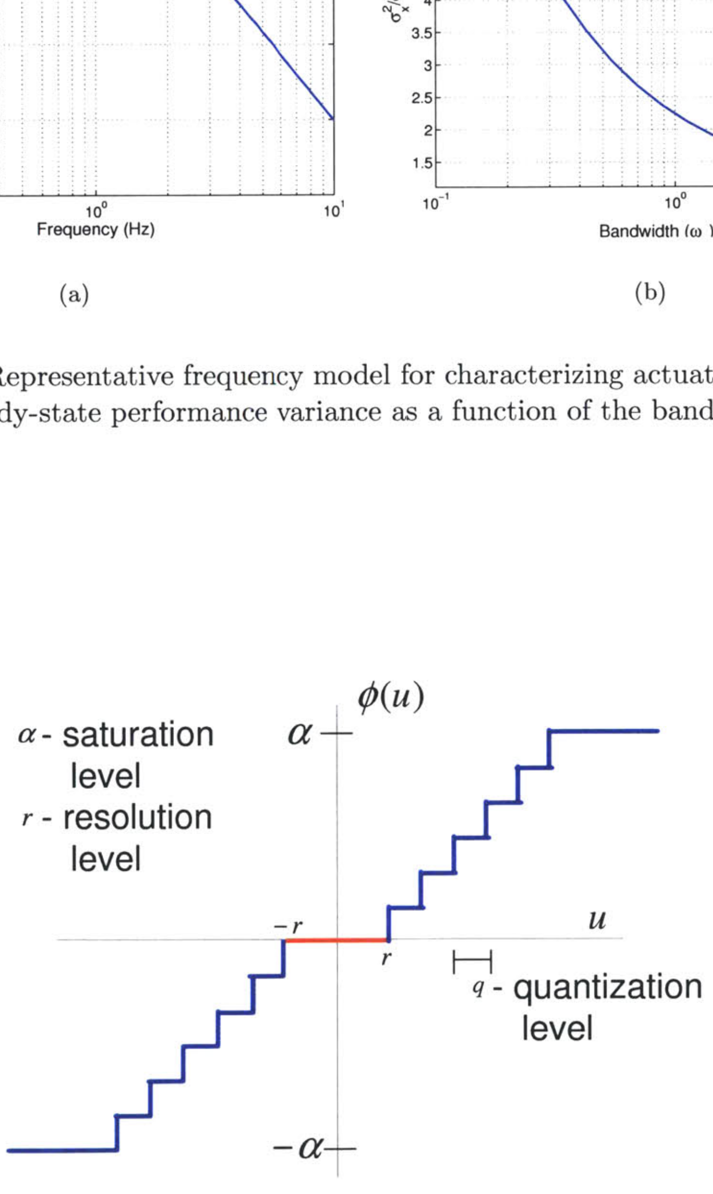

Figure 3-9: Representative input-output relationship of actuator with constraints including saturation level α, quantization level q, and resolution r

is discussed first, and the nonlinear constraints are then added to characterize other actuator limitations. Let G_{A_i} be the i^{th} actuator frequency response with state-space model $(A_{a_i}, B_{a_i}, C_{a_i}, D_{a_i})$, with $D_{a_i} = 0$ since there is assumed to be no direct feed-through in these filters. The system model presented in Section 3.1.2 with plant dynamics $(A_p, [B_w\, B_u], C_p)$ and disturbance innovations model (A_d, B_d, C_d) can be further augmented to include actuator dynamics:

$$\begin{aligned}
\begin{bmatrix} \dot{x}_p \\ \dot{x}_d \\ \dot{x}_{a_1} \\ \vdots \\ \dot{x}_{a_{n_u}} \end{bmatrix} &= \begin{bmatrix} A_p & B_w C_d & B_{u_1} C_{a_1} & \cdots & B_{u_1} C_{a_{n_u}} \\ 0 & A_d & 0 & \cdots & 0 \\ 0 & 0 & A_{a_1} & \cdots & 0 \\ \vdots & \vdots & \vdots & \ddots & \vdots \\ 0 & 0 & 0 & \cdots & A_{a_{n_u}} \end{bmatrix} \begin{bmatrix} x_p \\ x_d \\ x_{a_1} \\ \vdots \\ x_{a_{n_u}} \end{bmatrix} \\
&\quad + \begin{bmatrix} 0 \\ B_d \\ 0 \\ \vdots \\ 0 \end{bmatrix} w + \begin{bmatrix} 0 \\ 0 \\ B_A \end{bmatrix} \tilde{u} \qquad (3.16) \\
y &= \begin{bmatrix} C_p & 0 & 0 & \cdots & 0 \end{bmatrix} \begin{bmatrix} x_p \\ x_d \\ x_{a_1} \\ \vdots \\ x_{a_{n_u}} \end{bmatrix},
\end{aligned}$$

where

$$B_A = \begin{bmatrix} B_{a_1} & & 0 \\ & \ddots & \\ 0 & & B_{a_{n_u}} \end{bmatrix},$$

B_{u_i} is the i^{th} column of the B_u matrix, and n_u is the number of actuators. The above model assumes an input disturbance. An output disturbance model can be obtained easily by setting B_w in the above equal to zero, and replacing the first zero submatrix in the equation defining y with C_d.

The overall dynamical model above is shown schematically in Figure 3-10. This block diagram incorporates the linear dynamics of the plant (optics and spacecraft), disturbances

(G_w), and actuator frequency response (G_{A_i}). The full state-space description of the integrated model shown in Equation 3.16 can be written in the compact form

$$\dot{x} = Ax + B_1 w + B_2 \phi(u) \quad (3.17)$$

$$y = C_1 x. \quad (3.18)$$

where ϕ is now a vector of nonlinear functions, whose ith component ϕ_i represents the saturation, resolution, and quantization of characteristics of the ith actuator. This is the basic framework for the system analysis undertaken in this thesis.

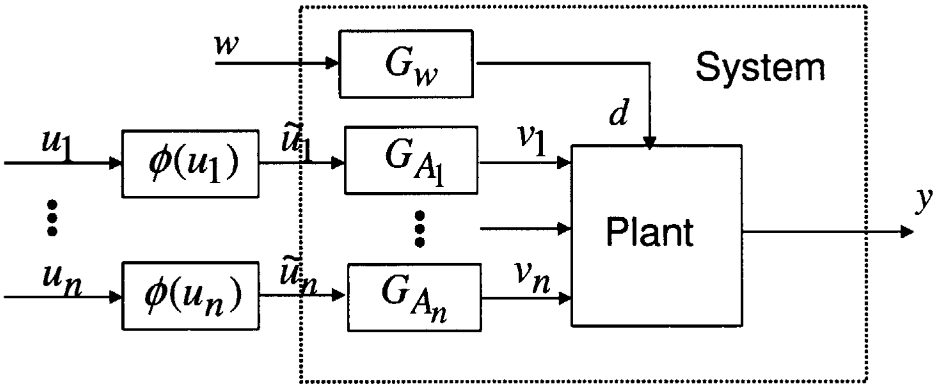

Figure 3-10: Overall system model of the plant, disturbance, and actuators

3.3 Actuators for Space Interferometers

This section examines in greater detail the electromechanical properties of the four basic types of actuators used in space interferometry missions to control the optical pathlength: piezoelectric actuators, voice coils, DC motors, and spacecraft thrusters. In addition to characterizing the bandwidth and nonlinear parameters of each of the actuators, the following sections also attempt to characterize the efficiency of each actuator in terms of the mechanical output it provides for a given electrical power input. Since power resources are limited onboard the spacecraft, it is important to quantify the power consumed by these actuators; subsequent analysis will attempt to design controllers that minimize consumption of total electrical power.

3.3.1 PZT actuator

The PZT (Plumbum Zirconate Titanate) translator or actuator uses piezoelectric materials to convert electrical energy into mechanical energy and vice versa. When an electric field is applied to piezoelectric material, it is capable of very fine, sub-nanometer, position changes when unloaded, and can move at very high frequencies (20-50 kHz). The typical stroke of a PZT actuator is on the order of tens or hundreds of μm [30] depending on the design. For ODL applications, these actuators usually have a stroke between 5-30 μm and a bandwidth of 2-4 kHz while carrying light loads, although the specific combination of parameters used may be a design tradeoff. The equivalent force limitations will depend on the load mass acted on by the PZT actuator.

Since the displacement of a PZT actuator is not influenced by mechanical friction or stiction, its theoretical resolution is unlimited. However, in reality the performance of the actuator can be affected by electronic noise in the amplifier that provides the actuating voltage, the precision of the mechanical mounting, and a number of other factors, so the achievable PZT resolution is usually considered to be on the order of one tenth of a nanometer ($r \approx 0.1nm$). More detailed descriptions of PZTs can be found on the tutorial website provided by Physik Instrumente [30] or other principal suppliers.

A circuit model describing the electromechanical properties of a PZT is shown in Figure 3-11(a). The blocked force generated by the PZT is directly proportional to the voltage across the capacitor; equivalently the unblocked position or length of the PZT is proportional to the charge Q contained in the capacitor C. A small voltage drop occurs at the series resistance R_s, and a much bigger resistor R_d is used in parallel to model the PZT self-discharge. The PZT discharge is usually very small and can often be neglected, in a first approximation. During the charging process, only the R_sC circuit needs to be considered and its dynamical model is a simple first order system:

$$V_{ext} = R_s \frac{dQ}{dt} + \frac{1}{C} Q,$$

where Q is the charge on the capacitor. The response of this RC-circuit from V_{ext} to Q with a time constant of $R_sC = 50$ μs is shown in Figure 3-11(b). For a wide range of frequencies, the voltage across the capacitor is essentially equal to the voltage applied, and therefore, the blocked force generated from the PZT, F_{pzt}, is proportional to the voltage applied

$$F_{pzt} \approx K_f V_{ext},$$

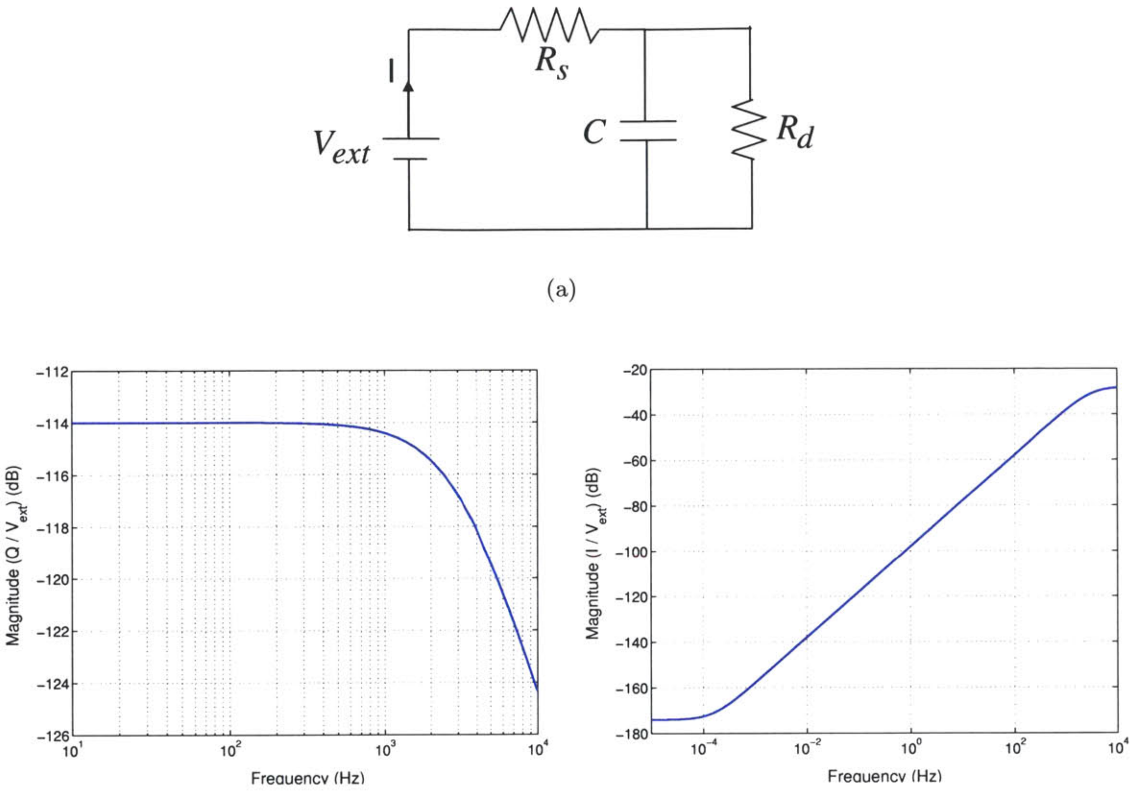

(a)

(b)

(c)

Figure 3-11: (a) Equivalent circuit model of the PZT actuator (b) Electrical circuit response of the PZT actuator (c) Transfer function from input voltage to current output

where $K_f = K_{pzt}d_{33}L_o/t$, and K_{pzt} is the stiffness of the actuator, d_{33} is the PZT strain coefficient, L_o is the nominal length, and t is the thickness of the PZT. The 3 kHz bandwidth of this response shown in Figure 3-11(b) is typical for a PZT.

In order to estimate the power drawn by the PZT actuator, the equivalent impedance of the complete circuit is computed,

$$\mathcal{Z}(s) = \frac{V(s)}{I(s)} = \frac{R_sR_dCs + (R_s + R_d)}{R_dCs + 1}$$

The transfer function from the external voltage to the current is then the inverse of the impedance,

$$\begin{aligned} \frac{I(s)}{V(s)} &= \frac{R_dCs + 1}{R_sR_dCs + (R_s + R_d)} \\ &= \frac{1}{R_s + R_d}\left(\frac{\tau_1 s + 1}{\tau_2 s + 1}\right), \end{aligned}$$

where $\tau_1 = R_d C$ and $\tau_2 = C(R_s R_d)/(R_s + R_d)$. Since $R_s \ll R_d$, the transfer function looks similar to a high pass filter as shown in Figure 3-11(c).

At low frequencies, $I(s) \approx V(s)/(R_s + R_d)$ and the power drawn is approximately $P = V_{ext}^2/(R_s + R_d) \approx V_{ext}^2/R_d$, which is typically quite small. The PZT actuator is unique in that it requires very little power to maintain a constant force or displacement at DC. At high frequencies, $I(s) \approx V(s)/R_s$, and the power drawn is approximately $P = V_{ext}^2/R_s$ which can be appreciable, on the order of $V_{ext}^2/25$ for a typical PZT. Using representative values $R_s = 25\Omega$, $R_d = 500M\Omega$, and $C = 2\mu F$, and $K_f = 0.18$ N/V, the force-to-power ratio for a PZT at low frequencies is on the order of 10^7 N/W and at high frequencies on the order of 1 N/W.

In the mid-range of frequencies, the power consumed by a PZT actuator is frequency dependent, with the magnitude of the current rising steadily from its low to its high frequency limit. Some care must be taken to correctly quantify the power usage in this frequency range, given the phase differences between voltage and current in this transition region. A more detailed discussion of PZT power usage will be provided in Chapter 6.

3.3.2 Voice coil

The voice coil is a direct drive linear actuator, which consists of a moving component and a fixed component. The moving component is a tube with wires wound around it. The fixed component is composed of a permanent magnet, surrounding the outer layer of the tubular coils, and a ferromagnetic magnet that fits inside the moving tube [84]. When a voltage is applied across the leads of the coil, the magnetic field generates a force on the moving component, creating linear motion. The force generated is directly proportional to the current in the coil. Voice coil strokes may range from microns to centimeters, and for space interferometer applications, the stroke range is typically on the order of 1-5 mm (0.02-0.2 in) for the current delay line designs, although again this may be a design parameter. The resolution of the voice coil is in the sub-micron level ($r < 0.1$ μm), and more information on voice coil properties is available in the application manual provided by BEI technologies [84] and other suppliers.

An equivalent circuit model for the voice coil actuator is shown in Figure 3-12(a). When an external voltage V_{ext} is applied to the circuit, the current I flows through the coil windings or the circuit resistor R. The actuator creates a back electromotive force (EMF) voltage

V_{emf} that is proportional to the speed of the moving coil. The EMF is often quite small, and neglecting it reduces the circuit model to

$$V_{ext} = L\frac{dI}{dt} + RI.$$

This is a first order system with an electric time constant of L/R. Assuming typical voice coil electrical properties $L = 350\ \mu\text{H}$ and $R = 3\Omega$, the response of the electrical circuit from the external voltage input to current output is plotted in Figure 3-12(b). Note that the electrical bandwidth is approximately 1 kHz. For electromechanical devices such as the voice coil, the electrical bandwidth is usually much larger than the mechanical bandwidth. Therefore, the bandwidth of the voice coil will be limited by the mechanical system setup.

The instantaneous power drawn by this circuit is the product of the source voltage and the loop current. Since the inductance loss is typically much smaller than the resistive loss, the power usage can be approximated by $P = I^2R$ over most frequencies of interest. In addition, the current is directly proportional to the force generated, so $P = (F/(K_f))^2R$, where K_f is the force constant which converts amperes to Newtons. The force constant is typically in the range of 1-5 N/A, and the power ratio is on the order of 1 N/W.

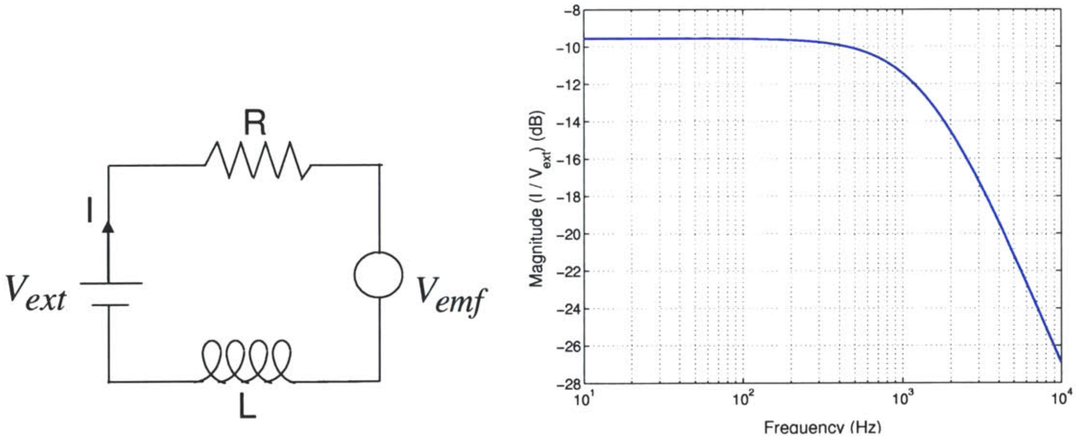

(a) (b)

Figure 3-12: (a)Voice coil equivalent circuit (b) Voice coil electric circuit response

3.3.3 DC motor

The direct current (DC) motor is another electromechanical system that converts electrical power into mechanical power. This is accomplished via the interactions of two magnetic fields - one field is produced by a permanent magnet assembly, and the other produced by an electrical current flowing through the motor windings. The interaction of these two fields will generate a torque that rotates the rotor, and as the rotor turns, the current in the winding is commutated to produce a continuous torque output [71]. If the rotor is attached to wheels and cables, it can provide transitional motion. The force generated in the cable is proportional to the current flowing in the armature conductor.

There is no physical limit on the DC motor stroke, but the range of translational motion is usually limited by the translating component. For example, the DC motor used for the JPL optical delay line has a stroke of 14 cm due to track length limitations. DC motors do have maximum torque limits, and these can vary greatly depending on motor design and size. The motors used in JPL prototype delay lines typically have a torque limit on the order of 1 Nm ($\alpha \approx 1$ Nm).

The minimum translational movement created by a motor drive depends on the drive screw pitch, gear ratio, and motor angular resolution. In reality the actual resolution is likely to be worse than the estimated value due to stiction, backlash, play, etc. Due to these practical limitations, the achievable resolution is typically about a micron ($r \approx 1\mu$m) [54].

A typical circuit model of a DC motor is very similar to the voice coil as shown in Figure 3-12(a). When the external voltage V_{ext} is applied to the circuit, the current I flows through the resistor R representing the armature winding resistance. A back EMF is generated from the motor that is proportional to the speed of operation. The inductance L denoting the armature winding inductance also causes a small voltage drop. The time constant for the DC motor is approximately 10-15 ms, so the frequency bandwidth is around 60-100 Hz. Similar to the voice coil, a mechanical system driven by a DC motor will likely have a bandwidth much smaller than the electrical bandwidth.

Similar to the voice coil, the power usage for the DC motor can also be estimated as $P = I^2R$, since the inductance L is typically much smaller than R. The torque-to-power ratio is approximately 1 Nm/W.

3.3.4 Thrusters

There are many types of space propulsion systems, but only a few of them are suitable for space interferometry missions. Chemical or cold gas thrusters usually have too coarse a resolution for this application, and the impulsive opening and closing of valves to regulate the force applied to the spacecraft can excite unacceptably high vibrations on the optics, beyond the ability of the ODL to suppress.

Recent studies have shown that Colloid and Field Emission Electric Propulsion (FEEP) thrusters are promising candidates that may meet the gentle thrusting requirements [18, 28, 53, 65]. The primary advantages of these two types of systems over other types of thrusters such as cold gas and pulsed plasma thrusters (PPT) are their capabilities of low thrust resolution ($r \sim 0.1$ μN), continuous throttleability, high efficiency (>60%), and high specific impulse (>500 s) [28]. PPTs have smaller specific impulse and discrete thrust levels. Typical cold gas thrusters have much lower specific impulse, and it would be a tremendous challenge to manufacture nozzles and valves reliable enough to produce micro-Newton levels of thrust [65]. At higher thrust levels, the pulsed operation of the traditional cold gas thrusters may induce significant disturbances to the optical instrument onboard the space interferometer.

The maximum thrust levels for FEEP and Colloids may range from 0.5 μN to 100 μN depending on the configuration of the propulsive device. The electrical bandwidth of these actuators is approximately 10 Hz [53]. These thrusters are complex devices, and summarizing their operation concisely is difficult; detailed descriptions of their operation can be found in [65]. For both FEEP and Colloidal thrusters, the thrust-to-power ratio is on the order of 10 μN/W [53].

Table 3.1 summarizes the approximate stroke range, resolution, and bandwidth of the actuators considered above. The information is obtained from sources cited above and respective manufacturer websites. Notice that the operational range and resolution of the thruster are described in terms of force. Since the thrusters can push the spacecraft around with no theoretical position limitations, there is no stroke limit for this actuator type, only a force limit. Similarly the DC motor itself does not have a stroke limitation, but it does have a maximum torque limit. The bandwidth of the voice coil and DC motor are estimated from their electrical time constants. Their actual bandwidths are expected to be much lower and will depend on the corresponding mechanical system setup.

Table 3.1: Interferometer actuator properties

Actuator Type	PZT Actuator	Voice Coil	DC motor	Thruster
Stroke/ Force Limits (α)	5-30 μm	1-5 mm	0.5-1.32 Nm	0.5 - 100 μN
Resolution (r)	$\sim$ 0.1 nm	$< 0.1\mu$m	1 μm	0.1 μN
Bandwidth (ω_a)	2-4 kHz	$<$ 1 kHz	$<$ 100 Hz	$\sim$ 10 Hz
Power Ratio	Low Freq. $\approx 10^7$ N/W High Freq. $\approx$ 1 N/W	1-10 N/W	1.5 Nm/W	10-17 μN/W

3.4 Staging Control

Suppose a single actuator were available to control the spacecraft position with nanometer accuracy, and maintain this accuracy in the face of high frequency perturbations. Then there would be no need to employ the array of actuators studied above. This single idealized actuator by itself could make the minute, rapid position corrections needed to keep the optical geometry in the required alignment. Unfortunately, no such actuator exists. Instead the collection of actuators in a space interferometer attempt to approximate the response of this hypothetical ideal using separate input stages of complementary stroke, resolution, and bandwidth characteristics. We will call such an approach a "staged actuation system".

Actuators with larger maximum output tend to be lower bandwidth and coarser resolution, while the high bandwidth actuators tend to have smaller maximum output and finer resolution. Given a staged actuation system, the challenge is to determine how to use the individual actuators appropriately in order to satisfy the system requirements. "Staging control" is defined as a control strategy that specifies how to piece together the individual actuators into the best possible approximation to the idealized actuator above. A staging control law has to answer a number of important questions: Where should the "hand-off" frequencies be? What is the correct tradeoff between the stroke of one actuator and the bandwidth of another? What is the most power efficient use of the available actuators?

The first task in attempting to answer some of these questions is to understand how actuator capabilities and constraints affect the system performance. An analytical technique for predicting system performance that takes into account actuator nonlinearities is vitally necessary to be able to design a staging control law. This is the topic of the next chapter.

3.5 Summary

In this chapter, the optical geometry introduced in the previous chapter is embedded in dynamical models subject to environmental disturbances and actuator inputs. The models considered are linear and time invariant, with input nonlinearities describing the effects of actuator saturation, resolution, and quantization. Space interferometers utilize several actuators with overlapping bandwidth and stroke, a configuration known as a staged actuation system. The open challenge, examined in subsequent chapters, is to determine the most efficient way to use these actuators cooperatively so as to obtain the best possible closed-loop performance.

Chapter 4

Stochastic Performance Prediction

As discussed in the previous chapter, obtaining maximum performance from a space interferometer may require utilizing actuators in regions where their nonlinear aspects cannot be ignored. These nonlinear effects complicate the task of predicting the closed-loop performance which can be obtained from a specified feedback control law. The purpose of this chapter is to develop methods which can accurately predict the closed-loop performance, while taking into account the nonlinear characteristics of the actuators.

The performance of interest in this thesis is the steady-state, root-mean-square (RMS) deviation of the actual optical geometry from the idealized geometry as discussed in Chapter 2. In particular, methods must be determined to keep these deviations below the levels identified in Chapter 3, for example, RMS deviations of the optical path length less than 3 nm for a typical extrasolar planet detection mission. Since many of the disturbances acting on the interferometers are random in nature, the performance analysis must directly address the stochastic aspect of the problem, in the context of the dynamical model constructed in Chapter 3.

Numerical simulation to determine the steady-state performance of a nonlinear system is one possible approach, however these simulations typically require intensive computation to achieve statistical reliability, and are too time consuming to be useful at a system design level. Moreover, the actual task of accurately simulating a stochastic nonlinear differential equation is itself a topic of active research [7]. Simply adding a stochastic input to a standard Runge-Kutta solver is known to have very weak accuracy (i.e. $\mathcal{O}(\Delta t)$ even for a 4th order algorithm which provides a deterministic solution accuracy of $\mathcal{O}((\Delta t)^5)$ [7]).

Ideally a quick analytical approximation of the expected variance would be much more desirable, allowing system level design trades to be conducted in a more timely fashion. This chapter attempts to formally develop the required prediction methodology for nonlinear stochastic differential equations as discussed in Section 4.1. Two useful theoretical frameworks, stochastic Lyapunov methods and stochastic linearization techniques, are summarized in Section 4.2, and a simple scalar example problem is used to demonstrate the application of these methods. Then the full development of a performance prediction method for multi-state and multi-input systems is described in Section 4.3. Following a discussion of the numerical aspects of computing these predictions in Section 4.4, a number of more complex examples are analyzed to demonstrate the accuracy and utility of the proposed performance prediction method. The final section then formally analyzes the closed-loop stability (in the sense of Lyapunov) of stochastic systems with input nonlinearities.

4.1 Stochastic Differential Equations

From Chapter 3, the stabilization problem to be addressed in this thesis can be summarized as a set of nonlinear stochastic differential equations.

$$\begin{aligned} dx &= Ax\,dt + B_1\,dw + B_2\phi(u)\,dt \qquad (4.1)\\ y &= C_1x \\ u &= Kx \end{aligned}$$

where x is a $n \times 1$ vector containing the states of the system, w is a $n_w \times 1$ vector of disturbance inputs, u is a $n_u \times 1$ vector of control inputs, y is a $n_y \times 1$ vector of output deviations, and the matrices (A, B_1, B_2, C_1, K) are assumed to have appropriate dimensions. The disturbance w is a standard Wiener process, which is a Gaussian process with zero mean and independent increments [11]. Although the Wiener process is sample-path continuous, it is almost surely not differentiable at any time $t \geq 0$. Therefore, instead of writing Equation 4.1 as a deterministic ordinary differential equation as shown in Equation 3.17, it is expressed symbolically in terms of the differentials or a stochastic differential equation (SDE).

The general system model (A, B_1, B_2, C_1) incorporates the plant, disturbance, and actuator dynamics. Due to the nonlinearity $\phi(u)$, the closed-loop dynamics (4.1) are nonlinear, stochastic differential equations. To exactly determine the RMS output deviations for these dynamics, it is necessary to find the resulting probability density function (PDF) of $x(t)$. This requires solving the Fokker-Planck equation [11, 43], which is a partial differential equation that describes the time evolution of the PDF, $p_x(x,t)$, [78]:

$$\frac{\partial p_x}{\partial t} = -\sum_{i=1}^{n} \frac{\partial \left[\sum_{j=1}^{n} A_{ij} x_j + \sum_{l=1}^{n_u} B_{2_{il}} \phi_l(k_l x)\right]}{\partial x_i} \frac{\partial p_x}{\partial x_i} + \frac{1}{2} \sum_{i=1}^{n} \sum_{j=1}^{n} \frac{\partial^2 (B_1 B_1^T)_{ij}}{\partial x_i \partial x_j} \frac{\partial^2 p_x}{\partial x_i \partial x_j} \quad (4.2)$$

The subscript ij or il denotes the (i,j) or (i,l) element of the corresponding matrix. Note that the density $p_x(x,t)$ is not necessarily stationary. A stationary solution, assuming one exists, can be obtained by setting $\frac{\partial p_x}{\partial t} = 0$, and solving the resulting partial differential equation in x.

Unfortunately, closed-form solutions usually do not exist for Equation 4.2, even in the steady-state limit, and there are very few general results available. For nonlinear systems, the density function may not even be zero mean, or Gaussian, despite the fact that the driving Wiener process has these features. One of the few cases for which an exact solution is known is when the system is completely linear, with $\phi(u) = u$. Then, if the matrix $A + B_2K$ is Hurwitz, the PDF of the state vector x converges to a stationary Gaussian distribution with zero mean and covariance Σ_{xx} given by

$$(A + B_2K)\Sigma_{xx} + \Sigma_{xx}(A + B_2K)^T + B_1B_1^T = 0. \quad (4.3)$$

as described in Section 3.1.2 above. The asymptotic RMS output deviations are then given by the standard deviation

$$\sigma_{y_i} = \sqrt{C_{1_i} \Sigma_{xx} C_{1_i}^T}. \quad (4.4)$$

where C_{1_i} is the ith row of the matrix C_1.

In the case that ϕ is the quantization and saturation nonlinearity considered in the previous chapter, Liberzon and Brockett [42] have found a steady-state solution for the Fokker-Planck equation, assuming that the feedback stabilizes the closed-loop system. Under these conditions, they show that the closed-loop density function will converge to a piecewise Gaussian function, of the form,

$$p_x(x) = \gamma e^{-\frac{1}{2} x^T Q^{-1} x - \zeta \int_0^{Kx} \phi(v) dv} \quad (4.5)$$

where γ and ζ are scalar normalization constants, and matrix Q satisfies the Lyapunov equation $AQ + QA^T = -B_1B_1^T$. Representative plots of PDFs corresponding to Equation 4.5

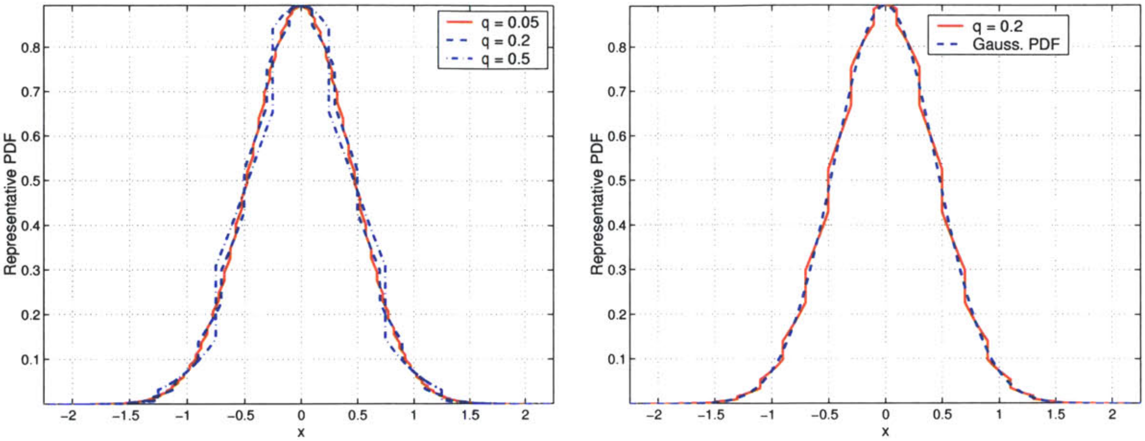

(a) (b)

Figure 4-1: (a) Representative plots of piecewise Gaussian PDF (b) PDF curves of a piecewise Gaussian function (solid) and a single Gaussian function (dashed)

are shown in Figure 4-1(a). Three different curves corresponding to different quantization levels are shown in this figure, and they illustrate that as the quantization level decreases, the piecewise Gaussian approaches a smooth Gaussian-like distribution.

Analytic computations with the density function given by Equation 4.5 are burdensome for anything other than a scalar system. However, even for relatively large quantization levels, densities of this form can be closely *approximated* by a single ideal Gaussian distribution, as illustrated in Figure 4-1(b). The use of a single Gaussian distribution to model the closed-loop density has been extensively studied in previous work [20, 33, 69, 78]. The objective is to find one covariance matrix, $\hat{\Sigma}_{xx}$, for a single, continuous Gaussian density that best approximates the true state covariance of Equation 4.1. Numerical simulations have shown that such an approximation strategy typically provides prediction within 5%-15% of the numerically computed values. The accuracy tends to improve for plants with sharper high frequency roll-offs, as they attenuate the high frequency components of the input caused by quantization jumps and saturation effects [20].

The central question, addressed below, is whether it is possible to *analytically* determine the best Gaussian approximation directly from the system dynamics and nonlinear characteristics of the actuators. In the following sections, the necessary equations describing this approximation will be developed, and numerical methods for their solution discussed.

4.2 Performance Prediction - Two Useful Theorems

This section introduces two important theorems which will be useful in determining a closed-loop Gaussian density function which closely approximates the steady-state solutions of the Fokker-Planck equation. The first of these is a stochastic version of the classical Lyapunov theorem, and the second describes the technique of stochastic linearization. The two approaches are described in detail below and a comparison of predictions made by the two methods will be discussed in the following section for a simple example problem.

4.2.1 Stochastic Lyapunov method

Stochastic stabilization of nonlinear systems has been the subject of considerable recent interest in the nonlinear controls community [12, 15, 42, 59]. Most of this work assumes multiplicative noise models, where stochastic disturbances multiply functions of one or more of the state variables. Under these conditions it is possible to develop nonlinear control laws which actually force the closed-loop state to zero, even in the presence of nonzero disturbances. The noise model considered in this thesis, however, is additive: the impact of the disturbance on the state evolution is directly proportional to dw (4.1). Hence, these new control strategies cannot be directly applied to the problem at hand. However, recent work using Lyapunov-like theorems can be adapted to the additive noise model, providing conditions which ensure the existence of a steady-state density, as well as providing methods for predicting the statistics of the resulting stationary solution [77].

The study of stochastic Lyapunov extensions trace back to the work of Has'minskǐ in 1980 [25], and a concise summary of some of this work can be found in a survey conduced by Thygesen [77]. In this section, important definitions and theorems of stochastic Lyapunov techniques are described. Readers are assumed to be familiar with the standard Lyapunov analysis for deterministic systems as described in [34], for example.

A general nonlinear stochastic process can be defined by the following stochastic differential equation (SDE),

$$dx = f(x)\,dt + g(x)dw, \tag{4.6}$$

where x is in Euclidean space $\mathbb{R}^n$, and w is the n_w-dimensional Wiener process. The differential generator $\mathcal{L}$ maps $\mathcal{C}^2$ functions ($V : \mathbb{R}^n \to \mathbb{R}$) to $\mathcal{C}^0$ functions ($\mathcal{L}V : \mathbb{R}^n \to \mathbb{R}$),

$$\mathcal{L}V(x) = V_x(x)\,f(x) + \frac{1}{2}\mathrm{tr}\left\{g^T(x)\,V_{xx}\,g(x)\right\}, \tag{4.7}$$

where V_x and V_{xx} are the first and second partial derivative of V with respect to x, respectively. The stochastic differential operator $\mathcal{L}V$ is similar to the deterministic differentiator $\dot{V}$, except for the additional term $\operatorname{tr}\left\{g^T(x)\, V_{xx}\, g(x)\right\}$ which incorporates the effects of the stochastic input.

A function $V : \mathbb{R}^n \rightarrow \mathbb{R}$ is *proper* if it satisfies

$$a(|x|) \leq V(x) \leq b(|x|)$$

for some strictly increasing functions a and b, with $a(0) = b(0) = 0$, and $a(|x|) \rightarrow \infty$ as $|x| \rightarrow \infty$. For this study, a *Lyapunov* function is a proper function which is $\mathcal{C}^2$ on $\mathbb{R}^n \setminus 0$.

Theorem 4.1 [*Zakai,69*] *Assume there exist positive numbers $R_o > 0$ such that*

$$\mathcal{L}V(x) < 0 \tag{4.8}$$

for all x satisfying $|x| > R_o$. Then the process described by Equation 4.6 admits a stationary probability distribution.

This theorem essentially extends the uniform ultimate boundedness property [34] for the deterministic behavior of a nonlinear system, to provide similar boundedness guarantees for the statistical properties of a stochastic nonlinear system. Versions of Theorem 4.1 can be found in [89, 25, 77] and proofs are also in these references.

Furthermore, the following proposition can be very helpful in making more constructive arguments about numerical bounds on the distribution of x, assuming it has been shown to be asymptotically stationary.

Proposition 4.1 [*Zakai,69*] *With the same assumptions as Theorem 4.1, let $h : \mathbb{R}^n \rightarrow \mathbb{R}$ be such that*

$$\mathcal{L}V(x) + h(x) \leq 0$$

for all $x \in \mathbb{X}$. Then

$$\mu(h) = E\{h(x(t))\} \leq 0,$$

provided $t > 0$ and x is distributed according to the stationary measure μ. In addition, if $\mathcal{L}V(x) + h(x) = 0$, then $E\{h(x(t))\} = 0$ [89].

Lyapunov functions can thus be used to both guarantee the existence of an invariant distribution and to provide a performance bound. Note that the same Lyapunov function need not be used for each argument: one Lyapunov function may be used to demonstrate stationarity, and a second used to obtain a performance bound.

For a simple example of the utility of the above facts, consider the linear SDE

$$\begin{aligned} dx &= Ax\,dt + B_1\,dw \\ y &= C_1 x. \end{aligned}$$

which is Equation 4.1 with $K = 0$. Assuming the matrix A is Hurwitz, the steady-state variance of the output can be determined as described above

$$\begin{aligned} \lim_{t\to\infty} E\|y(t)\|^2 &= \operatorname{tr}\left\{C_1 P C_1^T\right\} \\ AP + PA^T + B_1 B_1^T &= 0. \end{aligned} \tag{4.9}$$

Alternately, one may also use

$$\begin{aligned} \lim_{t\to\infty} E\|y(t)\|^2 &= \operatorname{tr}\left\{B_1^T Q B_1\right\} \\ A^T Q + QA + C_1^T C_1 &= 0, \end{aligned} \tag{4.10}$$

where the equivalence (duality) of the two forms is demonstrated in, e.g. [91].

The latter of these expressions can be derived directly from the stochastic Lyapunov theorems above. Since A is Hurwitz, it is possible to find a positive definite matrix, $Q > 0$, such that $QA + A^T Q = -C_1^T C_1$ [34]. Choose the quadratic Lyapunov function,

$$V = x^T Q x,$$

which satisfies

$$\begin{aligned} \mathcal{L}V &= x^T(A^T Q + QA)x + \frac{1}{2}\operatorname{tr}\left\{B_1^T Q B_1\right\}, \\ &= -x^T C_1^T C_1 x + \frac{1}{2}\operatorname{tr}\left\{B_1^T Q B_1\right\}. \end{aligned}$$

Since the trace of $B_1^T Q B_1$ is bounded, as $|x| \to \infty$, the magnitude of the first term becomes larger than the second term, which makes $\mathcal{L}V$ negative, and Theorem 4.1 is satisfied, ensuring an asymptotically stationary distribution for $x(t)$. Now let $h(x) = x^T C_1^T C_1 x - \operatorname{tr}\left\{B_1^T Q B_1\right\}$, then

$$\mathcal{L}V(x) + h(x) = 0.$$

Hence, using Proposition 4.1, the steady-state output variance is given by

$$E\{x^T C_1^T C_1 x\} = E\{y^T y\} = \operatorname{tr}\left\{B_1^T Q B_1\right\}. \tag{4.11}$$

Comparing Equation 4.10 and Equation 4.11, the Lyapunov performance prediction is actually exact in the linear case.

4.2.2 Statistical/Stochastic linearization

Another useful tool for analysis of stochastic systems is the technique of stochastic linearization. Stochastic (or statistical) linearization utilizes a quasi-linear approximation of the nonlinearities in a system with Gaussian random inputs [20, 21]. Quasi-linearization is quite different from ordinary linearization of a nonlinear component. In both approximation strategies an equivalent gain is used to replace a static nonlinearity. However, in ordinary linearization the corresponding gain is a constant, depending only on the equilibrium point of the system (usually taken as 0), whereas the stochastic linearization gain is actually a *function*, which depends upon the statistics of the input to the nonlinearity.

Theorem 4.2 *Given a single-valued nonlinear component, ϕ, driven by a zero-mean, stationary Gaussian process u as shown in Figure 4-2. The response of the nonlinear system $v = \phi(u)$ can be approximated by an equivalent linear, time invariant filter N that minimizes the mean-squared approximation error,*

$$\min E\{e(t)^2\} = \min E\{(v(t) - \hat{v}(t))^2\}.$$

If the nonlinear component is static or memoryless, the linear filter is a scalar gain given by [20],

$$N(u) = \frac{E\{u\phi(u)\}}{E\{u^2\}} = \frac{E\{u\phi(u)\}}{\sigma_u^2},$$

where $E\{u\phi(u)\}$ is the cross-correlation between the input process u and the output process v evaluated at zero time lag.

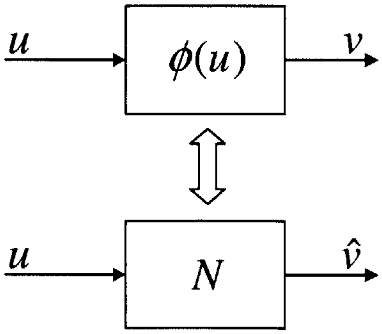

Figure 4-2: Stochastic linearization of a static nonlinear element

Gelb and Vander Velde [20] have a thorough discussion on such an approximation technique, and the claims made in the above theorem can also be found in their reference.

Furthermore, [21, 60] show that the equivalent gain can also be computed by

$$N = E\{\phi'(u)\}, \tag{4.12}$$

where $\phi'(u)$ is the derivative of $\phi(u)$ with respect to u. From this equation, N can be computed easily if $d\phi/du$ is a computable function of u.

4.2.3 Scalar application of Theorems 4.1 and 4.2

To illustrate the ideas introduced so far, consider a simple nonlinear SDE

$$\begin{aligned} dx &= -xdt + dw + \phi(u)dt, \\ y &= x \\ u &= -kx, \end{aligned}$$

where x, w, and u have scalar values. Since the output y is the same as the state x here, the RMS output deviations are the same as the state variance. To make the example more specific, $\phi(\cdot)$ is assumed to be a saturation function with saturation level α in this example.

Exact solution

For this simple system, the exact steady-state PDF can be computed from the Fokker-Planck equation Equation 4.2,

$$p_x(x) = \begin{cases} \gamma e^{-(1+k)x^2} & |kx| \leq \alpha \\ \gamma e^{-x^2-2\alpha/k(|kx|-\alpha^2/2)} & |kx| > \alpha \end{cases}$$

The exact steady-state performance can then be obtained by numerically integrating

$$\sigma_y^2 = \sigma_x^2 = \int_{-\infty}^{\infty} x^2 p_x(x)dx$$

for a specified value of k.

Linear prediction

If the input nonlinearity is ignored, implicitly assuming that the input remains within the linear region of the actuator, the steady-state performance σ_y^2 is trivially found from $\sigma_y^2 = C_1PC_1^T = P$ (since $C_1 = 1$ here), and P satisfies

$$AP + PA^T + B_1B_1^T = 0 \;\Leftrightarrow\; -(1+k)P - P(1+k) + 1 = 0,$$

(using $A - B_2K = (1+k)$ and $B_1 = 1$), so that

$$\sigma_y^2 = \sigma_x^2 = \frac{1}{2}\frac{1}{1+k}, \tag{4.13}$$

Lyapunov (nonlinear) prediction from Theorem 4.1

Define the quadratic Lyapunov function,

$$V = \frac{1}{2}x^2.$$

which satisfies

$$\mathcal{L}V = -x^2 - x\phi(kx) + 1/2.$$

Since ϕ is a saturation nonlinearity, $x\phi(kx) \geq 0$ for any positive k, hence for $x^2 > 1/2$, $\mathcal{L}V$ becomes negative, and Theorem 4.1 is satisfied. The closed-loop system will thus asymptotically converge to a solution with a stationary density. Define

$$h(x) = x^2 + x\phi(x) - 1/2$$

Then $\mathcal{L}V + h(x) = 0$, satisfies Proposition 4.1 and hence

$$\begin{aligned} E\{x^2 + x\phi(kx) - 1/2\} &= 0 \\ \sigma_x^2 + E\{x\phi(kx)\} - 1/2 &= 0. \end{aligned} \tag{4.14}$$

In order to compute $E\{x\phi(kx)\}$, it is necessary to know the asymptotic density function of x. As suggested in Section 4.1, a Gaussian distribution with variance $\hat{\sigma}_x^2$ will be assumed, and the conditions which must be satisfied by $\hat{\sigma}_x$ determined. The expected value of $x\phi(kx)$ can then be calculated by direct integration using the assumed density,

$$\begin{aligned} E\{x\phi(kx)\} &= \int_{-\infty}^{\infty} x\phi(kx)p_x(x)dx \\ &= \int_{-\infty}^{\infty} x\phi(kx)\frac{1}{\sqrt{2\pi}\hat{\sigma}_x}\exp\left(\frac{-x^2}{2\hat{\sigma}_x^2}\right)dx \\ &= k\,\mathrm{erf}\left(\frac{\alpha}{\sqrt{2}k\hat{\sigma}_x}\right)\hat{\sigma}_x^2, \end{aligned}$$

where erf($\cdot$) is the standard error function

$$\mathrm{erf}(x) = \frac{2}{\sqrt{\pi}}\int_0^x \exp(-t^2)dt.$$

Substituting this result into Equation 4.14, the unknown variance $\hat{\sigma}_x^2$ must satisfy

$$\hat{\sigma}_x^2 + k\,\mathrm{erf}\left(\frac{\alpha}{\sqrt{2}k\hat{\sigma}_x}\right)\hat{\sigma}_x^2 - \frac{1}{2} = 0, \tag{4.15}$$

This is a nonlinear algebraic equation which must be solved numerically to obtain $\hat{\sigma}_x$.

Stochastic linearization (nonlinear) prediction from Theorem 4.2

Before examining the solution of Equation 4.15 numerically, consider instead an application of the stochastic linearization technique to the same scalar problem. The equivalent "linearized" system is given by

$$\begin{aligned} dx &= -xdt + dw - Nkxdt \\ &= -(1+Nk)\,x\,dt + dw. \end{aligned}$$

Treating N as a constant, the steady-state performance of this system can be computed easily using linear system methods as

$$\hat{\sigma}_x^2 = \frac{1}{2}\frac{1}{1+Nk}, \tag{4.16}$$

where $\hat{\cdot}$ is again used to indicate that $\hat{\sigma}_x$ is an estimate of the true σ_x. However, N and $\hat{\sigma}_x$ *are not independent.* N is a *function* of the density $p_u(u)$ and $p_u(u) = p_x(kx)$ here, and hence the two equations are coupled.

To analytically determine this coupling, again assume that the density of x will be Gaussian with variance $\hat{\sigma}_x$. The equivalent gain for the saturation function ϕ is computed as

$$N(\hat{\sigma}_x) = \operatorname{erf}\left(\frac{\alpha}{\sqrt{2}\hat{\sigma}_u}\right) = \operatorname{erf}\left(\frac{\alpha}{\sqrt{2}k\hat{\sigma}_x}\right). \tag{4.17}$$

Solving Equations 4.16 and 4.17 simultaneously shows that the closed-loop variance estimate must satisfy

$$\hat{\sigma}_x^2 + k\operatorname{erf}\left(\frac{\alpha}{\sqrt{2}k\hat{\sigma}_x}\right)\hat{\sigma}_x^2 - \frac{1}{2} = 0. \tag{4.18}$$

Note that although the system is "linearized", it is still necessary to solve a nonlinear equation in order to obtain the closed-loop performance. Since the stochastic "gain", N, depends on the input to the nonlinearity, the resulting system is not really linear because N has nonlinear dependence on σ_x. Note also that the condition which $\hat{\sigma}_x$ must satisfy is exactly the same as the one derived from the stochastic Lyapunov method (Equation 4.15).

Comparison of predictions

Figure 4-3(a) shows the different predictions developed above for the RMS variations in the output y as a function of the controller gain k when saturation level of the actuator is $\alpha = 1$. The solid line illustrates the predicted performance from the solution of Equations 4.15 or

4.18, the dashed-dotted line shows the exact solution, and the circles indicate the estimates computed from numerical simulation of the differential equation. The three estimates are quite close, differing by at most 5% for all values of k. Note that the numerical simulation itself contains errors approximating the exact closed-loop performance, a consequence of the limited accuracy of conventional differential equation solvers for systems with stochastic inputs [7].

Figure 4-3(b) compares the steady-state performance of the predicted output deviation obtained by ignoring the actuator saturation effects. The solid line shows the nonlinear system performance, and the dashed line shows the linear prediction from Equation 4.13. Note that the relative error between the two predictions grows unbounded as the gain increases. Unlike the Lyapunov and stochastic linearization predictions, the linear method incorrectly predicts that RMS output deviations are a monotonically decreasing function of the gain k. In fact, as the true solution curve shows, RMS performance is limited by the nonlinear characteristic of the actuator. RMS performance better than about 0.175 units is *not achievable* using this actuator. If the designer decides to ignore actuator saturation he may obtain overly optimistic performance predictions, when the indicated performance may not, in fact, be physically achievable.

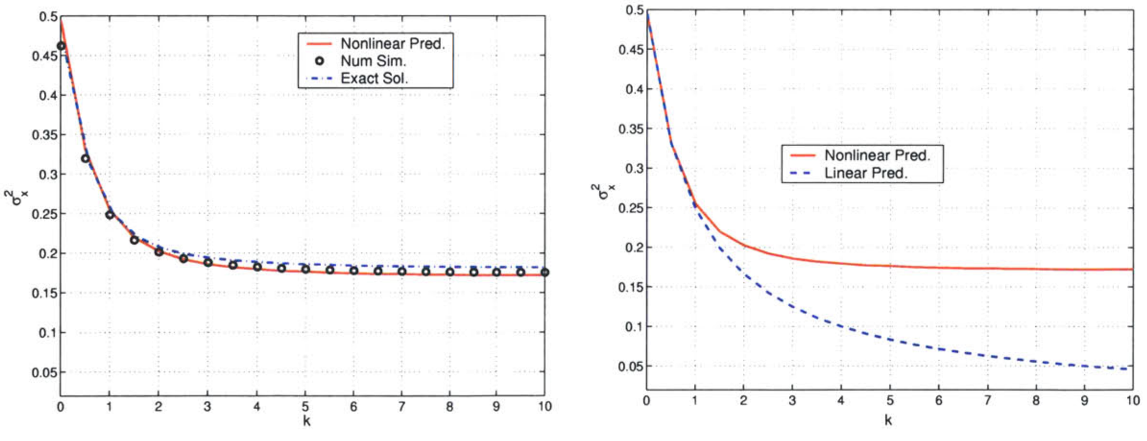

(a) (b)

Figure 4-3: Steady-state variance of x as a function of the controller gain

The achievable performance limitations inherent in a particular combination of quantization and saturation for an actuator are not immediately obvious, and an important application of the above ideas for system design will be to make such predictions analytically. The objective of the following section is thus to extend the above prediction methods to systems with an arbitrary number of states and inputs.

4.3 Multi-input, N-DOF Performance Prediction

In the simple, scalar example above, under the assumption of an ideal Gaussian closed-loop density, the stochastic Lyapunov and stochastic linearization methods give identical predictions. In the general case, considered below, the two approaches will be shown to again make the same predictions, but via equations which are *dual* to each other. In the analysis below, it is assumed that the controller K is chosen so that the closed-loop system is stable, despite effects of saturation. Closed-loop stability concerns will be addressed in the final section of this chapter.

4.3.1 Some useful identities

Before discussing the application of stochastic Lyapunov and stochastic linearization techniques on multi-dimensional and multi-input systems, an important property of Gaussian random vectors is discussed first. This property and the subsequent equations presented below will be useful to the development of multi-input and N-DOF systems.

For a zero-mean, Gaussian input random vector $x \in \mathbb{R}^n$, the correlation between x and a scalar nonlinear function, $\phi(x) : \mathbb{R}^n \to \mathbb{R}$ is given by [33, 69],

$$E\{x\phi(x)\} = E\{xx^T\}E\{\nabla\phi(x)\}, \tag{4.19}$$

where ∇ is the gradient vector defined by

$$\nabla = \left[\frac{\partial}{\partial x_1}, \frac{\partial}{\partial x_2}, \dots, \frac{\partial}{\partial x_n}\right]^T.$$

This result can be extended to compute the correlation between a vector function, $\phi : \mathbb{R}^n \to \mathbb{R}^m$, and a Gaussian random vector x. The function $\phi(x)$ is a vector composed of single-valued functions, ϕ_i,

$$\phi(x) = [\phi_1(x), \phi_2(x) \cdots \phi_m(x)]^T,$$

and the correlation can be found using Equation 4.19, together with the linearity of the expectation operator:

$$\begin{aligned} E\{x\phi^T(x)\} &= E\{[x\phi_1(x), x\phi_2(x), \cdots, x\phi_m(x)]\} \\ &= E\{xx^T\}[E\{\nabla\phi_1(x)\}, E\{\nabla\phi_2(x)\}, \cdots, E\{\nabla\phi_m(x)\}] \\ &= E\{xx^T\}E\{\nabla\phi^T\}, \end{aligned} \tag{4.20}$$

where $E\{\nabla\phi^T\}$ is a matrix of dimension $n \times m$ with the (i, j) element given by $\frac{\partial\phi_j}{\partial x_i}$. Note that if ϕ is a *non-interacting* function such that $\phi_i(x) = \phi_i(x_i)$, with the same length as the vector x ($m = n$), then the term $E\{\nabla\phi^T\}$ is a *diagonal* matrix with the i^{th} diagonal entry given by $\frac{\partial\phi_i}{\partial x_i}$.

Now, let $\psi(x) = \phi(Kx)$ be a $n_u \times 1$ vector. The correlation between x and $\psi(x)$ can be computed from Equation 4.20,

$$\begin{aligned} E\{x\psi^T(x)\} &= E\{[x\psi_1(x), x\psi_2(x), \ldots, x\psi_{n_u}(x)]\} \\ &= E\{xx^T\}E\{[\nabla_x\psi_1(x), \nabla_x\psi_2(x), \ldots, \nabla_x\psi_{n_u}(x)]\} \\ &= \Sigma_{xx}E\{\nabla_x\psi^T(x)\} \end{aligned} \tag{4.21}$$

where ∇_x denotes that the partial derivative vector is with respect to x. Using the vector chain rule, this partial derivative term is computed as

$$E\{\nabla_x\psi^T(x)\} = E\{(\nabla_x u)(\nabla_u\phi^T(u))\} = K^T E\{(\nabla_u\phi^T(u))\}, \tag{4.22}$$

where $\nabla_u\phi^T(u)$ is the partial derivative of $\phi(u)$ with respect to u. As a result, $E\{x\phi^T(Kx)\}$ and $E\{\phi(Kx)x^T\}$ can be expressed as

$$E\{x\phi^T(Kx)\} = \Sigma_{xx}K^T N^T \tag{4.23}$$

$$E\{\phi(Kx)x^T\} = NK\Sigma_{xx} \tag{4.24}$$

where

$$N^T = E\{uu^T\}^{-1}E\{u\phi^T(u)\} = \Sigma_{uu}^{-1}E\{u\phi^T(u)\} \tag{4.25}$$

$$= E\{\nabla_u\phi^T(u)\} \tag{4.26}$$

The last substitution uses the result from Equation 4.20 and is an extension of the single input-output case described in Theorem 4.2 [19]. Note that the term N is the multi-dimensional version of the stochastic linearized gain given by Equation 4.12.

The exact expression of N depends on the nonlinear function ϕ which is chosen to characterize various actuator nonlinearities. For the actuator properties considered in this thesis, each element of the vector function ϕ describes the saturation or quantization characteristics of one actuator input. Since the constraints and limitations of one actuator is assumed not to affect the other actuator properties, the i^{th} element of the nonlinear function ϕ_i is only a function of the input u_i. Therefore, the resulting gain matrix is diagonal with the diagonal element given by

$$N_{ii}(\sigma_{u_i}) = E\{\phi_i'(u_i)\}, \tag{4.27}$$

where $i = [1, \ldots, n_u]$.

Although N is diagonal, the correlation matrix between the inputs u and outputs v of the nonlinear function ϕ will generally still be a fully populated matrix since $E\{uv^T\} = E\{u\phi(u)^T\} = NE\{uu^T\} = NK\Sigma_{xx}K^T$. This means that the output v_i of the i^{th} nonlinearity ϕ_i indirectly depends on the other inputs u_j, $j \neq i$, through the correlation of u_j with u_i implicit in the feedback control law, and the "mixing" that occurs through plant dynamics.

4.3.2 Stochastic Lyapunov prediction

With the tools introduced above, this section discusses the application of stochastic Lyapunov methods on system performance prediction. A general quadratic Lyapunov function is used for this development:

$$V = x^T P x, \tag{4.28}$$

where P is a symmetric, positive definite matrix. Evaluating Equation 4.7 along trajectories of system Equation 4.1 yields

$$\mathcal{L}V(x) = x^T PAx + x^T A^T Px + x^T PB_2\phi(Kx) + \phi^T(Kx)B_2^T Px + \operatorname{tr}\left\{B_1^T PB_1\right\} \tag{4.29}$$

Assume for the moment that it can be shown that $\mathcal{L}V(x)$ becomes negative as x grows larger than a ball with radius R_o. Let $h(x) = -\mathcal{L}V(x)$, then Proposition 4.1 gives the performance estimate as,

$$E\{-[x^T PAx + x^T A^T Px + x^T PB_2\phi(Kx) + \phi^T(Kx)B_2^T Px]\} = \operatorname{tr}\left\{B_1^T PB_1\right\} \tag{4.30}$$

Now, using $E\{x^T Px\} = \operatorname{tr}\left\{E\{Pxx^T\}\right\}$ Equation 4.30 can be rewritten as

$$\operatorname{tr}\left\{E\{-[PAxx^T + A^T Pxx^T + PB_2\phi(Kx)x^T + B_2^T Px\phi^T(Kx)]\}\right\} = \operatorname{tr}\left\{B_1^T PB_1\right\}.$$

Assume that the stationary distribution of x is Gaussian with covariance $\hat{\Sigma}_{xx}$. Using the linearity of the expectation operator

$$\operatorname{tr}\left\{-[PA\hat{\Sigma}_{xx} + A^T P\hat{\Sigma}_{xx} + PB_2E\{\phi(Kx)x^T\} + B_2^T PE\{x\phi^T(Kx)\}]\right\} = \operatorname{tr}\left\{B_1^T PB_1\right\}. \tag{4.31}$$

From the discussion in Section 4.3.1, with our existing assumption that x has a Gaussian distribution then

$$\begin{aligned} E\{\phi(Kx)x^T\} &= NK\hat{\Sigma}_{xx} && (4.32) \\ E\{x\phi^T(Kx)\} &= \hat{\Sigma}_{xx}K^T N^T. && (4.33) \end{aligned}$$

Substituting these equations into Equation 4.31,

$$\begin{aligned} \operatorname{tr}\left\{B_1^T PB_1\right\} &= \operatorname{tr}\left\{-[PA\hat{\Sigma}_{xx} + A^T P\hat{\Sigma}_{xx} + PB_2NK\hat{\Sigma}xx + B_2^T P\hat{\Sigma}_{xx}K^T N^T]\right\} \\ &= \operatorname{tr}\left\{-[PA + A^T P + PB_2NK + K^T N^T B_2^T P]\hat{\Sigma}_{xx}\right\} \\ &= \operatorname{tr}\left\{-[P(A + B_2NK) + (A + B_2NK)^T P]\hat{\Sigma}_{xx}\right\} && (4.34) \end{aligned}$$

Although this equation is in a more simplified form than Equation 4.30, it is still not immediately obvious how it can be used to predict the system performance. The equation cannot be solved for $\hat{\Sigma}_{xx}$ directly, since the gain N depends on the density function of u which in turn will depend on $\hat{\Sigma}_{xx}$. This inter-dependence suggests that some kind of iterative scheme will be required in order to solve the problem.

Since ϕ is assumed to be noninteracting, N is diagonal with its ith diagonal entry given by $N_{ii} = E\{\phi_i'(u_i)\}$ where the expectation is over the distribution of u_i. This distribution will be Gaussian, since x is assumed Gaussian, and u is a linear function of x. The expectation can thus be evaluated to determine the diagonal entries of N as a function of the (as yet unknown) control variances $\hat{\sigma}_{u_i}$, i.e. $N_{ii} = f_i(\hat{\sigma}_{u_i})$ where f_i is a nonlinear function determined by the nonlinearity ϕ_i. For a convenient shorthand, collect the n_u terms $\hat{\sigma}_{u_i}$ into a single vector $\hat{\sigma}_u$, and write $N(\hat{\sigma}_u)$ to denote the diagonal matrix of nonlinear functions $f_i(\hat{\sigma}_{u_i})$. Note that $\hat{\sigma}_u = \sqrt{\operatorname{diag}(K\Sigma_{xx}K^T)}$ (taking square roots component-wise).

For any given N, if $A+B_2NK$ is Hurwitz it is possible to find P_i such that the following Lyapunov equation is satisfied:

$$P_i(A+B_2NK)+(A+B_2NK)^TP_i \quad = \quad -K_i^TK_i \tag{4.35}$$

where K_i is the i^{th} row of the control matrix K. Substituting this result into Equation 4.34

$$\operatorname{tr}\left\{K_i^TK_i\Sigma_{xx}\right\} = \operatorname{tr}\left\{B_1^TP_iB_1\right\}. \tag{4.36}$$

Since $\operatorname{tr}\left\{K_i^TK_i\Sigma_{xx}\right\} = K_i\Sigma_{xx}K_i^T = \hat{\sigma}_{u_i}^2$,

$$\hat{\sigma}_{u_i}^2 = \operatorname{tr}\left\{B_1^TP_iB_1\right\}. \tag{4.37}$$

If there are n_u control inputs, a family of Lyapunov solutions P_i can be used to compute the variance of each input as shown in the above equation. However, the $\hat{\sigma}_{u_i}$ computed in Equation 4.37 must be consistent with the one used to compute N. Therefore, the following set of equations must be satisfied *simultaneously*

$$P_i(A+B_2N(\hat{\sigma}_u)K)+(A+B_2N(\hat{\sigma}_u)K)^TP_i = -K_i^TK_i \tag{4.38}$$

$$\hat{\sigma}_{u_i}^2 = \operatorname{tr}\left\{B_1^TP_iB_1\right\} \tag{4.39}$$

for $i = 1, \ldots, n_u$. Algorithms which solve these equations will be presented in Section 4.4.

After determining a $\hat{\sigma}_u$ and N which satisfy the consistency constraints (4.38) and (4.39), the steady-state, closed-loop performance can be computed from a slightly different Lyapunov equation,

$$P_{y_i}(A+B_2N(\hat{\sigma}_u)K)+(A+B_2N(\hat{\sigma}_u)K)^TP_{y_i} = -C_{1_i}^TC_{1_i}, \tag{4.40}$$

where P_{y_i} is a symmetric, positive definite matrix that replaces the role of P_i in the above development, and C_{1_i} is the i^{th} row of the output matrix C_1. Substituting this equation into Equation 4.34,

$$\begin{aligned} \operatorname{tr}\left\{C_{1_i}^TC_{1_i}\hat{\Sigma}_{xx}\right\} &= \operatorname{tr}\left\{B_1^TP_{y_i}B_1\right\} \\ \hat{\sigma}_{y_i}^2 &= \operatorname{tr}\left\{B_1^TP_{y_i}B_1\right\}, \end{aligned} \tag{4.41}$$

which produces the desired steady-state estimate of the i^{th} RMS output y_i.

In summary, the $2 \times n_u$ sets of equations (4.38, 4.39) must be solved simultaneously to obtain correct $\hat{\sigma}_u$ and N. Then, the $2 \times n_u$ equations (4.40,4.41) must be solved to determine the performance prediction $\hat{\sigma}_y$. Note that in this approach $\hat{\Sigma}_{xx}$ is not computed directly, only $\hat{\sigma}_u$ and N are needed to predict the output variance $\hat{\sigma}_y$.

4.3.3 Stochastic linearization prediction

The extension of the stochastic linearization technique from the single DOF to the multi-DOF and multi-input case is fairly straightforward. Applying stochastic linearization to the nonlinear input system,

$$dx = (Ax + B_2\phi(Kx))dt + B_1 dw$$

the resulting "linearized" system can be expressed as

$$d\hat{x} = (A + B_2 NK)\hat{x}dt + B_1 dw,$$

where N is the stochastic linearized gain. Assuming a Gaussian distribution for the random variable u, the gain N can be computed as

$$N = E\{uu^T\}^{-1}E\{u\phi(u)^T\} = E\{\nabla_u \phi(u)^T\}. \tag{4.42}$$

Again, assuming the nonlinearities ϕ_i are noninteracting, N is a diagonal matrix, and the ith diagonal entry depends only on the distribution of the ith input u_i.

Treating N as a constant for the moment, if $A + B_2NK$ is Hurwitz, an estimate of the steady-state covariance matrix is obtained by solving the Lyapunov equation:

$$(A + B_2NK)\hat{\Sigma}_{xx} + \hat{\Sigma}_{xx}(A + B_2NK)^T = -B_1B_1^T. \tag{4.43}$$

The solution $\hat{\Sigma}_{xx}$ is the steady-state covariance matrix of the quasi-linearized system. The corresponding variance of each control input u_i is given by

$$\hat{\sigma}_{u_i}^2 = K_i\hat{\Sigma}_{xx}K_i^T, \tag{4.44}$$

where K_i is the i^{th} row of the controller gain matrix K.

However, N is not truly a constant, but rather depends on the distribution of u. Since this distribution is Gaussian, N is a function of the variances $\hat{\sigma}_{u_i}^2$, and N is diagonal with $N_{ii} = f_i(\hat{\sigma}_{u_i})$. Adopting the notation of the previous section, write the gain as $N(\hat{\sigma}_u)$, where $\hat{\sigma}_u$ is the n_u length vector containing the $\hat{\sigma}_{u_i}$, so that $\hat{\sigma}_u = \sqrt{\text{diag}(K\hat{\Sigma}_{xx}K^T)}$. Consistency then requires the simultaneous solution of

$$(A + B_2N(\hat{\sigma}_u)K)\hat{\Sigma}_{xx} + \hat{\Sigma}_{xx}(A + B_2N(\hat{\sigma}_u)K)^T = -B_1B_1^T. \tag{4.45}$$

$$\hat{\sigma}_u^2 = \text{diag}(K\hat{\Sigma}_{xx}K^T). \tag{4.46}$$

Once N and $\hat{\sigma}_u$ have been found which solve the consistency conditions (4.43) and (4.46), the steady-state output variance is calculated as

$$\sigma_{y_i}^2 = C_{1_i} \hat{\Sigma}_{xx} C_{1_i}^T. \tag{4.47}$$

where C_{1_i} is the i^{th} row of the output matrix C_1.

4.3.4 Duality

The prediction calculations of the two different methods above are summarized in this section. In order to compute the control variance, the stochastic Lyapunov prediction requires solving a family of Lyapunov equations

$$P_i A_{cl}(\hat{\sigma}_u) + A_{cl}^T(\hat{\sigma}_u) P_i = -K_i^T K_i, \tag{4.48}$$

where $A_{cl}(\hat{\sigma}_u) = A + B_2 N(\hat{\sigma}_u) K$ and the individual control variances are given by

$$\hat{\sigma}_{u_i}^2 = \operatorname{tr}\left\{ B_1^T P_i B_1 \right\}. \tag{4.49}$$

For the stochastic linearization technique, only one Lyapunov equation is needed,

$$A_{cl}(\hat{\sigma}_u) \hat{\Sigma}_{xx} + \hat{\Sigma}_{xx} A_{cl}^T(\hat{\sigma}_u) = -B_1 B_1^T, \tag{4.50}$$

where A_{cl} is the same as above, and the individual control variances are given by

$$\hat{\sigma}_{u_i}^2 = K_i \hat{\Sigma}_{xx} K_i^T. \tag{4.51}$$

In both cases, the Lyapunov equation is coupled with the control variance equation, since they both depend on $\hat{\sigma}_u$. The two equations are considered solved if they can be satisfied simultaneously.

When taking a closer look at the two sets of consistency equations, it is clear that the stochastic Lyapunov equations are "dual" to the stochastic linearization equations. One set of equations can be changed to the other by making the substitution of (A_{cl}^T, K_i^T, B_1^T) for (A_{cl}, B_1, K_i). This result is exactly parallel to the familiar controller/observer duality seen in linear system theory.

Now consider the performance variance calculations. After satisfying the consistency constraints of the control variance equations for $\hat{\sigma}_u$, the stochastic Lyapunov technique requires the solution of a different Lyapunov equation

$$P_{y_i} A_{cl}(\hat{\sigma}_u) + A_{cl}(\hat{\sigma}_u)^T P_{y_i} = -C_{1_i}^T C_{1_i}, \tag{4.52}$$

and the variance of each output is given by

$$\hat{\sigma}^2_{y_i} = \mathrm{tr}\left\{B_1^T P_{y_i} B_1\right\}. \tag{4.53}$$

The stochastic linearization technique uses the same Lyapunov function as used in its consistency equations Equation 4.50,

$$A_{cl}(\hat{\sigma}_u)\hat{\Sigma}_{xx} + \hat{\Sigma}_{xx}A_{cl}^T(\hat{\sigma}_u) = -B_1B_1^T, \tag{4.54}$$

and the variance of each output is given by

$$\sigma^2_{y_i} = \mathrm{tr}\left\{C_{1_i}\hat{\Sigma}_{xx}C_{1_i}^T\right\}. \tag{4.55}$$

Again, this set of equations is dual to the stochastic Lyapunov case, replacing $(A_{cl}^T, C_{1_i}^T, B_1^T)$ for (A_{cl}, B_1, C_{1_i}).

Since the set of equations from stochastic Lyapunov is dual to the set of equations from stochastic linearization, these two analytical performance prediction methods are actually equivalent. The duality between the two techniques are summarized in Table 4.1, where $X = \mathrm{lyap}(A, C)$ is the short-hand notation for solving the Lyapunov equation: $AX + XA^T = -C$.

Table 4.1: Duality between stochastic Lyapunov and stochastic linearization performance prediction techniques

	Stochastic Lyapunov		Stochastic Linearization
Consistency	$P = \mathrm{lyap}(A_{cl}(\hat{\sigma}_u)^T, K_i^T K_i)$		$\hat{\Sigma}_{xx} = \mathrm{lyap}(A_{cl}(\hat{\sigma}_u), B_1B_1^T)$
	$\hat{\sigma}^2_{u_i} = \mathrm{tr}\left\{B_1^T P B_1\right\}$		$\hat{\sigma}^2_{u_i} = K_i^T\hat{\Sigma}_{xx}K_i^T$
	(A_{cl}^T, K_i^T, B_1^T)	$\Leftrightarrow$	(A_{cl}, B_1, K_i)
Output variance	$P_y = \mathrm{lyap}(A_{cl}^T, C_1^T)$		$\hat{\Sigma}_{xx} = \mathrm{lyap}(A_{cl}, B_1)$
	$\hat{\sigma}^2_y = B_1^T P_y B_1$		$\hat{\sigma}^2_y = C_1^T\hat{\Sigma}_{xx}C_1^T$
	$(A_{cl}^T, C_{1_i}^T, B_1^T)$	$\Leftrightarrow$	(A_{cl}, B_1, C_{1_i})

4.4 Computational Methods

From the previous section, the stochastic Lyapunov technique is dual to the stochastic linearization technique, and therefore, they are equivalent analysis tools. More importantly the consistency conditions for the stochastic linearization calculations require solution of only one Lyapunov equation, whereas the stochastic Lyapunov technique requires solutions to a family of Lyapunov equations. Since both methods can arrive at the same results, use of the stochastic linearization equations is simpler and minimizes the number of computations required. The following section discusses some basic numerical techniques for solving the equations required to develop an accurate prediction of the closed-loop output variance for a specified state feedback control law.

4.4.1 Computation of the gain functions N

If the actuator nonlinearities consist of resolution, quantization, and saturation, a nonlinear function which describes the input-output relationship of the nonlinear component can be expressed as

$$\phi_i(u_i) = \begin{cases} +\alpha_i, & u_i \geq \alpha_i \\ q_i * \text{round}(u_i/q_i), & r_i < u_i < \alpha_i \\ 0, & -r_i \leq u_i \leq r_i \\ q_i * \text{round}(u_i/q_i), & -\alpha_i < u_i < -r_i \\ -\alpha_i, & u_i \leq -\alpha_i \end{cases} \tag{4.56}$$

where α_i is the saturation level, q_i is the quantization level, and r_i is the resolution level of the actuator. The notation round$(\cdot)$ rounds its component to the nearest integer, so that the output $\phi_i(u_i)$ can only take on integral multiple values of q_i. For convenience, assume that $\alpha_i = M_i q_i$ and $r = L_i q_i$, i.e. the saturation and resolution levels are integer multiples of the quantization step size. Carrying out the expectation $E\{\phi_i'(u_i)\}$, the stochastic linearization gain for this nonlinearity can be written as

$$N_{ii}(\hat{\sigma}_u) = f_i(\hat{\sigma}_{u_i}) = \frac{2r_i}{\sqrt{2\pi}\hat{\sigma}_{u_i}} \exp\left(\frac{-r_i^2}{2\hat{\sigma}_{u_i}^2}\right) + \frac{2q_i}{\sqrt{2\pi}\hat{\sigma}_{u_i}} \sum_{k=L_i}^{M_i} \exp\left(\frac{-(2k-1)^2 q_i^2}{8\hat{\sigma}_{u_i}^2}\right), \tag{4.57}$$

If quantization is not taken into account, the gain N_{ii} for resolution plus saturation is given by

$$N_{ii}(\hat{\sigma}_u) = \text{erf}\left(\frac{\alpha_i}{\sqrt{2}\hat{\sigma}_{u_i}}\right) - \text{erf}\left(\frac{r_i}{\sqrt{2}\hat{\sigma}_{u_i}}\right) + \frac{2r_i}{\sqrt{2\pi}\hat{\sigma}_{u_i}} \exp\left(\frac{-r_i^2}{2\hat{\sigma}_{u_i}^2}\right) \tag{4.58}$$

For the simplest case, where only saturation limits are considered, the stochastically linearized gain becomes the limit of Equation 4.57 as q_i and $r_i \to 0$

$$N_{ii}(\hat{\sigma}_u) = \text{erf}\left(\frac{\alpha_i}{\sqrt{2}\hat{\sigma}_{u_i}}\right). \tag{4.59}$$

A representative plot of N_{ii} as a function of $\hat{\sigma}_{u_i}$ for the saturation-only case is shown in Figure 4-4(a). In this case, N_{ii} is a strictly decreasing function of $\hat{\sigma}_{u_i}$, and the value of N_{ii} stays close to 1 if the system operates in the linear region, $\phi_i(u_i) = u_i$. As the control gain increases, the RMS control σ_{u_i} also increases, but the actual control signal cannot increase without bound due to saturation effects. Therefore, the gain N_{ii} decreases with σ_{u_i} to model the effect that the actual control signal of the system is limited. Since the available control is limited, the achievable performance of the system will also be limited. This result has already been demonstrated earlier in Section 4.2.3, where the output deviation does not decrease with increasing controller gains as shown by Figure 4-3(b).

For the saturation plus quantization and resolution case, representative N_{ii} curves are shown in Figure 4-4(b). In this plot, the dashed line illustrates N_{ii} for the saturation plus resolution case. This curve has three general regions: N_{ii} first increases with $\hat{\sigma}_{u_i}$, then $N_{ii} \approx 1$, and finally N_{ii} decreases with $\hat{\sigma}_{u_i}$. In the flat section of the curve, where $N_{ii} \approx 1$, the system is operating in the linear region, so N_{ii} does not change the effective controller gain. By comparing Figures 4-4(b) and 4-4(a), the region where N_{ii} decreases with $\hat{\sigma}_{u_i}$ is clearly caused by saturation effects. As a result, in the region where N_{ii} increases with $\hat{\sigma}_{u_i}$, the system must be affected by resolution effects. Recall that resolution acts as a deadzone function on the control input. As the RMS control $\hat{\sigma}_{u_i}$ decreases, an increasing fraction of the actuator output becomes 0 after passing through the resolution (deadzone) nonlinearity. Therefore, the N_{ii} curve decreases as $\hat{\sigma}_{u_i}$ decreases to illustrate that the effective control gain is reduced due to resolution effects.

The dashed-dotted line shown in Figure 4-4(b) illustrates the saturation plus quantization case. This curve exhibits similar behavior as the saturation plus resolution case. The stochastic gain N_{ii} varies between 0 and 1 - when N_{ii} is close to 1, the actuator is operating in its linear region; when N_{ii} is close to 0, the actuator is either near saturation (on the right side of the curve), or in quantization region (on the left side) depending on the magnitude of $\hat{\sigma}_{u_i}$. The quantizer thus also induces a deadzone effect, since the actuator output becomes zero if its input lies below the first quantization level.

When saturation is combined with quantization and resolution effects, the corresponding N_{ii} curve is marked by x's in Figure 4-4(b). Interestingly this curve lines up closely to the saturation plus resolution case. When the resolution level is greater than the quantization level ($r_i > q_i$), the left half of the N_{ii} curve is dominated by resolution effects. This result is

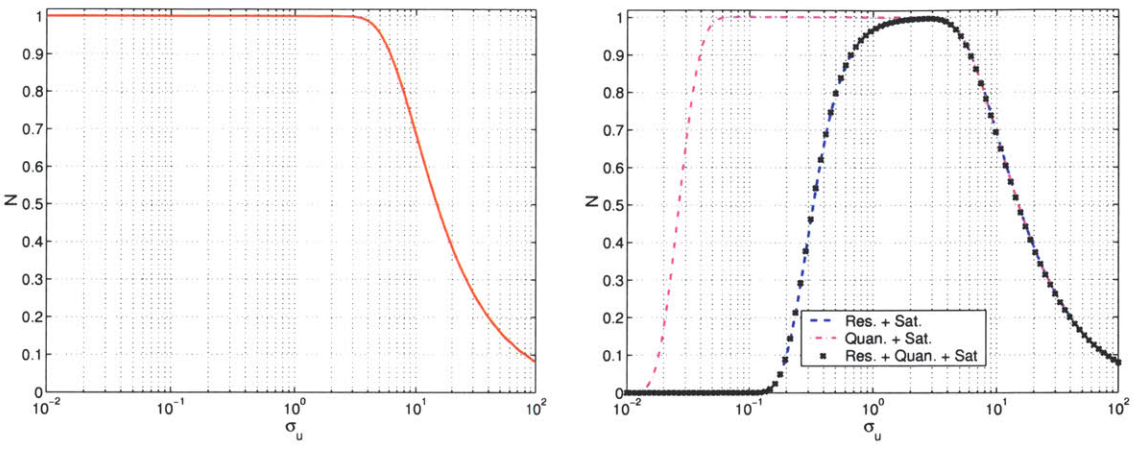

(a) (b)

Figure 4-4: Stochastically linearized gain N as a function of input variance $\hat{\sigma}_u$ ($\alpha = 10$, $q = 0.1$, $r = 0.5$) (a) saturation only (b) saturation plus resolution

not surprising since that part of the curve primarily illustrates the deadzone phenomenon caused by quantization and resolution effects. The N curve does not appear to be very sensitive to the jumps caused by the quantizer. It is well known that dithering can improve the performance of the system [17] and can also smooth the nonlinear function like the one described in Equation 4.56 [20]. From this perspective, adding random noises to the system can effectively smooth the quantizer jumps, and hence, the stochastic linearization gain is insensitive to small quantization levels.

An important observation is that the probability that u_i is smaller than the saturation limit α_i can be computed by

$$\begin{aligned}\mathcal{P}\{|u_i| \leq \alpha_i\} &= \int_{-\alpha_i}^{\alpha_i} \frac{1}{\sqrt{2\pi}\sigma_{u_i}} \exp\left(\frac{-u_i^2}{2\sigma_{u_i}^2}\right) dx \\ &= \operatorname{erf}\left(\frac{\alpha_i}{\sqrt{2}\sigma_{u_i}}\right)\end{aligned}$$

Notice that the above expression is the same as the stochastic linearized gain for the saturating actuator given in Equation 4.59. As a result, when saturation is the only actuator nonlinearity considered, the stochastic linearized gain N_{ii} is also the probability that the actuator does not saturate. Reciprocally, $1 - N_{ii}$ is the probability of saturation, i.e. $\mathcal{P}\{|u_i| > \alpha_i\}$. This parameter plays an important role in a system study or a tradeoff analysis. Since $1 - N_{ii}$ estimates the percentage of time that the ith actuator spends in saturation, it would be desirable to look for solutions that minimize $1 - N_{ii}$ in order to preserve the actuator lifetime during a mission.

4.4.2 Numerical solution techniques

Consider the single-input case first, and assume that $N(\hat{\sigma}_u)$ is a strictly decreasing function of $\hat{\sigma}_u$. In this case, a simple bisection method can be used to solve the above equations for a single input problem. Recall that $N = f(\hat{\sigma}_u) = E\{\phi'(u)\}$, and define g as the unique inverse of f, so that $\hat{\sigma}_u = g(N) = f^{-1}(N)$. Given a system $(A, [B_1 B_2], C_1, 0)$ and a controller K, the stochastic linearization algorithm used for performance variance is summarized here.

1. Let $N_H = 1$ and $N_L = 0$.
2. Set $\tilde{N} = \frac{N_H + N_L}{2}$, where $\tilde{N}$ is an estimate of the value N which satisfies the consistency conditions.
3. Solve Equation 4.43 for the corresponding steady-state covariance matrix estimate $\tilde{\Sigma}_{xx}$
$$(A + B_2 \tilde{N} K)\tilde{\Sigma}_{xx} + \tilde{\Sigma}_{xx}(A + B_2 \tilde{N} K)^T = -B_1 B_1^T.$$
4. Solve for the corresponding estimate $\hat{\sigma}_u$ using the state covariance matrix
$$\hat{\sigma}_u^2 = K \tilde{\Sigma}_{xx} K^T.$$
5. Solve for $\tilde{\sigma}_u$ from $\tilde{N}$
$$\tilde{\sigma}_u^2 = g^2(\tilde{N})$$
6. Define an error measure $\delta = \hat{\sigma}_u^2 - \tilde{\sigma}_u^2$
7. If $\delta < 0$, $N_L = \tilde{N}$; otherwise, $N_H = \tilde{N}$
8. Repeat steps 2-7 until $|\delta| < \epsilon$, where $\epsilon > 0$ is the tolerance on the error measure.
9. Solve the Lyapunov equation with the final estimate $\hat{N}$ which satisfies the error tolerance in the previous step.
$$(A + B_2 \hat{N} K)\hat{\Sigma}_{xx} + \hat{\Sigma}_{xx}(A + B_2 \hat{N} K)^T = -B_1 B_1^T.$$

10. Determine the steady-state output variance from

$$\hat{\sigma}_{y_i}^2 = C_{1_i} \hat{\Sigma}_{xx} C_{1_i}^T.$$

For the multi-input case, the consistency constraint has to be satisfied for each input variance (Equation 4.50) and the associated Lyapunov equation (Equation 4.51). Since $u = Kx$, the control inputs are coupled through the dynamic coupling of the plant states. As a result, even if N is assumed to be diagonal, the control couplings may prevent the use of simple bisection methods. In this case, general purpose nonlinear optimization algorithms must be used to solve the problem. One possible algorithm is the multi-resolution, exhaustive search technique described below. This algorithm is described using two control inputs as an example; it can be easily extended for an arbitrary number of actuators.

1. Let N_1 and N_2 be a grid of points between 0 and 1

2. At each grid point, the estimated linearization gain $\tilde{N}$ is given by

$$\tilde{N} = \begin{bmatrix} \tilde{N}_1 & 0 \\ 0 & \tilde{N}_2 \end{bmatrix}$$

3. Solve the steady-state covariance matrix P at each grid point

$$(A + B_2 \tilde{N} K)\tilde{\Sigma}_{xx} + \tilde{\Sigma}_{xx}(A + B_2 \tilde{N} K)^T = -B_1 B_1^T.$$

4. Solve for $\hat{\sigma}_u$ at each grid point from $\tilde{\Sigma}_{xx}$

$$\begin{aligned} \hat{\sigma}_{u_1}^2 &= K_1 \tilde{\Sigma}_{xx} K_1^T \\ \hat{\sigma}_{u_2}^2 &= K_2 \tilde{\Sigma}_{xx} K_2^T \end{aligned}$$

5. Solve for control variance from $\tilde{N}$ at each grid point

$$\begin{aligned} \tilde{\sigma}_{u_1}^2 &= g_1^2(\tilde{N}_1) \\ \tilde{\sigma}_{u_2}^2 &= g_2^2(\tilde{N}_2) \end{aligned}$$

6. Collect the $\tilde{\sigma}_{u_i}$ into a vector $\tilde{\sigma}_u$, and similarly collect the $\hat{\sigma}_{u_i}$ into a vector $\hat{\sigma}_u$. Define the vector $e = \hat{\sigma}_u - \tilde{\sigma}_u$ for each grid point, and define a corresponding error measure

$$\delta = \|e\|^2$$

7. Repeat 2-6 for each grid point, and find the grid point corresponding to the minimum error δ

8. Generate a refined grid of N_1 and N_2 centered around the minimum δ grid point. Repeat steps 2-7 until the minimum δ is less than some specified accuracy ϵ, or the grid size is smaller than a threshold.

9. Solve the Lyapunov equation with the final estimate $\hat{N}$ which satisfies the error tolerance in the previous step.

$$(A + B_2\hat{N}K)\hat{\Sigma}_{xx} + \hat{\Sigma}_{xx}(A + B_2\hat{N}K)^T = -B_1B_1^T.$$

10. The predicted steady-state output variance is given by

$$\sigma_{y_i}^2 = C_{1_i}\hat{\Sigma}_{xx}C_{1_i}^T.$$

Using duality, the same algorithms above may also be used for stochastic Lyapunov replacing (A_{cl}, B_1, K_i) with (A_{cl}^T, K_i^T, B_1^T) and (A_{cl}, B_1, C_{1_i}) with $(A_{cl}^T, C_{1_i}^T, B_1^T)$. The Lyapunov equation associated with control variance computation has to be solved n_u times, where n_u is the number of actuators, in order to obtain $\hat{\sigma}_u$ for each actuator input.

4.4.3 Dealing with non-monotonic N_{ii}

When N_{ii} is a strictly decreasing function of $\hat{\sigma}_{u_i}$ such as the saturation-only case, the algorithm above can find the required solution to the consistency equations. In the saturation plus resolution and/or quantization case, the N_{ii} curve is a strictly increasing function of $\hat{\sigma}_{u_i}$ at low $\hat{\sigma}_{u_i}$ and then a strictly decreasing function of $\hat{\sigma}_{u_i}$ at high $\hat{\sigma}_{u_i}$. As a result, the function $f_i(\hat{\sigma}_{u_i})$ is not uniquely invertible. There may be two possible values of $\hat{\sigma}_{u_i}$ for any given N_{ii}, corresponding to the left ("resolution") half of the curve, and the right ("saturation") half.

For this problem, each linearization curve can be separated into left and right halves, on which the N vs σ_u curve is invertible, and the optimization routine set to search for a solution in both sections. For example, if there is one actuator input, the bisection algorithm can be used to search for a solution in the right half of the N curve, and also search for a solution in the left half of the N curve. The solution which satisfies the consistency constraint, $\delta < \epsilon$, will be taken as the final solution. If the system has two actuators, there are a total of four possible solution search regions: (resolution region of u_1, resolution region of u_2), (resolution region of u_1, saturation of u_2), etc. The consistency measure δ is evaluated for each of these four possibilities, and the case with the lowest error is the solution. For n_u actuators there will be 2^{n_u} regions which need to be checked.

4.5 Multivariate Examples

This section illustrates application of the above techniques to a few examples of multi-dimensional and multi-input systems. Both techniques are used for the following examples to verify that they indeed provide the same results.

Example 4.1 ***Two-state, one-input***

The first example is a two-state, spring-mass system with a single input as shown in Figure 4-5, with dynamics given by

$$\begin{aligned} dx &= Axdt + B_1 dw + B_2 \phi(u) dt \\ y &= C_1 x \\ u &= Kx, \end{aligned} \tag{4.60}$$

where

$$A = \begin{bmatrix} 0 & 1 \\ -\omega_n^2 & 0 \end{bmatrix} \quad B_1 = \begin{bmatrix} 0 \\ 1 \end{bmatrix} \quad B_2 = \begin{bmatrix} 0 \\ 1 \end{bmatrix} \quad C_1 = [1\ 0],$$

with $\omega_n = 1$ Hz. The nonlinear function $\phi(u)$ is assumed to be a saturation function with saturation level $\alpha = 4$.

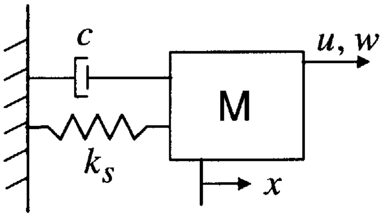

Figure 4-5: Single mass-spring example

The feedback gain for this system is $K = [-118.4,\ -17.8]$ which, if actuator saturation were ignored, would create closed-loop poles with a damping of 0.7 and a natural frequency of 2 Hz. The expected output variance ignoring the saturation would be $\hat{\sigma}_y = 1.78 \times 10^{-4}$.

The stochastic linearization method is used first to predict the steady-state performance of the system. Utilizing the bisection algorithm described in Section 4.4, the results are summarized as follows:

$$N = 0.64, \quad \hat{\sigma}_u^2 = 19.3, \quad \hat{\sigma}_y^2 = 3.8 \times 10^{-4}$$

Exactly the same results are also obtained from the stochastic Lyapunov technique. A numerical simulation using a fixed-step, fourth order Runge-Kutta algorithm is conducted to verify these results. The numerical simulation estimate of the steady-state performance is approximately 4.0×10^{-4}, so there is a 7.5% difference between the predicted performance and the numerical simulation. Since the stochastic linearization technique typically has a prediction error within 10% of the actual value, this result is expected.

Note that the actual output variance is more than twice as large as the linear prediction. This is due to the saturation of the actuator, which is saturating approximately $100 \times (1 - N) = 36\%$ of the time.

Example 4.2 ***Four-state, two-input***

This example uses a double spring-mass system as illustrated in Figure 4-6. Each of the masses is controlled by a separate actuator and the general dynamics is the same as Equation 4.60 with the system matrices given by

$$A = \begin{bmatrix} 0 & 0 & 1 & 0 \\ 0 & 0 & 0 & 1 \\ -\frac{k_1}{m_1} & \frac{k_1}{m_1} & -\frac{c_1}{m_1} & \frac{c_1}{m_1} \\ \frac{k_1}{m_2} & -\frac{(k_1+k_2)}{m_2} & \frac{c_1}{m_2} & -\frac{(c_1+c_2)}{m_2} \end{bmatrix} \quad B_1 = \begin{bmatrix} 0 & 0 \\ 0 & 0 \\ \frac{1}{m_1} & 0 \\ 0 & \frac{1}{m_2} \end{bmatrix}$$

$$B_2 = \begin{bmatrix} 0 & 0 \\ 0 & 0 \\ \frac{1}{m_1} & 0 \\ 0 & \frac{1}{m_2} \end{bmatrix} \quad C_1 = \begin{bmatrix} 1 & 0 & 0 & 0 \\ 0 & 1 & 0 & 0 \end{bmatrix},$$

where $m_1 = m_2 = 2$, $c_1 = c_2 = 0.1$, $k_1 = 1$, and $k_2 = 4$. The state vector contains the position and velocity of each mass, $x = [x_1, x_2, \dot{x}_1, \dot{x}_2]^T$. The nonlinear component ϕ is a noninteracting saturation function with saturation levels $\alpha_1 = \alpha_2 = 2$. The controller gain

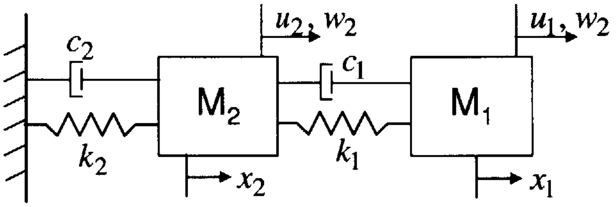

Figure 4-6: Double mass-spring example

is selected so that the closed-loop system consists of two critically damped, second-order pole pairs with natural frequencies of 2 and 3 rad/sec respectively. The resulting controller gain is

$$K = -\begin{bmatrix} 17.0 & 1.0 & 8.4 & 0.1 \\ 1.0 & 3.0 & 0.1 & 5.5 \end{bmatrix},$$

If the system were linear, the expected output variances would be 0.3×10^{-2} and 1.1×10^{-2} for output one and two, respectively.

The stochastic Lyapunov and linearization analysis techniques are used again to predict the steady-state performance of the system. Using the procedures outlined previously, they both arrive at the same results:

$$N_1 = 0.57 \qquad N_2 = 0.89$$

$$\hat{\sigma}^2_{u_1} = 6.41 \qquad \hat{\sigma}^2_{u_2} = 1.61$$

$$\hat{\sigma}^2_{y_1} = 0.96 \times 10^{-2} \quad \hat{\sigma}^2_{y_2} = 1.3 \times 10^{-2}$$

The same numerical simulation used for the previous examples is applied here to simulate this dynamical system and estimate the steady-state performance. The numerical estimates for the output variances are $\sigma^2_{y_1} = 1.07 \times 10^{-2}$ and $\sigma^2_{y_1} = 1.14 \times 10^{-2}$, so there is about a 10% difference between the simulation and the predicted results.

Again note that the linear prediction is off by more than a factor of three in the prediction of $\sigma^2_{y_1}$, which is again due to the fact that the actuators are saturating 43% and 11% of the time respectively.

Example 4.3 *Two-state, two-input*

This example uses a two-state, spring-mass system with two control inputs and one disturbance input. The plant itself is critically damped with a natural frequency of 50 Hz.

The disturbance spectrum is not a constant as that used in the previous examples, but it is modelled as the output of the second order filter

$$G_w(s) = \frac{F_w}{s^2 + 2\zeta_w \omega_d s + \omega_d^2},$$

driven by white noise. The parameters $F_w = 5$, $\zeta_w = 0.707$, and $\omega_d = 10$ Hz are used in this example, and the disturbance is modelled to enter the plant at the output. Two actuator filters G_{A_1} and G_{A_2} are also added to capture the bandwidth of each actuator, and they are modelled as critically damped second order low pass filters with frequencies at $\omega_{a_1} = 2$ Hz and $\omega_{a_2} = 20$ Hz. A block diagram of this system is illustrated by the composite model in Chapter 3 (see Figure 3-10), and methods to integrate the various models together are also discussed in that chapter. The actuator model again only incorporates saturation effects, with saturation levels of $\alpha_1 = 100$ and $\alpha_2 = 5$. These actuator properties are chosen to reflect a realistic staged actuation system, where one actuator has high saturation level but low bandwidth, and the other actuator has low saturation level but high bandwidth.

The output of the system is the deviation in the position of the mass x_1 from 0. The control input was designed to minimize the following cost,

$$J = \min_u \int_0^\infty y^2(t) + u^2(t) dt$$

under the assumption that the actuators do not saturate. This results in a feedback gain matrix of

$$K = -\begin{bmatrix} 1.6 & 141.6 & 30.1 & 1019.7 & 8.1 & 1.0 & 44.5 & 2820.0 \\ 14.5 & 2081.0 & 8.1 & 1028.1 & 31.8 & 6182.5 & 91.5 & 10194 \end{bmatrix}$$

If the linear assumption were satisfied, the expected output variance would be about $\sigma_y^2 = 225.6$.

The Stochastic linearization and Lyapunov techniques are used make more accurate predictions of the steady-state output variance of y in this problem. Again, both methods converged to identical predictions, which are summarized as follows:

$$N_1 = 1.0, \qquad N_2 = 0.33$$

$$\hat{\sigma}_{u_1}^2 = 15.0, \quad \hat{\sigma}_{u_2}^2 = 139.0, \quad \hat{\sigma}_y^2 = 370.5$$

Numerical simulations are again conducted to verify the prediction results. The estimated variance from time simulation is about 364, so there is a 2% difference between the simulation and the predicted results.

Again, the prediction using the linear assumption is off by more than 50%, primarily because the smaller actuator is saturating 67% of the time. More importantly, the change in output variance caused by the nonlinearity means that the K above is not in fact the minimizing solution for the cost functional J, considering the actual closed-loop dynamic response. Accurately accomplishing the desired control power vs output RMS tradeoff expressed in such a cost function must take the nonlinear effects into account. The next chapter will build upon the ideas above to develop an algorithm for accomplishing the desired tradeoff in a manner which accurately incorporates the effects of nonlinear actuators.

Example 4.4 ***Resolution and quantization effects***

In the examples above, the stochastically linearized gains N_{ii} were monotonic functions of each $\hat{\sigma}_i$. This section presents a simple example, where a system has input nonlinearities consisting of quantization, resolution, and saturation.

Consider the same single DOF problem as the one examined in Section 4.2.3

$$dx = -xdt + dw + \phi(kx),$$

where $\phi(\cdot)$ now describes both uniform quantization and saturation. Using stochastic linearization and Equation 4.57, the nonlinear algebraic equation for $\hat{\sigma}_{\hat{x}}$ is expressed as

$$\hat{\sigma}_{\hat{x}}^2 + k\left(\frac{2q}{\sqrt{2\pi}k\hat{\sigma}_{\hat{x}}}\sum_{k=1}^{m}\exp\left(\frac{-(2k-1)^2q^2}{8k^2\hat{\sigma}_{\hat{x}}^2}\right)\right)\hat{\sigma}_{\hat{x}}^2 - \frac{1}{2} = 0.$$

where here $\alpha = 2$ and $q = 0.5$.

The stochastic Lyapunov and stochastic linearization solutions of the above equation as a function of k are plotted in the solid line of Figure 4-7(a). Numerical simulations using a fixed-step, fourth order Runge-Kutta algorithm are used to estimate the actual steady-state performance of this problem, and the results are plotted as a dashed line in the figure. The predicted performance using stochastic linearization is close to the numerical simulation predictions with a maximum difference less than 5%. For comparison purposes, the predicted output variance of the system with only saturation constraints is plotted as a dashed-dotted line in Figure 4-7(a). Comparing the solid and the dashed-dotted line, it is clear that the effect of quantization is most pronounced at low control gain.

The corresponding N curves for this example, is plotted in Figure 4-7(b). This plot looks similar to Figure 4-4, where N is plotted as a function of $\hat{\sigma}_u$. Since the RMS control

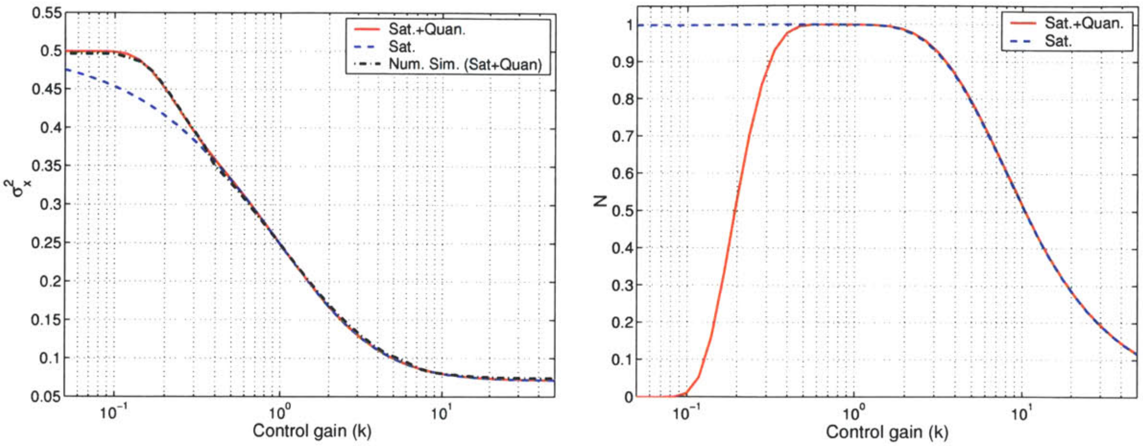

(a)

(b)

Figure 4-7: Comparison of quantization and saturation effects on performance (a)$\hat{\sigma}_x^2$ versus controller gain (b)N versus controller gain

$\hat{\sigma}_u$ increases with increasing control gain k, the N curves have similar shapes either plotted as a function of $\hat{\sigma}_u$ or k. For the saturation plus quantization case, the system is mostly affected by quantization effects at low control gain, $k < 0.5$, and operates in the linear region for $k = 0.5 - 2$. For control gain greater than $k = 2$, the system will start experiencing saturation effects as the output variance asymptotes to its achievable limit as illustrated in Figure 4-7(a).

This example shows that the system performance can be affected by quantization effects at low control gains. However, such effects do not limit the system performance the same way as saturation limitations. If most of the control signal is in the deadzone region of the quantizer, it is always possible to increase the control gain in order to boost the control signal outside the deadzone region. Hence, the output variance decreases as the control gain increases as shown in Figure 4-7(a). If saturation effects are present, the output variance will asymptote to some limiting value and will not continue to decrease as control gain increases. In summary, quantization can affect system performance, but it cannot *limit* the performance in the same fashion as saturation effects.

4.6 Stability

Most stability analysis of linear systems with input nonlinearities like saturation are carried out using deterministic Lyapunov theory, or its close relatives the Circle or Popov criteria. For example, it is straightforward to show that the system (4.1) is at least locally stable when $dw = 0$ provided that $A + B_2K$ is Hurwitz [34]. The guaranteed regions of local stability can be further extended by taking into account the "average" linear behavior of the nonlinear function ϕ, such as using the stochastic linearization N above [21].

Unfortunately, proofs of the above facts rely on the identification of compact invariant sets for the closed-loop trajectory of the system (4.1). While this technique works in the deterministic case, in the stochastic case there is a nonzero probability that the disturbance will push the state out of any specified compact set. Hence such results cannot be used to assess the stability of a stochastic system with input nonlinearities.

One possible method for avoiding these techniques is to use the stochastic version of the Lyapunov theorem in Section 4.2.1, to determine conditions under which a stationary density function can be assured to exist for the nonlinear process. If A itself is Hurwitz, it is possible to find a positive definite matrix P, such that for any given positive definite Q, [34]

$$AP + PA^T = -Q. \tag{4.61}$$

The quadratic Lyapunov function

$$V = x^T Px, \tag{4.62}$$

then satisfies

$$\begin{aligned}\mathcal{L}V(x) &= x^T PAx + x^T A^T Px + x^T PB_2\phi(Kx) + \phi^T(Kx)B_2^T Px + \operatorname{tr}\left\{B_1^T PB_1\right\} \\ &= x^T(PA + A^T P)x + 2x^T PB_2\phi(Kx) + \operatorname{tr}\left\{B_1^T PB_1\right\} \\ &= -x^T Qx + 2x^T PB_2\phi(Kx) + \operatorname{tr}\left\{B_1^T PB_1\right\} \\ &\leq -\lambda_{\min}(Q)\,\|x\|^2 + 2\,\|x\|\,|PB_2|\,\|\phi(Kx)\| + \operatorname{tr}\left\{B_1^T PB_1\right\} \qquad (4.63)\end{aligned}$$

where λ_{min} denotes the minimum eigenvalue, the term $\|\cdot\|$ is the standard vector 2-norm, and $|PB_2|$ is the induced matrix norm on PB_2. In this equation, the nonlinear vector $\phi(Kx) \in \mathbb{R}^{n_u}$ describes actuator characteristics considered in this thesis, and therefore, $\|\phi(Kx)\|$ is bounded due to saturation limitations. In addition, the 2-norm on the nonlinear vector is upper bounded by its infinity norm,

$$\begin{aligned} \|\phi(Kx)\| &< \sqrt{n_u}\,\|\phi(Kx)\|_\infty \\ &= \sqrt{n_u}\max_{1\leq i\leq n_u}|\phi_i| = \sqrt{n_u}\alpha_{\max}, \end{aligned}$$

where $\alpha_{\max}$ is the largest saturation level.

Substituting the above result into Equation 4.63

$$\mathcal{L}V \leq -\lambda_{\min}(Q)\,\|x\|^2 + 2\,\|x\|\,|PB_2|\sqrt{n_u}\alpha_{\max} + \mathrm{tr}\left\{B_1^T P B_1\right\}. \tag{4.64}$$

For sufficiently large $\|x\|$, the second order term dominates and in particular $\mathcal{L}V$ becomes negative, hence Theorem 4.1 is satisfied. This shows that stationary density exists for the system described by Equation 4.1 when A is Hurwitz and actuator inputs are limited by saturation.

Interestingly, the above argument does not depend upon the feedback gain K. If $A + B_2NK$ is not Hurwitz, the local "linearization" becomes unstable. However, the state is still stochastically stable in the RMS sense (i.e. bounded second moment), by the above argument, but the state variance may become quite large. One method of bounding this worse-case variance σ^2_{WC} is presented here. Applying Young's inequality [47], Equation 4.64 can be written as

$$\mathcal{L}V \leq -(\lambda_{\min}(Q) - \frac{\gamma}{2})\,\|x\|^2 + \frac{2}{\gamma}|PB_2|^2 n_u\alpha_{\max}^2 + \mathrm{tr}\left\{B_1^T P B_1\right\}, \tag{4.65}$$

for any positive constant $\gamma > 0$. Without loss of generality, let $\gamma = \lambda_{\min}(Q) = \lambda_Q$. Substituting this value of γ into the above equation,

$$\mathcal{L}V \leq -\frac{1}{2}\lambda_Q\,\|x\|^2 + \frac{2}{\lambda_Q}|PB_2|^2 n_u\alpha_{\max}^2 + \mathrm{tr}\left\{B_1^T P B_1\right\}. \tag{4.66}$$

The bound on the variance of x can be estimated using Proposition 4.1, and it is given by

$$\hat{\sigma}^2_{x,WC} = E\{\|x\|^2\} \leq \frac{2}{\lambda_Q}\left(\frac{2}{\lambda_Q}|PB_2|^2 n_u\alpha_{\max}^2 + \mathrm{tr}\left\{B_1^T P B_1\right\}\right). \tag{4.67}$$

Since the output is a linear combination of the states ($y = C_1x$), an upper bound on the output variance when $A + B_2NK$ is not Hurwitz is

$$\hat{\sigma}^2_{y,WC} = E\{\|y\|^2\} \leq \|C_1\|^2\,E\{\|x\|^2\}. \tag{4.68}$$

On the other hand, if $A + B_2NK$ is Hurwitz, the local linearization is stable, and the state variance can be estimated by the prediction tools developed from Section 4.3.3 above:

$$\hat{\sigma}_x^2 = E\{\|x\|^2\} = \text{tr}\left\{\hat{\Sigma}_{xx}\right\}, \tag{4.69}$$

where $\hat{\Sigma}_{xx}$ is the state covariance matrix which satisfies

$$(A + B_2NK)\hat{\Sigma}_{xx} + \hat{\Sigma}_{xx}(A + B_2NK)^T = -B_1B_1^T, \tag{4.70}$$

and the stochastic linearization gain N must satisfy the consistency constraints discussed in Section 4.3.3.

In summary, when the Hurwitz condition is satisfied, the bound on the state variance is given by Equations 4.69 and 4.70. When the Hurwitz condition is violated, the local linearization becomes unstable. However, the actual nonlinear system has a stationary density function, and a bounded output variance given by Equation 4.67, although this variance is much larger than the state variance obtained when $A + B_2NK$ is Hurwitz. A graphical representation of the two bounds is shown in Figure 4-8 for a two state system.

All the example problems presented in this chapter do have a controller that satisfies the Hurwitz condition. However, it is not generally true that $A + B_2NK$ is Hurwitz for an arbitrary K. The control synthesis suggested in the next chapter will discuss the implication of the Hurwitz condition in more detail and provide a methodology to ensure that this property holds true during the control design process.

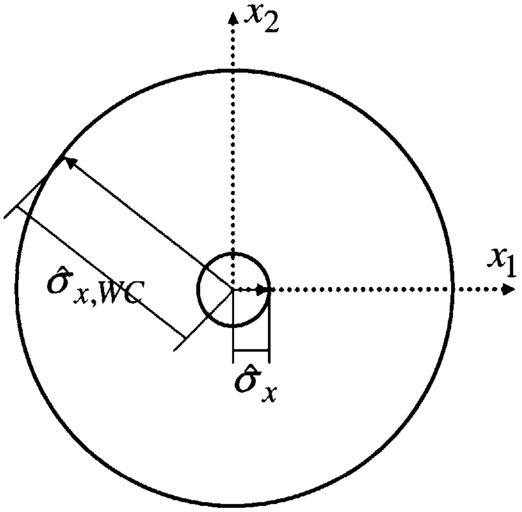

Figure 4-8: Spheres with radii defined by the standard deviation of the state. (inner sphere - satisfies Hurwitz condition, outer sphere - does not satisfy Hurwitz condition)

4.7 Summary

Given that a stationary density function exists, two methods for steady-state performance prediction are presented in this chapter. One method is derived from the stochastic Lyapunov approach and the other is based on stochastic linearization. These methods assume that the density function is Gaussian and produce a set of dual equations that need to be solved to analytically estimate the steady-state performance. As a result, the Lyapunov approach is equivalent to the stochastic linearization technique. Software algorithms are also presented in this chapter to aid the solution search procedure, and numerous examples are shown above to validate the analytical performance predictions.

It should be noted that the controllers used in the above examples are chosen somewhat arbitrarily, since the prediction analysis only requires a stabilizing control design. However, for the space interferometer missions, the control design must stabilize the ideal optical geometry to a specified RMS tolerance under random perturbations. In addition, since the resources are limited onboard a spacecraft, it is necessary to penalize the control effort or power usage. A control synthesis framework that uses the analytical framework presented above to characterize actuator constraints, while satisfying RMS performance requirements and minimizing control effort is presented in the next chapter.

Chapter 5

Staged Controller Synthesis

The tradeoff attempted in Example 4.3 of Chapter 4 typifies the controller synthesis ideas examined in this chapter: find a feedback control law achieving a specified level of closed-loop performance, while minimizing the total required mechanical or electrical power and *taking into account the nonlinearities and bandwidth constraints of the available actuators.* As the examples of the previous chapter have shown, when input nonlinearities are taken into account the closed-loop performance can diverge substantially from the performance predicted by linear techniques. Indeed, actuator limitations may even result in a desired closed-loop performance level being *unachievable.*

The classical LQR or $\mathcal{H}_2$ framework for performing this kind of tradeoff, which uses linear predictions of the closed-loop performance, is thus unsuitable as a design tool for the actuator models considered in this thesis. In the development below, extensions of the $\mathcal{H}_2$ framework are examined which incorporate the nonlinear performance prediction techniques of Chapter 4. The resulting *stochastic linearized LQR* or "SLQR" methodology is one possible technique for automating the design of a controller which balances the competing objectives and limitations of a staged actuation system. Moreover, the proposed control design technique also provides a system analysis tool that is very useful for examining the sensitivity of the desired performance to variations in the actuator characteristics.

Gökçek et al. were the first to study the combination of stochastic linearization and LQR/LQG control, and coined the term "SLQR" to describe the resulting algorithm [21]. Their work extensively studied the case of a single, saturating actuator. Although [21] does mention the multi-input case, and other types of nonlinearities, the necessary equations and solution techniques needed for these situations are not as straightforward as they suggest. The analysis below formally extends the SLQR methodology to the multi-input setting, and to the variety of nonlinear actuator models examined above.

Section 5.1 first formally presents the problem statement, and the controller synthesis theory is developed in Sections 5.2 and 5.3. Numerical techniques for determining the solution of the coupled equations which describe the desired controller are discussed in Section 5.4. A series of examples demonstrating the control design methodology, and its utility as a system design tool, are discussed in Section 5.5. Section 5.6 describes a further extension to SLQR: saturation weighting, allowing the designer to explicitly influence the probability of saturation for each of the actuators during operation. Finally, the extension of the techniques discussed in this chapter to output feedback designs are discussed in Section 5.7.

5.1 Formal Problem Statement

The dynamics of the stabilization problem examined in this chapter are given by

$$\begin{aligned} dx &= Ax\,dt + B_1\,dw + B_2\phi(u)\,dt \\ y &= C_1 x \\ u &= Kx \end{aligned} \tag{5.1}$$

where $\phi(u)$ describes the nonlinear characteristics of the actuators, assumed noninteracting $\phi_i(u) = \phi_i(u_i)$ and the generalized A matrix incorporates the dynamics of the optical system, the actuator bandwidth filters, and disturbance innovations filter as discussed in Chapter 3. The objective is to find the feedback gains K in order to minimize the following cost function

$$J(K) = \hat{\sigma}_y^2 + \rho \sum_{i=1}^{n_u} \rho_i \hat{\sigma}_{u_i}^2, \tag{5.2}$$

As opposed to conventional $\mathcal{H}_2$ control, the notation $\hat{\cdot}$ on the variances is used to emphasize that these quantities will be estimated using the analytical prediction techniques described in Chapter 4, and hence will capture the effects of the actuator nonlinearities. The parameter $\rho > 0$ expresses the desired tradeoff between closed-loop performance, measured by the output variance, and the amount of control power used to achieve a given performance level. The parameters $\rho_i > 0$ are used to express the relative importance of each input variance in this tradeoff, differentially weighting the use of different actuators, for example to reflect force/Watt differences in total power consumption.

From the analysis described in the previous chapter, the steady-state variances in the above cost function can be obtained by solving the following equations:

$$(A + B_2 N(\hat{\sigma}_u)K)\hat{\Sigma}_{xx} + \hat{\Sigma}_{xx}(A + B_2 N(\hat{\sigma}_u)K)^T = -B_1 B_1^T. \tag{5.3}$$

$$\hat{\sigma}_{u_i}^2 = K_i \hat{\Sigma}_{xx} K_i^T, \tag{5.4}$$

$$\sigma_y^2 = \mathrm{tr}\left\{C_1 \hat{\Sigma}_{xx} C_1^T\right\}. \tag{5.5}$$

where again the shorthand $\hat{\sigma}_u$ is used for the vector of standard deviations $\hat{\sigma}_{u_i}$, and the noninteracting assumption on ϕ implies that N is diagonal, with $N_{ii}(\hat{\sigma}_u) = f_i(\hat{\sigma}_{u_i}) = E\{\phi_i'(u_i)\}$ as discussed above. This is a set of coupled, nonlinear equations which must be satisfied simultaneously in order to determine a set of variance estimates consistent with the assumption of an asymptotically stationary Gaussian distribution on the closed-loop dynamics.

To move closer to the classical $\mathcal{H}_2$ terminology, define a performance variable z which includes the output and control terms in J

$$z = \begin{bmatrix} C_1 \\ 0 \end{bmatrix} x + \begin{bmatrix} 0 \\ D_{12} \end{bmatrix} u,$$

where D_{12} is a diagonal matrix with diagonal entries $\sqrt{\rho\rho_i}$. Using the equations above, the performance cost can be written as

$$\begin{aligned} J &= \hat{\sigma}_z^2 \\ &= \mathrm{tr}\left\{C_1 \hat{\Sigma}_{xx} C_1^T\right\} + \mathrm{tr}\left\{D_{12} K \hat{\Sigma}_{xx} K^T D_{12}^T\right\}, \end{aligned} \tag{5.6}$$

where $\hat{\Sigma}_{xx}$ is the covariance matrix of the Gaussian approximation to the asymptotic distribution of x. The objective is to determine the gain K such that the performance cost J is minimized.

5.2 Saturated $\mathcal{H}_2$ Controller

One well established linear controller design that minimizes a quadratic cost function similar to Equation 5.6 is the standard LQR/LQG technique. However, such a technique does not take actuator nonlinearities into account, and therefore, it is necessary to use the prediction tool developed in Chapter 4 to accurately estimate the resulting closed-loop performance of the nonlinear system. An example of such an LQR plus stochastic linearization performance prediction technique, hereafter denoted (LQR+SL), was given in Example 4.3 above. This section gives additional examples to illustrate the LQR+SL control design methodology, and identifies several possible drawbacks to this approach.

Consider a single actuator system with dynamics given by:

$$\begin{aligned} dx &= Ax\,dt + B_1\,dw + B_2\phi(u)\,dt, \\ y &= C_1 x, \end{aligned} \tag{5.7}$$

where the open-loop system has three poles at -0.01, and hence,

$$A = \begin{bmatrix} 0 & 1 & 0 \\ 0 & 0 & 1 \\ -1\times10^{-6} & -3\times10^{-4} & -3\times10^{-2} \end{bmatrix}$$

$$B_1 = B_2 = B = \begin{bmatrix} 0 \\ 0 \\ 1 \end{bmatrix} \quad C_1 = \begin{bmatrix} 1 & 2 & 1 \end{bmatrix}$$

The LQR control design minimizes the following cost function,

$$\begin{aligned} J &= E\left\{\int_0^\infty y^2(t) + \rho u^2(t)dt\right\} \\ &= \operatorname{tr}\left\{C_1\Sigma_{xx}C_1^T\right\} + \operatorname{tr}\left\{D_{12}K\Sigma_{xx}K^TD_{12}^T\right\}. \end{aligned}$$

In this example, the control weighting parameter ρ is varied over a wide range. At each ρ, a LQR controller is computed assuming that there are no actuator nonlinearities. The closed-loop output variance of the system with a saturating actuator is then calculated from the performance prediction tool developed in Chapter 4.

Figure 5-1(a) shows the output variance as a function of the control weighting ρ when the saturation level $\alpha = 3$. As ρ decreases, the control usage becomes cheaper, so larger control command is used to suppress more output variance. Therefore, the closed-loop variance is an increasing function of ρ. The probability of saturation corresponding to each control design is illustrated in Figure 5-1(b). The actuator saturates less than 1% of the time for

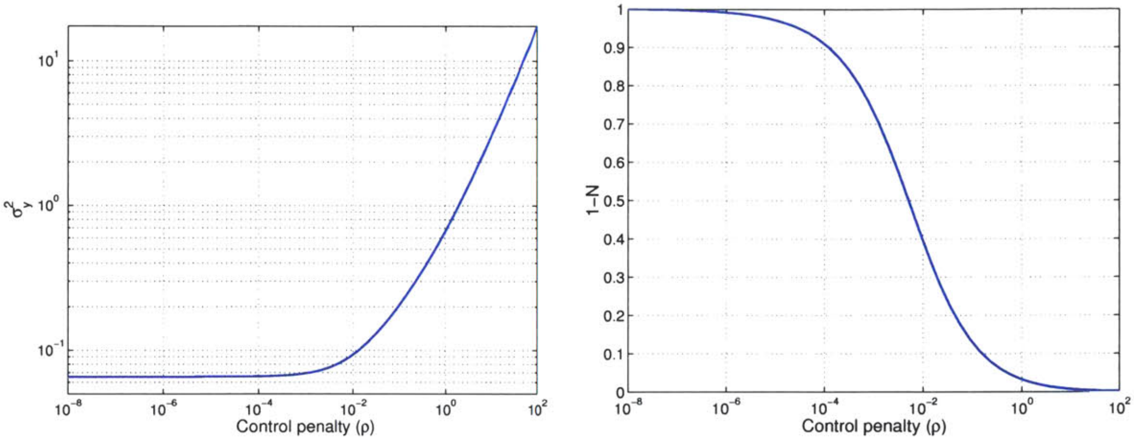

(a) (b)

Figure 5-1: LQR + SL controller design: (a) Output variance as a function of ρ (b) Probability of saturation as a function of ρ

$\rho > 4$ ($\hat{\sigma}_y^2 = 1.62$) and becomes more likely to saturate for smaller values of ρ, reaching asymptotically an achievable performance of $\hat{\sigma}_y^2 = 0.065$. By "serially" computing the LQR gain K, then the corresponding stochastic linearization gain N and the performance $\hat{\sigma}_y$ from the methods of Chapter 4, a designer can iterate on ρ to achieve the required level of performance. Thus, ρ offers a mean to "tune" the LQR+SL design for a desired performance.

Note that a change in the saturation level α will not affect the LQR solution for K, since the LQR algorithm does not "know" about the saturation. This change in α will, however, change the performance $\hat{\sigma}_y$ and the probability of saturation $1 - N$ of the actuator. These changes reveal a potential difficulty in the LQR+SL design process. Since the LQR control gain K is computed independent of the saturation level α, and hence of the stochastic linearization gain N, there is no guarantee that $A + B_2NK$ is Hurwitz. When this Hurwitz condition is violated, the prediction tool developed in Chapter 4 can no longer be used to estimate the closed-loop performance. Indeed, the linearized closed-loop system may be (locally) unstable for a given LQR gain K and saturation level α as discussed in Section 4.6.

To illustrate this phenomenon, the dynamic system presented in Equation 5.7 is again used here. In this problem, the LQR feedback gain K corresponding to $\rho = 4$ is used, and the effect of different saturation levels α on the resulting closed-loop system is examined.

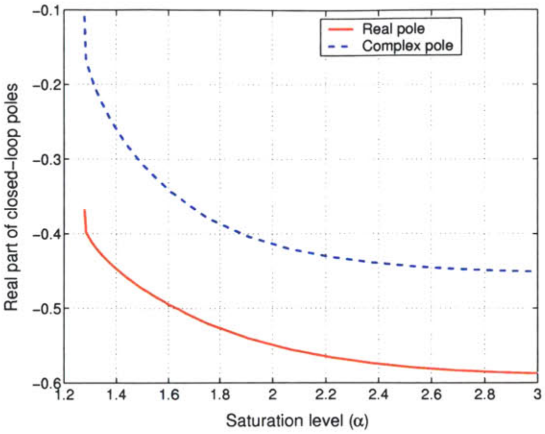

Figure 5-2: LQR + SL controller design: real part of closed-loop eigenvalues eig($A+B_2NK$) as a function of saturation levels

For the problem considered, there are a total of three linearized closed-loop poles - one real and one complex pair. The real part of the closed-loop poles are plotted in Figure 5-2 as a function of the saturation level α. At smaller saturation levels, the actuator becomes more likely to saturate, so the probability of saturation increases, or equivalently, N decreases. A decrease in N causes a decrease in the effective controller gain and pushes the real part of the closed-loop poles closer to the origin. For α below approximately 1.28, the prediction algorithm can no longer find N such that the consistency equations of Chapter 4 are satisfied.

Numerical simulations of the above dynamic system are conducted to verify the observed results. Two saturation levels are chosen for these simulations: one of them is selected to be 1.285, which is slightly above the critical level ($\alpha = 1.28$), while the other is set at the critical level. The simulated system output y for both cases is shown in Figure 5-3(a) and 5-3(b). For the subcritical value of $\alpha = 1.285$, $A + B_2NK$ is Hurwitz and the observed variance is close to the predicted value. For the critical value $\alpha = 1.28$, N has decreased so that $A+B_2NK$ is no longer Hurwitz, and the system exhibits local instability about $y = 0$. It is important to note that y does not actually become unbounded, however, its variance becomes very large. As discussed at the end of Chapter 4, when $A+B_2NK$ is not Hurwitz, the nonlinear system is still stochastically stable with bounded second moment, but the state variance will be much larger than the variance can be obtained when the Hurwitz condition is satisfied.

In addition to the phenomenon identified above, another potential drawback of the

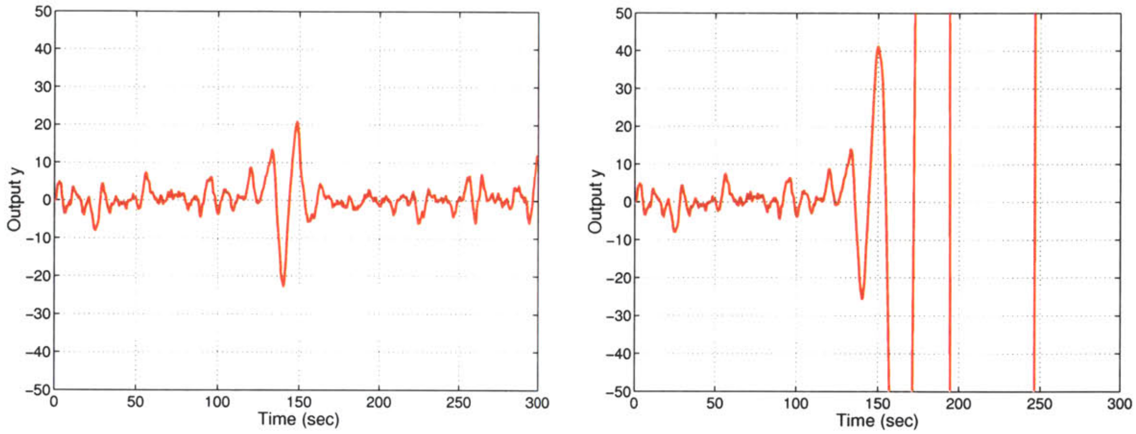

(a) (b)

Figure 5-3: Numerical simulation of a linear system with saturated LQR control (a) saturation level $\alpha = 1.285$ (b) saturation level $\alpha = 1.28$

LQR+SL strategy is in the multi-actuator controller design. To achieve a specified closed-loop performance using the serial design process outline above, it may be necessary to change the control weighting ρ_i of each actuator separately to reflect the different saturation levels of each actuator. However, if ρ_i have been specifically chosen to represent, for example, the electrical or mechanical power requirements on each actuator, independent adjustment of each ρ_i in this fashion will not preserve the proper relative control weightings. Consequently the resulting cost function may not have any physical meaning and may be undesirable for the specific design objectives.

Thus, rather than designing a controller by LQR techniques, then predicting the performance in a serial fashion, it would seem more sensible to *couple* the prediction tool with the controller design process. In such a technique, K would be designed with the knowledge of the resulting N, enabling the $A + B_2NK$ Hurwitz condition to be continually maintained. This technique could also automatically accomplish the desired tradeoffs for a multi-actuator system by directly adjusting the gains in K to account for the different actuator probabilities of saturation. A control synthesis approach that merges the prediction tool of Chapter 4 and the $\mathcal{H}_2$ optimization techniques is the focus of the rest of this chapter.

5.3 Stochastic Linearized $\mathcal{H}_2$ Controller

The control synthesis problem can be posed as a quadratic ($\mathcal{H}_2$) optimization problem,

$$\begin{aligned} K &= \arg\min_K \hat{\sigma}_z^2 \\ &= \arg\min_K \left(\operatorname{tr}\left\{C_1\hat{\Sigma}_{xx}C_1^T\right\} + \operatorname{tr}\left\{D_{12}K\hat{\Sigma}_{xx}K^TD_{12}^T\right\}\right). \end{aligned} \tag{5.8}$$

and the variances must satisfy the constraints posed by Equation 5.3 and 5.4. The latter of these can be rewritten as

$$Y_iK\hat{\Sigma}_{xx}K^TY_i^T = g_i^2(N_{ii}), \tag{5.9}$$

where Y_i is a $1 \times n_u$ row vector with 1 in the ith column and zeros elsewhere, and from Chapter 4, $g_i(N_{ii})$ is defined as the inverse function of N_{ii}, i.e. $N_{ii}(\hat{\sigma}_u) = f_i(\hat{\sigma}_{u_i})$ with $\hat{\sigma}_{u_i} = g_i(N_{ii}) = f^{-1}(N_{ii})$. For nonlinearities where f_i is not uniquely invertible, the techniques of Chapter 4 can be used to split this function into two invertible sections in the search for a solution.

The above formulation turns the control synthesis problem into a constrained nonlinear optimization, which can be solved by Lagrange multiplier techniques [90]. For this problem, the Lagrangian is defined by

$$\begin{aligned} \Psi &= \operatorname{tr}\left\{C_1\hat{\Sigma}_{xx}C_1^T\right\} + \operatorname{tr}\left\{D_{12}K\hat{\Sigma}_{xx}K^TD_{12}^T\right\} + \sum_{i=1}^{n_u}\lambda_i(Y_iK\hat{\Sigma}_{xx}K^TY_i^T - g_i^2(N_{ii})) \\ &\quad +\operatorname{tr}\left\{[(A+B_2NK)\hat{\Sigma}_{xx} + \hat{\Sigma}_{xx}(A+B_2NK)^T + B_1B_1^T]Q\right\} \end{aligned} \tag{5.10}$$

where Q and λ_i are Lagrange multipliers. Differentiating Ψ with respect to K, N_{ii}, $\hat{\Sigma}_{xx}$, Q, and λ_i respectively, the following necessary equations are obtained for the minimizing solution:

$$\frac{\partial\Psi}{\partial K} = 0 \;\Rightarrow\; \{NB_2^TQ + [D_{12}^TD_{12} + \textstyle\sum_{i=1}^{n_u}\lambda_iY_i^TY_i]K\}\hat{\Sigma}_{xx} = 0,$$

$$\text{or} \qquad \{NB_2^TQ + \Phi K\}\hat{\Sigma}_{xx} = 0 \tag{5.11}$$

where $\Phi = [D_{12}^TD_{12} + \Lambda]$ is diagonal with $\rho\rho_i + \lambda_i$ on the i^{th} diagonal, and Λ is a diagonal matrix with elements λ_i. Next, from $\frac{\partial\Psi}{\partial N_{ii}} = 0 \;\Rightarrow$

$$B_{2i}^TQ\hat{\Sigma}_{xx}K_1^T - \frac{\lambda_i\, g_i(N_{ii})}{g_i'(N_{ii})} = 0, \tag{5.12}$$

where B_{2i} is the i^{th} column of B_2, $g_i(\cdot)$ is a function of N_{ii} only, and $g_i'(N_{ii})$ is the partial derivative with respect to N_{ii}. Next for $\frac{\partial\Psi}{\partial\hat{\Sigma}_{xx}} = 0 \;\Rightarrow$

$$(A + B_2NK)^TQ + Q(A + B_2NK) + K^T(D_{12}^TD_{12} + \sum_{i=1}^{n_u}\lambda_iY_i^TY_i)K + C_1^TC_1 = 0.$$

This expression can be simplified using the definition of Φ

$$(A + B_2NK)^TQ + Q(A + B_2NK) + K^T\Phi K + C_1^TC_1 = 0. \tag{5.13}$$

Finally, the derivatives of $\frac{\partial\Psi}{\partial Q}$ and $\frac{\partial\Psi}{\partial\lambda_i} = 0$ recover the two constraint equations given by Equation 5.3 and Equation 5.9, respectively.

The optimal controller is found by solving Equation 5.11,

$$K = -\Phi^{-1}NB_2^TQ. \tag{5.14}$$

Substituting Equation 5.14 into Equation 5.13, a Riccati equation describing Q is found,

$$A^TQ + QA - QB_2N\Phi^{-1}N^TB_2^TQ + C_1^TC_1 = 0. \tag{5.15}$$

Substituting Equation 5.14 into Equation 5.3, the closed-loop Lyapunov equation can be written as

$$(A - B_2N\Phi^{-1}NB_2^TQ)\hat{\Sigma}_{xx} + \hat{\Sigma}_{xx}(A - B_2N\Phi^{-1}NB_2^TQ)^T + B_1B_1^T = 0. \tag{5.16}$$

Pre- and post-multiply Equation 5.11 by Y_i and $K^TY_i^T$,

$$\begin{aligned} Y_i\Phi K\hat{\Sigma}_{xx}K^TY_i^T + Y_iNB_2^TQ\hat{\Sigma}_{xx}K^TY_i^T &= 0 \\ (\rho\rho_i + \lambda_i)Y_iK\hat{\Sigma}_{xx}K^TY_i^T + N_{ii}B_{2i}^TQ\hat{\Sigma}_{xx}K_i^T &= 0. \end{aligned}$$

By substituting in Equation 5.9 and Equation 5.12 for the first and second term in the left-hand-side of the above equation, an equation relating λ_i and N_{ii} is found

$$\lambda_i + \frac{\rho\rho_i\, g_i(N_{ii})}{g_i(N_{ii}) + N_{ii}g_i'(N_{ii})} = 0. \tag{5.17}$$

Finally substitute Equation 5.14 into Equation 5.9 to obtain

$$Y_i\Phi^{-1}NB_2^TQ\hat{\Sigma}_{xx}QB_2N\Phi^{-1}Y_i^T - g_i^2(N_{ii}) = 0. \tag{5.18}$$

The five equations, or necessary conditions, (5.14)-(5.18) must be simultaneously satisfied in order to find the minimizing solution to the constrained optimization problem. Due to the similarity between this optimization problem and the standard LQR problem, the resulting control design is referred to as the stochastically linearized (or, given the duality demonstrated in Chapter 4, the stochastic Lyapunov) LQR technique – SLQR for short [21].

A stability related note should also be made here. Recall in the previous chapter, the stochastic Lyapunov performance analysis requires that $A+B_2NK$ be Hurwitz. Since N is a diagonal matrix with elements in $(0, 1]$, it does not change the controllability/stabilizability or observability/detectability of the system. If the system (A, B_2) is stabilizable and detectable, the Riccati equation (5.15) has a positive semi-definite, stabilizing solution for any given N [91]. As a result, the SLQR control synthesis procedure ensures that $A+B_2NK$ is Hurwitz, and hence the performance prediction technique developed in the previous chapter can be used.

5.4 Multi-input SLQR Solution Methods

Solving the coupled nonlinear equations (5.14)-(5.18) is a nontrivial task. There are algorithms available to aid the solution process in MATLAB or other numerical programming packages, but most of them require explicit computation of the gradients with respect to unknowns (K, N_{ii}, $\hat{\Sigma}_{xx}$, Q, and λ_i). Since the above equations are coupled, the associated gradient equations also turn out to be a coupled set of nonlinear equations which cannot be solved explicitly. As a result, algorithms that do not require gradient information must be used to solve this problem. The standard MATLAB algorithms for this situation have not proven sufficiently robust to reliably find a consistent solution, and even simulated annealing [35] has difficulties converging.

A numerical solution procedure is relatively straightforward for systems with a single input for which the nonlinearity ϕ is a simple saturation. This is the case studied in [21]. In such a case, the N function is a strictly decreasing function of $\hat{\sigma}_u$, and a simple bisection algorithm is sufficient to solve the problem. This idea can be extended to single input problems with non-monotonic N curves, such as the saturation plus quantization and/or resolution nonlinearities. In this case the N curve can be divided into two halves: the "resolution" side, on which the N curve is a strictly increasing function of $\hat{\sigma}_u$, and the "saturation" side, on which the curve is a strictly decreasing function of $\hat{\sigma}_u$. The bisection algorithm can then be used to find a possible solution on either side of the N curve. If a solution exists on both sides of the curve, i.e. all five necessary conditions are satisfied, the solution with the lowest cost J is the solution.

Bisection does *not* extend to a multi-input problem. As discussed above, the coupling of the input variances through the gain matrix K means that independent line searches on $\hat{\sigma}_{u_i}$ will not generally be sufficient to find a solution to the necessary equations. Instead, an iterative, exhaustive search algorithm similar to the one described in Chapter 4 is used in this thesis for the general problem. This section outlines the application of this method to the solution of the necessary equations (5.14)-(5.18).

1. Discretize the possible set of N_{ii} into a grid of points between 0 and 1. Each of these points corresponds to a "trial" gain matrix $\tilde{N}$.

2. Compute the diagonal elements of Λ for each $\tilde{N}$ using Equation 5.17.

$$\lambda_i + \frac{\rho\rho_i\, g_i(\tilde{N}_{ii})}{g_i(\tilde{N}_{ii}) + \tilde{N}_{ii} g_i'(\tilde{N}_{ii})} = 0.$$

3. Solve the Riccati equation given by Equation 5.15 at each grid point with associated values of $\tilde{N}$ and Λ.

$$A^T Q + QA - QB_2\tilde{N}\Phi^{-1}\tilde{N}^T B_2^T Q + C_1^T C_1 = 0,$$

   where $\Phi = (\Lambda + D_{12}^T D_{12})$.

4. Find the optimal controller at each grid point (Equation 5.14)

$$K = -\Phi^{-1}\tilde{N}B_2^T Q.$$

5. Solve for the closed-loop Lyapunov equation (Equation 5.16

$$(A + B_2\tilde{N}K)\hat{\Sigma}_{xx} + \hat{\Sigma}_{xx}(A + B_2\tilde{N}K)^T + B_1 B_1^T = 0.$$

6. Check the consistency constraint for each control variance (Equation 5.18)

$$Y_i K\hat{\Sigma}_{xx}K^T Y_i^T - g_i^2(\tilde{N}_{ii}) = \delta_i,$$

   where δ_i is an error measure on how close the consistency constraint is satisfied. The quantity δ_i is the i^{th} component of the vector δ, which has a length equal to the number of actuators.

7. Compute the 2-norm of the vector δ at the current grid point $\tilde{N}$.

8. Repeat the above steps for each grid point, then determine which grid point has the minimum δ.

9. Refine the grid for $\tilde{N}$ around the location of minimum δ and repeat steps 2-8 until δ is less than a specified tolerance ϵ.

Similar to the single actuator case, when both saturation and resolution or quantization are considered, the algorithm has to check for solutions in two possible regions of *each* actuator. For example, if two actuators are used, there are a total of four possible solution regions: (resolution region of u_1, resolution region of u_2), (resolution region of u_1, saturation of u_2), etc. The solution from these four possibilities with the lowest total cost is then the SLQR solution.

For a given plant, actuator model, and relative control weightings ρ_i let `[`$K, \hat{\Sigma}_{xx}$`]=SLQR(`ρ`)` denote the solution to the necessary equations determined from the procedure above. The predicted closed-loop performance obtained using control law $u = Kx$ is then

$$\sigma_y = \sqrt{C_1 \hat{\Sigma}_{xx} C_1^T} \tag{5.19}$$

assuming a single output for clarity. The main control objective is to meet a specific performance requirement, $\sigma_y \leq \sigma_{y,target}$. To meet this target, the overall control weighting parameter ρ can be iterated until the desired performance is achieved. Since the performance can be shown to be a monotonic function of ρ for the problems considered, a bisection algorithm on ρ can be used to conduct the performance iteration, iteratively calling `SLQR(`ρ`)` until the performance target is achieved. As a result, the optimization algorithm has two loops - the inner loop searches for the solution to the above consistency equations and the outer loop performs ρ iteration until the desired performance is achieved. Sample MATLAB code that implements these two loops is shown in Appendix C.

5.5 Example Applications and Design Tradeoffs

This section presents a number of simple example problems to illustrate the SLQR solution technique. The examples serve to highlight the differences between SLQR and classical LQR, as well as illustrating the ways that SLQR analysis can be used for system design tradeoff analysis. The examples below are based on the simple mass-spring systems examined in the previous chapter. Chapter 6 will explore in greater detail application of the SLQR methodology to space interferometry systems.

5.5.1 Single actuator problem

Consider again the single spring-mass system

$$m\ddot{x} + c\dot{x} + kx = \phi(u) + d,$$

with input control force u and disturbance force d, assumed to have units of Newtons, and here suppose $m = 1, c = 1.26, k = 3.95 \times 10^3$, which corresponds to an open-loop natural frequency of 10 Hz with 1% damping. For this problem, ϕ is a saturation nonlinearity, with saturation level $\alpha = 1$.

The disturbance innovations filter is a second order low pass transfer function

$$d = G_w(s)w = \frac{F_d\omega_d^2}{s^2 + 2\zeta_d\omega_d + \omega_d^2}w,$$

where w is the zero-mean white noise, F_d controls the intensity of the disturbance, ω_d is the disturbance corner frequency, and ζ_d is the effective disturbance damping ratio. The values of these parameters are $F_d = 0.45$, $\omega_d = 50$ Hz, and $\zeta_d = 0.01$ in this example; the PSD of the disturbance is shown in Figure 5-4(a). The controlled output of the system is defined as the position deviation of the mass. The open-loop transfer function from disturbance w to the output deviation y is plotted in Figure 5-4(b).

Example 5.1 ***ρ variations***

In this study, the overall control penalty ρ is varied over a wide range in order to visualize the tradeoff between predicted closed-loop performance $\hat{\sigma}_y$ and corresponding control input $\hat{\sigma}_u$. A secondary objective is to quantify the accuracy of the SLQR predictions, by comparing the predicted output and control variances with those computed by numerically simulating the nonlinear closed-loop dynamics.

The solid line shown in Figure 5-5(a) illustrates the output variance $\hat{\sigma}_y^2$ obtained from the SLQR prediction as a function of ρ. As the control penalty decreases, the algorithm permits greater control usage which in turn permits smaller output variances. Hence $\hat{\sigma}_y^2$ is an increasing function of ρ. However, the control input cannot grow arbitrarily large due

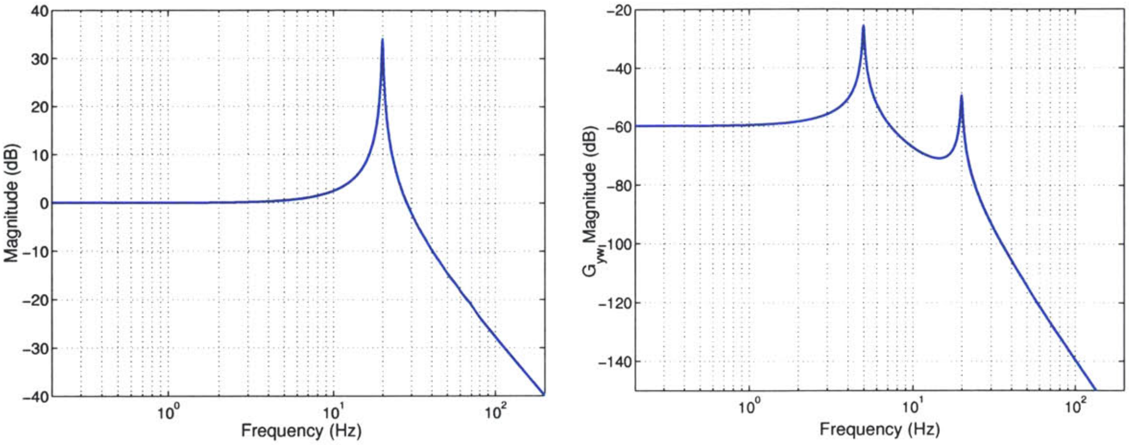

(a) (b)

Figure 5-4: (a) Disturbance spectrum of the single actuator problem (2) Open-loop transfer function from disturbance w to controlled output y

to saturation limitations. As a result, the achievable performance is limited; that is, there is an asymptotic value of $\hat{\sigma}_y^2$ below which the output variance cannot be decreased.

Figure 5-5(b) shows the $1 - N$ curve, which is also the probability of saturation in this case. As ρ decreases, the input to the actuator increases, and the actuator becomes more and more likely to saturate. As $1 - N$ approaches 1, the actuator is saturating almost all the time, and hence is approaching a "bang-bang" operating limit, in which it is operating in saturation virtually 100% of the time. The output variance achieved in this "bang-bang" control limit is approximately 3.6×10^{-4}, and represents the achievable performance limit for this system.

From a systems perspective, Figure 5-5(a) and Figure 5-5(b) can be used in conjunction to make design decisions. For example, the performance curve flattens at $\rho \approx 10^{-7}$; very little performance improvement is gained by further decreasing ρ. For this value of ρ, the actuator saturates about 55% of the time. Decreasing ρ to 10^{-6}, for example, results in a design with approximately 10% more output variance, but almost a 50% decrease in the probability of saturation (down to 0.3, or 30% of the time).

The dashed line in Figure 5-5(a) illustrates the output variance computed from numerical simulations as a function of ρ. The predicted SLQR solution agrees reasonably well with the numerical simulation results, and the maximum difference between the two performance prediction methods is less than 8 %.

Finally, a family of classical LQR controllers are designed for this example problem, assuming that there are no saturation effects $\phi(u) = u$. The expected linear output variance from the LQR control design is shown as a dashed line in Figure 5-6(a), and the SLQR results are plotted as a solid line for comparison. If the LQR controller is used in the system with actuator nonlinearities, the performance of the closed-loop system may be estimated by exhaustive numerical simulations or the performance prediction tool developed in Chapter 4. The second technique can obtain results much faster than the first, and it is the LQR+SL design methodology as discussed in Section 5.2. The LQR+SL estimate of output variance is illustrated as a dotted line in Figure 5-6(a).

For large control weighting ($\rho > 2\times10^{-5}$), all three curves lie closely together, indicating that the actuator operates mostly in its linear region. Comparisons between each pair of the three curves are made in order to reinforce ideas previously discussed or to add insights to the different control design schemes:

- Comparison between SLQR (solid) and LQR (dashed) - Since the LQR method does not take saturation into account the curves diverge sharply as ρ decreases below 2×10^{-5}, which from Figure 5-5(b) is when the actuator begins to saturate an appreciable fraction of the time. The LQR design indicates that arbitrarily small output variance can be obtained, while the SLQR design illustrates the performance is limited due to saturation effects.

- Comparison between LQR (dashed) and LQR+SL (dotted) - The LQR variance deviates greatly from the LQR+SL prediction for $\rho < 10^{-5}$, since it does not account for saturation effects. This phenomenon again demonstrates that the expected system performance may differ significantly from the actual performance when saturation effects are ignored.

- Comparison between SLQR (solid) and LQR+SL (dotted) - The output variance estimated from the LQR+SL technique is significantly worse than the SLQR solution for small values of ρ (less than 10^{-7}), and the variance of LQR+SL continues to deteriorate as ρ decreases. There is a small region around 4×10^{-7} where the LQR controller can obtain the achievable performance that the SLQR controller recovers in the cheap control limit ($\rho \to 0$). For this single actuator problem, it is possible to use the analysis tool to find an appropriate LQR controller which achieves similar level of performance as the SLQR design. In this case, $A + B_2NK$ is Hurwitz for each of the LQR designs studied, however, the Hurwitz condition will not always be satisfied, as discussed in Section 5.2.

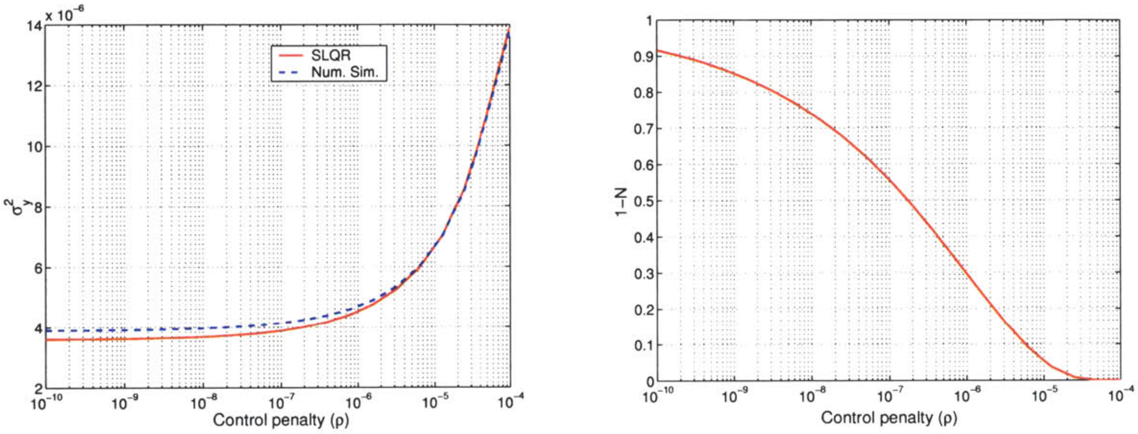

(a) (b)

Figure 5-5: Single actuator examples: (a) Output variance as a function of ρ (b) Probability of saturation as a function of ρ

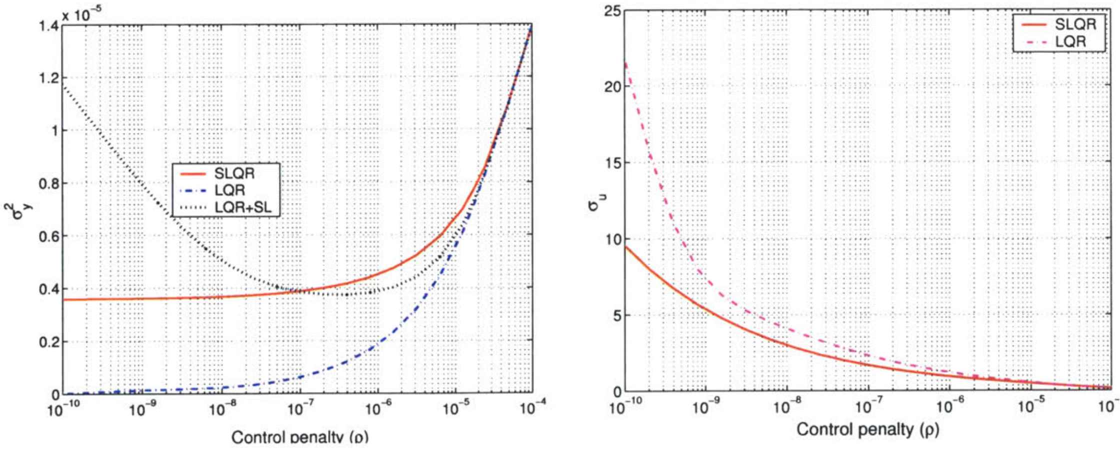

(a) (b)

Figure 5-6: Single actuator examples: (a) Output variance computed from SLQR, LQR, and LQR+SL techniques (b) Control variance as a function of ρ

Example 5.2 ***Effects of saturation***

This example studies the effect of the saturation level. For each saturation level, the desired closed-loop control is to reduce the open-loop RMS $\hat{\sigma}_y$ by a factor of 2, so the closed-loop $\hat{\sigma}_y = 0.0024$. Instead of using ρ as a design parameter, it is iterated until the specified performance is achieved. In Figure 5-7(a), both N (dashed line) and $1 - N$ (solid line) are shown. In this case, $1 - N$ is the probability of saturation, and as shown this quantity decreases as α_1 increases. If the actuator has a saturation level greater than 1.6, the desired closed-loop performance can be achieved without saturating the actuator.

Recall that u is the ideal control command, and v is the actual control signal acting on the system. The estimated $\hat{\sigma}_u$ (solid) and $\hat{\sigma}_v$ (dashed) are plotted in Figure 5-7(b). Under the stochastic linearization framework, v is approximated by Nu, so $\hat{\sigma}_v \approx N\hat{\sigma}_u$. In this figure the level of σ_v required to achieve the same closed-loop performance remains constant regardless of the saturation level. However, σ_u increases as saturation level decreases. Since the SLQR algorithm takes saturation nonlinearities into account during the gain design phase, it automatically adjusts control gain as a function of the predicted N, so that the net control input acting on the plant remains the same.

Combining the results of this example with the ρ variation analysis of the previous example, the tradeoff among performance, saturation level, and probability of saturation for this system may be summarized on a single plot. Figure 5-8 shows the contours of constant $1 - N$ (probability of saturation) as a function of the RMS output level σ_y and saturation level α. The heavy solid line in the plot represents the achievable performance limit for each actuator size. Below this line are unachievable combinations of performance and actuator size; above it, the contour lines show the degree of saturation necessary for a particular actuator size to maintain a target performance. Above the last contour line, actuators are essentially working in their linear regions to maintain the corresponding performance levels. Note that Figure 5-7(a) is essentially a "slice" through this contour plot, along a line parallel to the α axis at a height of $\hat{\sigma}_y = 2.4 \times 10^{-3}$.

Such a plot can be an important design aid when selecting an actuator. Given a target performance level, for example $\hat{\sigma}_y = 10^{-3}$, following a line parallel to the α axis shows that achieving this performance requires an actuator with at least 2.2 N maximum output, although this actuator will be saturating virtually 100% of the time. If the actuator can be selected to have 4 N maximum output, the 10^{-3} performance can be maintained with virtually no saturation. Alternately, for the 2 N actuator, if the performance requirement can be relaxed to closer to 2×10^{-3}, this actuator can provide that level of performance with again no saturation. Of course, different sized actuators will likely also have different bandwidths, complicating the tradeoff analysis, but this simple example suggests the utility of the SLQR analysis for automating certain aspects of a system design study.

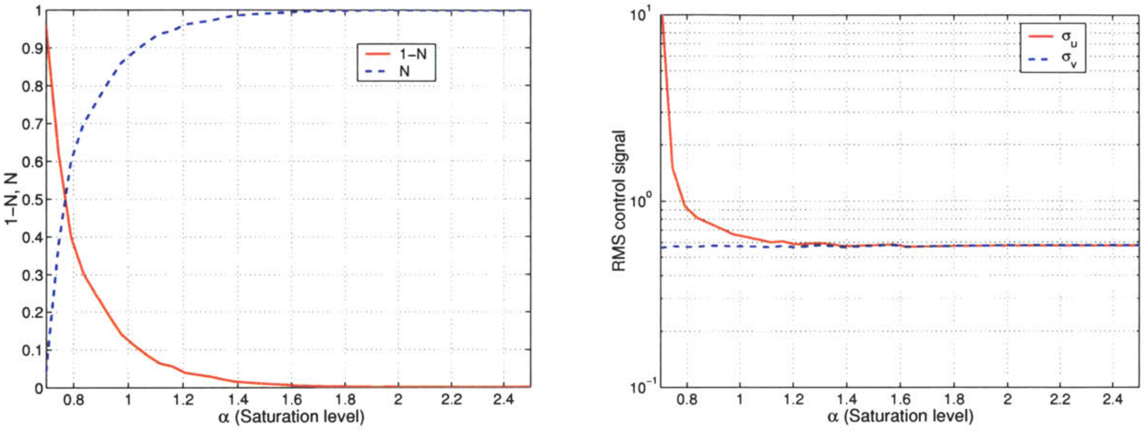

(a)

(b)

Figure 5-7: Saturation effects of a single actuator: (a) $1-N$ and N as functions of saturation level α (b) RMS control $\hat{\sigma}_u$ and $\hat{\sigma}_v$ as functions of saturation level α

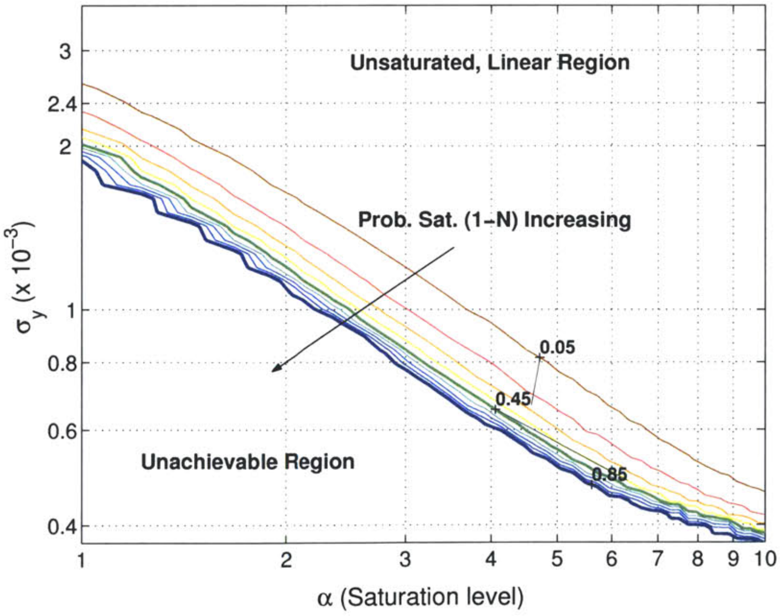

Figure 5-8: Contour plot of probability of saturation (1-N) as a function of performance and saturation level

Example 5.3 ***Effects of bandwidth***

In this example the effects of actuator bandwidth are studied. The single, spring-mass system is representative of a simple actuator model, assuming that the bandwidth is characterized by the natural frequency of the second order filter (ω_n), and the mass is the load on the actuator. For this case study, the control objective is again to reduce the open-loop RMS output deviations by a factor of 2 to $\hat{\sigma}_y = 2.4 \times 10^{-3}$. The saturation level chosen for this problem is 2.5, so that the nominal system is not affected by saturation effects. The probability of saturation $(1 - N)$ of the nominal system with a bandwidth at $\omega_n = 10$ Hz is approximately zero as illustrated in Figures 5-7(a) and 5-8

Figure 5-9(a) and Figure 5-9(b) show the probability of saturation and $\hat{\sigma}_u$ as functions of ω_n, respectively. Not surprisingly, as the bandwidth decreases, more control input is required in order to achieve the specified closed-loop performance. As this input increases, the actuator will become more likely to saturate, and thus, both σ_u and $1 - N$ increase as bandwidth decreases. Both curves asymptote to a limit around 2 Hz, which suggests that when the actuator bandwidth is lower than this level, the desired performance cannot be achieved with a 2.5 N actuator.

The limitation in achieving the desired performance is due to saturation effects. If there is no saturation limit, as the bandwidth decreases the actuator could maintain the necessary control authority over the motion of the mass by correspondingly increasing the magnitude of the inputs to the actuator. However, when saturation effects are present, there is an upper limit to the increased input which can be used to compensate for the decreased bandwidth, up to the "bang-bang" limit of the actuator, occurring when $1 - N$ approaches 1. Thus, the interaction between saturation level and actuator bandwidth also plays an important role in the multi-actuator problem, as the examples below will further demonstrate.

Example 5.4 ***Effects of resolution***

Resolution is another parameter that can affect the system performance in addition to saturation and bandwidth. To study resolution effects, saturation and bandwidth are fixed in the problem above as $\alpha = 2.5$ and $\omega_n = 10$ Hz. The objective of the closed-loop controller is to again attenuate the open-loop RMS output by a factor of two, corresponding to a closed-loop output standard deviation of about 2.4×10^{-3}.

Figure 5-10(a) shows N as a function of resolution level. Recall that the resolution level r indicates the width of the deadzone around the zero input level in the actuator response.

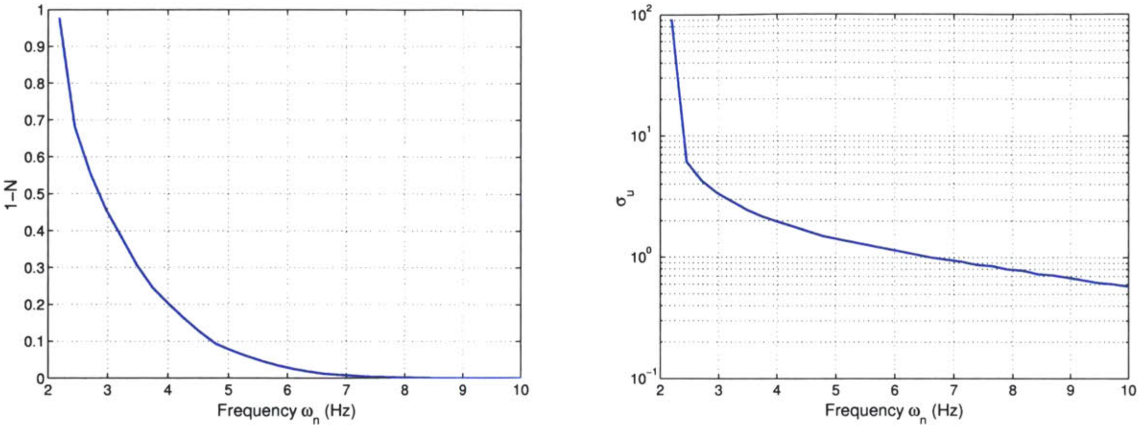

(a) (b)

Figure 5-9: Bandwidth effects of a single actuator: (a) $1 - N$ as a function of the actuator bandwidth (b) RMS control $\hat{\sigma}_u$ as a function of actuator bandwidth

When resolution is taken into account, $1 - N$ is no longer precisely the probability of saturation, at least for small $\hat{\sigma}_u$, but N is still a measure of the linearity of the system. When N is close to 1, the system operates almost linearly and $\phi(u) \approx u$. As $\hat{\sigma}_u$ decreases, however, N decreases, indicating that a larger fraction of the actuating signal lies in the resolution deadzone and hence transmits no force to the mass. Figure 5-10(a) illustrates that the parameter N decreases as the deadband size increases.

The amount of RMS control used to achieve the desired closed-loop performance is shown in Figure 5-10(b), and is seen to be a monotonically increasing function of deadzone size. As the deadzone size increases, a wider range of actuator inputs become ineffective in applying force to the system. Hence SLQR generates larger actuator inputs $\hat{\sigma}_u$ in order to meet the performance requirements. Physically, rather than "wasting" control effort (electrical power, etc) driving the actuator with input signals that produce no effect on the plant, the SLQR algorithm increases the actuator input to keep a sufficient fraction of the input above the deadzone level. This example also shows how the SLQR algorithm again automatically adjust the control gains to compensate for nonlinear characteristics of the actuator.

Note that the effects of resolution are negligible in this analysis if the deadzone size is less than about 10% of the saturation level ($r < 0.25$). Experimentation with similar examples suggests that this is a useful rule of thumb for system design, although it should

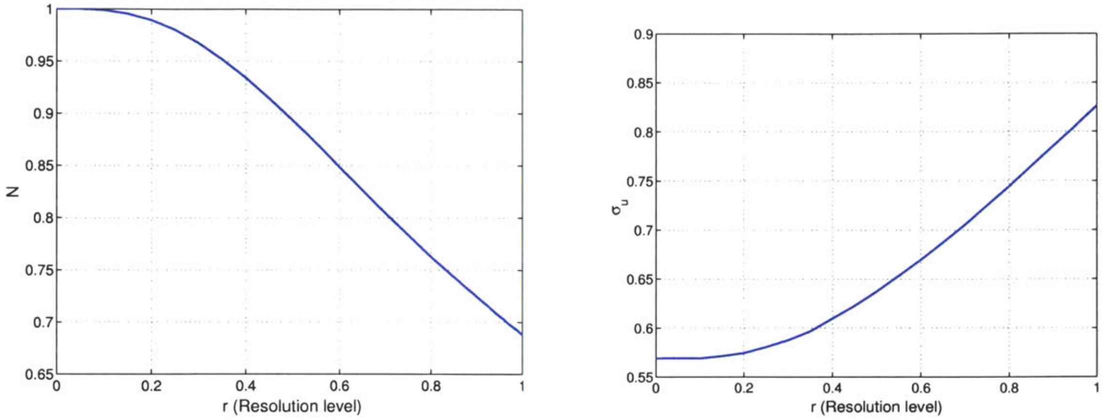

(a)

(b)

Figure 5-10: Resolution effects of a single actuator: (a) Gain N as a function of the resolution level (b) RMS control $\hat{\sigma}_u$ as a function of the resolution level

be checked formally using the above techniques for any particular application.

5.5.2 Two-actuator sample problem

This second set of example problems examines two actuators acting on a spring-mass system similar to the above plant, here taken to be critically damped with a natural frequency of 50 Hz. The dynamics of the overall system are the same as the "two-state, two-input" example problem used in Example 4.3. The disturbance spectrum is again modelled as a second order system ($F_d = 5$, $\zeta_w = 0.707$, $\omega_d = 10$ Hz), but in this example entering the plant at its output. Filters G_{a_1} and G_{a_2} capture the bandwidth of each of the two actuators, and are modelled here as damped second-order systems with natural frequencies $\omega_{a_1} = 2$ Hz, $\omega_{a_2} = 20$ Hz respectively. The saturation characteristics of each actuator were modelled; one actuator saturates at $\alpha_1 = 100$ and the other at $\alpha_2 = 5$. Resolution and quantization were not modelled in this example. The actuator characteristics above were selected to reflect a typical staged actuation system, with one high bandwidth actuator of limited force output, and a second lower bandwidth actuator with significantly more force output.

The controlled output of the system is again the position deviations of the mass. The magnitude of the open-loop linear transfer function from disturbance to output is plotted as a solid line in Figure 5-11. The transfer functions from actuator 1 and actuator 2 to

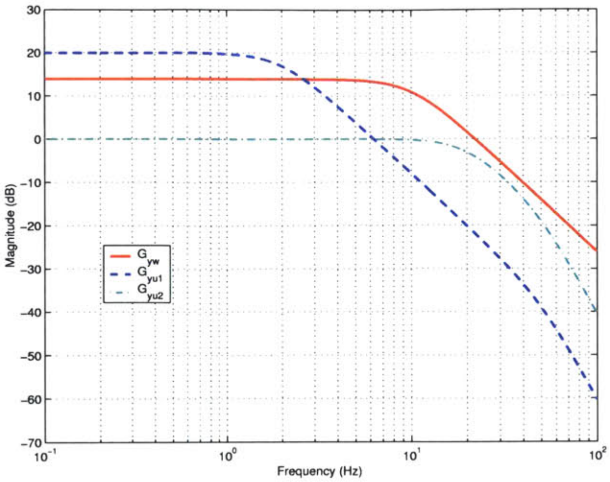

Figure 5-11: Linear open-loop transfer functions: from disturbance input to output (solid-line); from actuator 1 to output (dashed line); from actuator 2 to output (dashed-dotted line)

the output are illustrated as a dashed line and a dashed-dotted line, respectively, in this figure. Clearly the first actuator has more authority on output deviation at low frequencies, but it has a smaller bandwidth than the second actuator, and hence is much less effective at higher frequencies. At high frequencies, the second actuator has almost an order of magnitude greater authority over the motion of the mass than the first actuator.

The Bode diagrams suggest a natural "hand-off" frequency between the two actuators at around 6 Hz. Below this frequency, actuator 1 has more authority on the output, and above this frequency, actuator 2 has more authority. Without saturation limitations, of course, either actuator acting in isolation could bring the output RMS to below any desired level, simply by using sufficiently large feedback gains. However, with the assumed saturation properties, there is a limit to the output of each actuator, and hence the two actuators will have to collaborate in order to suppress broadband disturbances. This is the essence of a staged control system, and the examples below illustrate how SLQR helps to automate the design process for such a system.

Example 5.5 ***ρ variations***

Similar to the single actuator example, the overall weighting ρ on the control cost is varied over a large range to examine the behavior of the performance output $\hat{\sigma}_y$ and the control effort $\hat{\sigma}_u$ of each actuator. The relative control weightings ρ_1 and ρ_2 are set to

1 here to penalize the actuator usage equally. The closed-loop output variance $\hat{\sigma}_y^2$ using the SLQR control design is shown as a solid line in Figure 5-12(a), and it is an increasing function of control penalty ρ. The output variance asymptotes to about 100 in the cheap control limit due to saturation limitations. The dashed line in this figure illustrates the LQR variance prediction; since this prediction ignores saturation effects, the variance estimate can approach 0 as ρ decreases.

If the LQR control design were used in the system with saturation actuators, the stochastic Lyapunov or stochastic linearization (SL) technique may be used to predict the output performance of the closed-loop system. As presented in Section 5.2, this predicted performance is denoted by LQR+SL and is plotted as a dotted line in Figure 5-12(a). The LQR+SL output variance first decreases with ρ but starts to increase when ρ becomes less than 10^{-4}; increasing the control gain using the LQR design actually degrades the performance of the system. For this problem, it is interesting to note that there is no case where the LQR design out performs the SLQR design.

The probability of saturation of the SLQR and LQR+SL designs are shown in Figure 5-12(b) as solid and dotted lines, respectively. There are two curves for each control design, corresponding to the probability of saturation of each of the actuators. Clearly the LQR design is not aware that actuator 2 is in saturation for more than 90% of the time, and attempts to use it as much as possible. Since actuator 2 cannot deliver the authority commanded by the LQR design, the system performance (dotted line) is significantly different from the expected performance (dashed line) as shown in Figure 5-12(a).

One could argue that the LQR+SL performance can be improved by adjusting the relative actuator weighting ρ_i in the cost function, so actuator 2 does not operate near saturation for most of the time. Such a procedure can certainly be accomplished by having the control designer adjusting the actuator penalty at each design point and use the analysis tool developed here to determine if the probability of saturation is adequate for each actuator. In fact, the designer may use any technique, not just LQR, together with the analysis tool of Chapter 4 to synthesize the desired controller. However, it may be desirable to specify the relative control weightings in the cost function according to metrics such as the electrical power usage. If these weightings are varied as tuning knobs to find the desired performance, the resulting cost function does not retain the intended control cost metrics and becomes nonphysical.

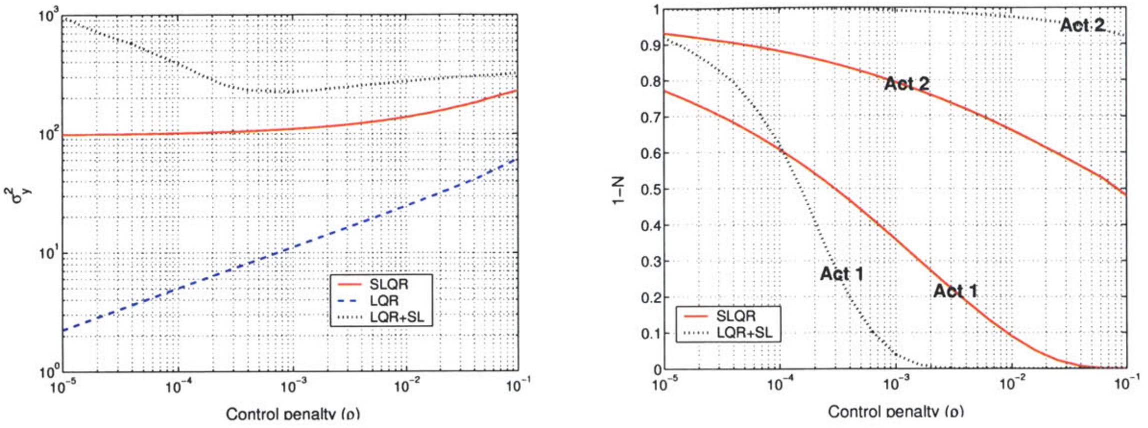

(a)

(b)

Figure 5-12: Two actuator example: (a) Output variance $\hat{\sigma}_y^2$ as a function of control penalty ρ. (b) RMS control input $\hat{\sigma}_u$ as a function of ρ

The SLQR technique suggested here is a desirable option to accomplish a large number of trade studies quickly and is capable of maintaining the relative control weightings in the cost function while searching for the desired solution. It takes disturbance and actuator properties into account, and thereby, systematically creating optimal staged controllers without the need of a designer to constantly tune the controller parameters. The utility of SLQR technique on multi-actuators are demonstrated in the following examples and applied to the pathlength control problems in the next chapter.

Example 5.6 ***Variations in saturation level 1***

In this example, SLQR is used to examine the effect of variations in the saturation level of actuator 1 is examined, with the saturation level of actuator 2 fixed at $\alpha_2 = 5$. The control objective here is to reduce the open-loop RMS output deviations by a factor of 2, resulting in a target closed-loop output standard deviation of about 12. The cost function places equal weight on each control variance, $\rho_1 = \rho_2$, and the overall control weight ρ is iterated until the desired closed-loop performance is obtained.

As the saturation level of actuator 1 increases, both actuators become less likely to saturate as shown in Figure 5-13(a) and (b). Actuator 1 almost never saturates when its saturation level is greater than 140. However, the probability of saturation for actuator 2 asymptotes to about 0.6 as α_1 increases. Since actuator 2 is more effective in the higher frequency region, it is less costly to work actuator 2 harder at those frequencies in order to

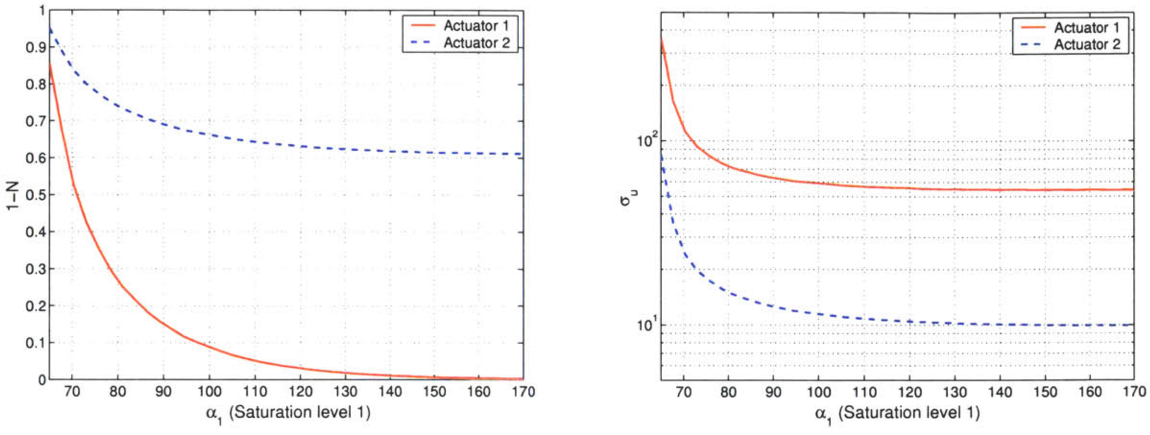

(a)

(b)

Figure 5-13: Saturation effects of actuator 1: (a) $1 - N$ as a function of saturation level α_1 (b) RMS control input $\hat{\sigma}_u$ as a function of saturation level α_1

attenuate high frequency disturbances.

Notice that the disturbance has appreciable energy in the high frequency region where actuator 2 has a factor of 10 greater authority over the motion of the mass than actuator 1. Suppressing the effects of the disturbance in this band would thus require approximately 50 N RMS input from actuator 1, as compared to the 5 N RMS or so used by actuator 2. Since the control variance terms are weighted equally in the cost function, SLQR opts to use the smaller actuator more, despite the fact that this puts the actuator into saturation a high percentage of the time. Relatively weighting the variance terms would be one way to alter this tradeoff; Section 5.6 will explore a more direct method of influencing the saturation levels of the ultimate design point if this is desired.

Finally, note that the saturation curves levels off after $\alpha_1 \approx 100$. Increasing the saturation level of the first actuator beyond this point will not cause much additional change in the saturation state of either actuator to maintain the target performance level. The nominal value of $\alpha_1 = 100$ will be used in the examples which follow.

Example 5.7 ***Variations in saturation level 2***

In this example, the saturation level of actuator 1 is fixed at 100, and the SLQR algorithm is used to examine the effects of decreasing the saturation level of actuator 2. Figure 5-14 shows that as the saturation level of actuator 2 decreases, the probability of saturation of both actuators increases. This result demonstrates that if the second actuator

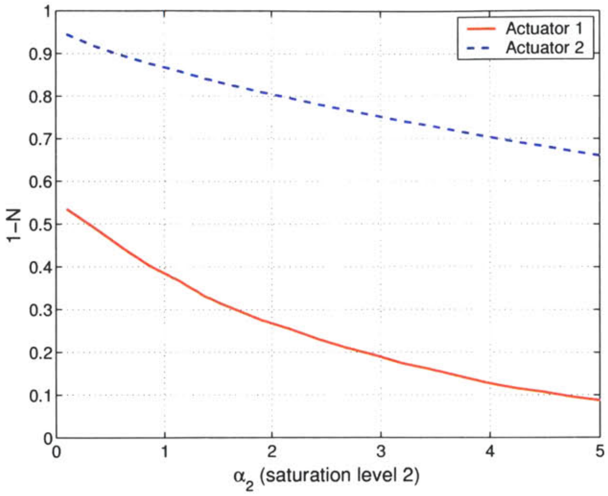

Figure 5-14: Saturation effects of actuator 2: $1 - N$ as a function of saturation level α_2

has smaller saturation level, the first actuator will have to work harder in order to meet the closed-loop performance requirements. In addition, the probability of saturation of actuator 1 increases more steeply as α_2 decreases than actuator 2, since it is not as effective at the high frequency region.

Example 5.8 ***Effects of bandwidth***

Another factor that may cause actuator 1 to work harder is a decrease in bandwidth of actuator 2. In this example, the bandwidth of actuator 2 is decreased from the nominal 20 Hz to the bandwidth of actuator 1 set at $\omega_{n1} = 2$ Hz. The saturation levels of both actuators are fixed at $\alpha_1 = 100$ and $\alpha_2 = 5$. The target closed-loop performance is to reduce the open-loop RMS output by half in each of the cases.

Figure 5-15(a) shows the probability of saturation, and Figure 5-15(b) shows the RMS control (σ_u) of both actuators as functions of ω_{n_2}. The solid and dashed lines show the responses for actuator 1 and actuator 2, respectively. As the bandwidth of actuator 2 decreases from the nominal 20 Hz, actuator 1 starts to work harder and becomes more likely to saturate in order to maintain the same level of performance. With less authority at higher frequencies, actuator 2 also has to work harder as its bandwidth decreases; however, the amount of change is not as drastic as actuator 1. In addition, when ω_{n_2} decreases below 6 Hz, actuator 2 is used less since it no longer has a bandwidth advantage over actuator 1. When both actuators have the same bandwidth, they each saturate about 55%-60% of the time.

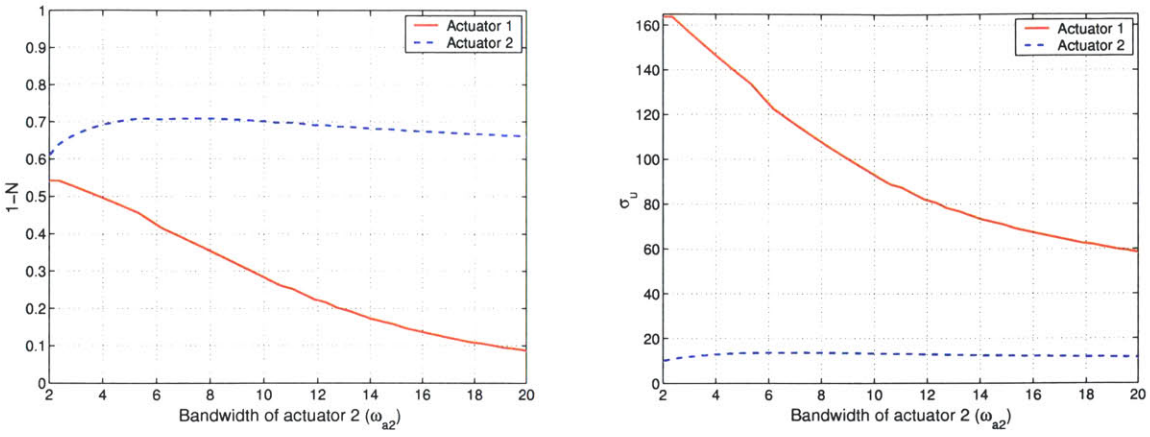

(a)

(b)

Figure 5-15: Bandwidth effects of actuator 2: (a) $1 - N$ as a function bandwidth ω_{a_2} (b) RMS control input $\hat{\sigma}_u$ as a function of bandwidth ω_{a_2}

Additional examples and tradeoff studies for multi-input systems will be conducted for space interferometer systems in Chapter 6. The following sections examine some useful additional extensions of the SLQR methodology.

5.6 Saturation Weighted SLQR

In addition to penalizing the RMS control input $\hat{\sigma}_u$, other cost metrics can also be added to the optimization problem introduced in Section 5.1. For example, another important metric on control effort is how frequently the actuator saturates. Due to mechanical fatigue or duty cycle limits, it may be desirable to limit the saturation of a subset of the actuators in a multi-input problem. Alternately, it may be desirable to saturate the actuators equally, so that one actuator does not fail due to mechanical or material failure before the other one.

In those cases where quantization effects are negligible as compared to the saturation effects, or when quantization can be modelled as additive noise, it is reasonable to model saturation as the only nonlinearity. In such a case, the linearization gain N provides an estimate of the probability of saturation ($P_{\text{sat}} = 1 - N$) of the actuator. In order to explicitly penalize the probability of saturation, it is possible to directly include this parameter in the cost function:

$$\begin{aligned} J(K) &= \hat{\sigma}_y^2 + \rho \sum_{i=1}^{n_u} \rho_i \hat{\sigma}_{u_i}^2 + \sum_{i=1}^{n_u} \upsilon_i \left[1 - N_{ii}(\hat{\sigma}_u)\right] \\ &= \mathrm{tr}\left\{C_1 \hat{\Sigma}_{xx} C_1^T\right\} + \mathrm{tr}\left\{D_{12} K \hat{\Sigma}_{xx} K^T D_{12}^T\right\} + \sum_{i=1}^{n_u} \upsilon_i \underbrace{(1 - N_{ii})}_{P_{\mathrm{sat},i}}, \end{aligned}$$

where υ_i adjusts the penalty on the probability of saturation of the i$^{\text{th}}$ actuator, and $D_{12}^T D_{12}$ is again a diagonal matrix with elements $\rho\rho_i$ that penalize control usage. The optimization problem is again formulated as

$$K = \arg\min_K J(K) \tag{5.20}$$

with constraints given by Equations 5.3 and 5.9. The Lagrangian is formed by extending Equation 5.10 to incorporate probability of saturation parameters,

$$\begin{aligned} \Psi &= \mathrm{tr}\left\{C_1 R C_1^T\right\} + \mathrm{tr}\left\{D_{12} K R K^T D_{12}^T\right\} + \sum_{i=1}^{n_u} \upsilon_i (1 - N_{ii}) \\ &+ \mathrm{tr}\left\{[(A + B_2 N K)\hat{\Sigma}_{xx} + \hat{\Sigma}_{xx}(A + B_2 N K)^T + B_1 B_1^T] Q\right\} \\ &+ \sum_{i=1}^{n_u} \lambda_i (Y_i K R K^T Y_i^T - g_i^2(N_{ii})), \end{aligned} \tag{5.21}$$

where Q and λ_i are the Lagrange multipliers associated with the constraint equations.

Taking the first partial derivative of Ψ with respect K, N_{ii}, Q, $\hat{\Sigma}_{xx}$, and λ_i and setting them equal to zero, a set of nonlinear algebraic equations is obtained:

$$K = -\Phi^{-1} N B_2^T Q \tag{5.22}$$

$$\lambda_i + \frac{0.5\upsilon_i N_{ii} + \rho\rho_i g_i^2(N_{ii})}{g_i^2(N_{ii}) + N_{ii} g_i(N_{ii}) g_i'(N_{ii})} = 0 \tag{5.23}$$

$$A^T Q + Q A - Q B_2 N \Phi^{-1} N^T B_2^T Q + C_1^T C_1 = 0 \tag{5.24}$$

$$(A + B_2 N K)\hat{\Sigma}_{xx} + \hat{\Sigma}_{xx}(A + B_2 N K)^T + B_1 B_1^T = 0 \tag{5.25}$$

$$Y_i K R K^T Y_i^T - g_i^2(N_{ii}) = 0 \tag{5.26}$$

The derivation of these equations is shown in Appendix A. This set of equations is similar to the ones obtained in Section 5.3. The only significant difference is Equation 5.23 that describes the coupling between λ_i and N_{ii}. The same numerical algorithm described in Section 5.4 can be used to find the solutions to the above equations.

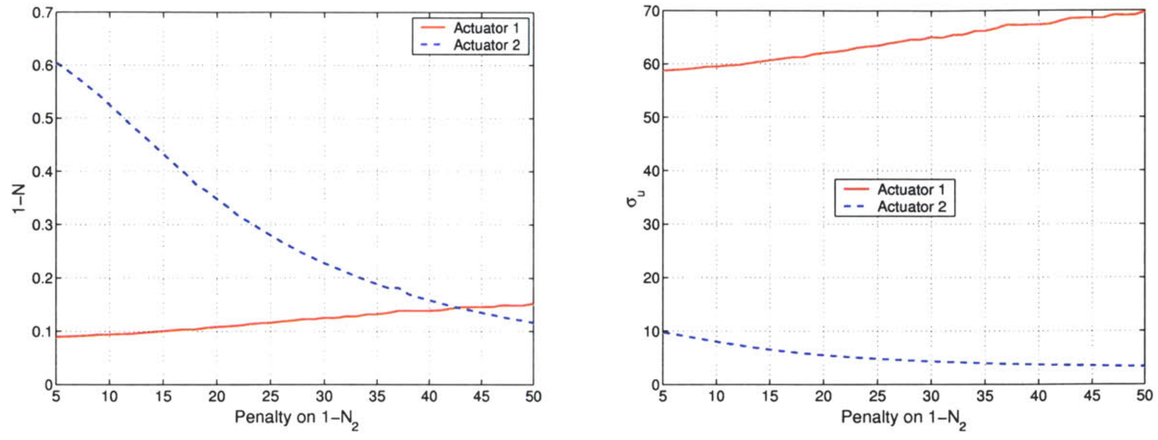

(a)

(b)

Figure 5-16: Effect of penalty on probability of saturation of actuator 2 (a) $1 - N$ as a function of υ_2 (b) RMS control input $\hat{\sigma}_u$ of each actuator as a function of υ_2

To illustrate the utility of this modification, consider the two-actuator problem presented in the previous section. The same plant, disturbance, and actuator dynamics models are used, with the saturation levels set at $\alpha_1 = 100$ and $\alpha_2 = 5$. Recall that for these saturation levels, the probabilities of saturation found in the previous example are $1 - N_1 = 0.09$ and $1 - N_2 = 0.66$. The controller design is iterated on ρ to achieve the same closed-loop RMS performance σ_y as above.

The only variable in this case is the additional penalty on the probability of saturation. The penalty on $1 - N_1$, υ_1, is fixed at 1, and the penalty on $1 - N_2$, υ_2, is varied over a range. Figure 5-16(a) shows the $1 - N$ curve for each actuator as a function of υ_2; the solid line and dashed line represent actuator 1 and 2, respectively. As the penalty on $1 - N_2$ increases, the probability of saturation of actuator 2 decreases, which is the expected result. It is interesting to note that by saturating actuator 1 slightly more, the probability of saturation on the second actuator can be greatly reduced while maintaining the same closed-loop performance. Since actuator 1 has much larger maximum force output, increasing its probability of saturation slightly allows a dramatic reduction in the probability of saturation of actuator 2.

5.7 Output Feedback Designs

The above analysis assumes that the entire state vector x is available for feedback in the closed-loop system. This is almost never the case in practice, since it is often not possible to measure all the states in the system, and certainly the disturbance states in the innovations filter are fictitious and cannot be measured. As a result, the above technique must be extended to utilize only output feedback. The extension to output feedback from the SLQR control design for a single saturating actuator has been presented by Gökçek [21]. As with the basic SLQR technique above, the output feedback results are extended in this section to incorporate multiple actuators and more general actuator nonlinearities.

The general system dynamics can be summarized as

$$\begin{aligned} \dot{x} &= Ax + B_1 w_1 + B_2 \phi(u) \\ z &= \begin{bmatrix} C_1 \\ 0 \end{bmatrix} x + \begin{bmatrix} 0 \\ D_{12} \end{bmatrix} u \\ y_m &= C_2 x + D_{21} w_2 \end{aligned} \tag{5.27}$$

where z is the performance variable that contains the controlled output, $y = C_1 x$, and the control penalty, $D_{12}u$. The measurement output is denoted by y_m. The state disturbance is w_1, and the measurement noise is w_2, assumed to be uncorrelated, zero mean, unit-intensity white noise processes. The intensity of w_1 and w_2 can be changed by changing the values of matrices B_1 and D_{21}, respectively.

A general form of an output feedback controller for this system is [91]

$$\dot{x}_c = A_c x_c - B_c y_m \tag{5.28}$$

$$u = K x_c \tag{5.29}$$

The objective is to find a control design (A_c, B_c, K) that minimizes the cost:

$$\begin{aligned} J(K) &= \hat{\sigma}_y^2 + \rho \sum_{i=1}^{n_u} \rho_i \hat{\sigma}_{u_i}^2 \\ &= \operatorname{tr}\left\{ C_1 \hat{\Sigma}_{xx} C_1^T \right\} + \operatorname{tr}\left\{ D_{12} K \hat{\Sigma}_{x_c x_c} K^T D_{12}^T \right\}. \end{aligned} \tag{5.30}$$

The derivation in Appendix B shows that the optimal controller is given by

$$A_c = A + B_2 N K + B_c C_2 \tag{5.31}$$

$$\begin{aligned} B_c &= -PC_2^T(D_{21}D_{21}^T)^{-1} && (5.32) \\ K &= -\Phi^{-1}NB_2^TQ, && (5.33) \end{aligned}$$

where $N_{ii} = f(\hat{\sigma}_{u_i})$, $\Phi = D_{12}^TD_{12} + \Lambda$, and (N, P, Q, R, S, Λ) are solutions to the following nonlinear set of equations,

$$\lambda_i + \frac{\rho\rho_i g_i(N_{ii})}{g_i(N_{ii}) + N_{ii}g_i'(N_{ii})} = 0 \tag{5.34}$$

$$AP + PA^T - PC_2^T(D_{21}D_{21}^T)^{-1}C_2P + B_1B_1^T = 0 \tag{5.35}$$

$$A^TQ + QA - QB_2N\Phi^{-1}NB_2^TQ + C_1^TC_1 = 0 \tag{5.36}$$

$$(A + B_2NK)R + R(A + B_2NK)^T + PC_2^T(D_{21}D_{21}^T)^{-1}C_2P = 0 \tag{5.37}$$

$$(A + B_cC_2)^TS + S(A + B_cC_2) + QB_2N\Phi^{-1}NB_2^TQ = 0 \tag{5.38}$$

$$Y_iKRK^TY_i^T - (g_i(N_{ii}))^2 = 0 \tag{5.39}$$

which again represent a coupled set of nonlinear equations which must be solved simultaneously. A numerical algorithm for accomplishing this is discussed in the next section. Due to the similarity of the above control design and the standard LQG problem, the solution of the above optimization problem is referred to as the SLQG control design.

5.7.1 Numerical solution procedure for SLQG

Comparing the SLQR and SLQG problem, there are two additional equations that must be solved in the SLQG design. Numerical algorithms similar to that used in Section 5.4 can be extended to solve the above nonlinear equations.

1. Discretize the possible solutions N_{ii} into a set of grid points between 0 and 1.
2. For each point in the grid form a trial solution $\tilde{N}$.
3. Compute the diagonal elements of Λ for each $\tilde{N}$ using Equation 5.34.

   $$\lambda_i + \frac{\rho\rho_i\, g_i(\tilde{N}_{ii})}{g_i(\tilde{N}_{ii}) + \tilde{N}_{ii}g_i'(\tilde{N}_{ii})} = 0$$

4. Solve the "control" Riccati equation given by Equation 5.36 at each grid point.

   $$A^TQ + QA - QB_2\tilde{N}\Phi^{-1}\tilde{N}B_2^TQ + C_1^TC_1 = 0,$$

   where $\Phi = (\Lambda + D_{12}^TD_{12})$.

5. Find the optimal controller gain K at each grid point as defined by Equation 5.33
$$K = -\Phi^{-1}\tilde{N}B_2^T Q.$$
6. Solve the "observer" Riccati equation given by Equation 5.35
$$AP + PA^T - PC_2^T(D_{21}D_{21}^T)^{-1}C_2P + B_1B_1^T = 0$$
7. Find the optimal observer gain B_c (Equation 5.32)
$$B_c = -PC_2^T(D_{21}D_{21}^T)^{-1}$$
8. Solve the closed-loop Lyapunov equation (Equation 5.37)
$$(A + B_2\tilde{N}K)R + R(A + B_2\tilde{N}K)^T + PC_2^T(D_{21}D_{21}^T)^{-1}C_2P = 0$$
9. Check the consistency constraint from Equation 5.39
$$Y_iKRK^TY_i^T - (g_i(\tilde{N}_{ii}))^2 = \delta_i,$$
where δ_i is the i^{th} component of the vector δ, which has a length equal to the number of actuators.
10. Compute the 2-norm of δ for each grid point and determine which grid point has the minimum δ.
11. Refine the grid point with minimum δ into finer grid points and repeat items 2-10 until δ is less than a specified tolerance.

5.7.2 Numerical example

The two-actuator sample problem presented in Section 5.5.2 is used again here to illustrate the SLQG algorithm. The intensity of the noise measurement is taken as $\mu I = D_{21}D_{21}^T$, where μ will be a variable parameter. The actuator saturation levels are taken to be $\alpha_1 = 100$ and $\alpha_2 = 5$.

Figure 5-17(a) shows the RMS output $\hat{\sigma}_y$ as a function of control penalty ρ. Three different curves are shown corresponding to different values of the noise intensity μ. The SLQR solution obtained above is also plotted on this figure (solid line) for comparison. More importantly, notice that the achievable performance is an increasing function of μ. Starting from the SLQR limit, increasing levels of noise in the sensor measurements result in progressively larger minimum output variance.

Figure 5-17(b) and Figure 5-17(c) show the probability of saturation $1 - N$ and RMS control σ_u, respectively. These values do not change much with the noise intensity levels considered, since the noise intensity is small compared to the intensity of the disturbance.

Notice that the SLQG solutions converge toward the SLQR solutions as the measurement noise μ is decreased. If the noise intensity is small compared to other disturbances in the system, the RMS output jitter, N, and RMS control input will be very similar to the results obtained in the SLQR case. This situation is likely to occur for the space interferometer mission, since laser metrology with accuracy on the order of sub-nanometers will be used to measure the position changes of various optical devices. For such a system, the SLQR solution is sufficiently accurate for carrying out preliminary design tradeoffs.

5.8 Summary

This chapter has presented one possible synthesis technique for staged control systems. The proposed controller design attempts to meet the target performance objectives while minimizing the mechanical or electrical control power required. Unlike classical $\mathcal{H}_2$ algorithms, the current design takes actuator nonlinearities into account by using the analytical prediction tool developed in the previous chapter. Several examples are shown in this chapter in order to demonstrate the utility of the proposed control design framework. Some important findings from these examples are summarized here:

- Saturation and bandwidth limit the achievable performance of the system. For a given set of actuators, SLQR can accurately predict what the performance limit will be in the cheap control limit, and can thus assist in actuator selection at the system design level.

- Ignoring saturation nonlinearity at design time, or simply allowing a classical LQR controller to saturate in general may produce significantly worse performance than the controller provided by SLQR. The performance predicted by LQR diverges sharply from the actual nonlinear performance when the actuator operates in its nonlinear region. LQR designs may be serially followed by a stochastic linearization analysis of the closed-loop performance, but such a design may not guarantee that $A + B_2NK$ is Hurwitz. It can also be difficult to tune the design for required performance in the multi-input case. By coupling the control design and prediction analysis together, the SLQR algorithm avoids these difficulties.

- For actuators in which the dominant nonlinearity is saturation, the parameter N_{ii}, computed as part of the SLQR optimization process, predicts the saturation state of the actuator during closed-loop operation $p_{sat}(u_i) = 1 - N_{ii}$. This parameter can be tuned directly by using the saturation weighted SLQR extension.

- Saturation level and bandwidth of each actuator play an important role in the multi-actuator control design problem. There exists a natural frequency "hand-off" between the stronger/slower and weaker/faster types of actuators, determined by the relative bandwidths and saturations. The control techniques proposed in this chapter can automatically determine this hand-off, balancing the capabilities of each actuator against the disturbance spectrum to meet the performance target.

With the insight developed from the relatively simple examples above, Chapter 6 will explore how the controller design strategy discussed in this chapter can be employed for space interferometry applications.

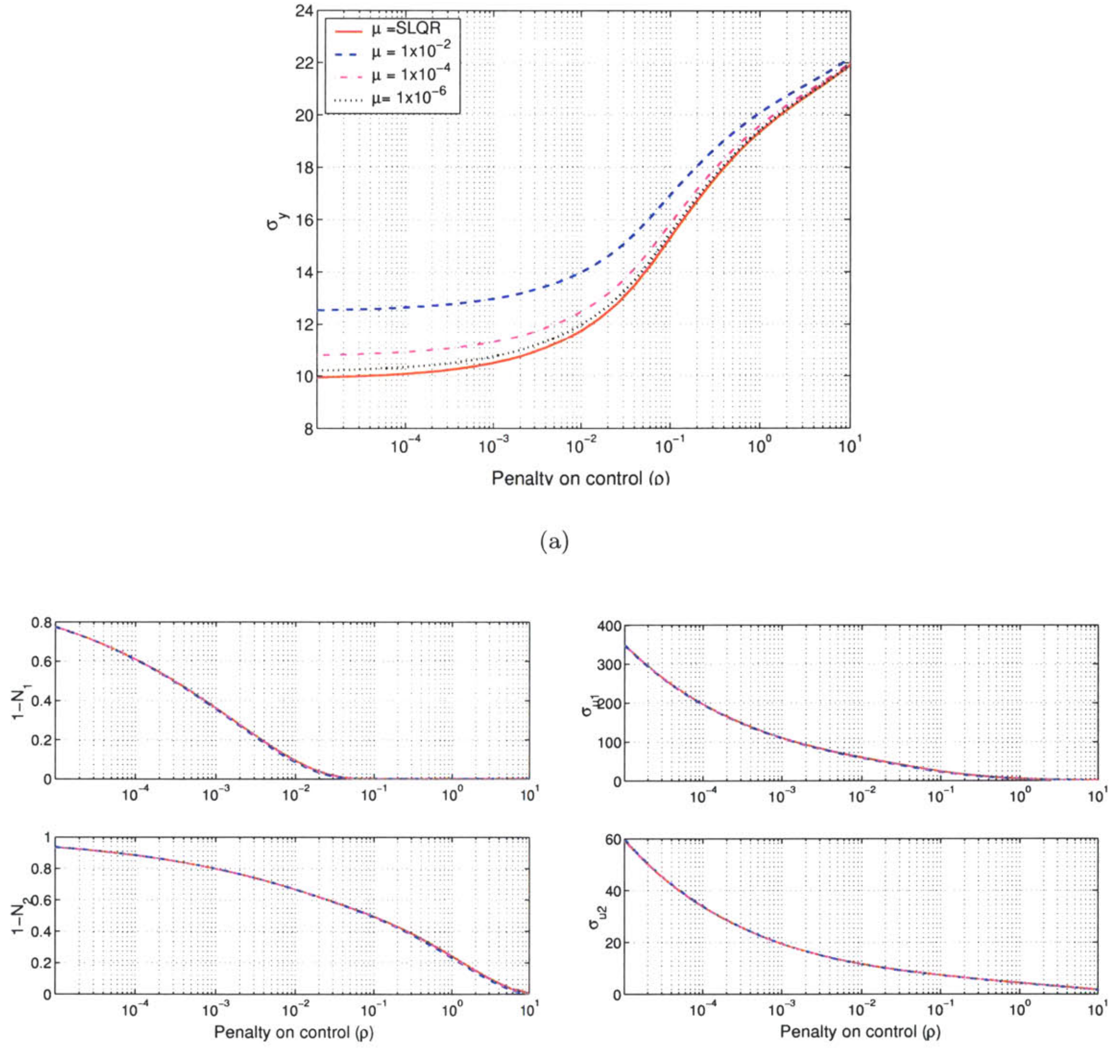

(a)

(b)

(c)

Figure 5-17: SLQG sample problem: (a) Controlled output as a function of ρ (b) Probability of saturation of each actuator as a function of ρ (c) RMS control input as a function of ρ

Chapter 6

Staging Control of Optical Pathlength

The goal of the controller designs examined in this chapter is to achieve the 3nm optical path difference (OPD) stabilization determined in Chapter 2 for accurate extra-solar planet detection, while minimizing the total required mechanical or electrical power supplied by the actuators. As discussed in Chapter 3, no single actuator can provide the combination of stroke and bandwidth needed to accomplish this task in the expected disturbance environment, and therefore, a staged actuation system with multiple actuators of overlapping stroke and bandwidth will be employed to stabilize the optics of space based interferometer missions. This chapter uses the SLQR framework developed in Chapters 4 and 5 to suggest a simplified design process for determining controllers with the required stabilization properties.

The intention here is also to offer a possible alternative to the more classical, loop-shaping designs commonly used for ODL control [23, 27, 46], and to analytically quantify some of the design and performance tradeoffs inherent in such systems. One of the major drawbacks of the previous ODL control designs is the effort required to shape the input-output transfer function loop, since the control parameter tuning process can be difficult and time consuming. The control algorithm proposed in the previous chapter offers a methodology that automatically synthesizes a controller, as a consequence of optimizing the performance metric, and does not require additional tuning on the control parameters. In addition, this framework also indirectly quantifies and controls the expected saturation level in order to enforce lifetime limits on actuators. Loop-shaping techniques can only estimate the saturation state of the actuators through exhaustive numerical simulations.

The system models used for the pathlength control benchmark problems considered in this chapter are presented in Section 6.1. Controller designs for a two-stage optical delay line (ODL) are discussed first in Section 6.2, with numerous examples and trade studies. These designs attempt to minimize the total mechanical energy used by the actuators. Section 6.3 re-examines the two-stage problem using instead electrical energy in the cost function, and illustrates how the saturation weighting discussed in Chapter 5 can be employed to further shape the resulting designs. Finally the design and analysis framework is extended to a three-actuator system, using thruster control of the spacecraft relative position as the third stage.

6.1 System Models

A typical ODL consists of a three-staged system: a D. C. servomotor, a voice coil, and a piezoelectric actuator (PZT) [23, 46, 27]. A common reference design is shown in Figure 6-1 which consists of an optical assembly cage, or "Cat's eye", sitting on a trolley moved by the motor. Flexures between the trolley platform and the cage are used to partially isolate the cage from motor induced vibrations. The voice coil is used to move the cage or the primary mirror position against the trolley, while the PZT changes the position of the secondary mirror. Often, there is an opposing ("reactuated") PZT stack on the secondary mirror designed to partially decouple PZT and voice coil inputs and to attenuate the impact of high frequency disturbance on the cages. The entire assembly is mounted inside the spacecraft during an interferometry mission.

The VC and PZT constitute two layers of "fine" control over the OPD via the corresponding small changes they make in the relative positions of the mirrors. The DC motor is used for coarser control, compensating for larger (centimeter or greater) offsets in the relative positions of the spacecraft, and for achieving initial "fringe lock" acquisition of the observation target. The most common scenario uses the motor to achieve the initial lock, then the motor position is fixed and the OPD stabilized by the voice coil and PZT during the observation mode.

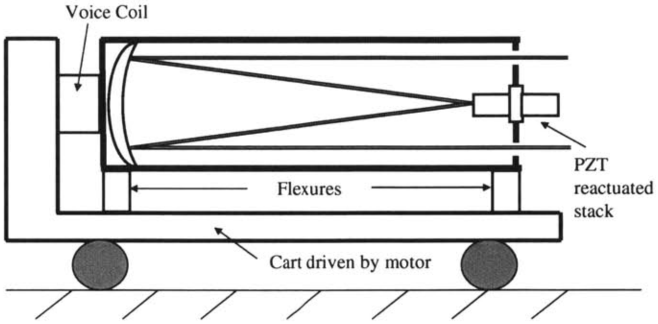

Figure 6-1: Generic Optical Delay Line Diagram [23, 27]

6.1.1 Two-stage Design: Fixed ODL

The preliminary controller development will be directed towards the benchmark problem shown in Figure 6-2, which captures many interesting aspects of ODL dynamics. In this model the relative positions of the spacecraft are assumed approximately constant, and the trolley carrying the optics is held fixed in place at a distance along the track which removes most of the coarse OPD. The OPD is then stabilized against residual small path length variations by continuous adjustment of the voice coil and the PZT. This is the usual operating configuration for a space interferometry system during its observation mode.

In the lumped-mass model of this situation shown in Figure 6-2, M_1 is the total cage mass including the primary mirror and PZT masses. This mass is much larger than the flat secondary mirror mass M_2. The first (K_1) and second (K_2) spring stiffnesses represent the case-trolley flexure and PZT stiffness, respectively. The voice coil is the first stage actuator (u_1), which pushes against the cage and the primary mirror in order to change the optical pathlength by varying the positions of the Cat's eye assembly relative to the cart. Fine stage control is provided by the PZT (u_2); there is an equal and opposite PZT stack pushing against the carriage to reduce the coupling to the motion of the Cat's eye.

A physical model for this system is developed from Lagrangian dynamics [9] as

$$M\ddot{q} + C\dot{q} + Kq = Fu + Gw, \tag{6.1}$$

$$M = \begin{bmatrix} M_1 & 0 & 0 \\ 0 & m_2 & 0 \\ 0 & 0 & m_2 \end{bmatrix} \quad C = \begin{bmatrix} c_1 + 2c_2 & -c_2 & -c_2 \\ -c_2 & c_2 & 0 \\ -c_2 & 0 & c_2 \end{bmatrix} \quad K = \begin{bmatrix} k_1 + 2k_2 & -k_2 & -k_2 \\ -k_2 & k_2 & 0 \\ -k_2 & 0 & k_2 \end{bmatrix}$$

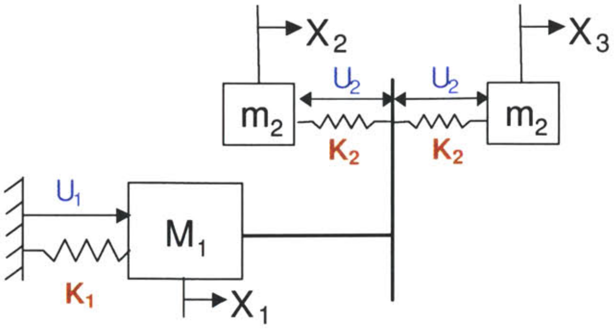

Figure 6-2: Two-stage benchmark problem (M_1 = 1Kg, M_2 = 5g, K_1 = 1250 N/m, $K_2 = 1 \times 10^6$ N/m)

$$F = \begin{bmatrix} 1 & 0 \\ 0 & -1 \\ 0 & 1 \end{bmatrix} \quad G = \begin{bmatrix} 1 \\ 0 \\ 0 \end{bmatrix}$$

where $q = [x_1,\ x_2,\ x_1]^T$ is the state vector, $u = [u_1,\ u_2]^T$ is the control input vector, w is the disturbance input, model here as an input disturbance entering the plant in the same manner as the voice coil. This is used to model vibrations transmitted through the spacecraft structure to the trolley and ultimately to the Cat's eye. The damping matrix C consists of VC and PZT damping coefficients (c_1, c_2), and the stiffness matrix K consists of flexure stiffness and PZT material stiffness (k_1, k_2). The physical parameters of the ODL model and stroke ranges of these actuators are selected to be representative of those delay lines currently being studied at the NASA Jet Propulsion Laboratory (JPL) [23, 27], which corresponds to approximately $M_1 = 1$ Kg, $m_2 = 5$ g, $k_1 = 1250$ N/m, $k_2 = 1 \times 10^6$ N/m, $c_1 = 1.41$ N/m/s, and $c_2 = 77.8$ N/m/s. With these parameters, the voice coil has a maximum stroke of ±1.5 mm – that is, the maximum deflection from the voice coil will not exceed ±1.5 mm. Similarly, the PZT has a maximum travel of ±10 μm with an equivalent force limit of ±2 N.

6.1.2 Three-stage design: ODL and Spacecraft

Traditional spacecraft designs use gas jet thrusters for adjusting their relative position and attitude, however these actuators introduce large vibrations into the onboard optics. As a result, most interferometry missions are planned to make observations while the spacecraft thruster system is disengaged. Essentially, the spacecraft will be maneuvered into the correct positions, then allowed to "drift" uncontrolled while the observations are made.

The gentle force applied by the new FEEP thrusters, discussed in Chapter 3, offers the possibility of continuing to control the spacecraft relative positions even while observations are occurring, potentially coupling the spacecraft rigid body controller directly to the optical stabilization loop. With such a coupling, the DC motor driven trolley could be omitted from the ODL design, since the spacecraft could be gently moved back and forth by the thrusters directly to achieve the initial fringe lock and to adjust OPD. As a result, micro-Newton thrusters like FEEPs are actively being considered as the 3^{rd} stage to the interferometer path length control system, replacing the role of the motor stage [65]. Since thrusters are already needed for rigid-body control, it can simplify the overall mechanical design, and moreover will potentially allow near-continuous observations as opposed to the burn-and-drift strategies currently proposed. The three-stage designs considered in this section will examine this configuration.

In order to capture the rigid body dynamics of the spacecraft and its thrusters, an additional stage is added to the two-stage benchmark problem. The three-stage benchmark problem has the structure illustrated in Figure 6-3. The dynamic equation of this system has the same form as Equation 6.1 with the matrices now given by

$$M = \begin{bmatrix} M_t & 0 & 0 & 0 \\ 0 & M_1 & 0 & 0 \\ 0 & 0 & m_2 & 0 \\ 0 & 0 & 0 & m_2 \end{bmatrix} \quad C = \begin{bmatrix} c_1 & -c_1 & 0 & 0 \\ -c_1 & c_1 + 2c_2 & -c_2 & -c_2 \\ 0 & -c_2 & c_2 & 0 \\ 0 & -c_2 & 0 & c_2 \end{bmatrix}$$

$$K = \begin{bmatrix} k_1 & -k_1 & 0 & 0 \\ -k_1 & k_1 + 2k_2 & -k_2 & -k_2 \\ 0 & -k_2 & k_2 & 0 \\ 0 & -k_2 & 0 & k_2 \end{bmatrix} \quad F = \begin{bmatrix} 1 & -1 & 0 \\ 0 & 1 & 0 \\ 0 & 0 & -1 \\ 0 & 0 & 1 \end{bmatrix}$$

where the state vector is augmented to $q = [x_t, x_1, x_2, x_3]$. The stiffness and damping coefficients will be those defined previously for the two-stage system, and the anticipated spacecraft mass for the TPF mission is approximately $M_t = 500$ Kg [2].

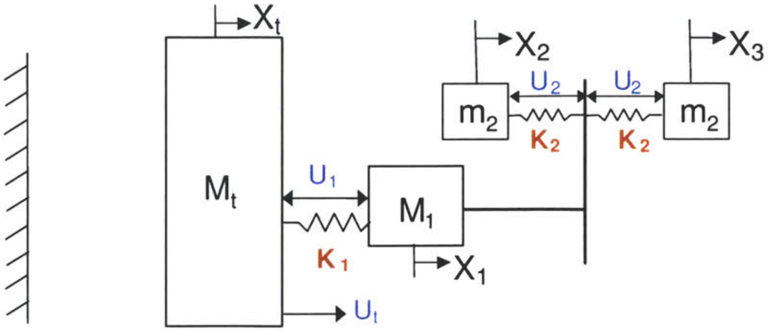

Figure 6-3: Three-stage benchmark problem

6.1.3 Model Scaling

Before forming the state-space model of the overall system for either of the above models, it is important to note that the states and input-output parameters span a large numerical range. For example, the maximum displacement of VC is around 10^{-3} m, the maximum displacement of PZT is on the order of 10^{-6} m, and the desired performance is on the nanometer level, 10^{-9} m. Severe numerical problems exist when solving the Riccati equations or Lyapunov equations for such ill-conditioned systems. In order to preserve precision in numerical computations, the system state, input, and output units should be normalized with care to improve the numerical conditioning of the problem. The methodology suggested below is an adaptation of that discussed in [63].

First, the states of interest for OPD stabilization are actually the relative displacements of the VC and PZT actuators. To reflect this interest, a state transformation matrix is introduced to change the inertial referenced states to relative actuator displacements,

$$\tilde{q} = \begin{bmatrix} 1 & 0 & 0 & 0 \\ -1 & 1 & 0 & 0 \\ 0 & 1 & -1 & 0 \\ 0 & -1 & 0 & 1 \end{bmatrix} \begin{bmatrix} x_t \\ x_1 \\ x_2 \\ x_3 \end{bmatrix}.$$

and hence, inverting the transformation matrix

$$q = T_s\tilde{q} = \begin{bmatrix} 1 & 0 & 0 & 0 \\ 1 & 1 & 0 & 0 \\ 1 & 1 & -1 & 0 \\ 1 & 1 & 0 & 1 \end{bmatrix} \tilde{q}. \tag{6.2}$$

Now the relative displacements can be normalized by the maximum stroke of each actuator:

$$\tilde{q} = U_s\bar{q} \tag{6.3}$$

where U_s is a diagonal, state normalization matrix, whose diagonal elements are the maximum stroke of each actuator, e.g. $\tilde{q}_{t_{max}}$, $\tilde{q}_{1_{max}}$, $\tilde{q}_{2_{max}} = \tilde{q}_{3_{max}}$. In the thruster case, there is no theoretical limit on the stroke range, so its maximum stroke is approximated as the largest anticipated position change of the spacecraft during observation.

Similarly the inputs can also be normalized by their maximum possible values,

$$F = T_f\bar{F}, \tag{6.4}$$

where T_f is the input normalization matrix with diagonal elements given by the maximum available force output of each actuator.

Applying the normalization factors to the equation of motion, the final normalized equation has the form

$$MT_sU_s\ddot{\bar{q}} + CT_sU_s\dot{\bar{q}} + KT_sU_s\bar{q} = T_fF,$$

and can be written as

$$\bar{M}\ddot{\bar{q}} + \bar{C}\dot{\bar{q}} + \bar{K}\bar{q} = \bar{F},$$

using the substitution $\bar{M} = MT_sU_s$, $\bar{C} = CT_sU_s$, $\bar{K} = KT_sU_s$, and $\bar{F} = T_fF$. The corresponding state-space model (A_p,B_p,C_p,D_p) of the plant dynamics are described as

$$A_p = \begin{bmatrix} 0 & I \\ -\bar{M}^{-1}\bar{K} & -\bar{M}^{-1}\bar{C} \end{bmatrix} \quad B_p = \begin{bmatrix} 0 \\ \bar{M}^{-1}\bar{F} \end{bmatrix}$$

$$C_p = 2\begin{bmatrix} \tilde{q}_{t_{max}} & \tilde{q}_{1_{max}} & -\tilde{q}_{2_{max}} & 0 & \cdots & 0 \end{bmatrix} \quad D_p = \begin{bmatrix} 0 & 0 \end{bmatrix}$$

The state vector in this model is chosen to represent the relative displacements of the PZT and voice coil actuators, and the absolute displacement of the spacecraft. The output of the plant corresponds to the OPD for the interferometer. The vector C_p includes the maximum stroke of each actuator in order to recover the true relative displacement from the state normalization. The factor of two in C_p comes from the fact that a unit position change in the mirror positions would cause two units of change in total OPD.

After combining the plant dynamics with disturbance and actuator dynamics, the integrated model can be expressed by the familiar SDE:

$$\begin{aligned} dx &= Ax\,dt + B_1\,dw + B_2\phi(u)\,dt \\ z &= \begin{bmatrix} C_1x \\ D_{12}u \end{bmatrix}, \end{aligned}$$

where $y = C_1x$ is the performance output or the deviation of OPD. This output can also be normalized by the desired OPD RMS performance level,

$$y = Z_{opd}\bar{y}, \tag{6.5}$$

so that

$$z = \begin{bmatrix} Z_{opd}^{-1}C_1x \\ D_{12}u, \end{bmatrix}$$

and the system output becomes the percentage of the desired performance output. That is, the performance objective of $\leq$ 3 nm RMS OPD is expressed in the scaled coordinate by $\sigma_{\bar{y}} \leq 1$.

The model scaling suggested in this section dramatically improves the numerical conditioning of the OPD control problems considered below. All the problems below will follow the above scaling scheme, so the over-bar notation is dropped for simplicity in the sequel.

Design criteria

The controllers to be designed for each of the models above must ensure (to the extent the actuators permit it) stabilization of the OPD such that the RMS value of $\bar{y}$ is approximately one, and such that the cost functional introduced in Chapter 5 is minimized:

$$J(K) = \hat{\sigma}_{\bar{y}}^2 + \rho \sum_{i=1}^{n_u} \rho_i \hat{\sigma}_{u_i}^2. \tag{6.6}$$

Full state feedback is assumed for these designs, so that $u = Kx$, and the relative weights ρ_i will be chosen to effect a specific input-magnitude/accuracy tradeoff. The initial designs in Section 6.2 will use $\rho_1 = \rho_2 = 1$, penalizing directly RMS force input from the actuators, while Section 6.3 will utilize a slightly different weighting, explained below, which penalizes the RMS current draw, and hence the battery drain, of the control system. The SLQR design procedure of Chapter 5 will be used to determine the desired feedback matrix K in all cases, and the parameter ρ will be iterated until the desired closed-loop performance target on $\hat{\sigma}_{\bar{y}}$ is achieved.

6.2 Two-Stage Designs

In this section, control designs for the two-stage benchmark problem described in Section 6.1.1 are examined. The actuators are expected to operate in a broadband stochastic environment, so it is important to examine how each input influences the output across a range of operating frequencies. Figure 6-4 shows the Bode diagrams for the open-loop transfer functions from u_1 and u_2 to the re-scaled output, plotted as solid (voice coil) and dashed lines (PZT) respectively. Note that these are linear loop transfer functions and do not include saturation effects; i.e. they are computed assuming $N_{11} = N_{22} = 1$. The voice coil transfer function has a resonance at around 5.6 Hz corresponding to the cage flexure mode, and its frequency response rolls off quickly afterwards. The PZT has significantly lower D.C. gain, but it has a much larger bandwidth, out to about 2200 Hz. From Chapter 3, the dynamics introduced by the electronics of each actuator are negligible up to approximately 3-5 kHz, which is considerably beyond the mechanical bandwidth of the system. Accordingly, the electrical filtering will be neglected in the designs below.

The disturbance input for the benchmark problem is representative of a vibration transmitted to the cage of the ODL by the spacecraft bus. It thus enters the plant dynamics in the same way as the voice coil input. The nominal disturbance assumed for the designs has normalized power spectral density (PSD) shown in Figure 6-5. This PSD profile is coarsely representative of a broadband disturbance vibration arising from unbalanced reaction wheels on a spacecraft [57].

The saturation levels for these inputs are determined from the electro-mechanical properties of each actuator and their corresponding maximum theoretical deflections. The maximum force inputs in this model were computed from JPL design documentation and manufacturer spec sheets to be 2 N and 10 N, respectively for the voice coil and PZT [30, 84]. Application of these inputs at D. C. will cause each actuator to achieve its respective maximum deflection. For the current JPL design, the resolution level of the PZT is on the order of one or sub-nanometer, which is 3 orders of magnitude smaller than its maximum defection. The voice coil actuator has no friction and stiction, so it has very good mechanical resolution; however, its resolution can be limited by quantization. The effect of quantization and resolution will be considered in Section 6.2.3; the designs below initially assume that saturation is the dominant nonlinear effect in the dynamics.

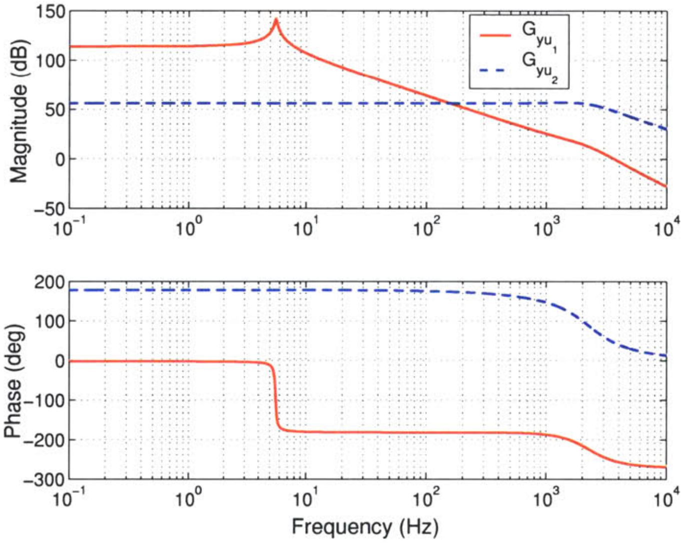

Figure 6-4: Plant transfer functions. Solid: voice coil to output; Dashed: PZT to output.

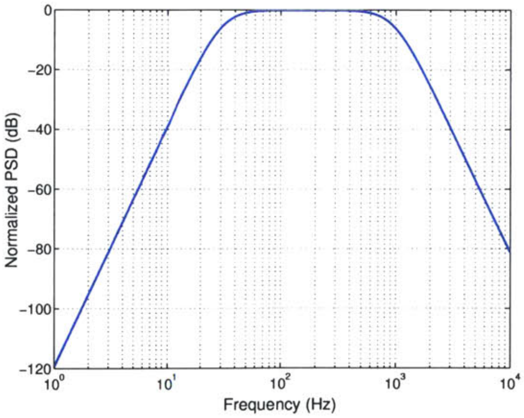

Figure 6-5: Disturbance PSD normalized to its maximum

6.2.1 Vibration Suppression

For relatively "small" disturbances, the saturation characteristics of the actuators will not be an issue and linear state feedback should easily be capable of reducing the closed-loop OPD to the desired 3 nm level. As the magnitude of the disturbance input increases, however, the actuators will need to work harder to maintain the desired 3 nm closed-loop performance. For some level of disturbance intensity, the actuators will no longer have sufficient control authority to achieve the desired closed-loop performance.

To examine this tradeoff, the investigation below examines a series of cases where the intensity of the disturbance is varied, but the overall shape of its PSD remains the same, as shown in Figure 6-5. For each intensity level, there is a corresponding open-loop output RMS $\sigma_{open} = \hat{\sigma}_y$ when $u = 0$ and, up to some critical limit, there exists a control design that reduces the $\hat{\sigma}_y$ to less than 3 nm RMS in the closed loop (when $u = K\,x$). In this fashion a family of control designs can be generated, parameterized by different input noise levels. Since the physical meaning of a specific disturbance intensity is difficult to visualize, the solutions presented below are instead parameterized by the corresponding open-loop RMS levels σ_{open} of OPD which each disturbance intensity provokes.

PZT actuating alone

Before examining the complete solution with both actuators, it is instructive to examine the performance which can be achieved using just one of the two actuators. Figure 6-6 demonstrates the case when the PZT is used alone to reduce OPD perturbations. In Figure 6-6(a), the plot shows RMS control signals σ_u, normalized by its maximum force input (10 N), as a function of σ_{open}. For reference, the corresponding LQR designs, which neglect the nonlinear characteristic of the actuator, are shown as the dashed line on the plot.

Notice that the LQR and SLQR solutions coincide until the normalized σ_u reaches about 50% of its maximum input level, at which point the SLQR solution diverges rapidly from the LQR solution. This phenomenon occurs because the actuator starts to saturate for larger input disturbances. As the disturbance magnitude increases, corresponding to larger equivalent open-loop OPD variance, the SLQR solution asymptotes rapidly upwards at a value of σ_{open} equal to approximately 16 μm. For σ_{open} greater than this value, the

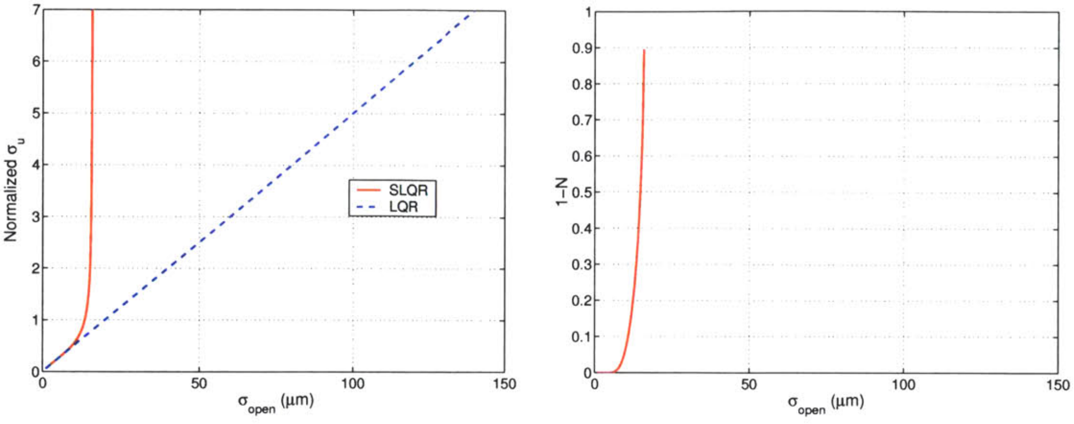

(a) (b)

Figure 6-6: PZT actuating alone (a) Normalized RMS control signal (b)$1 - N$, probability of saturation

actuator does not have enough authority to maintain the 3 nm closed-loop performance. Therefore, this point can be considered the achievable performance for the PZT actuator; it is the largest σ_{open} that can be suppressed by the PZT alone to achieve the closed-loop requirement. Of course, the LQR solution, which does not take into account actuator saturation limits, incorrectly predicts that the closed-loop performance requirement may be achieved for arbitrarily large open-loop disturbances.

Figure 6-6(b) shows the probability of saturation, or equivalently the percentage of time that the actuator spends in saturation. For σ_{open} below 5.5 μm, the probability of saturation is small, and this corresponds to the region where SLQR and LQR solutions are almost indistinguishable. For these disturbance levels the PZT is essentially acting in its linear region. As the σ_{open} level increases to the PZT's achievable performance point, the $1 - N$ curve asymptotes in the same way as the normalized σ_u and approaches the value of 1, indicating 100% probability of saturation. When $1 - N$ is close to 1, the actuator is saturating almost all the time, and therefore, it is near its "bang-bang" limit.

Voice coil actuating alone

Figure 6-7(a) illustrates the corresponding performance obtained using the voice coil alone to attempt to achieve the closed-loop performance of 3 nm RMS OPD. Similar behavior is observed as in the PZT alone case; the LQR and SLQR solutions are coincident until about the voice coil's RMS utilization approaches 50% of its maximum input, then rapidly diverge with the SLQR solution approaching an asymptote at about 42 μm of open-loop OPD. Thus 42 μm RMS is the largest amount of open-loop OPD which can be suppressed to the 3nm RMS level using the voice coil alone. This asymptotic limit is again shown in the $1-N$ curve Figure 6-7(b) for this scenario, which rapidly increases to the limiting value of 1 (100% saturated; bang-bang limit) as the open-loop OPD approaches 42 μm.

With its larger stroke, the voice coil can obtain better achievable performance, suppressing larger σ_{open} than the PZT. However, note that the maximum extension of the voice coil is 1.5 mm, and is thus capable of inducing a 3 mm change in OPD (recall that one unit of change in voice coil or PZT causes two units of change in OPD). The achievable open-loop rejection limit of 42 μm is barely 1.5% of the maximum possible voice coil OPD change (3 mm). Compare with the PZT case above, where the 16μm rejection limit is 75% the maximum piezo OPD change (20 μm). This discrepancy is primarily a result of the low bandwidth of the voice coil transfer function as compared with the spectrum of the driving noise in this example. Since the transfer function from voice coil to OPD rolls off quickly after its resonance (Figure 6-4), the voice coil does not have sufficient authority at the plant output to compensate for disturbances with significant, high frequency content. As a result, the voice coil cannot utilize its stroke range efficiently to reduce high frequency disturbances, whereas the PZT with its higher bandwidth can utilize almost all of its deflection range to suppress the effect of such disturbances.

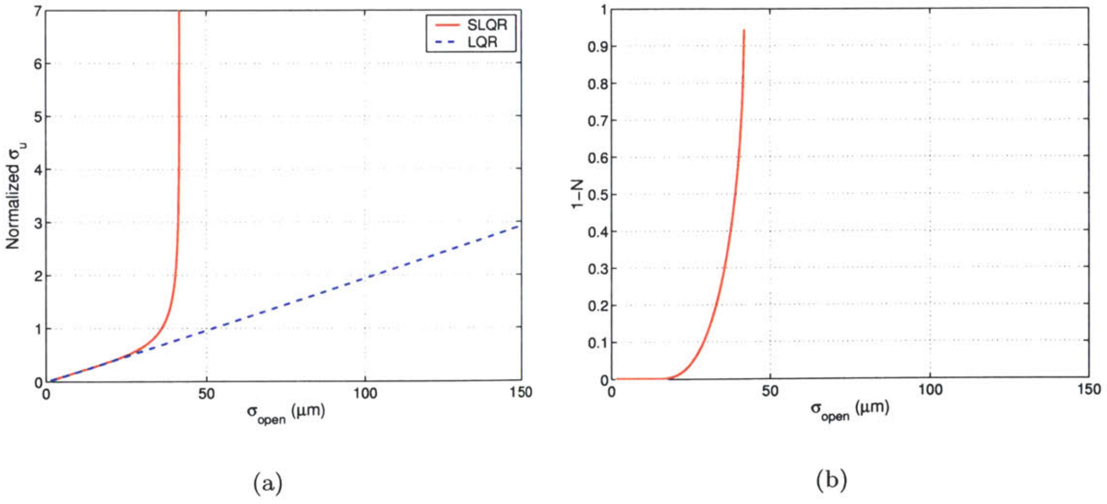

(a) (b)

Figure 6-7: Voice coil acting alone (a) Normalized RMS control signal (b)$1-N$, probability of saturation

PZT and voice coil actuating together

Finally, Figure 6-8(a) shows results for the case when PZT and voice coil work together. In this figure, solid and dashed lines represent the voice coil and PZT inputs when the two actuators operate together, and the dashed-dotted and dotted lines show VC and PZT when they act alone. It is clear that with both actuators operating jointly they can suppress much larger ranges of σ_{open} while achieving the closed-loop performance requirement. The achievable performance for this case is slightly greater than 150 μm RMS open-loop OPD – almost a factor of four larger than that achievable using either actuator in isolation. From Figure 6-8(b), both the PZT and the voice coil stay in their linear regions for much larger values of σ_{open} than when either actuator acts alone.

Figure 6-8(c) compares the SLQR solution (solid and dashed lines) with the LQR solution (dashed-dotted and dotted lines). For the PZT actuator, the LQR and SLQR curves stay close together until about 50 μm, at which point the VC starts to saturate. After this point, the PZT begins to work harder and deviates from the nominal LQR solution in order to prevent voice coil from being driven into saturation. When the PZT starts to saturate around $\sigma_{open} = 110\,\mu$m, it no longer has sufficient authority to desaturate the voice coil, so the voice coil SLQR solution deviates from the LQR solution and both actuators saturate quickly after this point.

It is also interesting to observe that, in addition to the achievable performance limits identified, the analysis above provides additional information useful for the practical operation of these systems, especially in the predictions of the degree of saturation. For example, from Figure 6-8, the SLQR analysis predicts that this control strategy can reject open-loop OPD perturbations up to 60 μm RMS while keeping both actuators below 10% saturation with this disturbance spectrum. Up to 120 μm can be rejected while keeping both actuators below 50% saturation. This kind of information can be quite useful at the system design level for life-cycle analysis of the actuators.

Control authority "hand-off"

Chapter 3 discussed the idea of an optimal "hand-off" frequency for the actuators of a staged control system, reflecting the manner in which the control algorithm assigns responsibility to each actuator for suppressing the disturbance over a particular range of frequencies. This

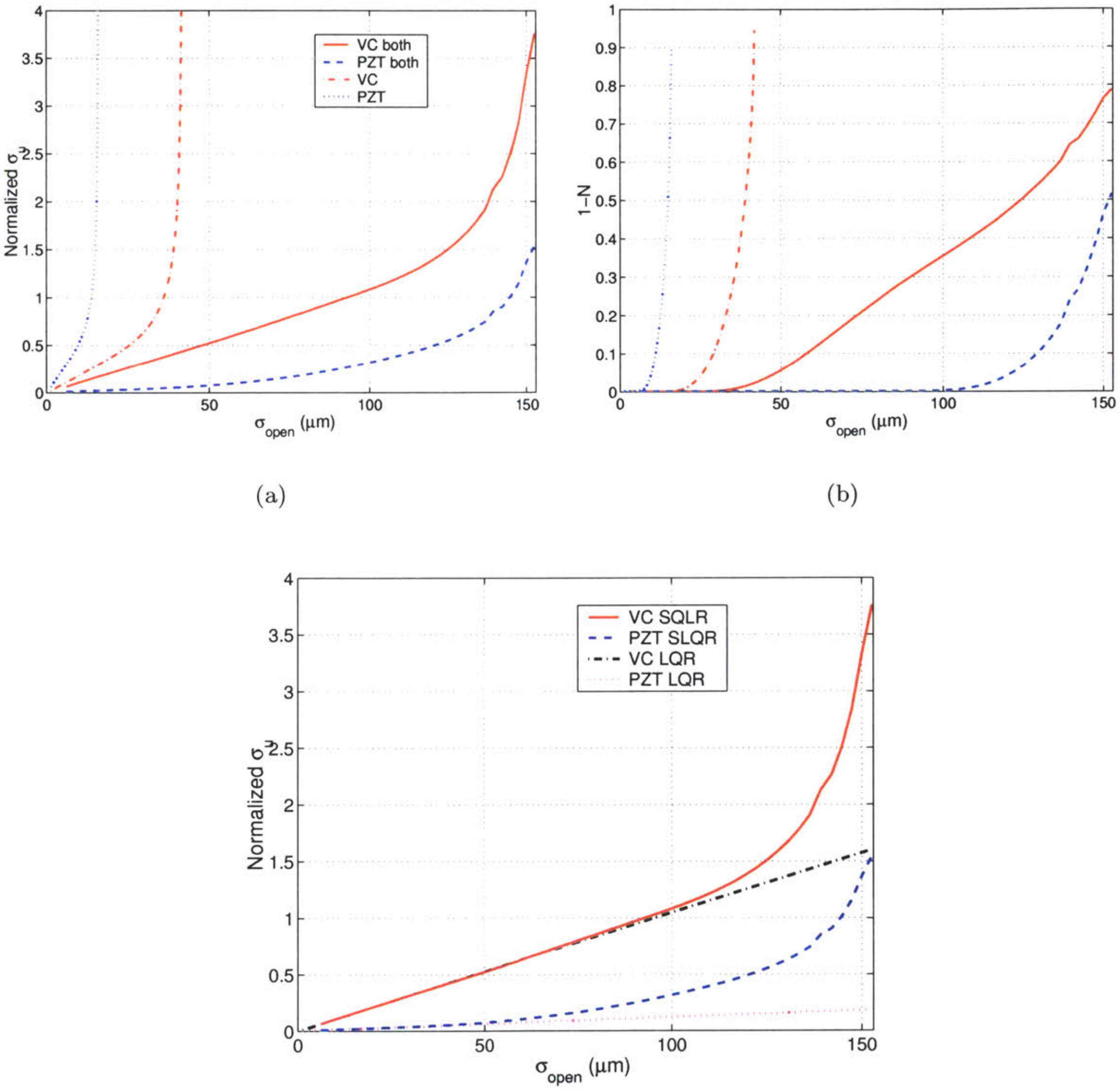

(a)

(b)

(c)

Figure 6-8: Voice coil and PZT actuating jointly (a) Normalized RMS control signal (b)1-N, probability of saturation (c) Comparison with LQR solutions section examines how the SLQR control algorithm designs this hand-off for the two-stage OPD stabilization problem, and in particular it demonstrates how the relative saturation levels of each actuator serve to modify the hand-off frequency.

Analyzing the hand-off frequency requires examining the closed-loop response of the system in the frequency domain. Using the gain matrix N determined from the consistency constraints of the SLQR algorithm, these responses can be determined from the closed-loop dynamic model

$$\begin{aligned} dx &= (A + B_2NK)\,x\,dt + B_1dw \\ u &= Kx, \end{aligned} \tag{6.7}$$

allowing computation of the effective closed-loop transfer functions T_{u_iw} from the disturbance w to each of the control inputs u_i.

Figure 6-9(a) shows the family of T_{u_iw} curves corresponding to the LQR designs for the two-stage model above. The solid and dashed lines are the transfer functions from disturbance w to voice coil (T_{u_1w}) and PZT (T_{u_2w}), respectively. As the disturbance magnitude increases, each of the transfer functions is correspondingly shifted upwards but otherwise remains unchanged. In particular, the hand-off frequencies of the LQR designs, indicated by circles on the plot where the two transfer functions cross, remain identical regardless of the disturbance intensity.

The corresponding SLQR results are presented in Figure 6-9(b). Clearly the transfer functions in this case do not simply shift upward as disturbance intensity increases. The mid-range peak of voice coil transfer function, for example, becomes narrower and occurs earlier in frequency as the disturbance intensity increases. More significantly, the crossing between the voice coil and PZT magnitude plots moves to the right, indicating that the hand-off frequency increases as the disturbance magnitude increases. This effect was not seen in the LQR designs of Figure 6-9(a) and is a consequence of the relative saturation states of the two actuators as the disturbance intensity increases.

A naive interpretation of Figure 6-9(b) would lead to an opposite interpretation of relative actuator usage than that offered in the previous section. Since the hand-off of control authority from voice coil to PZT occurs at progressively higher frequency as the actuators saturate, it would appear that the voice coil is taking on more control responsibility to prevent the PZT from saturating. However, such an interpretation neglects the dramatically different effect each actuator input has on the OPD. As shown in Figure 6-4, the voice coil has much more authority on the output OPD at low frequencies. As a result, only a small u_1 is needed to produce a large change in OPD at low frequency, while a very large u_1 is needed to provoke even small OPD changes at high frequency. Conversely, only a small PZT command, u_2, is required to produce large changes in OPD at high frequencies.

To compensate for these differences, Figure 6-10(b) shows the result of passing each actuator transfer function $T_{u_i w}$ through the corresponding plant dynamics G_{yu_i}. This figure hence shows the changes in OPD each actuator provokes so as to counter the effect of the disturbance, thus providing a more accurate picture of the manner in which the PZT and voice coil partition disturbance rejection responsibilities in the frequency domain.

The hand-off frequency, at which the voice coil and PZT transfer functions cross, is again emphasized by a circle in Figure 6-10(b). To the left of the circle, the voice coil has more authority, and to right of the circle, the PZT authority surpasses that of the voice coil. As the voice coil saturates with increasing disturbance intensity, the hand-off moves to *lower* frequencies, so that the PZT starts to take over more of the high frequency authority from the VC. Measured in this fashion, this motion of the hand-off frequency corresponds with the earlier observation that PZT is effectively *desaturating* the voice coil, by taking over from the voice coil disturbance suppression responsibilities at high frequencies. Finally, Figure 6-10(a) shows the corresponding OPD hand-off for the LQR design family. Recall from Figure 6-9(a) that the hand-off frequency is invariant for each disturbance intensity, since the LQR designs do not take the actuator saturation states into account.

The controller designs developed from the SLQR algorithm thus use the VC at the low frequency region where its most effective in reducing RMS OPD and use PZT more in the 100+ Hz region as the VC becomes more saturated. This strategy is one of the key heuristics used in many of the semi-classical approaches to the design of a staging control law for optical delay lines [23, 46], where an integrator is augmented into the voice coil loop so as to force the voice coil to take responsibility for low frequency disturbances. It is interesting to observe that this SLQR analysis has essentially arrived at the same design, in a more or less automatic fashion, as a consequence of optimizing the performance metric given by Equation 6.6 above.

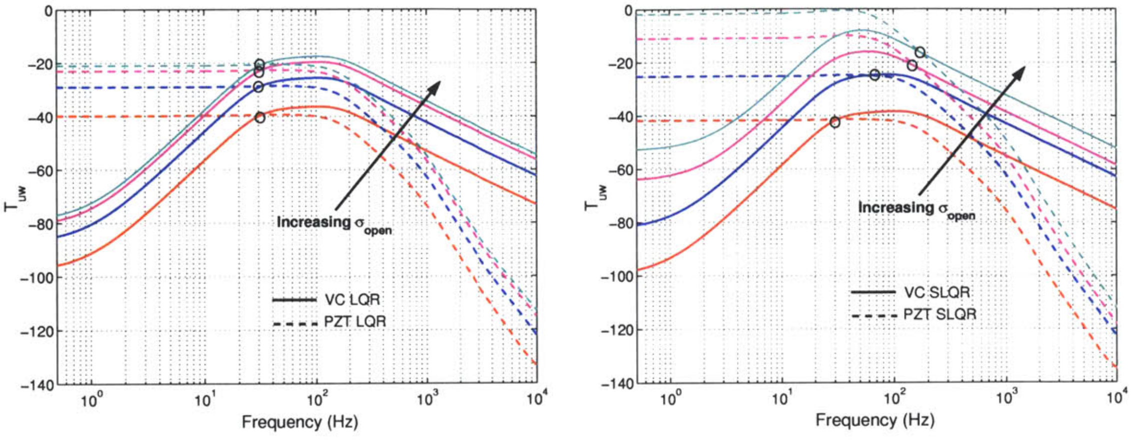

(a)

(b)

Figure 6-9: Closed-loop linearized transfer function from disturbance to each actuator (VC - solid line, PZT - dashed line): (a) LQR results (b) SLQR results

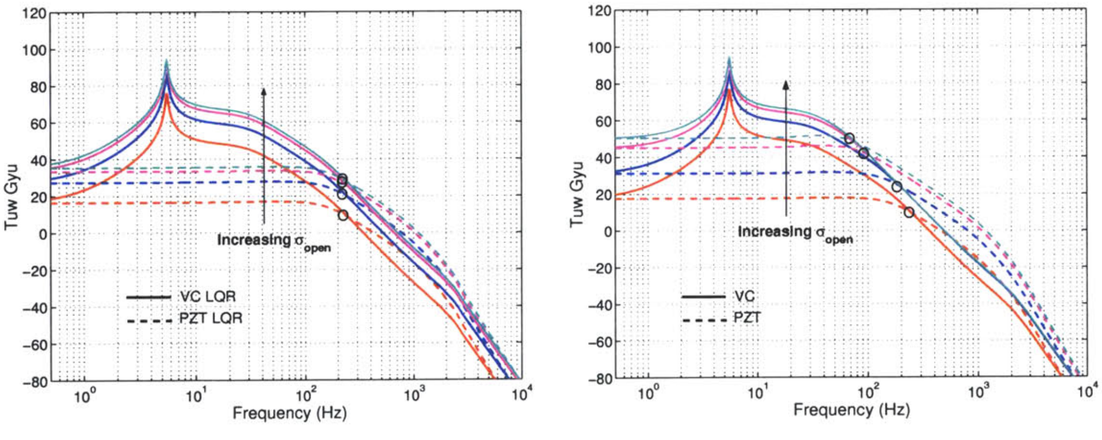

(a)

(b)

Figure 6-10: Closed-loop transfer function from disturbance to the effective output (VC -solid line, PZT - dashed line): (a) LQR results (b) SLQR results

6.2.2 Disturbance spectrum variations

The previous analysis is based on a disturbance spectrum with fixed shape and varying intensity levels. The innovations filter associated with the disturbance spectrum is essentially a second order bandpass Butterworth filter with corner frequencies at $F_{low} = 30$ and $F_{high} = 1000$ Hz. The objective of this section is to examine the effects of changing the corner frequencies of the innovations filter, and hence to examine to effects on the design when the disturbance energy is distributed over lower, or higher, frequency bands.

Low frequency spectrum variations

This first example explores the effect of changing the low corner frequency of the innovations filter from the original 30 Hz to three other frequencies - 0, 10, and 100 Hz. When $F_{low} = 0$ Hz, the innovations filter becomes a low pass filter, and the disturbance has nontrivial energy all the way down to DC. As in the case studies above, for each disturbance spectrum a family of designs was explored corresponding to increasing disturbance intensity, until both actuators reach their achievable performance limits.

Figure 6-11(a) shows the normalized $\hat{\sigma}_u$ corresponding to four sets of disturbance spectra, where each spectrum has the same high corner frequency $F_{high} = 1000$ Hz and different low corner frequency F_{low}. In this figure, the solid and dashed lines indicate VC and PZT actuator, respectively. The results obtained form the previous section are labelled by $F_{low} = 30$ Hz for comparison purposes. Figure 6-11(b) shows the corresponding probability of saturation curves. As the low frequency corner of the disturbance spectrum decreases, the shape of all four sets of curves remains similar, but they are shifted along the x-axis.

Note that as the low frequency content of the disturbance increases, (F_{low} decreasing) the system is able to reject a larger amount of RMS OPD variance σ_{open}. This is a consequence of the voice coil frequency response. In the designs of the previous section, much of the disturbance energy was concentrated in frequency bands where the voice coil has minimal authority over the output. Thus the voice coil could not operate at maximum effectiveness to eliminate those disturbances, requiring the desaturating effort of the PZT to achieve an adequate design. The VC has very large authority in the low frequency region, however, and as more of the disturbance energy is concentrated there, the voice coil can be used more efficiently to reject disturbance effects in this frequency range.

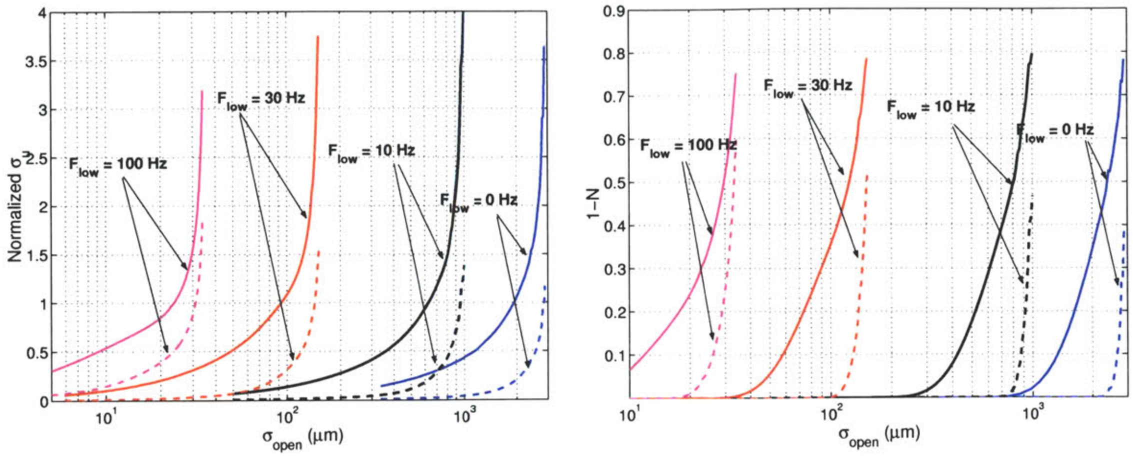

(a) (b)

Figure 6-11: Decreasing the lower frequency of disturbance spectrum: (a) Normalized RMS control signal versus σ_{open} (b) Probability of saturation $1 - N$ versus σ_{open}

To illustrate this increased efficiency, Figure 6-12 shows the probability of saturation of the VC actuator when it is used alone to suppress the different disturbances. Again, the $F_{low} = 30$ Hz plot is the same as Figure 6-7(b) and is shown for comparison. As more and more of the disturbance energy is at lower frequency, the voice coil becomes increasingly effective in suppressing the disturbance by itself. In the limit when $F_{low} = 0$ the voice coil, acting alone, can suppress 1.2 mm of open-loop OPD perturbations. This is 40% of its maximum stroke, indicating that the voice coil can be used far more efficiently for this kind of disturbance, as compared to the 1.5% of its capability which was used in the nominal $F_{low} = 30$ case.

A different perspective on the increasing utilization of the voice coil at lower frequencies as F_{low} decreases can be seen in the family of transfer functions $G_{\bar{y}u_i}T_{u_iw}$ shown in Figure 6-13. As the low frequency content of the disturbance increases, the compensating motion the voice coil creates in the OPD becomes significantly more prominent in the low frequency region. Indeed, comparing the sequence (a)-(d) as F_{low} decreases, only the voice coil response is affected at low frequencies by the downward shift in the disturbance spectrum. For the case $F_{low} = 0$, the transfer function shows the voice coil demonstrating orders of magnitude more authority over OPD than the PZT at low frequencies, which is the expected result.

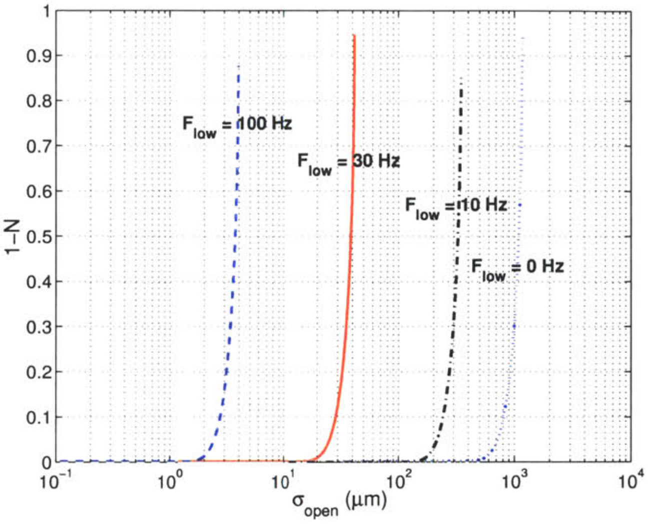

Figure 6-12: Probability of saturation of the VC actuator with lower frequency disturbance spectra.

High frequency spectrum variations

The second set of analysis focuses on the effects of changing the high frequency roll-off of the disturbance spectrum. In these examples, the innovations filter is designed to have the original low frequency corner at $F_{low} = 30$ Hz, while the high frequency corner is changed to 800 and 1200 Hz from the original 1000 Hz. The above analysis is repeated here for different levels of F_{high}.

The results are shown in Figure 6-14(a) and Figure 6-14(b). As illustrated by these figures, the RMS control input $\hat{\sigma}_u$ and the probability of saturation $1 - N$ are actually relatively insensitive to the changes in the high corner frequency F_{high}. Since the disturbance enters the plant the same way as the VC actuator, its effects are filtered by the ODL plant itself. As shown in Figure 6-4, the transfer function from the VC input to the OPD output rolls off at around 5.5 Hz, so the high frequency components of the disturbance (800-1200 Hz) are so effectively attenuated by the natural plant dynamics there is no need of additional actuator effort to suppress the additional high frequency components of the disturbance.

Note that this result may not be true if the modelled disturbances act directly at the plant output. Without filtering the disturbance through the plant as in this example, extending the disturbance frequency spectrum in the high frequency region will directly increase the open-loop RMS OPD and may cause both actuators to saturate at a lower $\hat{\sigma}_{open}$.

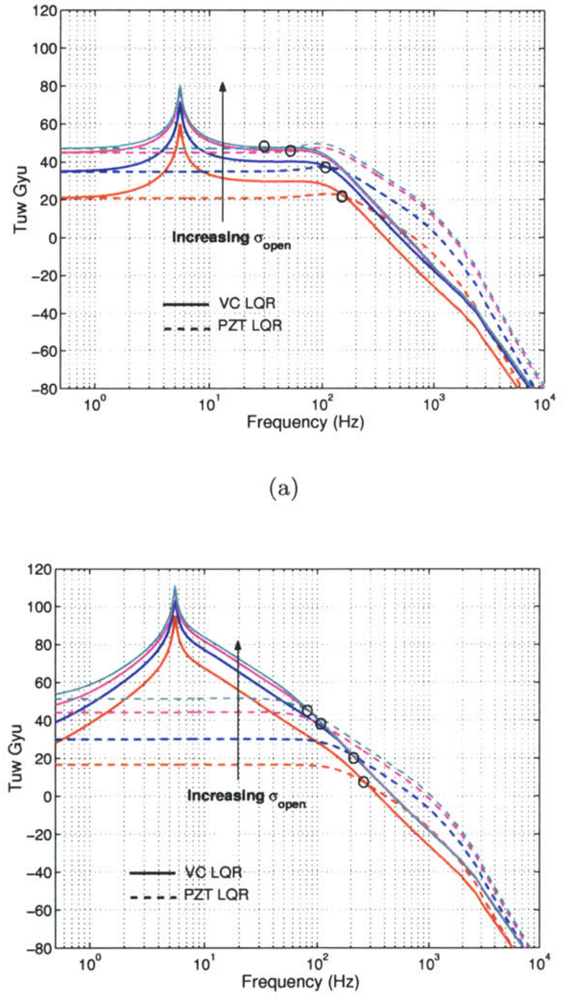

(a)

(b)

(c)

(d)

Figure 6-13: Closed-loop transfer function from disturbance to the effective output (VC - solid line, PZT - dashed line) for various disturbance spectra: (a) $F_{low} = 100$ Hz (b) $F_{low} = 30$ Hz (c) $F_{low} = 10$ Hz (d) $F_{low} = 0$ Hz

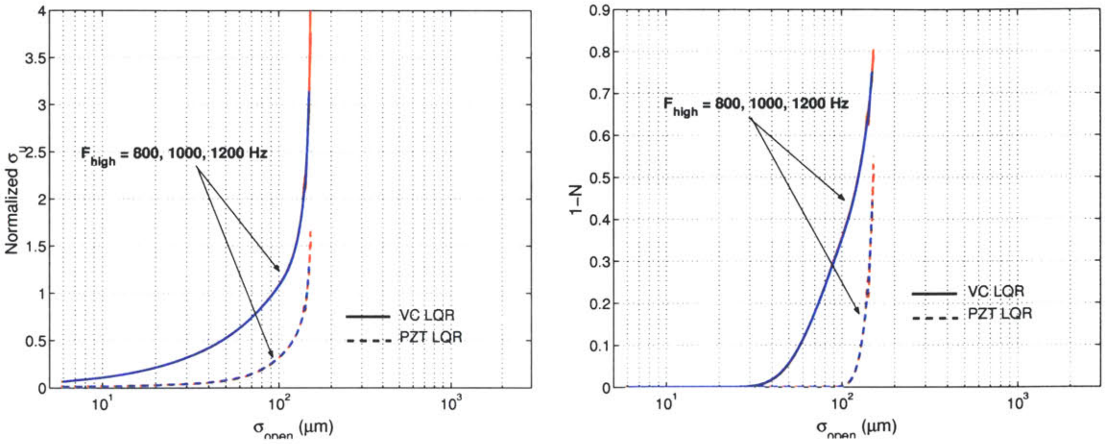

(a)

(b)

Figure 6-14: Changing the high frequency corner of disturbance spectrum: (a) Normalized RMS control signal versus σ_{open} (b) Probability of saturation $1 - N$ versus σ_{open}

6.2.3 Quantization Effects

Quantization effects on the two-stage system are examined in this section. For this study, the disturbance frequency spectrum is again given by Figure 6-5, and a relatively small intensity is assumed, corresponding to an open-loop RMS output of $\hat{\sigma}_{open} = 2.5\,\mu$m. In the nominal design for this situation considered above, where there are no quantization effects, both actuators are operating in their linear regions as shown by Figure 6-8(b).

To examine quantization effects on the voice coil, its step size is varied from 0 to 30% of the voice coil stroke. For each step size, the control design is iterated until the desired closed-loop RMS OPD is achieved. Figure 6-15(a) shows the normalized $\hat{\sigma}_u$ for each actuator as a function of the percent stroke. Note that as q increases, the RMS input to the voice coil also increases. This is mainly due to the fact that the voice coil must be driven harder as the quantization step increases in order to have any authority over the OPD motion. This effect starts to become noticeable in this example when the quantization step size exceeds 10% of the voice coil stroke. As a design rule of thumb, if the quantization level is less than 10% of the maximum input, the quantization effects on performance is negligible. Since resolution induce similar effects as quantization in the stochastic stabilization problem, this rule also applies to resolution effects as discussed in 5.4.

Figure 6-15(b) shows the linearization gain N as a function of q. At low q, both actuators operate in the linear region where $N_{11} = N_{22} = 1$. As q increases, more of the VC control input becomes ineffective due to quantization effects, so the linearization gain N_{11} of the VC decreases to reflect this phenomena. In this case, the algorithm decides that it is less costly to bring the VC out of the deadzone region rather than to increase the PZT control signal in order to maintain the desired output performance. By taking into account the decrease in effective gain N_{11} as a function of the quantization level, the SLQR algorithm increases the voice coil command to essentially "kick" the actuator out of the effective deadzone around the origin.

Assuming that a 12-bit D/A converter is used, the quantization level for ±2 N of the VC input is around 10^{-3} N. The level at which quantization effects begin to influence the performance of the system in this example is about $q = 0.2$N, which is more than two orders of magnitude above the quantization level in this study. Thus, the effect of quantization on nominal system performance is expected to be negligible, and will hence be neglected in the remaining examples. Of course, this assumption would have to be validated for the actual hardware and expected disturbance spectrum for a particular system. Even if the quantization is found to be non-negligible, the SLQR design procedure can be used as shown above to modify the design to maintain the required performance despite the quantization effects.

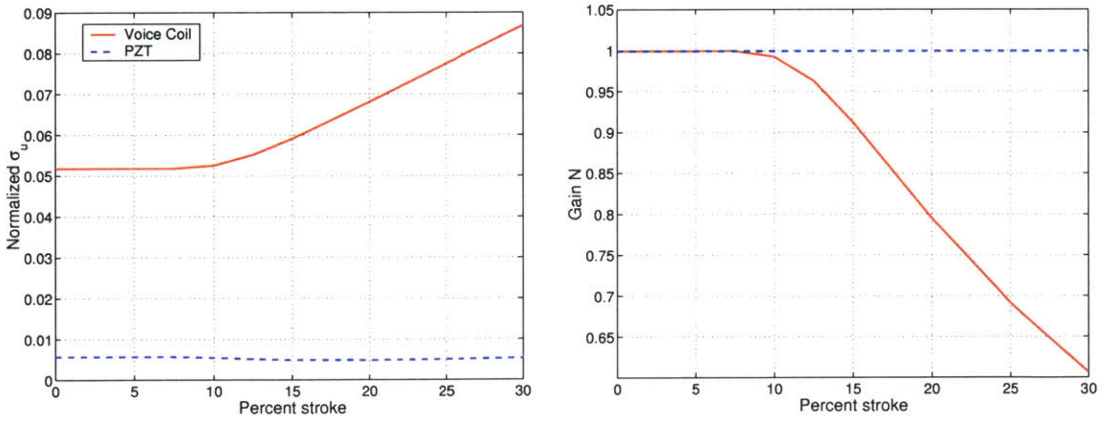

(a)

(b)

Figure 6-15: Quantization effects on the Voice Coil (a) Normalized RMS control signal versus quantization percent stroke of the voice coil (b) Linearization gain N versus percent stroke

6.3 Two-Stage, Minimum Electrical Power Designs

For spacecraft applications, the actuators are typically driven by power amplifiers which draw current from rechargeable battery sources. Therefore, the steady-state RMS current is one measure of how much each actuator consumes the electrical resources supplied by the batteries, and is potentially a more meaningful measure of control effort for a space interferometry control system to minimize.

The force applied by the voice coil is directly proportional to the current it draws as discussed in Chapter 3, i.e. $F_{vc} = K_f I_{vc}$. Penalizing the voice coil current usage in the cost function is thus straightforward by choosing $\rho_1 = 1/K_f^2$ in Equation 6.6. On the other hand, the force generated by the PZT actuator depends on the applied voltage, and there is a more dynamic relationship between the voltage applied to the PZT and the corresponding current it draws. The dynamics of this electrical relationship must be taken into account to correctly analyze the RMS current draw of the PZT.

Recall from Chapter 3 that the PZT current and voltage can be related by the following transfer function:

$$\frac{I_{pzt}(s)}{V_{pzt}(s)} = G(s) = \frac{1}{R_t}\left(\frac{\tau_1 s + 1}{\tau_2 s + 1}\right), \tag{6.8}$$

where $R_t = R_s + R_d$, $\tau_1 = R_d C$, and $\tau_2 = (R_s R_d)/(R_s + R_d)$. The source resistance and the PZT discharge resistance are denoted by R_s and R_d, respectively. This transfer function can be separated into two parts,

$$\begin{aligned} G(s) &= G_1(s) + G_2(s) \\ G_1(s) &= \frac{1}{R_t}\frac{\tau_1 s}{\tau_2 s + 1} \\ G_2(s) &= \frac{1}{R_t}\frac{1}{\tau_2 s + 1}. \end{aligned}$$

Using typical parameters described in Chapter 3, $\tau_1 = 1000$ and $\tau_2 = 5 \times 10^{-5}$, resulting in a high pass transfer function $G_1(s)$ and a low pass transfer function $G_2(s)$ both with corner frequency at approximately 3 kHz.

Parseval's Theorem can then be used to compute

$$\begin{aligned} \int_0^\infty |I_{pzt}(t)|^2 dt &= \frac{1}{2\pi}\int_{-\infty}^{\infty} |I_{pzt}(j\omega)|^2 d\omega = \frac{1}{2\pi}\int_{-\infty}^{\infty} |(G_1(j\omega) + G_2(j\omega))V_{pzt}(j\omega|^2 d\omega \\ &= \frac{1}{2\pi}\int_{-\infty}^{\infty} \left[|G_1(j\omega)|^2 + G_1(j\omega)G_2^*(j\omega) + G_2(j\omega)G_1^*(j\omega) + |G_2(j\omega)|^2\right] \\ &\quad \times |V_{pzt}(j\omega)|^2 d\omega \end{aligned}$$

To simplify this integral further, note that the electrical bandwidth of 3 kHz is about a kHz larger than the mechanical bandwidth of the system. The effective operating range of the mechanical components is thus below the upper $1/\tau_2$ corner frequency of the transfer functions above. In this frequency region, G_1 and G_2 are 90° out of phase, and hence the cross terms in the integral above evaluate to zero. Moreover, in this frequency range the low-pass filter G_2 has approximately the constant magnitude $1/R_t$, so that this approximation can be used to further simplify. The result is then

$$\int_0^\infty |I_{pzt}(t)|^2 dt \approx \frac{1}{2\pi}\int_{-\infty}^\infty |G_1(j\omega)|^2 |V_{pzt}(j\omega)|^2 d\omega + \int_{-\infty}^\infty |V_{pzt}(j\omega)|^2/R_t^2 d\omega$$

and hence

$$\int_0^\infty |I_{pzt}(t)|^2 dt \approx \int_0^\infty |\tilde{I}_{pzt}(t)|^2 dt + \frac{1}{R_t^2}\int_{-\infty}^\infty |V_{pzt}(t)|^2,$$

where $\tilde{I}_{pzt}$ is the output response of a linear system driven by the voltage $V_{pzt}(t)$ with transfer function given by G_1.

Since G_1 is a high-pass filter, it has a nonzero feedthrough term which will introduce additional coupling into the necessary conditions for the SLQR design in Chapter 5. There does not appear to be a straightforward method for “untangling” this additional decoupling in the solution of the SLQR equations. However, the argument used above suggests that an additional roll-off can be added to G_1 at high frequencies without affecting the behavior of this transfer function in the mechanical operating range of the system. Thus G_1 can be replaced with

$$G_1'(s) = \frac{1}{R_t}\frac{\tau_1 s}{(\tau_2 s + 1)^2} \tag{6.9}$$

in the computation of $\tilde{I}_{pzt}$.

From the above development, a cost function which penalizes RMS current usage can now be expressed as

$$J = \hat{\sigma}_y^2 + \rho\left(\frac{1}{K_f^2}\hat{\sigma}_{u_{vc}}^2 + \hat{\sigma}_{\tilde{I}_{pzt}}^2 + \frac{1}{R_t^2}\hat{\sigma}_{V_{pzt}}^2\right) \tag{6.10}$$

where u_{vc} is the voice coil input, in Newtons, and V_{pzt} is the voltage applied to the PZT. The state-space model of the two-stage mechanical system introduced above is augmented in order to incorporate the additional filter $G_1'(s)$, so that $\tilde{I}$ is an output of the generalized plant. In terms of the voltage input, the PZT has a saturation level of ±50 V [30].

To examine in more detail the designs arising from minimization of Equation 6.10, the analysis conducted in Section 6.2.1 is repeated here, with the same disturbance spectrum and intensity range. Figure 6-16(a) illustrates the probability of saturation of the voice coil (solid line) and PZT actuator (dashed line) as a function of increasing σ_{open}, and Figure 6-16(b) shows the corresponding RMS σ_u curves. The design as a whole is capable of suppressing almost the same total level of open-loop OPD perturbations (145μm) as those above, but is quite distinctive in how it accomplishes this. In the new design the PZT saturates very quickly as a function of disturbance intensity, essentially reaching its "bang-bang" limit at approximately 40μm. Note that this is very close to the point where the PZT saturated in Section 6.2 when it alone was used to suppress OPD variations. The conclusion is that the SLQR algorithm with this cost function prefers to use the PZT almost exclusively to control the system. The voice coil is used appreciably only after the control authority of the PZT has been exhausted.

Such a result is obtained since the PZT draws significantly less current than the voice coil for a given OPD change, and hence, the cost function above is minimized by using the PZT actuator as much as possible. Although this result minimizes the RMS current, and hence the draw on the spacecraft batteries, it is undesirable to keep the PZT at or near 100% saturation because this may cause irreversible damage to the PZT material and ultimately cause it to fail. To explicitly limit the saturation state of the PZT, the saturation weighted SLQR algorithm of Section 5.6 can be used. In this approach the cost function is modified to

$$J = \hat{\sigma}_y^2 + \rho\left(\frac{1}{K_f^2}\hat{\sigma}^2_{u_{vc}} + \hat{\sigma}^2_{I_{pzt}} + \frac{1}{R_t^2}\hat{\sigma}^2_{V_{pzt}}\right) + \sum_i^{n_u} \upsilon_i(1 - N_{ii}) \tag{6.11}$$

where, to penalize only the PZT saturation state, $\upsilon_1 = 0$ and υ_2 will be varied over a range to explore its effect on the design.

Figure 6-16(c) and Figure 6-16(d) illustrate the probability of saturation of the voice coil and PZT actuator, respectively, as a function of increasing σ_{open} for the new cost function. The solid line in these figures correspond to the results above when there is no explicit penalty on saturation, $\upsilon_2 = 0$. The dashed curves in these figures show a family of solutions with various penalties on the PZT probability of saturation. It is clear that the PZT is still the preferred actuator in these designs, entering the saturation region well before the voice coil. Now however the explicit penalty on saturation prevents the PZT from being driven to its bang-bang limit, instead flattening out at a saturation state determined by the magnitude of the penalty υ_2 and holding this level until the performance limit of approx 145μm is reached. This illustrates the benefits of saturation weighting in an SLQR design, and can be very useful for applications where the saturation state must be explicitly constrained.

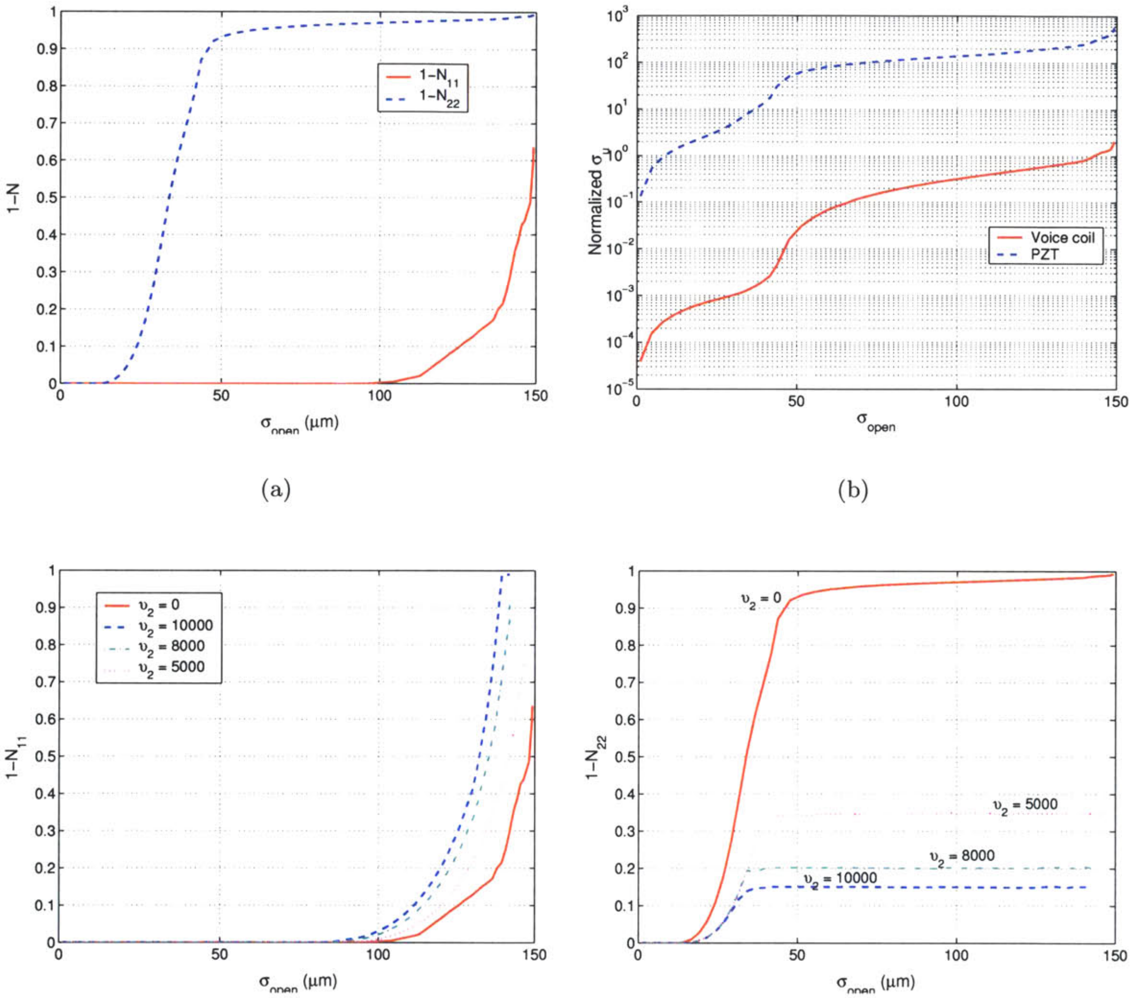

(a) (b)

(c) (d)

Figure 6-16: Penalize power/current usage from actuators (a) Probability of saturation of both actuators. (b) RMS control input σ_u of each actuator normalized by the corresponding saturation level. (c) Probability of saturation of VC when saturation state of PZT is directly penalized (d) Probability of saturation of PZT with different levels of saturation penalty υ

Frequency hand-off

The frequency responses of the above results are examined here to investigate the frequency hand-off between the voice coil and the PZT actuator. First, the frequency hand-off for minimizing the mechanical power is compared with the case when electrical power is minimized. Under mechanical power minimization, the frequency hand-offs between the two actuators occur around and beyond 100 Hz as shown in Figure 6-17(a). As the open-loop output RMS σ_{open} increases, the hand-off location moves to lower frequencies which indicates that the PZT is taking over more of the voice coil's high frequency responsibilities.

When the electrical power is minimized, the hand-off is below 10 Hz at low σ_{open}, and as the PZT saturates more with increasing σ_{open}, the hand-off moves to higher frequencies as demonstrated in Figure 6-17(b). The direction of the hand-off movement in this case is the opposite of the mechanical power minimization problem. Since the PZT actuator draws less current than the voice coil, the algorithm attempts to use PZT as much as possible to suppress the disturbances. Consequently the hand-off occurs at a much lower frequency, so the PZT has more authority than the voice coil for a large range of frequencies. It is also interesting that the shape of the PZT response changes significantly in the 10-100 Hz range for the two minimization criteria considered.

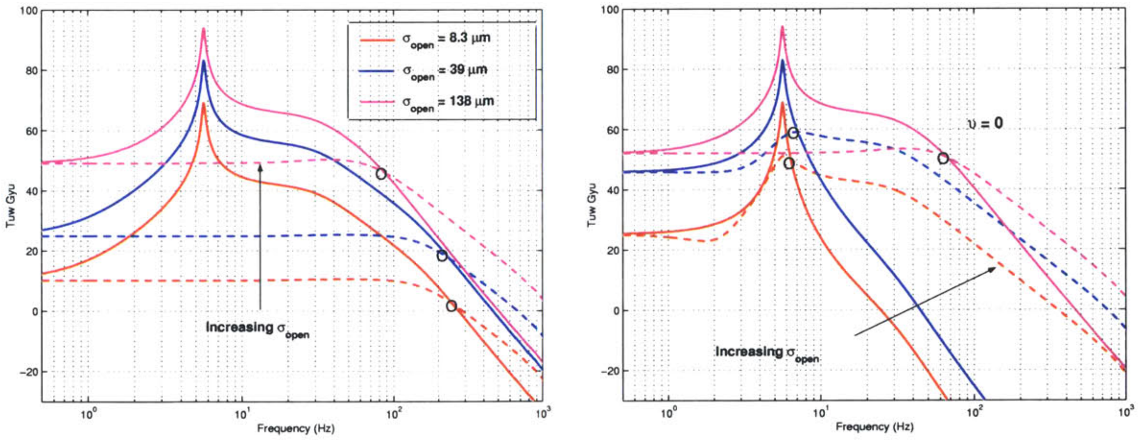

(a) (b)

Figure 6-17: (Frequency response from disturbance w through each actuator to the OPD output. Results associated with three σ_{open} values are presented for each case: (a) Minimizing mechanical power. (b) Minimizing electrical power

The frequency responses for different levels of saturation penalties υ are studied next. In Figure 6-18, three sub-figures are shown here; each corresponds to a different level of υ. These figures appear to be very similar; however, the hand-off frequency does increase with increasing saturation penalty on the PZT actuator. This result is sensible, since as the penalty on PZT saturation state increase, the voice coil has to work harder, with higher authority over a larger frequency range than PZT, in order to prevent PZT from saturating. The frequency hand-offs for the various cases described above are summarized in Table 6.1. For the electrical power case, the PZT does not saturate at small σ_{open}, $N_{22} \approx 1$, so the hand-off frequency stays the same as the penalty on PZT saturation increases. At larger σ_{open}, the PZT does start to saturate and the hand-off frequency increases with v for reasons described above.

Table 6.1: Summary of frequency hand-off between voice coil and PZT for both mechanical and electrical minimization

σ_{open} [μm]	8.3	39.2	138.1
Mechanical Power			
Hand-off [Hz]	246.8	235.0	86.0
Electrical Power			
Hand-off [Hz] $v = 0$	6.3	7.0	66.0
Hand-off [Hz] $v = 5 \times 10^3$	6.3	9.0	76.4
Hand-off [Hz] $v = 8 \times 10^3$	6.3	10.4	84.7
Hand-off [Hz] $v = 10 \times 10^3$	6.3	11.6	88.9

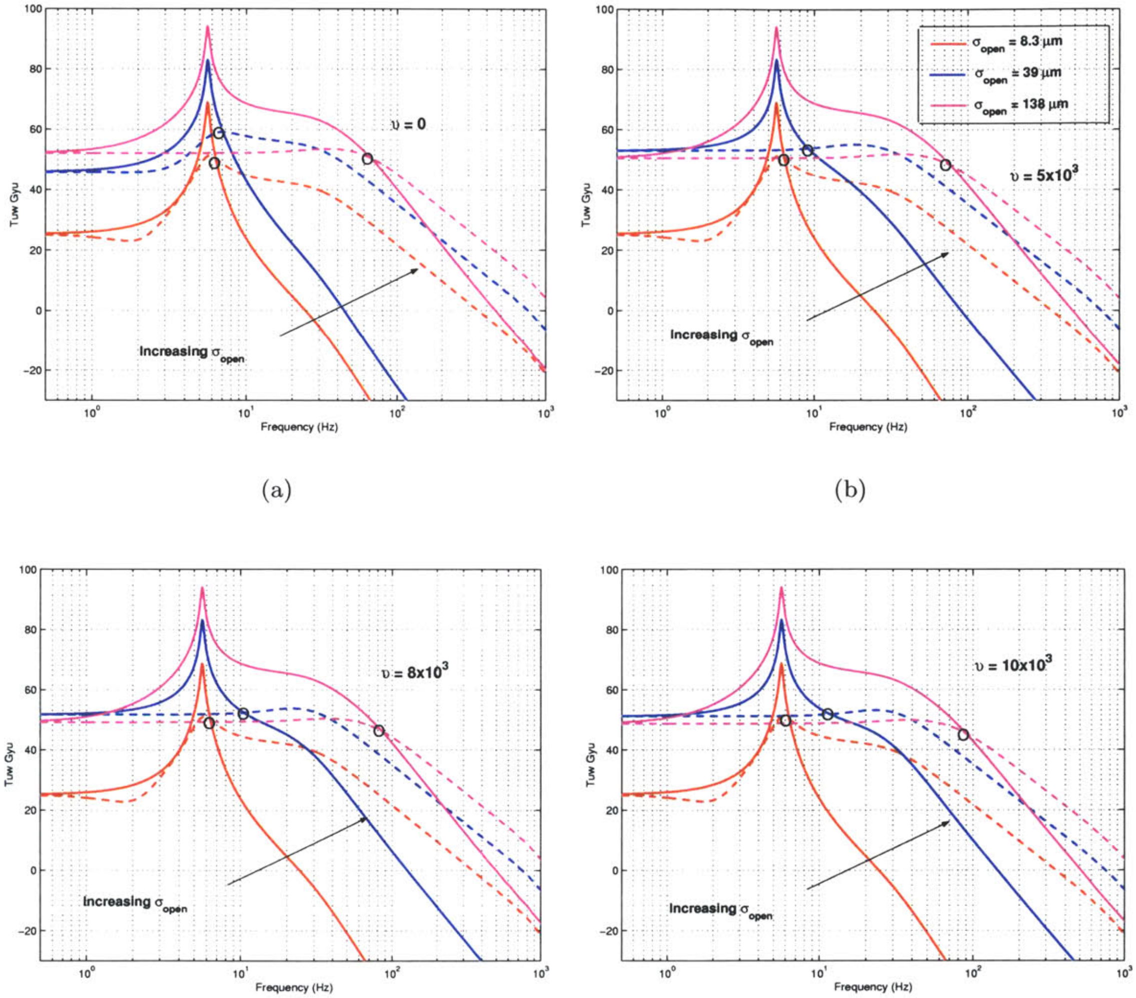

(a) (b)

(c) (d)

Figure 6-18: Frequency response for the power minimization case and difference level of penalty on PZT saturation state (a) $\upsilon = 0$ (b) $\upsilon = 5 \times 10^3$ (c) $\upsilon = 8 \times 10^3$ (d) $\upsilon = 10 \times 10^3$ (each plot displays three curves corresponding to three σ_{open} values)

6.4 Additional two-stage analysis

The previous analyses use a disturbance spectrum that is based on a broadband reaction wheel model and assume the disturbance enters the plant the same way as the voice coil. Since every wheel is built and mounted differently, it may not be possible to know the exact intensity level of the disturbance a priori. However, if the designer can estimate a range of disturbance intensities, the above analyses can be used to determine how hard the actuators must work in order to suppress the disturbances and achieve the desired performance.

In this section, more realistic disturbance models incorporating recently published experimental ODL disturbance spectra are considered. Since these models are measured from experimental data, the perturbations have been modelled as acting on the plant output directly. Using such an assumption, it is not necessary to create a physical model to characterize the relationship between the disturbance input and the plant output. In order to use the models reported in these papers [23, 57], the disturbance models are also assumed to be output disturbances, and as a reminder, the overall linear dynamic equations are discussed in 3.1.2.

The first part of this section compares the SLQR control designs with the currently proposed designs suggested by JPL engineers. Since the exact form of their controllers is not available, the comparison is limited to performance and general design issues. The second part of this section focuses on parameter trade studies and demonstrates how the SLQR framework can help in the actuator selection process.

6.4.1 JPL design comparisons

In the first analysis, the control designs proposed in the thesis are compared with the JPL delay line controllers. Various papers presented by JPL authors suggest a loop-shaping, classical control technique for solving the ODL control problem [23, 27, 46, 57]. These techniques have been demonstrated on experimental benchtop testbeds and have achieved closed-loop performance on the order of 3-30 nm. In these experiments, the optical delay line is placed on a fixed table. When the ODL cage is stationary, not moved by the motor, the perturbation on the OPD output has a PSD as shown by the solid line in Figure 6-19(a). When the motor moves the cage at a constant rate during the slew mode, the corresponding output disturbance PSD is shown by a solid line in Figure 6-19(b). Note that the two curves have similar spectra but different intensities. The open loop RMS OPD σ_{open} associated with the stationary case is approximately 0.6 μm, and the moving case is around 400 μm. These PSD curves are estimated from the experimental results presented in [23].

For the stationary case, the disturbance spectrum roll-off occurs within the bandwidth of the voice coil and PZT, and the open-loop RMS OPD (0.6 μm) is below the stroke of both actuators. As a result, when the SLQR control design is applied to this problem, either the PZT or the voice coil actuator alone is capable of achieving the desired 3 nm RMS OPD in the closed loop while operating in the linear region $N_{11} = N_{22} = 1$. Since the disturbance level for the stationary case is quite small, the actuators do not need to work hard to achieve the desired performance.

When the cage is moving at a constant rate, the amount of perturbation on the OPD increases dramatically ($\sigma_{open} = 400$ μm) as shown by Figure 6-19(b). For this larger level of disturbances, neither of the actuators working alone can achieved the desired closed-loop performance of 3 nm RMS OPD. However, when both actuators collaborate in the SLQR control scheme, they are able to suppress this larger disturbance and satisfy the closed-loop performance requirement without saturating, $N_{11} = N_{22} \approx 1$. The closed-loop OPD spectrum for the stationary and slewing case is shown as a dashed line in Figure 6-19(a) and Figure 6-19(b), respectively.

From this analysis, the control designs suggested in the thesis can achieve comparable closed-loop performance as the JPL designs. However, since the JPL designs are based on classical loop shaping techniques, the control engineers have to redesign each of the actuator loops whenever there is a change in the plant or disturbance environment. Unfortunately redesigning the controllers or tuning the control parameters may not be an easy task, because there are many degrees of freedom in shaping a particular transfer function loop. For example, the JPL designs typically involve an eighth order filter for each control loop, so the location of a total of 8 poles and up to 7 zeros must be tuned in order to find the desired controller. As a result, generating a reasonable controller will require a good control engineer spending time on placing zeros and poles in the correct location in order to obtain the desired loop shape.

On the other hand, the control design proposed in the thesis is based on modern optimization framework, and hence, the resulting algorithm provides a consistent, and automatic methodology for synthesizing controllers. Such an algorithm does not require tuning the control parameters directly and can save time during the control design process. It also allows the engineers to look over a family of solutions under different parameter variations and changes in the disturbance environment.

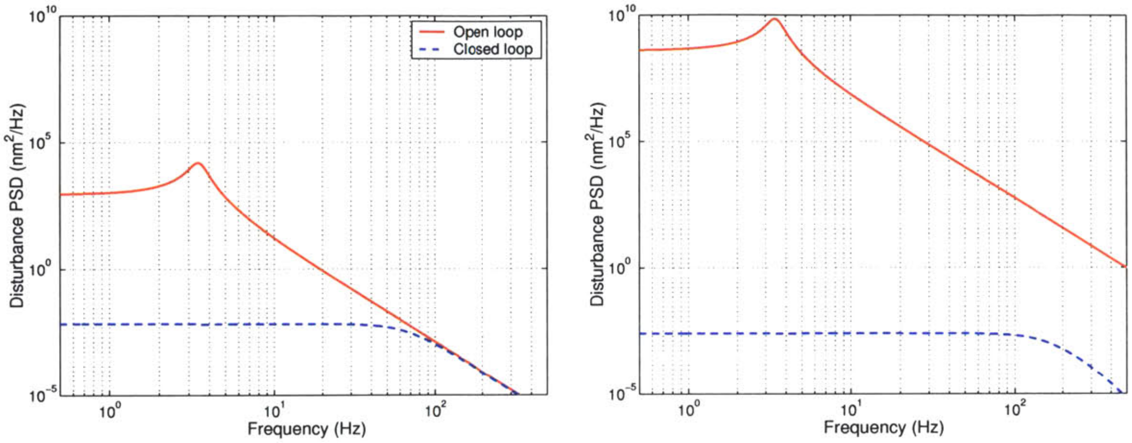

(a) (b)

Figure 6-19: Disturbance PSD on the OPD output. Solid line: Open-loop PSD estimated from JPL experimental results [23]. Dashed line: Closed-loop PSD obtained after applying active control to make $\hat{\sigma}_y$ 3 nm (a) stationary case where the ODL cage stays fixed. (b) slewing case where ODL cage is moved at a constant rate.

The disturbances modelled in [23] mainly captures the disturbance environment of an ODL sitting on a laboratory bench. During the actual space mission, the ODL will also experience disturbances induced by the reaction wheels. Since wheel induced vibrations are expected to be one of the largest disturbance sources onboard the spacecraft [38], it is necessary to also take their effects into account. Therefore, by merging the low frequency disturbances due to motor noises [23] and high frequency disturbances due to wheel imbalances [57], the resulting spectrum will be closer to the anticipated disturbance spectrum for the space mission. A nominal PSD representing this combined disturbance is shown as a solid line in Figure 6-20, and the corresponding σ_{open} is around 195 μm.

The SLQR control design with $\rho_1 = \rho_2 = 1$ is again applied to reduce the open-loop RMS OPD to the desired 3 nm RMS level in the closed loop. The probability of saturation for this disturbance model is about 30% for the voice coil and 20% for the PZT. Since the combined disturbance has a spectrum outside the voice coil bandwidth and an open-loop OPD above the stroke of the PZT, both actuators have to work together, even operate with appreciable saturation, in order to achieve the desired performance. This analysis demonstrates that it may be necessary to operate the actuators in their saturation regions under realistic nominal circumstances. If the engineers are not satisfied with the probabilities of actuator saturation for a given disturbance environment, actuator size can be changed in the ODL system design or explicit saturation penalties can be used to reduce these probabilities. The parametric studies using the combined disturbance model is presented in the next section.

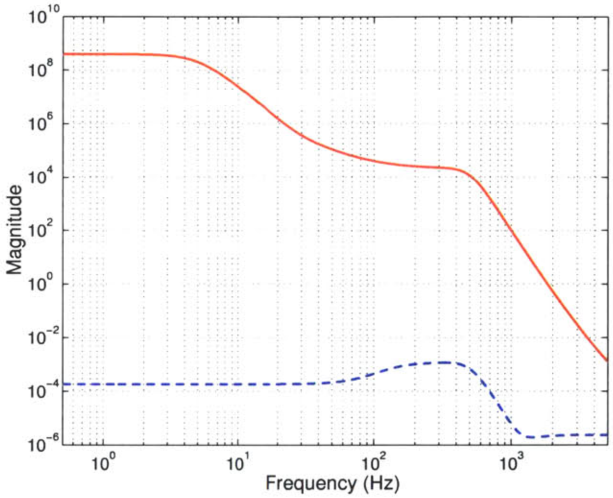

Figure 6-20: Combined disturbance PSD on the OPD output. Solid line: Open-loop PSD estimated from motor noise and reaction wheel disturbances. Dashed line: Closed-loop PSD obtained after applying active control to reduce $\hat{\sigma}_y \approx 3$ nm

6.4.2 Parameter Tradeoffs

Other design level tradeoffs can be examined using the framework developed in this thesis, evaluating the families of solutions as different system parameters are changed. For example, instead of varying disturbance intensity, one could fix the disturbance intensity as above and evaluate the tradeoff between saturation and bandwidth of the actuators. In this fashion, the SLQR framework above could also be a useful tool for sizing the components of ODL systems, given a realistic model of the expected disturbance environment.

PZT stroke and flexure stiffness

The first parameter study considers again a family of SLQR controller designs for the two-stage benchmark problem. There are two system parameters of interest in this trade study - the saturation level of the PZT actuator and the flexure stiffness of the Cat's eye cage. Since the flexure stiffness directly controls the bandwidth of the voice coil's authority on the output, it would be interesting to see how the mechanical design of the cage flexure may affect the control design solutions. For each combination of PZT saturation and flexure stiffness, the SLQR control design is again iterated until it obtains the desired 3 nm RMS closed-loop performance. For each chosen parameter the objective is to examine how the probability of saturation changes with system parameter variations.

The disturbance spectrum used in this example is composed of a low frequency component as well as a smaller magnitude, high frequency component as shown in Figure 6-20. As discussed in the previous section, the disturbance model results from merging two sets of experimental data: one corresponds to motor and the other to wheel induced vibrations, and the combined model corresponds to an open-loop OPD RMS of 195 μm. Using an output disturbance model ensures that the effects of the disturbance on OPD remain constant as the physical parameters in the plant are altered, allowing the available experimental data [23, 57] for the output spectra to be used directly.

Figure 6-21 illustrates the probability of saturation of VC and PZT as solid and dashed lines, respectively. Each set of curves (solid and dashed lines) correspond to a particular level of flexure stiffness. As the PZT stroke range increases, the probability of saturation of both actuator decreases. The PZT becomes unlikely to saturate if it has a stroke of at least 20μm for this level of disturbance intensity. From the PZT vendor catalog [30], such a PZT stroke level is well within the maximum stroke range. With the PZT out of saturation, the VC still has to work quite a bit in order to reduce the low frequency portion of the output disturbance to the specified closed-loop performance. Therefore, the probability of saturation for the VC, $1 - N_{11}$, levels off at high PZT stroke range. As the PZT stroke decreases, the probability of saturation approaches a limit where the PZT stroke is approximately 7.5 μm. If the PZT stroke is less than this value, the two-stage system will not be able to meet the desired performance.

The three sets of curves plotted in Figures 6-21 corresponds to flexure mode of $\omega_f = 5.5$,

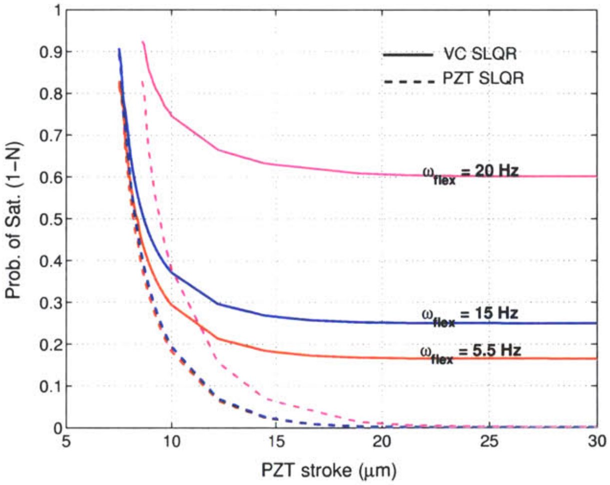

Figure 6-21: Parameter analysis on PZT stroke range and ODL flexure stiffness: probability of saturation of each actuator (solid line - voice coil and dashed line - PZT) (nominal $\omega_{flex} = 5.6Hz$)

15, and 20 Hz. Since the VC-cage system can be modelled as a second order filter, the flexure stiffness is expressed in terms of its natural frequency, i.e. $\omega_f = \sqrt{k_1/M_1}$, and the nominal flexure frequency for the above study is set at 5.6 Hz. For the given plant model and disturbance level, the voice coil becomes more likely to saturate as the flexure stiffness increases, since it is harder for the voice coil to affect the position of the ODL cage. If the disturbances are expected to have significant low frequency component, it is better to design the flexure stiffness as low as possible, so the voice coil can be more effective in reducing disturbances in the low frequency region.

PZT and voice coil strokes

The system parameter studies can also aid the actuator selection process. In this example, the stroke of the PZT and voice coil are varied over a reasonable range determined from their perspective vendor catalogs, and their probabilities of saturation for a given disturbance environment is examined. If the designer wishes to limit the probability of saturation in order to avoid excessive fatiguing of the actuators, he can choose actuator sizes that satisfy the saturation requirements for an expected disturbance level.

The disturbance spectrum used in this study is the same as the previous example and is shown in Figure 6-20. A typical voice coil stroke may range between 0.02 in (0.5 mm)

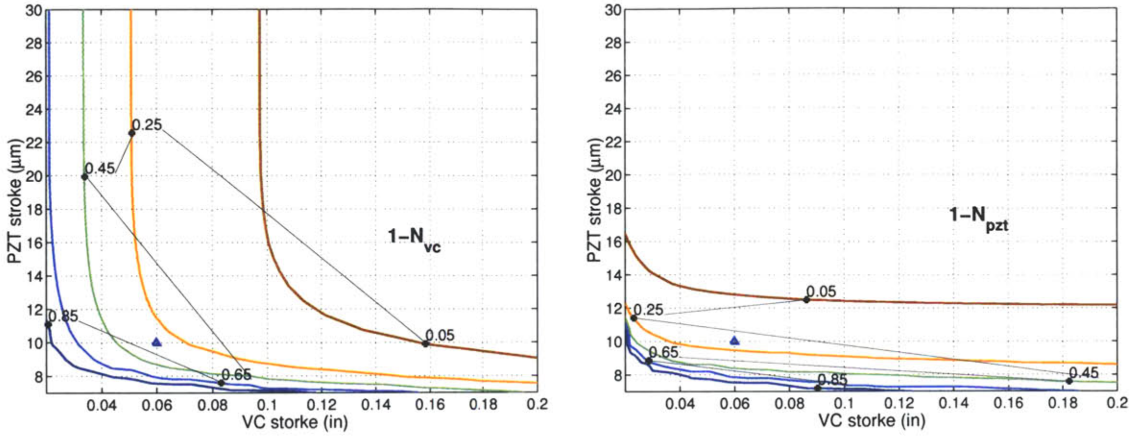

(a)

(b)

Figure 6-22: Contours of probability of saturation as a function of voice stroke and PZT stroke (a) voice coil (b) PZT

and 0.2 in (5 mm) [84], and the PZT stroke for the application considered is around 7-30 μm [30]. Figure 6-22(a) and Figure 6-22(b) are contour plots of probability of saturation of the voice coil and PZT actuator, respectively. If the designer wishes to limit the probability of saturation of both actuators to less than 5%, he can select the combination of PZT and voice coil stroke that follow the 0.05 $1 - N_{vc}$ and $1 - N_{pzt}$ contour lines. Since the actuator stroke is a discrete quantity, i.e. a PZT stroke of 14.29 μm may not be available, and making an actuator to that specification may be very costly, the cost and availability of the actuators are then used to narrow down the choices to possibly a few points on the contour line.

The small triangle on these plots indicate the nominal PZT and voice coil strokes (10 μm and 0.06 in) used for the two-stage actuator problem shown in the previous sections. This triangle may also act as a first iteration design. If the designer has additional funding to purchase new actuators, he may use these plots to decide on the best actuator to purchase in order to decrease the saturation degrees of the actuators.

The two studies shown in this section are only representative examples of the kinds of system analysis that can be conducted with the analysis and synthesis framework developed above. Many other combinations of parameter studies may also be performed to provide additional insights to the system designers.

6.5 Three Stage Design

In this section, the two-stage control design discussed in the previous section is extended to the three-stage design. The objective of this section is to demonstrate that the proposed staged-control design can be extended to more than 2 actuators, and to investigate the couplings of rigid body station keeping and optical element control. The problem setup is discussed in Section 6.1.2.

The linear open-loop transfer function from each actuator to the scaled output is shown in Figure 6-23. These plots are generated by assuming that the actuators are operating in their linear region, i.e. $N_{ii} = 1$. The peaks observed around 5.6 Hz describe the lightly damped, cage flexure mode of the ODL. The capability of each actuator on changing the OPD is also shown in the transfer function plot. The thruster has the most authority on the output OPD at low frequencies ($\omega < 0.0056$ Hz), the voice coil has most authority in the mid-frequency region (0.0056 Hz $< \omega <$ 160 Hz), and the PZT actuator is most effective in changing the OPD at high frequencies ($\omega > 160$).

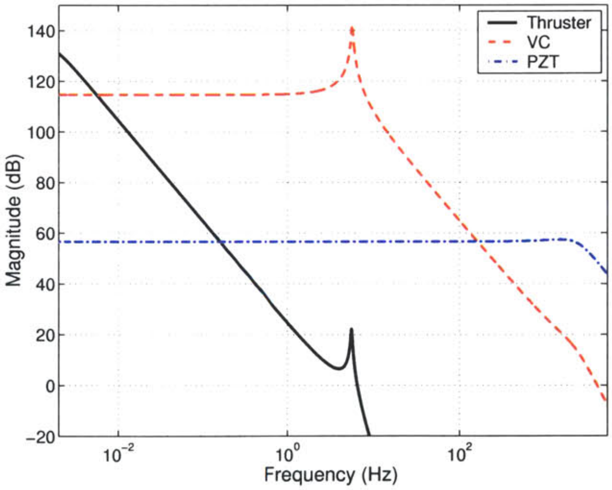

Figure 6-23: Linear open-loop transfer function from actuator input to plant output (solid line - thruster, dashed line - voice coil, dashed-dotted line - PZT actuator)

This figure also shows that the system has two "natural" hand-off frequencies at 0.0056 Hz and 160 Hz, where actuator authority changes between the thruster and the voice coil, and between the voice coil and the PZT. Furthermore, the frequency roll-off of each transfer function also models the bandwidth limitation of each actuator. The actuator force limitations are again determined from hardware specifications. The voice coil and PZT force limitations are the same as those used in the two-stage problems; they are 2 N and 10 N, respectively. The maximum thrust for a typical μN-thruster is approximately 100 μN [53].

The set of analyses conducted on the three actuator problem assumes an output disturbance model. There are three disturbance spectra examined in this section, each of which has significant frequency content in different regions of the frequency domain. One of them provokes mostly high frequency disturbances, the other one provokes low frequency disturbances, and the third one is a combination of the low and high frequency disturbances, which is similar to the experimental composite spectrum shown in Section 6.4.1. The intention is to investigate how the SLQR algorithm makes the actuator tradeoff for each of the disturbance spectra. Similar to the two-stage design problem presented in Section 6.2.1, the disturbance intensity is increased until the desired performance is no longer achievable. At each disturbance intensity level, the control design is iterated until it meets the desired closed-loop performance of 3 nm RMS OPD.

High frequency spectrum

The first spectrum is a bandpass filter that models mid- to high frequency disturbances as shown in Figure 6-24(a). Figure 6-24(b) illustrates the actuator probability of saturation as a function of open-loop RMS OPD σ_{open}, or equivalently, increasing disturbance intensity. For larger disturbance intensities, the actuators have to work harder in order to meet the performance requirement, and hence, they become more likely to saturate. Since most of the disturbance energy is concentrated in the high frequency region, the voice coil and PZT are used mostly to reduce this disturbance. On the other hand, the thruster has very small authority in high frequencies; therefore, it is not used as much as the other two actuators.

The frequency hand-offs between the PZT and the voice coil are shown as a function of increasing σ_{open} in Figure 6-24(c) and summarized in Figure 6-24(d). The hand-off frequency lowers from 224 Hz to about 75 Hz. As the disturbance intensity increases, the voice coil becomes more likely to saturate, so the hand-off frequency decreases which indicates that the PZT is taking more of the high frequency responsibility from the voice coil. The use of the PZT to "de-saturate" the voice coil has already been observed in the two-stage designs of Section 6.2.1 with a similar disturbance spectrum.

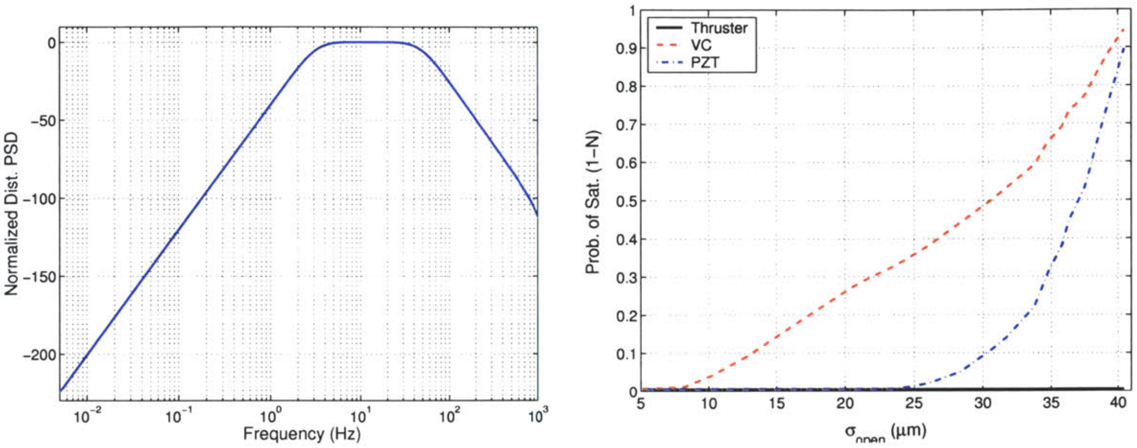

(a) (b)

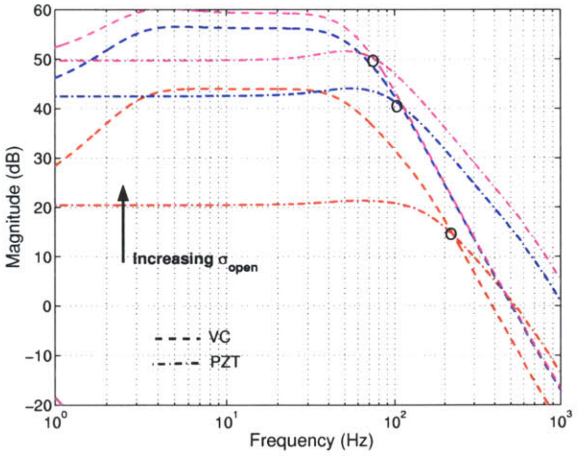

(c)

σ_{open} (μm)	5.1	23.8	37.4
Voice Coil (N_{22})	0.99	0.67	0.23
PZT (N_{33})	0.99	0.99	0.47
Hand-off (Hz) (VC-PZT)	224	107	75

(d)

Figure 6-24: Three-stage analysis with high frequency disturbance spectrum (a) Normalized disturbance PSD on the output (b) Probability of saturation of each actuator (solid - thruster, dashed - voice coil, dashed-dotted - PZT) (c) Frequency hand-off between voice coil and PZT (d) Summary of hand-off and actuator probability of saturation corresponding to three σ_{open} values used in (c)

Low frequency spectrum

The second set of analysis uses a low pass filter to model a low frequency disturbance environment as shown in Figure 6-25(a). The disturbance shape remains fixed but the disturbance level is increased in order to obtain a family of solutions. Figure 6-25(b) shows the probability of saturation of each actuator as a function of the open-loop RMS OPD σ_{open}. Since the disturbance energy is concentrated at low frequencies, the thruster and voice coil which possess large authority in this region are used to reduce most of these disturbances. The PZT with smaller authority at low frequencies is not used as much as the other two actuators in this design, and it does not saturate until much larger levels of σ_{open}.

When the disturbance intensity changes, the hand-off frequencies also change as shown in Figure 6-25(c). The top plot zooms into the low frequency range to better illustrate the hand-off between the thruster and the voice coil. As the disturbance level increases, the voice coil starts to saturate first, but the thruster prevents it from becoming completely saturated. Therefore, the hand-off frequency increases or moves to the right on the plot as an increasing function of σ_{open}. For this problem, the thruster/voice coil hand-off frequencies correspond to three increasing level of disturbance intensities are 0.043, 0.048, and 0.052 Hz. The bottom plot in Figure 6-25(c) shows the hand-off frequency between the voice coil and the PZT. Similar to the high frequency disturbance problem, the PZT attempts to desaturate the voice coil at high frequencies as the voice coil begins to saturate. In this case, the hand-off frequencies lowers from 362 Hz to 31 Hz. The hand-off frequency decreases or move to the left as the PZT takes more high frequency responsibility away from the voice coil.

Combined frequency spectrum

In reality, the system will likely experience a combination of low and high frequency disturbances as discussed above. The third set of analysis adds the low and high frequency disturbances used previously, and the combined disturbance is illustrated in Figure 6-26(a). The probability of saturation of each actuator as a function of σ_{open} is plotted in Figure 6-26(b). In this case, the control design prefers to use the voice coil, since it can effectively reduce both low and high frequency disturbances. As a result, the voice coil saturates first,

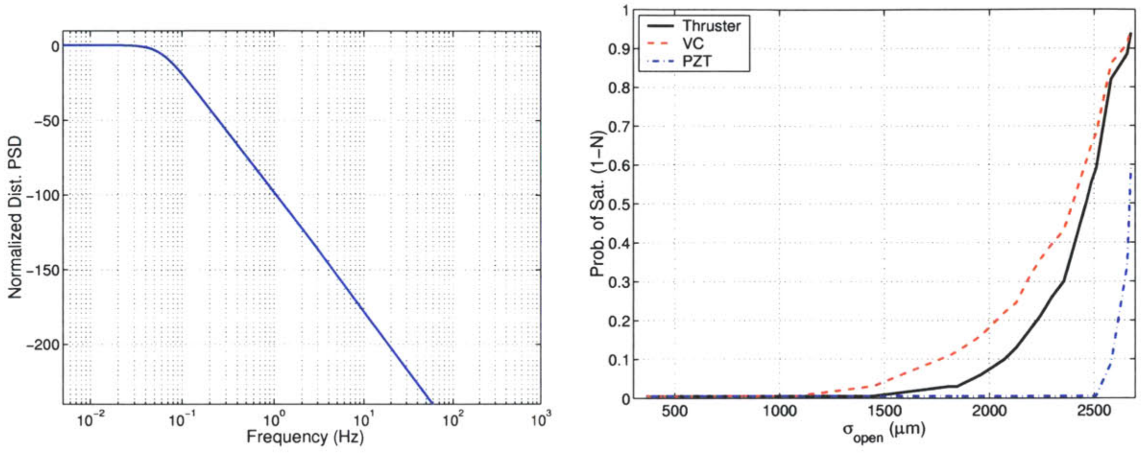

(a) (b)

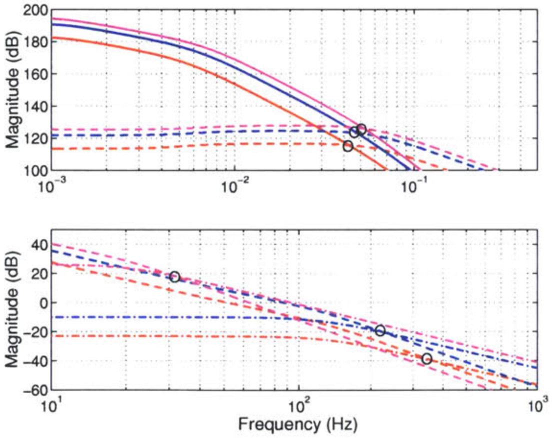

(c)

σ_{open} (μm)	724	1846	2660
Thruster (N_{11})	0.99	0.96	0.12
Voice Coil (N_{22})	0.99	0.88	0.09
PZT (N_{33})	0.99	0.99	0.66
Hand-off (Hz) (Thruster-VC)	0.043	0.048	0.052
Hand-off (Hz) (VC-PZT)	362	277	31

(d)

Figure 6-25: Three-stage analysis with low frequency disturbance spectrum (a) Normalized disturbance PSD on the output (b) Probability of saturation of each actuator (solid - thruster, dashed - voice coil, dashed-dotted - PZT) (c) Top plot: frequency hand-off between thruster and voice coil. Bottom plot: frequency hand-off between voice coil and PZT (d) Summary of N and hand-off frequencies at three σ_{open} values and the other actuators begin to help and become more likely to saturate at larger σ_{open}. Eventually all three actuators asymptote to a vertical limit correspond to $\sigma_{open} = 1350$ μm; above this level of open-loop RMS OPD, the actuators will no longer be able to achieve the 3 nm RMS OPD in the closed loop.

The frequency hand-offs for the combined disturbance case are shown in Figure 6-26(c). The top and bottom plots again demonstrate the frequency hand-off of thruster/voice coil and voice coil/PZT, respectively. The hand-off frequency between thruster and voice coil shifts to the right as the intensity level increases - 0.043, 0.069, 0.096 Hz. This phenomenon indicates that the thruster is attempting to de-saturate the voice coil and taking on more of the low frequency disturbances. The hand-off frequency between voice coil and PZT shifts to the left from 221 to 112 and then to 68 Hz as disturbance intensity increases. Similarly this behavior illustrates that the PZT tries to reduce the voice coil effort by suppressing more high frequency disturbances. The hand-off frequencies and the probability of saturation of each actuator corresponding to the three σ_{open} values used in Figure 6-26(c) are summarized in Figure 6-26(d).

Since the actual disturbance environment is not known in advance, it is difficult to determine the exact disturbance shape and level of the actual disturbances. The disturbance models used in the above analysis have incorporated as much of the realistic experimental data as currently available [23, 27, 46, 57]. In practice the designers will have to approximate the expected level and shape of the disturbance, and then use the proposed framework to examine actuator behaviors for a given disturbance model. Furthermore, the framework also allows the designer to investigate the sensitivity of the results to the frequency spectrum and/or intensity levels. Other system trade studies as performed for the two actuator system can also be conducted to provide more information to the system designer.

Before concluding this chapter, the partition of actuator authorities in the frequency domain for two disturbance intensity levels of the combined spectrum are illustrated in Figure 6-27(a) and 6-27(b). There is no new information introduced by these two figures. They are used simply to give a more complete picture of how the SLQR algorithm stages the available actuators for the control problem. Note that as the disturbance intensity increases, the voice coil portion of the spectrum is "squeezed" from both sides, as the PZT and thruster work harder to keep the voice coil out of saturation.

The actuator authority distribution for the closed-loop system is similar to that observed

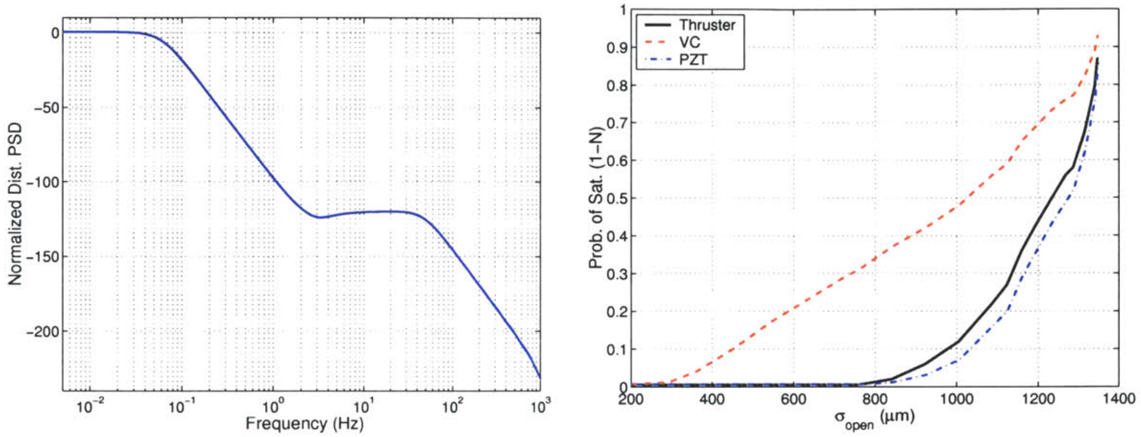

(a)

(b)

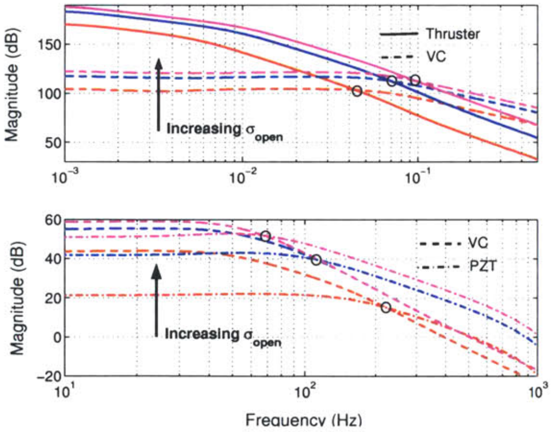

(c)

σ_{open} (μm)	181	761	1340
Thruster (N_{11})	0.99	0.99	0.21
Voice Coil (N_{22})	0.99	0.69	0.11
PZT (N_{33})	0.99	0.99	0.24
Hand-off (Hz) (Thruster-VC)	0.043	0.069	0.096
Hand-off (Hz) (VC-PZT)	221	112	68

(d)

Figure 6-26: Three-stage analysis with combined low and high frequency disturbances (a) Normalized disturbance PSD on the output (b) Probability of saturation of each actuator (solid - thruster, dashed - voice coil, dashed-dotted - PZT) (c) Top plot: frequency hand-off between thruster and voice coil. Bottom plot: frequency hand-off between voice coil and PZT in the open-loop plant. The thruster has more authority in low frequencies, the voice coil in mid frequencies, and the PZT in high frequencies. However, the closed-loop, hand-off frequencies are very different from the open-loop "natural" hand-offs (0.0056 Hz and 160 Hz). The controller has redistributed the actuator responsibilities in the closed loop, taking into account the disturbance spectrum, the open-loop dynamics, and the actuator saturation limitations. These plots are alternate ways for visualizing staged controller designs in the frequency domain.

6.6 Summary

The control synthesis framework presented in the previous chapter is applied to the optical pathlength control problem in this chapter. The capabilities of the tools developed in the thesis are demonstrated on the Two- and three-staged actuation systems. Important findings in this chapter are summarized as follows:

- By varying the disturbance intensity levels, the largest open-loop RMS OPD (σ_{open}) that can be reduced to less than 3 nm RMS OPD in the closed-loop can be determined.

- To understand how the controller accomplishes actuator staging, the control authority hand-off in the frequency domain can be visualized through linearized transfer functions. From these plots, the frequency at which one actuator hands-off control authority to another can be readily identified.

- As the disturbance increases, the hand-off frequencies in a classical LQR design remain fixed, since it is unaware that one or more actuators may begin to saturate. For the SLQR designs, the hand-off frequency shifts with changing disturbance levels to indicate that the controller is redistributing control authority among actuators as a function of actuator capabilities (e.g. bandwidth and saturation level).

- In addition to changing disturbance intensities, the proposed technique can be used to generate a family of solutions as the disturbance frequency spectrum changes, and thereby, testing the sensitivity of the SLQR solution to changes in the disturbance model.

- It is also possible to fix the disturbance model and evaluate the tradeoff between saturation and bandwidth of actuators. These studies have shown that it is more de-

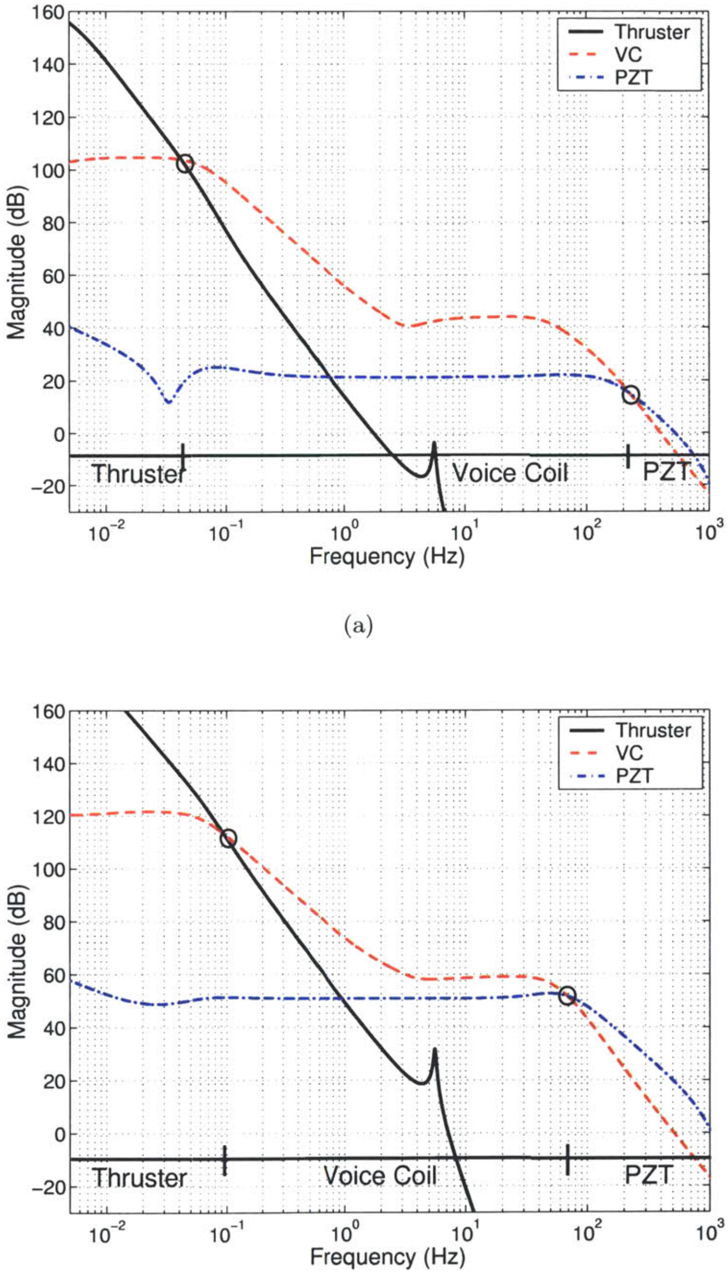

(a)

(b)

Figure 6-27: Visualization of actuator authority hand-off using combined disturbance spectrum at two σ_{open} values: (a)$\sigma_{open} = 181$ μm (b) $\sigma_{open} = 1340$ μm sirable to reduce the optical delay line flexure stiffness so that the voice coil may have high authority at the low frequency region. When high frequency disturbances are present, there is a minimum stroke requirement on the PZT. The proposed methodology can be used to find the minimum PZT stroke needed in order to achieve the desired performance requirement.

- The proposed tool may also aid designers in the actuator selection process. By plotting the probability of saturation contours as a function of actuator sizes for an expected disturbance model, the designer can choose combinations of actuator properties that satisfy the limits on the probability of saturation of each actuator while taking cost constraints into account.
- In this chapter, the minimum electrical power designs are presented. The minimum electrical power solutions tend to utilize the PZT as much as possible, which in turn cause the PZT to saturate quite often. However, excessive usage of the PZT actuator may damage its material and may even cause it to fail. The saturation weighings are then applied to generate a different family of solutions, so the designers can continue to penalize electrical power usage and limit the probability of saturation of each actuator at the same time.
- A three-stage design is presented at the end of this chapter to demonstrate the couplings between spacecraft control and optical control systems. The disturbance intensity is varied for this problem; the achievable performance and the probability of saturation of each actuator are computed for each intensity level. As the disturbance intensity increases, the thruster attempts to offload the voice coil low frequency responsibilities, so the hand-off frequency between the thruster and voice coil increases. The PZT actuator also tries to take the high frequency responsibilities away from the voice coil as the voice coil starts to saturate. Therefore, the hand-off frequency between the voice coil and the PZT decreases for larger disturbances.

Chapter 7

Conclusions and Recommendations

This chapter will provide a brief summary of the thesis. The major contributions of this work are highlighted, and future directions for extending the current framework are suggested.

7.1 Thesis Summary

Space-based interferometry is a promising technology that can greatly enhance astronomical imaging and may enable the detection of Earth-like planets outside of our solar system. However, studies have shown that these systems will require nanometer level stabilization of the optical instrument to achieve these science goals. For a typical TPF mission scenario, with four collecting apertures in a linear array configuration, a stochastic analysis of the effects of perturbations on the optical geometry shows that 3nm RMS stabilization of the optical path difference is required to achieve the extrasolar planet detection threshold.

The actual physical changes to the optical geometry of an interferometer will arise from vibrations and disturbances acting on the spacecraft and the optical devices. It is unlikely that the magnitude of the resulting geometric perturbations will be below the specified RMS levels. Therefore, a suitable actuation system and appropriate control strategy must be used to maintain the geometric perturbations within the specified tolerances.

If a single actuator with sufficient bandwidth and stroke were available, standard linear control synthesis techniques could be used to achieve the desired performance. Unfortunately, such an actuator does not exist – all physical actuators have saturation and bandwidth limits. Actuators with larger strokes tend to have lower bandwidth and coarser resolution, while the high bandwidth actuators tend to have smaller stroke and finer resolution. As a result, all current design candidates for space interferometer control plan to use several actuators with overlapping stroke and bandwidth characteristics, thus forming a *staged* actuation system that attempts to mimic the capabilities of the ideal single actuator.

In a staged actuation system, each actuator has bandwidth limitations and saturation constraints. While the bandwidth limitation can be modelled as a frequency domain roll-off, the saturation effects are nonlinear and it is much more difficult to accurately quantify their effect on closed-loop performance. It should be emphasized that one or more actuators in a staged actuation system are expected to saturate during normal operation; otherwise, there would be no need for staging. Saturation effects thus cannot be ignored, and must be handled properly in the staged controller design. Other actuator nonlinear effects, such as quantization and resolution, have been shown to be much less significant than saturation effects in the studies conducted in the thesis, and often can be neglected.

Given a staged actuation system and a specified feedback control law, the first challenge is to predict the closed-loop performance when it is subjected to random perturbations. Two analytical prediction methodologies are developed in this thesis, based on stochastic Lyapunov and stochastic linearization theories respectively. These two methods have been formally shown to be dual under the stationary Gaussian assumption, and both methods provide the same predictions. The analytical predictions from these analysis methods provide quick estimates of the nonlinear closed-loop performance, and have been shown to provide reasonably accurate approximation with errors typically less than 10% when compared with numerical simulations.

With a performance analysis tool in hand, the focus becomes the staged controller synthesis. In addition to satisfying closed-loop performance requirements, it is also important to minimize actuator usage due to limited power resources onboard the spacecraft carrying the optics. With these objectives, a standard LQR/LQG strategy would be appropriate, if saturation were not a concern. Since the actuators may in fact saturate, it is necessary to use the new performance prediction tool to estimate the nonlinear closed-loop performance. A staged controller could, in principle, be designed by iterating the classical LQR synthesis and new prediction analysis in a serial fashion until the desired performance is obtained. However, the resulting controller may not result in a stable stochastically linearized system; that is, $A + B_2NK$ may not be Hurwitz, since the LQR control synthesis does not take into account the stochastic linearization gain N which arises in the performance analysis.

To ensure stability of the stochastically linearized closed-loop system, a staged design methodology that couples the prediction analysis (stochastic linearization) with the LQR/LQG control synthesis is suggested in the thesis as a design methodology for staged control systems. By simultaneously solving the linear quadratic synthesis and stochastic linearization analysis problems (SLQR/SLQG), the resulting closed-loop system is guaranteed to have a locally stable stochastic linearization. Moreover, the control cost can be iterated in this framework to achieve a design with required performance, assuming the desired performance is within the capabilities of the actuators. The resulting staged controller design directly incorporates actuator bandwidth and saturation limitations and automatically trades these constraints to achieve the desired performance.

Returning to the original interferometer problem, the SLQR/SLQG algorithm is shown not only provide a suitable control design for a given optical system and disturbance environment, it is also capable of providing important design information such as the achievable performance and the probability of saturation of each actuator. By changing system parameters such as the size and bandwidth of the actuator and the disturbance model, the staged control algorithm can be used to investigate how each parameter affects the closed-loop performance or actuator saturation levels. Consequently the proposed algorithm enables system level trade studies as well as aiding the system designer in the actuator selection process.

7.2 Contributions

The following list summarizes the principle contributions made in this thesis:

- A statistical analysis technique has been developed in order to determine the optical tolerances needed for extra-solar planet detection for nulling interferometers. The technique developed is capable of examining the effects of multiple perturbations simultaneously, and investigating the influence of correlated disturbances on the interferometer performance. These capabilities significantly extend the previous results in this direction [64, 52] which examine only single variable perturbations.
- The statistical analysis was applied to a TPF baseline configuration consisting of four apertures in a linear interferometer array. The results show that to achieve a mean null

depth on the order of 10^{-6}, the acceptable level of RMS aperture shear (or effective change in baseline) is about 1 m, and the RMS optical path difference (OPD) must be maintained below 3 nm for a nominal wavelength of 10 μm. Previously, results of this form were available only for two-aperture systems [52]. The current development can quantify the RMS optical perturbations for an arbitrary number of apertures in any two-dimensional interferometer array.

- Two analytical tools were developed to predict the closed-loop RMS output for a stochastically driven feedback system with actuator nonlinearities. These approximation strategies were derived from both stochastic Lyapunov and stochastic linearization theories. Furthermore, the stochastic Lyapunov and stochastic linearization prediction methods were formally shown to result in a *dual* set of equations for predicting RMS performance. The use of stochastic Lyapunov theory for performance prediction in this fashion is a new result, as is the duality with stochastic linearization technique. The demonstration of a deep connection between these two methods presents a new perspective on stochastic linearization theory, and adds more rigor to this classic quasi-linearization technique.

- Explicit procedures and numerical algorithms for solving the coupled nonlinear equations which determine the output variance have been developed. MATLAB code was written to implement the numerical algorithms. The predicted variances are typically shown to be within 10% of the values observed from exhaustive numerical simulations.

- The standard LQR control synthesis followed by stochastic linearization prediction analysis (LQR+SL) has been demonstrated to have several drawbacks for controller designs with multiple saturating actuators. Since the LQR control synthesis is unaware of saturation limitations, the resulting controller may not provide local stability of the closed-loop nonlinear system. In fact, any control synthesis framework for such systems that does not properly incorporate the performance prediction in the control design procedure also cannot guarantee a locally stable closed-loop system.

- By merging the analytical prediction tool with $\mathcal{H}_2$ optimization, a controller synthesis technique (SLQR/SLQG) has been proposed which explicitly takes into account actuator nonlinearities and bandwidth. This control design significantly extends the prior work [21] which considered only a single saturating actuator. The new algorithm can handle multiple actuators, and more general actuator nonlinearities. Since the proposed SLQR/SLQG framework couples the controller design and performance prediction analysis, it also ensures that the resulting controller guarantees local closed-loop stability.

- The new multi-input SLQR/SLQG algorithms have been proposed as a formal synthesis tool for staging controller design, and their utility in this context demonstrated. The resulting staged control system is capable of making "optimal" hand-off choices based upon the linear and nonlinear characteristics of the actuators. The new controller is designed using modern optimization techniques, enabling rapid controller synthesis for system level trade studies. Previously, separate controllers were designed for each actuator loop [23, 27, 46, 57], and the authority hand-off was determined subjectively by the designers. In the absence of performance analysis for saturating actuators, studying system behavior required experiments or exhaustive simulations. These techniques often require substantial effort on controller parameter tuning and provide no guarantees of stability in the formal sense. All these concerns are addressed with the proposed synthesis methodology.

- Software algorithms and MATLAB code have been developed to solve the coupled multi-input SLQR/SLQG equations for staging control synthesis. The code is currently capable of solving up to a three-stage controller design, with an arbitrary state dimension.

- The use of proposed analysis and synthesis framework for system design studies has been extensively demonstrated, in particular to:
    1. Quantify achievable performance for stochastic systems with nonlinear actuator constraints.
    2. Quantify the utilization of each actuator by predicting the probability of saturation.
    3. Explicitly limit the saturation of a particular actuator in system designs.
    4. Examine the sensitivity of a particular design to changes in the physical parameters (actuator size and bandwidth) and disturbance environment.

    5. Quantify and visualize actuator control authority handoff for a given staged control configuration.

  None of the above studies, typical of the design concerns for a staging controller, could have been carried out with previously available techniques, except by exhaustive numerical simulations.

- The system design studies stated above are performed on the interferometer problem. Some of the lessons-learned are summarized here:

    1. Given a comparable disturbance spectrum, the proposed control design method achieves performance similar to the baseline JPL control designs, without the need to tune control parameters manually.
    2. Two parametric studies are used to demonstrate how the proposed tool can help with mechanical design decisions (flexure stiffness) and the actuator selection process (stroke of voice coil and PZT actuators). Since the proposed algorithm allows the actuator to operate in saturation, it enables use of smaller, lighter, and cheaper actuators while still achieving the desired performance.
    3. When electrical power must be minimized, the design process prefers to use the PZT until its control authority is exhausted. By explicitly also penalizing saturation of the PZT, the algorithm can be forced to utilize the voice coil so as to prevent excessive wear of this actuator.
    4. The proposed controller is applied to a three-stage benchmark problem in order to investigate the couplings of thruster and optical element control. The studies show that the proposed algorithm is capable of making the appropriate actuator trades for different disturbance environments. In contrast to the current "stop and observe" paradigm, this coupling of the spacecraft and optical control loops enables observations even while the spacecraft position is being actively controlled.

7.3 Recommendations for Future Work

There are several directions in which the work conducted for this thesis can be strengthened or extended:

- The tradeoff analysis performed for the space interferometer mission depends on the disturbance spectrum given. In order to improve the fidelity of analysis, a more accurate model of the expected disturbance environment for the optics of space interferometers is necessary. It is unlikely that an exact disturbance model will be available, but a good approximate of the shape and intensity of the disturbance spectrum may be used for a preliminary analysis. Since the controller redesign can be accomplished rapidly, it is used to test the sensitivity of the results to the disturbance models or update the designs as more accurate disturbance models become available.

- The present analysis and synthesis framework have been tested extensively on simple, representative models. However, they have not been directly tested on hardware. To demonstrate the applicability of this framework and develop confidence in the new technique, the control designs should be tested on JPL interferometer testbed and compared against other designs based on more traditional methods.

- Solving for the optimal controller requires the solution to a set of coupled nonlinear algebraic equations. The numerical routines employed for solving these equations are based on a exhaustive search method. Better nonlinear solvers should be implemented to improve the speed and robustness of the current numerical algorithm.

- Actuation and sensing systems are the two important components to a control system. The current framework has focused on the actuator limitations and staging of actuators with different characteristics. A natural extension of this work is to incorporate sensor nonlinearities in order to appropriately stage the usage of measurement sensors.

- The primary objective of the control system designed above is to reject random disturbances during the observation mode of the interferometer operation. Another interferometer mode of operation is the search mode, where the optical delay line may be commanded to follow a specified trajectory. Therefore, it is necessary to extend the current framework to include tracking applications in order to ensure that the performance requirement is met during all operations.

Bibliography

[1] J. R. P. Angel and N. J. Woolf. An imaging nulling interferometer to study extrasolar planets. *Astrophysical Journal*, 475:373–379, 1997.

[2] C. A. Beichman, N. J. Woolf, and C. A. Lindensmith. *The Terrestrial Planet Finder Book*. Jet Propulsion Laboratory, 1999.

[3] Dennis S. Bernstein and Anthony N. Michel. A chronological bibliography on saturating actuators. *International Journal of Robust and Nonlinear Control*, 5:375–380, 1995.

[4] Max Born and Emil Wolf. *Principles of Optics*. Cambridge University Press, seventh edition, 1999.

[5] R. N. Bracewell and R. H. MacPhie. Searching for nonsolar planets. *ICARUS*, 38:136–147, 1979.

[6] Roger W. Brockett and Daniel Liberzon. Quantized feedback stabilization of linear systems. *IEEE Transactions on Automatic Control*, 45(7):1279–1289, 2000.

[7] K. Burrage and P. M. Burrage. High strong order explicit Runge-Kutta methods for stochastic ordinary differential equations. *APPLIED NUMERICAL MATHEMATICS*, 22(1-3):81–101, November 1996.

[8] M. M. Colavita. Ground-based narrow-angle astrometry. In Peter Lawson, editor, *Principles of Long Baseline Interferometry*, pages 177–181. Jet Propulsion Laboratory, 2000.

[9] Stephen H. Crandall. *Dynamics of Mechanical and Electromechanical Systems*. Krieger, 1983.

[10] S. Crawshaw and G. Vinnicombe. Local stability properties of systems with saturation and deadzone nonlinearities. In *Proc. of 37th IEEE Conference on Decision & Control*, pages 897–902, Tampa, Florida, 1998.

[11] Sasha Cyganowski, Peter Kloeden, and Jerzy Ombach. *From Elementary Probability to Stochastic Differential Equations with MAPLE*. Springer, 2000.

[12] Hua Deng, Miroslav Krstić, and Ruth J. Williams. Stabilization of stochastic nonlinear systems driven by noise of unknown covariance. *IEEE Transactions on Automatic Control*, 46(8):1237–1253, 2001.

[13] Laila Elias. A structurally coupled disturbance analysis method using dynamic mass measurement techniques, with application to spacecraft- reaction wheel systems. Master's thesis, MIT, 2001.

[14] C. E. Eyerman and J. F. Shea. A systems engineering approach to disturbance minimization for spacecraft utilizing controlled structures technology. MITSERC Report 2-90, MIT, Aeronautics and Astronautics Department, 1990.

[15] P. Florchinger. Feedback stabilization of affine in the control stochastic differential systems by the control lyapunov function method. *SIAM Journal on Optimization*, 35:500–511, 1997.

[16] I-Kong Fong and Chih-Chin Hsu. State feedback stabilization of single input systems through actuators with saturation and deadzone characteristics. In *Proc. of 39th IEEE Conference on Decision & Control*, pages 3266–3271, Sydney, Australia, 2000.

[17] Gene F. Franklin, J. David Powell, and Michael L. Workman. *Digital Control of Dynamic Systems.* Addison-Wesley, 1990.

[18] Manuel Gamero-Castaño and Vladimir Hruby. Characterization of a colloid thruster performing in the micro-newton thrust range. *27th International Electric Propulsion Conference*, (IEPC-01-282), 2001.

[19] A. Gelb. *Applied optimal estimation.* M.I.T. Press, 1974.

[20] A. Gelb and W. E. Vander Velde. *Multiple-input describing functions and nonlinear system design.* McGraw-Hill, Inc., 1968.

[21] C. Gökçek, P. Kabamba, and S. Meerkov. An LQR/LQG theory for systems with saturating actuators. *IEEE Trans. Automatic Control*, 46:1529–1542, 2001.

[22] Joseph W. Goodman. *Introduction to Fourier Optics.* McGraw Hill, second edition, 1998.

[23] R. L. Grogan, G. H. Blackwood, and R. J. Calvet. Optical delay line nanometer level pathlength control law design for space-based interferometry. *SPIE Int. Symposium on Astronomical Interferometry*, April 1998.

[24] Homero Gutierrez. *Performance Assessment and Enhancement of Precision Controlled Structures During Conceptual Design.* PhD dissertation, MIT, Department of Aeronautics and Astronautics, 1999.

[25] R. Z. Has'minskǐ. *Stochastic Stability of Differential Equations.* Sijthoff & Nordhoff, 1980.

[26] Eugene Hecht. *Optics.* Addison-Wesley, fourth edition, 2002.

[27] J. J. Hench, B. Lurie, R. Grogan, and R. Johnson. Implementation of nonlinear control laws for an optical delay line. *IEEE Aerospace Conference*, March 2000.

[28] Vlad Hruby, Manuel Gamero-Castaño, Paul Falkos, and Suren Shenoy. Micro newton colloid thruster system development. *27th International Electric Propulsion Conference*, (IEPC-01-281), 2001.

[29] Tingshu Hu and Zongli Lin. Semi-global stabilization with guaranteed regional performance of linear systems subject to actuator saturation. In *Proc. of American Control Conference*, pages 4388–4392, Chicago, Illinois, June 2000.

[30] Physik Instrumente. http://www.physikinstrumente.de/products/section4/content.php.

[31] *JPL personal communication.*

[32] Arhtur E. Bryson Jr. and Yu-Chi Ho. *Applied Optimal Control.* Hemisphere Publishing Corporation, 1975.

[33] I. E. Kazakov. Generalization of the method of statistical linearization to multidimensional systems. *Auto. Remote Control*, 26:1201–1206, 1965.

[34] Hassan K. Khalil. *Nonlinear Systems.* Prentice Hall, second edition, 1996.

[35] S. Kirkpatrick, C. D. Gelatt, and M. P. Vecchi. Optimization by simulated annealing. *Science*, 220(4598):671–680, May 1983.

[36] Mayuresh V. Kothare, Peter J. Campo, Manfred Morari, and Carl N. Nett. A univied framework for the study of anti-windup designs. *Automatica*, 30(12):1869–1883, 1994.

[37] Toshihiro Kubo-oka and Arata Sengoku. Solar radiation pressure model for the relay satellite of selene. *Earth Planets Space*, 51:979–986, 1999.

[38] R. A. Laskin and M. S. Martin. Control/structure system design of a spaceborne optical interferometer. In *Proc. AAS/AIAA Astrodynmics Specialist Conference 89-424*, 1989.

[39] Kyung-Sup Lee and Abraham H. Haddad. Stabilization of stochastic quantized control systems. In *Proc. of American Control Conference*, pages 965–969, San Diego, CA, 1999.

[40] A. Leger, J. M. Mariotti, B. Menneson, M. Olivier, J. L. Puget, D. Rouan, and J. Schneider. Could we search for primitive life on extrasolar planets in the near future? the darwin project. *ICARUS*, 123:249–255, 1996.

[41] Daniel Liberzon. A hybrid control framework for systems with quantization. In *Proc. of 40th IEEE Conference on Decision & Control*, pages 1217–1222, Orlando, FL, 2001.

[42] Daniel Liberzon and Roger W. Brockett. Nonlinear feedback systems perturbed by noise: steady-state probability distributions and optimal control. *IEEE Transactions on Automatic Control*, 45(6):1116–1130, 2000.

[43] Daniel Liberzon and Roger W. Brockett. Spectral analysis of fokker-planck and related operators arising from linear stochastic differential equations. *SIAM Journal on Control and Optimization*, 38(5):1453–1467, May 2000.

[44] Zongli Lin. H_∞-almost disturbance decoupling with internal stability for linear systems subject to input saturation. *IEEE Transaction on Automatic Control*, 42(7):992–995, 1997.

[45] Ketao Liu, Robert E. Skelton, and Karolos Grigoriadis. Optimal controllers for finite wordlength implementation. *IEEE Transactions on Automatic Control*, 37(9):1294–1304, 1992.

[46] Boris J. Lurie, John J. Hench, Asif Ahmed, and Fred Y. Hadaegh. Nonlinear control of the optical delay line pathlength. *Proc. SPIE*, 3692, April 1999.

[47] P. Kokotovic M. Kristic, I. Kanellakopoulos. *Nonlinear and Adaptive Control Design.* John Wiley and Sons, Inc., 1995.

[48] Brian Makins. Interferometer architecture trade studies for the terrestrial planet finder mission. Master's thesis, MIT, 2002.

[49] X. Mao. Stochastic versions of the lasalle theorem. *Journal on Differential Equations*, 153:175–195, 1999.

[50] Rebecca Masterson. Development and validation of empirical and analytical reaction wheel disturbance models. Master's thesis, MIT, 1998.

[51] Bertrand Mennesson and Jean Marie Mariotti. Array configuration for a space infrared nulling interferometer dedicated to the search for earthlike extrasolar planets. *ICARUS*, 128:202–212, 1997.

[52] Bertrand Mennesson, Marc Ollivier, and Cyril Ruilier. Use of single-mode waveguilds to correct the optical defects of a nulling interferometer. *ICARUS*, 128:202–212, 1997.

[53] S. M. Merkowitz, P. G. Maghami, A. Sharma, W. D. Willis, and C. M. Zakrzwski. A μnewton thrust-stand for lisa. Technical report, NASA Goddard Space Flight Center.

[54] Maxon motor usa. *http://www.maxonmotorusa.com/products/.*

[55] Eric F. Mulder, Mayuresh V. Kothare, and Manfred Morari. Multivariable anti-windup controller synthesis using linear matrix inequalities. *Automatica*, 37:1407–1416, 2001.

[56] Nasa's origins program. *http://origins.jpl.nasa.gov/.*

[57] Gregory W. Neat, James W. Melody, and Boris J. Lurie. Vibration attenuation approach for spaceborne optical interferometers. *IEEE Trans. Control Systems Technology*, 6, November 1998.

[58] Bernt Øksendal. *Stochastic Differntial Equations.* Springer, 2000.

[59] Z. Pan and T. Başar. Backstepping controller design for nonlinear stochastic systems under a risk-sensitive cost criterion. *SIAM Journal on Optimization*, 37:957–995, 1999.

[60] A. Papoulis. *Probability, random variables, and stochastic processes.* McGraw-Hill, Inc., 1991.

[61] Thomas E. Pare, Haitham Hindi, Jonathan P. How, and D. Banjerdpongchai. Local control design for systems with saturating actuators using the popov criteria. In *Proc. of American Control Conference*, pages 3211–3215, San Diego, California, 1999.

[62] Thomas E. Pare, Haitham Hindi, Jonathan P. How, and Stephen P. Boyd. Synthesizing stability regions for systems with saturating actuators. In *Proc. of IEEE Conference on Decision & Control*, pages 1981–1982, Tampa, Florida, 1998.

[63] Jong-Koo Park and Chong-Ho Choi. Dynamic compensation methods for multivariable control systems with saturating actuators. *IEEE Transaction on Automatic Control*, 40(9):1635–1640, September 1995.

[64] Irene L. Porror, Wesley A. Traub, and Nathaniel P. Carleton. Effect of telescope alignment on a stellar interferometer. *Applied Optics*, 38:6055–6067, 1999.

[65] Jeffrey Reichbach. Micropropulsion system selection for precision formation flying satellites. Master's thesis, MIT, 2001.

[66] Wolfgan Reinelt. H_∞ loop shaping for systems with hard bounds. In *Proc. of Int Symp on Quantitative Feedback Theory and Robust Frequency Domain Methods*, pages 89–103, Durban, South Aferica, August 1999.

[67] Wolfgan Reinelt. Robust control of a two-mass-spring system subject to its input constraints. In *Proc. of American Control Conference*, pages 1817–1821, Chicao, Illinois, June 2000.

[68] Hanz Richter, Eduardo A. Misawa, and Brian D. O'Dell. Stability analysis of discrete linear systems with quantized input. In *Proc. of American Control Conference*, pages 2991–2996, Anchorage, AK, May 2002.

[69] J. B. Roberts and P. D. Spanos. *Random Vibration and Statistical Linearization.* John Wiley and Sons, 1990.

[70] Ali Saberi, Zongli Lin, and Andrew R. Teel. Control of linear systems with saturating actuators. *IEEE Transaction on Automatic Control*, 41(3):368–378, 1996.

[71] Floyd E. Saner. *Pittman, Servo Motor Application Notes.* Pittman, seventh edition, 1993.

[72] E. Serabyn. Nulling interferometry and planet detection. In Peter Lawson, editor, *Principles of Long Baseline Interferometry*, pages 273–292. Jet Propulsion Laboratory, 2000.

[73] Hector J. Sussmann, Eduardo D. Sontag, and Yudi Yang. A general result on the stabilization of linear systems using bounded controls. *IEEE Transaction on Automatic Control*, 39(12):2411–2424, 1994.

[74] Andrew R. Teel. Global stabilization and restricted tracking for multiple integrators with bounded controls. *Systems and Control Letters*, 18(12):165–171, 1992.

[75] Andrew R. Teel. Semi-global stabilization of linear null controllable systems with input nonlinearities. *IEEE Transaction on Automatic Control*, 40:96–100, 1995.

[76] T. A. ten Brummelaar. Design of stellar interferometers. In Peter Lawson, editor, *Principles of Long Baseline Interferometry*, pages 87–96. Jet Propulsion Laboratory, 2000.

[77] U. H. Thygesen. A survey of lyapunov techniques for stochastic differential equations. Technical Report 8, Tech. Univ. Denmark, 1987.

[78] Cho W.S. To. *Nonlinear Random Vibration: Analytical Techniques and Applications.* Swets and Zeitlinger B.V., 2000.

[79] Jet propulsion laboratory - terrestrial planet finder. *http://planetquest.jpl.nasa.gov/TPF/index.htm.*

[80] Wesley A. Traub. Beam combination and fringe measurement. In Peter Lawson, editor, *Principles of Long Baseline Interferometry*, pages 31–58. Jet Propulsion Laboratory, 2000.

[81] N. A. Tsyganenko. Global quantitative models of the geomagnetic field in the cislunar magnetosphere for different disturbance levels planet. *Space Science*, 35:1347–1358, 1987.

[82] Feng Tyan and Dennis S. Bernstein. Global stabilization of systems containing a double integrator using a saturated linear controller. *International Journal of Robust and Nonlinear Control*, 9:1143–1156, 1999.

[83] Stephen Unwin and Rudolph Danner. *The Space Interferometry Mission: Taking the Measure of the Universe.* Jet Propulsion Laboratory, 1999.

[84] Bei technologies, inc. *http://www.beikimco.com/products/actuator/guide/BEIKimco-VCA-AppGuide2002.pdf.*

[85] Bernard Widrow, Istvan Kollar, and Ming-Chang Liu. Statistical theory of quantization. *IEEE Transactions on Instrumentation and Measurement*, 45(2):353–361, 1996.

[86] Raymond G. Wilson. *Fourier Series and Optical Transform Techniques in Contemporary Optics.* Cambridge University Press, seventh edition, 1999.

[87] W. M. Wonham. Lyapunov criteria for weak stochastic stability. *Journal on Differential Equations*, 2:195–207, 1966.

[88] N. J. Woolf and J. R. P. Angel. Planet finder options i: New linear nulling array configurations. *Astronomical Society of Pacific Conference Series*, 119:285–293, 1997.

[89] Moshe Zakai. A lyapunov criterion for the existence of stationary probability distributions for systems perturbed by noise. *SIAM Journal on Control*, 7(3):390–397, 1969.

[90] K. Zhou, J. C. Doyle, and K. Glover. *Robust and Optimal Control.* Prentice-Hall, 1996.

[91] Kemin Zhou and John C. Doyle. *Essentials of Robust Control.* Prentice Hall, 1998.

Appendix A

Necessary Conditions for Saturation Weighted SLQR

The necessary conditions for obtaining the optimal controller while penalizing the probability of saturation in the cost function are described here. In order to explicitly penalize the probability of saturation, this parameter is directly included in the cost function:

$$\begin{aligned} J(K) &= \hat{\sigma}_y^2 + \rho \sum_{i=1}^{n_u} \rho_i \hat{\sigma}_{u_i}^2 + \sum_{i=1}^{n_u} \upsilon_i \left[1 - N_{ii}(\hat{\sigma}_u)\right] \\ &= \operatorname{tr}\left\{C_1 \hat{\Sigma}_{xx} C_1^T\right\} + \operatorname{tr}\left\{D_{12} K \hat{\Sigma}_{xx} K^T D_{12}^T\right\} + \sum_{i=1}^{n_u} \upsilon_i (1 - N_{ii}), \end{aligned}$$

where υ_i is a design parameter ("knob") that can be used to penalize the probability of saturation of the i^{th} actuator, and $D_{12}^T D_{12}$ is as before a diagonal matrix with elements $\rho\rho_i$.

The optimization problem is again formulated as

$$K = \arg\min_K J(K), \tag{A.1}$$

with two following constraint equations:

$$(A + B_2 N(\hat{\sigma}_u) K)\hat{\Sigma}_{xx} + \hat{\Sigma}_{xx}(A + B_2 N(\hat{\sigma}_u) K)^T = -B_1 B_1^T. \tag{A.2}$$

$$Y_i K \hat{\Sigma}_{xx} K^T Y_i^T = g_i^2(N_{ii}). \tag{A.3}$$

All of the above parameters have already been defined in Chapter 5. As a reminder, N_{ii} is the i^{th} diagonal element of matrix N, and it is a function of $\hat{\sigma}_{u_i}$, i.e. $N_{ii} = f_i(\hat{\sigma}_{u_i})$. The inverse function of f_i is defined as $\hat{\sigma}_{u_i} = g_i(N_{ii})$. The row vector Y_i has the i^{th} element equal to 1 and zeros elsewhere.

The Lagrange multiplier technique is applied to find the minimizing solution, and the Lagrangian is given here by

$$\begin{aligned} \Psi &= \operatorname{tr}\left\{C_1 R C_1^T\right\} + \operatorname{tr}\left\{D_{12} K R K^T D_{12}^T\right\} + \sum_{i=1}^{n_u} \upsilon_i (1 - N_{ii}) \\ &\quad + \operatorname{tr}\left\{\left[(A + B_2 N K)\hat{\Sigma}_{xx} + \hat{\Sigma}_{xx}(A + B_2 N K)^T + B_1 B_1^T\right] Q\right\} \\ &\quad + \sum_{i=1}^{n_u} \lambda_i \left(Y_i K R K^T Y_i^T - g_i^2(N_{ii})\right). \end{aligned} \tag{A.4}$$

Differentiating Ψ with respect to K, N_{ii}, $\hat{\Sigma}_{xx}$, Q, and λ_i, the following necessary conditions are found. Setting $\frac{\partial \Psi}{\partial K} = 0$ results in

$$\{NB_2^TQ + [D_{12}^TD_{12} + \sum_{i=1}^{n_u} \lambda_i Y_i^T Y_i]K\}\hat{\Sigma}_{xx} = 0$$

$$\{NB_2^TQ + \Phi K\}\hat{\Sigma}_{xx} = 0 \tag{A.5}$$

where $\Phi = D_{12}^TD_{12} + \sum_{i=1}^{n_u} \lambda_i Y_i^T Y_i = D_{12}^TD_{12} + \Lambda$ is a diagonal matrix with $\rho\rho_i + \lambda_i$ on the i^{th} diagonal, and Λ is also a diagonal matrix with elements λ_i. Next, setting $\frac{\partial \Psi}{\partial N_{ii}} = 0$,

$$-v_i + 2B_{2i}^TQ\hat{\Sigma}_{xx}K_1^T - \frac{2\lambda_i\, g_i(N_{ii})}{g_i'(N_{ii})} = 0, \tag{A.6}$$

where B_{2i} is the i^{th} column of B_2, and $g_i'(N_{ii})$ is the partial derivative of g_i with respect to N_{ii}. Next for $\frac{\partial \Psi}{\partial \hat{\Sigma}_{xx}} = 0$,

$$(A + B_2NK)^TQ + Q(A + B_2NK) + K^T(D_{12}^TD_{12} + \sum_{i=1}^{n_u} \lambda_i Y_i^T Y_i)K + C_1^TC_1 = 0.$$

This expression can be simplified using the definition of Φ

$$(A + B_2NK)^TQ + Q(A + B_2NK) + K^T\Phi K + C_1^TC_1 = 0. \tag{A.7}$$

Finally, the derivatives of $\frac{\partial \Psi}{\partial Q}$ and $\frac{\partial \Psi}{\partial \lambda_i} = 0$ recover the two constraint equations given by Equation A.2 and A.3, respectively.

The optimal controller is found by solving Equation A.5,

$$K = -\Phi^{-1}NB_2^TQ. \tag{A.8}$$

Substituting Equation A.8 into Equation A.7, a Riccati equation describing Q is found,

$$A^TQ + QA - QB_2N\Phi^{-1}NB_2^TQ + C_1^TC_1 = 0. \tag{A.9}$$

Substituting Equation A.8 into Equation A.2, the closed-loop Lyapunov equation can be written as

$$(A - B_2N\Phi^{-1}NB_2^TQ)\hat{\Sigma}_{xx} + \hat{\Sigma}_{xx}(A - B_2N\Phi^{-1}NB_2^TQ)^T + B_1B_1^T = 0. \tag{A.10}$$

To determine the necessary conditions for N_{ii} and λ_i, pre- and post-multiply Equation A.5 by Y_i and $K^TY_i^T$,

$$Y_i\Phi K\hat{\Sigma}_{xx}K^TY_i^T + Y_iNB_2^TQ\hat{\Sigma}_{xx}K^TY_i^T = 0. \tag{A.11}$$

Using the definition of Y_i, the above equation can also be expressed as

$$(\rho\rho_i + \lambda_i)Y_iK\hat{\Sigma}_{xx}K^TY_i^T + N_{ii}B_{2i}^TQ\hat{\Sigma}_{xx}K_i^T = 0. \tag{A.12}$$

By substituting in Equation A.3 and Equation A.6 for the first and second term in the left-hand-side of the above equation, an equation relating λ_i and N_{ii} is found

$$\lambda_i + \frac{0.5v_iN_{ii} + \rho\rho_i\, g_i^2(N_{ii})}{g_i^2(N_{ii}) + N_{ii}g_i(N_{ii})g_i\prime(N_{ii})} = 0. \tag{A.13}$$

Finally substitute Equation A.8 into Equation A.3 to obtain

$$Y_i \Phi^{-1} N B_2^T Q \hat{\Sigma}_{xx} Q B_2 N \Phi^{-1} Y_i^T - g_i^2(N_{ii}) = 0. \tag{A.14}$$

Equations A.8-A.14 are a set of nonlinear, coupled equations that need to be solved simultaneously in order to obtain the optimal controller. The numerical solution procedures suggested in Chapter 5 can be used to solve these equations, adding the terms in v_i as necessary.

Appendix B

Output Feedback Extension

The necessary equations for extending the full-state control strategy to output feedback control design are derived here. The system dynamics can be described by the following equations:

$$\begin{aligned} dx &= Axdt + B_1dw_1 + B_2\phi(u)dt \\ y &= \begin{bmatrix} C_1 \\ 0 \end{bmatrix} x + \begin{bmatrix} 0 \\ D_{12} \end{bmatrix} u \\ y_m &= C_2x + D_{21}dw_2 \end{aligned} \tag{B.1}$$

where y is the performance variable that contains the controlled output, $y = C_1x$, and the control penalty, $D_{12}u$. The measured plant output is denoted by y_m. The state disturbance is w_1, and the measurement noise is w_2, assumed to be uncorrelated, zero mean, unit-intensity white noise processes. The intensity of w_1 and w_2 can be changed by changing the values of matrices B_1 and D_{21}, respectively.

The general form of an output feedback controller for this system is

$$\begin{aligned} dx_c &= A_cx_cdt - B_cy_mdt \\ u &= Kx_c \end{aligned} \tag{B.2}$$

The objective is to find a control design (A_c, B_c, K) that minimizes the cost:

$$\begin{aligned} J &= \hat{\sigma}_y^2 + \rho\sum_{i=1}^{n_u}\rho_i\hat{\sigma}_{u_i}^2 \\ &= \text{tr}\left\{C_1\hat{\Sigma}_{xx}C_1^T\right\} + \text{tr}\left\{D_{12}K\hat{\Sigma}_{x_cx_c}K^TD_{12}^T\right\}. \end{aligned} \tag{B.3}$$

The first step in deriving the necessary equations is to combine the system states (x) with the controller states (x_c) into a single state vector $\bar{x} = [x\ x_c]^T$. Similarly, the disturbance and measurement noises can also be grouped into a single perturbation vector, $w = [w_1\ w_2]^T$. The closed-loop system can then be written as

$$\begin{aligned} d\bar{x} &= \bar{A}\bar{x}dt + \bar{B}_1dw \\ y &= \bar{C}\bar{x} \\ u &= \bar{K}\bar{x}, \end{aligned} \tag{B.4}$$

where

$$\bar{A} = \begin{bmatrix} A & B_2NK \\ -B_cC_2 & A_c \end{bmatrix} \quad \bar{B} = \begin{bmatrix} B_1 \\ -B_cD_{21} \end{bmatrix}$$

$$\bar{C} = \begin{bmatrix} C_1 & D_{12}K \end{bmatrix} \quad \bar{K} = \begin{bmatrix} 0 & K \end{bmatrix}$$

and stochastic linearization is used above to replace $\phi(u)$ with NKx_c. The constraint equations for N can be written as

$$\bar{A}\bar{P} + \bar{P}\bar{A}^T + \bar{B}_1\bar{B}_1^T = 0 \tag{B.5}$$

$$Y_iKP_{22}K^TY_i^T = g_i^2(N_{ii}), \tag{B.6}$$

where

$$\bar{P} = \begin{bmatrix} P_{11} & P_{12}^T \\ P_{12} & P_{22} \end{bmatrix}, \quad P_{11} = \hat{\Sigma}_{xx}, \quad P_{22} = \hat{\Sigma}_{x_cx_c}.$$

Rewriting the cost function from Equation B.3 as

$$J = \operatorname{tr}\left\{C_1P_{11}C_1^T\right\} + \operatorname{tr}\left\{D_{12}KP_{22}K^TD_{12}^T\right\}, \tag{B.7}$$

the Lagrangian technique is again used to obtain the necessary conditions for J to be minimized. Incorporating the constraint equations (B.5 and B.6), the Lagrangian for this problem is given by

$$\begin{aligned} \Psi \;=\; & \operatorname{tr}\left\{C_1P_{11}C_1^T\right\} + \operatorname{tr}\left\{D_{12}KP_{22}K^TD_{12}^T\right\} + \sum_{i=1}^{n_u} v_i(1 - N_{ii}) \\ & + \operatorname{tr}\left\{[\bar{A}\bar{P} + \bar{P}\bar{A}^T + \bar{B}_1\bar{B}_1^T]\bar{Q}\right\} \\ & + \sum_{i=1}^{n_u} \lambda_i(Y_iKP_{22}K^TY_i^T - g_i^2(N_{ii})), \end{aligned} \tag{B.8}$$

where $\bar{Q}$ is the Lagrange multiplier matrix,

$$\bar{Q} = \begin{bmatrix} Q_{11} & Q_{12} \\ Q_{12}^T & Q_{22} \end{bmatrix}.$$

Differentiating Ψ with respect to $(K, B_c, A_c, N_{ii}, \bar{P})$ and equating the results to zero, the necessary equations are obtained:

$$NB_2^T(Q_{11}P_{12}^T + Q_{12}P_{22}) + \Phi KP_{22} = 0. \tag{B.9}$$

$$Q_{22}B_cD_{21}D_{21}^T - (Q_{12}^TP_{11} + Q_{22}P_{12})C_2^T = 0. \tag{B.10}$$

$$Q_{12}^TP_{12}^T + Q_{22}P_{22} = 0. \tag{B.11}$$

$$-v_i + 2B_{2i}^T(Q_{11}P_{12}^T + Q_{12}P_{22})K_i^T - \frac{2\lambda_i\, g_i(N_{ii})}{g_i'(N_{ii})} = 0. \tag{B.12}$$

$$\bar{A}^T\bar{Q} + \bar{Q}\bar{A} + \lambda_i\bar{K}\Lambda\bar{K} = 0. \tag{B.13}$$

In addition, setting $\frac{\partial \Psi}{\partial Q} = 0$ and $\frac{\partial \Psi}{\partial \lambda_i} = 0$ will recover the two constraint equations (B.5, B.6).

To obtain the required relation between λ_i and N_{ii}, pre- and post-multiply Equation B.9 by Y_i and $K^T Y_i^T$, respectively.

$$\begin{aligned} Y_i \Phi K P_{22} K^T Y_i^T + Y_i N B_2^T (Q_{11} P_{12}^T + Q_{12} P_{22}) K^T Y_i^T &= 0 \\ (\rho \rho_i + \lambda_i) Y_i K P_{22} K^T Y_i^T + N_{ii} B_{2i}^T (Q_{11} P_{12}^T + Q_{12} P_{22}) K_i^T &= 0. \end{aligned}$$

Substituting Equation B.12 and B.6 into the above equation produces

$$\lambda_i + \frac{0.5 \upsilon_i N_{ii} + \rho \rho_i \, g_i^2(N_{ii})}{g_i^2(N_{ii}) + N_{ii} g_i(N_{ii}) g_i{\prime}(N_{ii})} = 0. \tag{B.14}$$

as the required constraint.

The optimal K is obtained by rearranging Equation B.9,

$$K = -\Phi^{-1} N B_2^T (Q_{11} P_{12}^T + Q_{12} P_{22}) P_{22}^{-1}. \tag{B.15}$$

Similarly, arrangement of Equation B.10 gives B_c as

$$B_c = Q_{22}^{-1} (Q_{12}^T P_{11} + Q_{22} P_{12}) C_2^T (D_{21} D_{21}^T)^{-1}, \tag{B.16}$$

where from Equation B.11

$$-Q_{22}^{-1} Q_{12}^T P_{12}^T P_{22}^{-1} = I. \tag{B.17}$$

Define $T^{-1} = -Q_{22}^{-1} Q_{12}^T$ and $T = P_{12}^T P_{22}^{-1}$. Then, according to Equation B.17, $T^{-1} T = I$. Furthermore, define

$$\begin{aligned} P &= P_{11} - P_{12}^T P_{22}^{-1} P_{12} \\ Q &= Q_{11} - Q_{12} Q_{22}^{-1} Q_{12}^T, \end{aligned}$$

and substitute the new variables (T, T^{-1}, P, Q) into Equations B.15 and B.16 to obtain

$$K = -\Phi^{-1} N B_2^T Q T, \tag{B.18}$$

$$B_c = -T^{-1} P C_2^T (D_{21} D_{21}^T)^{-1}. \tag{B.19}$$

Equation B.13 can be expanded into four separate equations,

$$A^T Q_{11} + Q_{11} A - C_2^T B_c^T Q_{12}^T - Q_{12} B_c C_2 + C_1^T C_1 = 0 \tag{B.20}$$

$$A^T Q_{12} + Q_{12} A_c - C_2^T B_c^T Q_{22} + Q_{11} B_2 N K = 0 \tag{B.21}$$

$$A_c^T Q_{12}^T + Q_{12}^T A - Q_{22} B_c C_2 + K^T N B_2^T Q_{11} = 0 \tag{B.22}$$

$$A_c^T Q_{22} + Q_{22} A_c + K^T N B_2^T Q_{12} + Q_{12}^T B_2 N K + K^T \Phi K = 0 \tag{B.23}$$

Similarly, Equation B.5 can also be expanded in the same fashion

$$A P_{11} + P_{11} A^T + B_2 N K P_{12} + P_{12}^T K^T N B_2^T + B_1 B_1^T = 0 \tag{B.24}$$

$$A_c P_{12} + P_{12} A^T + P_{22} K^T N B_2^T - B_c C_2 P_{11} = 0 \tag{B.25}$$

$$A P_{12}^T + P_{12}^T A_c^T + B_2 N K P_{22} - P_{11} C_2^T B_c^T = 0 \tag{B.26}$$

$$A_cP_{22} + P_{22}A_c^T - B_cC_2P_{12}^T - P_{12}C_2^TB_c^T + B_cD_{21}D_{21}^TB_c^T = 0 \tag{B.27}$$

Now pre-multiply Equation B.26 by T^{-1} and subtract the resulting equation from Equation B.27, to produce (after some additional manipulation)

$$A_c = T^{-1}(A + B_2NKT^{-1} + TB_cC_2)T. \tag{B.28}$$

If Equation B.21 is post-multiplied by T^{-1}, and the controller parameters (A_c, B_c, K) are substituted with Equations B.28, B.19, and B.18, respectively, the following Lyapunov equation is obtained,

$$(A - PC_2^T(D_{21}D_{21}^T)^{-1}C_2)^TS + S(A - PC_2^T(D_{21}D_{21}^T)^{-1}C_2) + QB_2N\Phi^{-1}NB_2^TQ = 0, \tag{B.29}$$

where $S = Q_{12}Q_{22}^{-1}Q_{12}^T$. By pre-multiplying Equation B.25 by T and again substituting in previously defined control parameters (A_c, B_c, K), a second Lyapunov equation is found:

$$(A - B_2N\Phi^{-1}NB_2^TQ)R + R(A - B_2N\Phi^{-1}NB_2^TQ)^T + PC_2^T(D_{21}D_{21}^T)^{-1}C_2P = 0, \tag{B.30}$$

where $R = P_{12}^TP_{22}^{-1}P_{12}$.

Substitute (A_c, B_c, K) into Equation B.20 and use Equation B.29 to obtain the control Riccati equation (B.38),

$$A^TQ + QA - QB_2N\Phi^{-1}NB_2^TQ + C_1^TC_1 = 0. \tag{B.31}$$

Repeating this procedure, substitute (A_c, B_c, K) into Equation B.24 and use Equation B.30 to obtain the estimator Riccati equation (B.39),

$$AP + PA^T - PC_2^T(D_{21}D_{21}^T)^{-1}C_2P + B_1B_1^T = 0 \tag{B.32}$$

¿From Equation B.18 and definitions of P and R above, the cost function given by Equation B.7 can be written as

$$J = \mathrm{tr}\left\{C_1(P + R)C_1^T + D_{12}KRK^TD_{12}^T\right\}, \tag{B.33}$$

In addition, a similarity transform can be applied to the observer based controller, $(A_c, B_c, K) \rightarrow (T^{-1}A_cT, TB_c, KT^{-1})$ to eliminate matrix T from Equations B.28, B.19, and B.18. As a result, the optimal output feedback controller can be computed by

$$\begin{aligned} A_c &= A + B_2NK + B_cC_2 & \text{(B.34)} \\ B_c &= -PC_2^T(D_{21}D_{21}^T)^{-1} & \text{(B.35)} \\ K &= -\Phi^{-1}NB_2^TQ, & \text{(B.36)} \end{aligned}$$

where (Λ, N, P, Q, R, S) are solutions to the above derived set of nonlinear, coupled algebraic equations:

$$\lambda_i + \frac{0.5\upsilon_iN_{ii} + \rho\rho_i\, g_i^2(N_{ii})}{g_i^2(N_{ii}) + N_{ii}g_i(N_{ii})g_i{\prime}(N_{ii})} = 0, \tag{B.37}$$

$$A^TQ + QA - QB_2N\Phi^{-1}NB_2^TQ + C_1^TC_1 = 0, \tag{B.38}$$

$$AP + PA^T - PC_2^T(D_{21}D_{21}^T)^{-1}C_2P + B_1B_1^T = 0, \tag{B.39}$$

$$(A + B_cC_2)^TS + S(A + B_cC_2) + QB_2N\Phi^{-1}NB_2^TQ = 0, \tag{B.40}$$

$$(A + B_2NK)R + R(A + B_2NK)^T + PC_2^T(D_{21}D_{21}^T)^{-1}C_2P = 0. \tag{B.41}$$

$$Y_iKRK^TY_i^T - (g_i(N_{ii}))^2 = 0 \tag{B.42}$$

Appendix C

MATLAB Code for Implementing Solution Methods

Representative MATLAB code is included here to illustrate software implementations of the numerical solution methods suggested in 5.4.

```
function out = dist_iter(opt,SLQR,sat)

%-----------------------------------------------------------------------
%
% Numerical algorithm for solving coulped SLQR necessary conditions
% for one or two actuator delay line system.  This code varies the
% disturbance intensity in order to obtain a family of solutions.  The
% algorithm also provides the LQR solutions for comparison purposes.
%
% Inputs:
%          opt = 1          % voice coil
%              = 2          % PZT
%              = 3          % voice coil + PZT
%
%          SLQR = 0         % LQR control design
%               = 1         % SLQR control design
%
%          sat = [.]        % saturation level of each actuator
%                             (default sat = [2 10]
%
% Outputs:  (the output parameters are saved in a structure form)
%
%          out.N = Stochastic linearization gain
%          out.Z = closed-loop RMS output
%          out.K = Optimal feedback gain
%          out.U = closed-loop RMS control
%          out.del = consistency constraint measure
%          out.rho = control penalty that achieves the desired performance
%          out.Q = Riccati equation solution
%          out.R = Lyapunov equation solution
%          out.Lam = Lagrange multiplier
%
% Written by:  Kuo-Chia Liu
%-----------------------------------------------------------------------

% Define performance targets
Ztarget = 1;
Ztol = Ztarget/100;

% Control penalties shape
if (opt>=3)
    rsize = eye(2);
    rhoN = zeros(1,2);
```

```
else
    rsize = 1;
    rhoN = 0;
end

% Define model parameters
% Number of measurements
Splnt.nmeas = 1;

% Number of actuators
if (opt>=3)
    Splnt.ncon = 2;
else
    Splnt.ncon = 1;
end
Splnt.xvmax = 1.5e-3;
Splnt.xpmax = 10e-6;

% Number of performance variables
Splnt.nz = 1;

% Disturbance parameters
Splnt.nw = 1;
Sdist.F = 1; Sact = 0;
Sdist.w = [30 1000];

plant = model_ODL(opt,Sdist,Sact,Splnt);

% Disturbance intensity levels
if opt == 1         % VC case
    distmag = 1e-2*[linspace(0.1,0.58,5) linspace(0.58,3.53,100)];
elseif opt == 2     % PZT case
    distmag = 1e-2*linspace(0.1,1.345,100);
elseif opt == 3     % VC + PZT
    distmag = 1e-2*[0.1 0.5 0.9 linspace(1,5,20)];
else
    disp('Incorrect option')
end


% Varying disturbance level
frst = 1;
rhold = 10;

for  kr = 1:length(distmag)

    Sdist.F = distmag(kr);
    plant = model_ODL(opt,Sdist,Sact,Splnt);

    % compute open loop variance
    Xopen = lyap(plant.a,plant.b(:,1)*plant.b(:,1)');
    stdOL(kr) = sqrt(plant.c(1,:)*Xopen*plant.c(1,:)');

    % use rho iteration to find the controller that satisfies performance target
    if SLQR
        [rhold,N(kr,:),Z(kr),K{kr},U(kr,:),J(kr),del(kr,:),rho_fin{kr},Qric{kr},Rlyap{kr},...
                LAM{kr}] = rho_iter(plant,Splnt,sat,rhoN,opt,SLQR,Ztarget,Ztol,frst,rhold);
    else
        [rhold,Z(kr),K{kr},U(kr,:),rho_fin{kr},Qric{kr},Rlyap{kr}] = ...
                rho_iter(plant,Splnt,sat,rhoN,opt,SLQR,Ztarget,Ztol,frst,rhold);
    end
    kr
end


% Generate output
if SLQR
    out.N = N;      out.Z = Z;          out.K = K;      out.U = U;
```

```
    out.del = del;  out.rho = rho_fin;  out.Q = Qric;   out.R = Rlyap;
    out.Lam = LAM;
else
    out.Z = Z;      out.K = K;          out.U = U;      out.rho = rho_fin;
    out.Q = Qric;   out.R = Rlyap;
end


%--------------------------------------------------------------------
%--------------------------------------------------------------------
function [rhold,varargout] = ...
rho_iter(plant,Splnt,sat,rhoN,opt,SLQR,Ztarget,Ztol,frst,rhold);

%--------------------------------------------------------------------
%
% The algorithm performs rho iteration until the predicted RMS output is
% equal or less than the specified RMS output.
%
%--------------------------------------------------------------------

lzt = log10(Ztarget); lzo = 0;

if (frst)
    frst = 0;
    rhoL = -2;                  %Initialize lower rho limit
    rhoU = 10;                  %Initialize upper rho limit
else
    rhoL = rhold - 1;
    rhoU = rhold + 1;
end

jj = 1; Z = 0;

rsize = eye(Splnt.ncon);
rhoM = rsize*(rhoL+rhoU)/2;

% rho iterate to achieve desired performance

while (abs(Z-Ztarget)>Ztol) & (jj<20)

    theRho = 10^rhoM;

    if (SLQR)           % Find SLQR solution
        if opt < 3      % Single actuator case
            [N,Z,K,U,J,Del,Qric,Rlyap,LAM] = slqr_bisect(plant,Splnt,sat,rhoM,rhoN);
        else            % Two actuator case
            Nmin = [0.01 0.01];
            Nmax = [0.999 0.999];
            [N,Z,K,U,J,Del,Qric,Rlyap,LAM] = ...
            slqr_mesh_ii(plant,Splnt,sat,rhoM,rhoN,Nmin,Nmax);
        end
    else                % Find LQR solution
        [Z,U,K,Q,R] = lqr_aliu_new(plant,Splnt,theRho);
        N = sat./sat;
        Del = 0*sat;
    end

    lz = log10(Z);
    rho = rhoM(1,1);

    if (jj<2)
        if Z>=Ztarget
            rhoU = rho;
        else
            rhoL = rho;
        end
        rhoM = rsize*(rhoL+rhoU)/2;
    else
```

```
        m = (lz-lzo)/(rho-rhold);
        rhoM = rsize*(rho + (lzt-lz)/m);
    end

    rhold = rho;
    jj = jj+1;
    lzo = lz;

end  % Found the desired controller

if (jj>=20)
    disp('Failed to find solution after 20 iterations');
    N = 2;
    break;
end

% Generate output
if (SLQR)
    varargout(1) = {N};     varargout(2) = {Z};      varargout(3) = {K};
    varargout(4) = {U};     varargout(5) = {J};      varargout(6) = {Del};
    varargout(7) = {rhoM};  varargout(8) = {Qric};   varargout(9) = {Rlyap};
    varargout(10) = {LAM};
else
    varargout(1) = {Z};     varargout(2) = {K};     varargout(3) = {U};
    varargout(4) = {rhoM};  varargout(5) = {Q};     varargout(6) = {R};
end


%-----------------------------------------------------------------------
%-----------------------------------------------------------------------
function [varargout] = slqr_bisect(plant,Splnt,sat,rhoU,rhoN)

%-----------------------------------------------------------------------
%
% Bisection algorithm that solves necessary conditions in order to obtain
% the optimal SLQR controller
%
%-----------------------------------------------------------------------

% System setup
[a,b,c,d] = ssdata(plant);

ncon = Splnt.ncon;
nw = Splnt.nw;
nz = Splnt.nz;
nmeas = Splnt.nmeas;

% Control penalty
d(nz+[1:ncon],nw+nmeas+[1:ncon]) = sqrt(rhoU);

nx = max(size(a));
[i,m] = size(b);
[p,i] = size(c);

p1 = p - nmeas;
m1 = m - ncon;

c1 = c(1:p1,:);
c2 = c(p1+1:p,:);
b1 = b(:,1:m1);
b2 = b(:,m1+1:m);

d11 = d(1:p1,1:m1);
d12 = d(1:p1,m1+1:m);
d21 = d(p1+1:p,1:m1);
d22 =d(p1+1:p,m1+1:m);

% Initialize N and del
```

```
N1 = 0;
N2 = 1;
del = 1;
kk = 1;

% Iterate until consistent constraints are satisfied
while (abs(del)>=1e-5) & (kk<=20)

    N = (N1 + N2)/2;
    x = sat./(sqrt(2)*erfinv(N));

    dfdSu = -sqrt(2/pi).*sat.*exp(-sat.^2/2./x.^2);

    if dfdSu == 0
        disp('Warning -- dfdSu = 0')
    end

    % Solve lambda
    LAM = dfdSu.*(-1/2*rhoN.*N - (d12'*d12)'.*x.^2)./(dfdSu + N.*x);
    LAM = LAM./x.^2;
    ndl = N./(d12'*d12+LAM);

    % Solve Riccati equation
    hamQ = [a -b2*N*ndl*b2';
        -c1'*c1 -a'];

    [y1,y2,fail] = ric_schr(hamQ);
    Q = y2/y1;

    if fail
        del = 1e5*ones(1,length(N));
        Q = 0;
        R = 0;
        disp('Warning -- Cannot solve Riccati solution')
        return
    end

    % Find feedback gain K
    K = ndl*b2'*Q;
    acl = a-b2*N*K;

    % Solve closed-loop Lyapunov equations
    R = lyap(a-b2*N*ndl*b2'*Q,b1*b1');

    % Compute delta
    tempvar = (b2'*Q*R*Q*b2)*ndl^2;

    del = tempvar-x^2;

    if del<0
        N1 = N;
    else
        N2 = N;
    end

    kk = kk+1;

    if kk == 100
        display('kk = 100')
    end

end            %end while loop (consistent constraints satisfied)


% Find closed-loop output variance and overall cost

stdZ = sqrt(trace(c1*R*c1'));
stdU= sqrt(diag(K*R*K'));
```

```
Jcost = stdZ^2+trace(rhoU*K*R*K');

% Output variables
varargout(1) = {N};       varargout(2) = {stdZ};      varargout(3) = {K};

varargout(4) ={stdU};     varargout(5) = {Jcost};     varargout(6) = {del};

varargout(7) = {Q};       varargout(8) = {R};         varargout(9) = {LAM};


%----------------------------------------------------------------------
%----------------------------------------------------------------------
function [N,stdZ,Klqr,stdU,Jcost,Del,Qi,Ri,LAMi] =
slqr_mesh_ii(plant,Splnt,sat,rhoU,...
    rhoN,Nmin,Nmax)

%-------------------------------------------------------------------------
%
% Exhaustive search algorithm that solves necessary conditions for the
% multi-actuator SLQR control problem.
%
%-------------------------------------------------------------------------

if nargin < 7
    N1max = 1-1e-8;
    N2max = 1-1e-8;
else
    N1max = Nmax(1);
    N2max = Nmax(2);
end

% Plant setup
as = plant.a;
bs = plant.b;
cs = plant.c;
ds = plant.d;

ncon = Splnt.ncon;
nw = Splnt.nw;
nz = Splnt.nz;
nmeas = Splnt.nmeas;

% Control penalty
ds(nz+[1:ncon],nw+nmeas+[1:ncon]) = sqrt(rhoU);


% Start main mesh iteration code
clear del

% Parameters to control mesh generation and refinement

fac = 5;
ncell = 11;
niter = 12;

ntol = 1e-3;
atol = 1-1e-5;

N1min = Nmin(1);
N2min = Nmin(2);

good = 0;

for kk = 1:niter,

    N1 = linspace(N1min,N1max,ncell);
    N2 = linspace(N2min,N2max,ncell);
```

```
    for ii=1:ncell,
        for jj=1:ncell,
            [deli,LAMi,Qi,Ri,klqr,su,sz] = EVAL_lqrsat(as,bs,cs,ds,nmeas,ncon,rhoN,...
                [N1(ii) N2(jj)],sat,0);
            del(ii,jj) = real(sqrt(deli'*deli));
        end
    end

    % find the minimum value in the current partition

    amin = min(del(:));

    if (N1max-N1min<ntol) & (N2max-N2min<ntol)
        [n1dex,n2dex]=find(del==amin);
        N = [N1(n1dex) N2(n2dex)];
        good = 1;
        break;
    end

    % find all elements of del within fac of amin
    nfac = 10^(-(kk-1));
    [n1dex,n2dex] = find(del<amin*(1+fac*nfac));

    % Determine the N1,N2 indices of elements of idx
    nmin = min(n1dex);
    if (nmin>1)
        nmin = nmin-1;
    end
    N1min = N1(nmin);

    nmin = min(n2dex);
    if (nmin>1)
        nmin = nmin-1;
    end
    N2min = N2(nmin);

    nmax = max(n1dex);
    if (nmax < ncell)
        nmax = nmax+1;
    end
    N1max = N1(nmax);

    nmax = max(n2dex);
    if (nmax < ncell)
        nmax = nmax+1;
    end
    N2max = N2(nmax);

end

if (~good)
    [N1min,N1max]
    [N2min,N2max]
    N=[N1min+N1max,N2min+N2max]/2;
end

% Solve for optimal controller and output variance after satisfying consistent constraint
[Fdel,LAMi,Qi,Ri,Klqr,stdU,stdZ] = EVAL_lqrsat(as,bs,cs,ds,nmeas,ncon,rhoN,N,sat,0);
stdU = stdU';
Jcost = stdZ.^2 + trace(rhoU*Klqr*Ri*Klqr');
Del = sqrt(Fdel'*Fdel);


%----------------------------------------------------------------------
%----------------------------------------------------------------------
function [del,LAM,Q,R,klqr,su,sz] = EVAL_lqrsat(a,b,c,d,p2,m2,rho,N,sat,flag)
%-----------------------------------------------------------------------
```

```
%
% This algorithm evaluates the consistency constraints for a given guess
% of N.  The variable del measures how well the constraint is satisfied.
% If the del is below the desired accuracy, this algorithm also provides
% the optimal control solutions.
%
%-----------------------------------------------------------------------

% Plant setup
nx = max(size(a));
[i,m] = size(b);
[p,i] = size(c);

p1 = p - p2;
m1 = m - m2;

c1 = c(1:p1,:);
c2 = c(p1+1:p,:);
b1 = b(:,1:m1);
b2 = b(:,m1+1:m);

d11 = d(1:p1,1:m1);
d12 = d(1:p1,m1+1:m);
d21 = d(p1+1:p,1:m1);
d22 = d(p1+1:p,m1+1:m);

% Solve for RMS control (x) from guess of N
x = sat./(sqrt(2)*erfinv(N));
dfdSu = -sqrt(2/pi)*sat.*(exp(-sat.^2/2./x.^2)./x.^2);

if find(dfdSu == 0)
    disp('Warning -- dfdSu = 0')
end

% Solve for lambda
LAM = dfdSu.*(-1/2*rho.*N - diag(d12'*d12)'.*x.^2)./(dfdSu.*x.^2 + N.*x);

N = diag(N); LAM = diag(LAM); x = diag(x);

% Solve Riccati equation
hamQ = [a -b2*N*inv(d12'*d12+LAM)*N*b2';
    -c1'*c1 -a'];

[y1,y2,fail] = ric_schr(hamQ); Q = y2/y1;

if fail
    del = 1e6*ones(length(N),1);
    Q = 0;
    R = 0;
    disp('Warning -- Cannot solve Riccati solution')
    return
end

% Solve control gain klqr
klqr = inv(d12'*d12+LAM)*N*b2'*Q;

% Solve Lyapunov equation
acl = a-b2*N*klqr; R = lyap(acl,b1*b1');

% Compute delta
suuhat2 = klqr*R*klqr';
su = real(sqrt(diag(suuhat2)));
sz = sqrt(trace(c1*R*c1'));

smallu = su<=1e-10; su = su + smallu*1e-5; Nhat = erf(sat'./(su*sqrt(2)));

del =diag(N)-Nhat;
```

5000
18